

KATHOLIEKE UNIVERSITEIT LEUVEN
FACULTEIT INGENIEURSWETENSCHAPPEN
DEPARTEMENT COMPUTERWETENSCHAPPEN
AFDELING NUMERIEKE ANALYSE EN
TOEGEPASTE WISKUNDE
Celestijnenlaan 200A – B-3001 Leuven

MULTISCALE AND EQUATION-FREE COMPUTING FOR LATTICE BOLTZMANN MODELS

Promotoren:
Prof. Dr. ir. D. Roose
Prof. Dr. ir. K. Lust
Prof. Dr. W. Vanroose

Proefschrift voorgedragen tot
het behalen van het doctoraat
in de ingenieurswetenschappen

door

Pieter VAN LEEMPUT

May 2007



KATHOLIEKE UNIVERSITEIT LEUVEN
FACULTEIT INGENIEURSWETENSCHAPPEN
DEPARTEMENT COMPUTERWETENSCHAPPEN
AFDELING NUMERIEKE ANALYSE EN
TOEGEPASTE WISKUNDE
Celestijnenlaan 200A – B-3001 Leuven

MULTISCALE AND EQUATION-FREE COMPUTING FOR LATTICE BOLTZMANN MODELS

Jury:
Prof. Dr. ir. D. Vandermeulen, voorzitter
Prof. Dr. ir. D. Roose
Prof. Dr. ir. K. Lust (U. Groningen, NL)
Prof. Dr. W. Vanroose (U. Antwerpen, B)
Prof. Dr. ir. A. Barbé
Prof. Dr. ir. S. Vandewalle
Prof. Dr. ir. B. Blanpain
Prof. Dr. M. Junk (U. Konstanz, D)

Proefschrift voorgedragen tot
het behalen van het doctoraat
in de ingenieurswetenschappen

door

Pieter VAN LEEMPUT

U.D.C. 519.6, 681.3*I6

May 2007

© Katholieke Universiteit Leuven — Faculteit Ingenieurswetenschappen
Arenbergkasteel, B-3001 Leuven, Belgium

Alle rechten voorbehouden. Niets uit deze uitgave mag worden vermenigvuldigd en/of openbaar gemaakt worden door middel van druk, fotokopie, microfilm, elektronisch of op welke andere wijze ook zonder voorafgaande schriftelijke toestemming van de uitgever.

All rights reserved. No part of the publication may be reproduced in any form by print, photoprint, microfilm or any other means without written permission from the publisher.

D/2007/7515/41

ISBN 978-90-5682-806-6

Multiscale and Equation-Free Computing for Lattice Boltzmann Models

Pieter Van Leemput
Department of Computer Science, K.U.Leuven
Celestijnenlaan 200A, B-3001 Leuven, België

Abstract

Many physical and chemical systems can be described at different levels of abstraction due to a separation of time and space scales in their dynamics. We consider two multiscale modeling techniques that take advantage of this scale separation: the equation-free framework developed by Kevrekidis *et al.*, which enables a time simulation for an unknown macroscopic model using only microscopic or mesoscopic simulations, and spatially hybrid models, which couple a microscopic/mesoscopic particle-based model to a macroscopic continuum model in space. At the microscopic/mesoscopic level, we consider lattice Boltzmann models (LBMs) for one-dimensional reaction-diffusion systems.

First, we show that time stepper based numerical bifurcation analysis techniques developed for partial differential equations (PDEs) can be used for LBMs as well. We use the LBM or the "coarse" equation-free time stepper wrapped around the LBM as the time stepper.

Second, we focus on the multiscale interfacing problem. During initialization and spatial coupling, one has to solve a one-to-many problem. A few macroscopic quantities have to be mapped to meaningful values for a larger set of microscopic/mesoscopic variables. We perform an extensive study of the influence of the initialization process (called lifting or reconstruction) on the minimal time step of the coarse time stepper and the accuracy of the results. Furthermore, we analyze the behavior of the so-called constrained runs initialization scheme for the LBMs considered. We prove that the scheme is unconditionally stable and that it converges to a first order correct approximation of the Chapman-Enskog relations. We also implement constrained runs schemes that use interpolation techniques to obtain a higher order accuracy.

Finally, we analyze the spatial discretization error of the hybrid model obtained by spatially coupling a LBM to a finite difference discretization of a PDE and show that the global error of the hybrid model is one order less accurate than the local error made at the interface. At the interface, the Chapman-Enskog relations or the constrained runs scheme can be used.

Preface

This thesis is the result of my 4.5 years of research in the field of numerical analysis and applied mathematics. Several people have helped me to get to this point and I would like to thank them here.

Foremost, I would like to thank my promotors: Dirk Roose, for his overall support and his strong believe in my abilities as a researcher, exemplified in the numerous conferences I could go to; Kurt Lust, for his substantial support on the numerical bifurcation analysis; and Wim Vanroose, for our excellent working relation and the many informal discussions we had. I thank my promotors and my assessors, Stefan Vandewalle and André Barbé, for carefully reading this manuscript, as well as the other jury members, Michael Junk, Bart Blanpain and Dirk Vandermeulen, for their contribution to my PhD defense. Let me also thank Yannis Kevrekidis for supporting our numerical analysis of the equation-free framework.

Over the last four years, we have established the *micro-macro* research group at the department. Dirk, Kurt, Giovanni, Christophe, Wim, Yves, Pieter G. and Sofie, thanks for creating this open platform for discussions. Special thanks go to Koen, Christophe and Giovanni for being nice office mates and for the excellent discussions, collaborations and conference company. Thanks also to the other TWR and DeptCW colleagues that I met during the years for providing a good working environment. In particular, I would like to thank Margot and Denise for taking care of all the administrative paperwork and Paul Dierckx, for the pleasant working relation in teaching exercises for his courses.

I have fond memories of the various conferences and workshops I have been to and the researchers I met there, in particular Frederik and Sander from MTM (completing the Flemish LBM community), the people at Woudschoten, the ICMMES conferences and the CCP5 workshop. Let me also mention my co-organizers of the PhDays, especially Jan, Christina, Joost, Johannes, Arthur and John. All the best to them.

Verder wil ik ook mijn vrienden bedanken: Maarten P., Maarten V.P., Tim, Tom, Vincent (o.a. voor de tijd op de RZDense), Christophe, Ilse, Katrien V.K. (o.a. voor het skiën), Daan (o.a. voor het snookeren), Annelies, Bart, Egeleen, Marjan, Pol, Sofie, Wouter D.C., Wouter M. (o.a.

voor de leuke tijd in Mechelen) en iedereen die na dit te lezen geheel terecht verontwaardigd is dat ik hem/haar ben vergeten te vermelden.

Tenslotte wil ik mijn vriendin Katrien en mijn ouders bedanken voor hun onvoorwaardelijke steun. Bedankt om er altijd voor mij te zijn en me te helpen bereiken bij wat ik wil bereiken. De toekomst ziet er mooi uit en dat heb ik voor een groot deel aan jullie te danken.

Pieter
May 2007

Contents

Preface **v**

Contents **vii**

Abbreviations **xi**

Notations **xiii**

1 Introduction **1**
1.1 Motivation 1
1.2 Aims 3
1.3 Outline 4

2 Modeling Across the Scales **7**
2.1 Introduction 7
2.2 Macroscopic Continuum Description 8
2.2.1 Differential Equations 8
2.2.2 PDE for Reaction-Diffusion Systems 9
2.3 Microscopic and Mesoscopic Models 10
2.4 Coarse-Graining and Model Reduction 11
2.4.1 Separation of Time Scales 11
2.4.2 A More Mathematical View 13
2.5 Equation-Free Computing 15
2.5.1 Equation-Free Framework 15
2.5.2 Coarse Time Stepper 16
2.5.3 Increasing Efficiency 18
2.5.4 This Thesis in the Equation-Free Context 20

3 Lattice Boltzmann Models **21**
3.1 Introduction 21
3.2 LBM for Reaction-Diffusion Systems 22
3.2.1 Collision Term 24

3.2.2 Reaction Term 25
3.3 Chapman-Enskog Expansion 25
3.4 Representation of the LBM State 27
3.5 Evolution Equations in Moment Space 29
3.6 Fick's Laws and the Particle Flux 30
3.7 FitzHugh-Nagumo Example 32
3.7.1 Macroscopic PDE Model 32
3.7.2 Mesoscopic Model 33
3.8 Distribution Dependent Reaction Term 34
3.8.1 Planar Streamer Fronts 34
3.8.2 D1Q3R Model 35
3.8.3 D1Q5R Multispeed Model 36
3.8.4 Chapman-Enskog Expansion for D1Q3R 36

4 Time Stepper Based Bifurcation Analysis 39
4.1 Introduction 39
4.2 System Descriptions 41
4.2.1 Macroscopic PDE Description 41
4.2.2 Mesoscopic LBM Description 42
4.2.3 Coarse Equation-Free LBM Description 42
4.3 Numerical Bifurcation Analysis 44
4.4 Bifurcation Diagrams 48
4.5 Dominant Eigenvalues and Stability 51
4.6 Time Stepper Calls 52
4.7 Conclusions 52

5 Initialization (Lifting or Reconstruction) 55
5.1 Introduction 55
5.2 Slaved State 56
5.3 Lifting (Reconstruction) 58
5.4 Healing Process 59
5.5 Bifurcation Diagram 61
5.6 Slaving and the Spectrum of the LBM 64
5.7 Discussion and Conclusion 65

6 Analysis of the Constrained Runs Scheme 69
6.1 Introduction 69
6.2 Constrained Runs Scheme 70
6.3 Stability Analysis 72
6.3.1 Useful Matrix Lemmas 73
6.3.2 Jacobian Matrix 74
6.3.3 A Note on Boundary Conditions 76
6.3.4 Stability Theorem 78

6.4 Convergence . . . 79
6.5 Numerical Results . . . 81
6.6 Comparison to the Scheme of Mei *et al.* . . . 86
6.7 Conclusions . . . 87

7 Constrained Runs: Applications and Extensions 89
7.1 Introduction . . . 89
7.2 Coarse-Grained Bifurcation Analysis . . . 90
7.3 Analysis for the D1Q3R Model . . . 92
7.3.1 Evolution Equations for the Moments . . . 92
7.3.2 Jacobian Matrix and Stability . . . 93
7.3.3 Convergence . . . 94
7.3.4 Numerical Verification . . . 94
7.4 Analysis for the D1Q5R Model . . . 96
7.4.1 Stability . . . 96
7.4.2 Numerical Verification . . . 97
7.5 Higher Order Constrained Runs Schemes . . . 98
7.5.1 Constrained Runs Revisited . . . 98
7.5.2 Constrained Runs with Linear Extrapolation . . . 99
7.5.3 Variant with Central Difference Discretization . . . 101
7.5.4 Time Simulation after Constrained Runs Initialization 103
7.5.5 Constrained Runs with Manifold Reconstruction . . . 105
7.6 Conclusions . . . 108

8 Hybrid Spatial Coupling 111
8.1 Introduction . . . 111
8.2 Setup . . . 113
8.3 Implementation . . . 115
8.3.1 Using Chapman-Enskog Slaving Relations . . . 115
8.3.2 Using Constrained Runs . . . 116
8.4 Error Analysis at Steady State . . . 116
8.4.1 CE-0 Coupling and Pure Diffusion . . . 117
8.4.2 CE-1 Coupling and Constant Reaction Term . . . 119
8.4.3 Discussion . . . 121
8.4.4 CE-1 Coupling and Non-Linear Reaction Term . . . 122
8.5 Numerical Results . . . 123
8.6 Conclusions . . . 130

9 Conclusions 133
9.1 Main Conclusions . . . 133
9.2 Contributions and Acknowledgements . . . 135
9.3 Directions for Future Research . . . 136
9.3.1 Efficient Lattice Boltzmann Simulations . . . 136

9.3.2 Hybrid Spatial Coupling 137
9.3.3 Equation-Free Computing 137

A Third Order Terms **141**

B Evolution Equations in Moment Space: Part 2 **143**
B.1 Discrete Evolution Equations for the Moments 143
B.2 Reduced PDE on the Manifold 146

C Proofs of the Matrix Lemmas **147**
C.1 Proof of Lemma 6.1 147
C.2 Proof of Lemma 6.2 148
C.3 Numerical Verification of Conjecture 6.3 150

Bibliography **151**

Scientific Résumé **173**

Dutch Summary **181**

Abbreviations

BGK	Bhatnagar-Gross-Krook collision model
CE-0	zeroth order Chapman-Enskog based spatial coupling
CE-1	first order Chapman-Enskog based spatial coupling
CE-2	second order Chapman-Enskog based spatial coupling
CR	constrained runs
CTS	coarse equation-free time stepper
D1Q3	one-dimensional lattice with 3 speeds
D1Q3R	D1Q3 lattice and LBE with distribution dependent reactions
D1Q5R	one-dimensional 5-speed lattice and LBE with distribution dependent reactions
FD	finite differences
FHN	FitzHugh-Nagumo reaction-diffusion system
LBE	lattice Boltzmann equation
LBM	lattice Boltzmann model
ODE	ordinary differential equation
PDE	partial differential equation

Notations

α	– mesoscopic growth rate for D1Q3R and D1Q5R – macroscopic growth rate in Fisher equation
γ	system parameters
δt	micro./meso. time step in CR scheme
ε	FHN parameter used as the bifurcation parameter
ϵ	– Chapman-Enskog tracer, the Knudsen number – a small parameter
ζ	– reparameterization variable for continuation – also used locally as indicated
η	asymptotic convergence factor of the CR scheme
θ	user-defined threshold or tolerance
λ_l	ODE-like eigenvalues
$\mu(U)$	lifting operator
μ_l	– eigenvalues of a Picard iteration scheme – Floquet multipliers
μ_m	eigenvalues of the CR time stepper
ν_i	BGK equilibrium weights: $\nu_i = 1/3$
$\xi(x,t)$	energy: scaled second order velocity moment of $f_i(x,t)$
$\tilde{\xi}$	CR fixed point energy
$\boldsymbol{\varrho}$	vector of all moments: $\boldsymbol{\varrho} = [\rho\ \phi\ \xi]'$
$\rho(x,t)$	particle density (concentration)
$\rho(x)$	density at steady state
$\rho^c(x)$	exact analytical density at steady state
$\rho^{FD}(x)$	solution of the FD PDE at steady state
$\rho^{(0)}$	macroscopic initial condition: $\rho^{(0)} = \rho(x,0)$
$\tilde{\rho}$	CR fixed point density *before* the final reset to $\rho^{(0)}$
$\hat{\rho}$	extrapolated density
$\sigma(\mathcal{C}_{\delta t})$	eigenvalue spectrum of CR map
τ	BGK relaxation time: $\tau = 1/\omega$
υ	macroscopic flow velocity
$\phi(x,t)$	momentum: first order velocity moment of $f_i(x,t)$

$\tilde{\phi}$	CR fixed point momentum
$\boldsymbol{\varphi}$	Vector of higher order moments: $\boldsymbol{\varphi} = [\phi\ \xi]'$
ψ_T	time integrated trajectory $y(T)$
ω	BGK relaxation parameter
$\bar{\omega}$	modified BGK parameter in D1Q3R scheme
Γ	number of system parameters
Δx	lattice spacing
Δt	LBM mesoscopic time step
ΔT	coarse macroscopic time step
Π	– partial derivative of φ_T to its initial state $y(0)$ – at a limit cycle, Π is the monodromy matrix
Ω_i	BGK collision term
a	matrix element of A: $a = b/2$
a_0, a_1	FHN parameters
ac	activator species
b	matrix element of A
c	matrix element of A: $c = b/4$
c_i	dimensionless particle velocity
d^{ac}, d^{in}	coefficient of the first order slaving relation for ϕ in absolute value
e_l	unit vector
$e^{(k)}$	error at k^{th} CR iteration
$\mathbf{f}$	vector of all distribution functions
$f_i(x,t)$	particle distribution function
$f_i^\star$	post-collision distribution function
f_i^{eq}	local BGK equilibrium distribution
$f_i^{[0]}, f_i^{[1]}, f_i^{[2]}, f_i^{[3]}$	zeroth to third order Chapman-Enskog terms
$\tilde{f}_i$	CR fixed point distribution function
g	right hand side of ODE
i	velocity index: $i \in \{-1, 0, 1\}$ for the D1Q3 model
in	inhibitor species
j	spatial index: $j = 1, \ldots, N$ – also used locally as indicated
$j(x,t)$	mass flux
k	– CR iteration number – also used locally as indicated
l	state vector index
m	degree of interpolating polynomial
n	– system's state dimension – also used locally as indicated
$n(y,\gamma;\zeta)$	scalar parameterizing equation
$p(u)$	right hand side of micro./meso. continuous equations

$\hat{p}(u)$	right hand side of micro./meso. time stepper
$q(y, T, \gamma)$	phase condition
r	– radius of the eigenvalue circle – also used locally as indicated
$s(U)$	slaving relations for the micro./meso. variables
s	– species superscript – also used locally as indicated
s_1	slope on the PDE domain
s_2	slope on the LBE domain
t	– discrete temporal coordinate – continuous temporal coordinate (from context)
u	microscopic or mesoscopic variables
v_i	dimensioned particle velocity
w_i	lifting or reconstruction weights
$w_0^\star$	weight for a variant of the simple lifting scheme
x	– discrete spatial coordinate – continuous spatial coordinate (from context)
x_j	explicitly discrete spatial coordinate
x_{pde}	PDE lattice site closest to the hybrid interface
x_{lbe}	LBE lattice site closest to the hybrid interface
y	state vector
A	Jacobian matrix for one species
B	matrix gathering the constants
$\mathcal{C}_{\delta t}$	constrained runs map
D	diffusion coefficient
$E(x)$	– error of the hybrid density at steady state – also used locally to denote the electrical field
E_0	maximal steady state error (at x_{lbe}) for CE-0 coupling
E_1	maximal steady state error (at x_{lbe}) for CE-1 coupling
$F(\rho)$	macroscopic force term
I	identity matrix
J	Jacobian matrix of the CR scheme
K	number of CR iterations
L	domain length
L_1	distance of the left boundary to x_{lbe}
L_2	distance of the right boundary to x_{lbe}: $L_2 = L - L_1$
$\mathcal{M}(u)$	restriction operator
M	conversion matrix between micro./meso. and macro. variables
N	number of lattice sites
$P(U)$	right hand side of reduced PDE/ODE
$P_d(U)$	discretized right hand side of reduced PDE/ODE

$\hat{P}(U)$	right hand side of reduced PDE/ODE time stepper
$\bar{P}(U,V)$	right hand side of PDE/ODE for U in moment space
$\bar{Q}(U,V)$	right hand side of PDE/ODE for V in moment space
$S(U)$	slaving relations for the higher order moments
R_i	LBM reaction force term
T	– end time for simulation – specifically for periodic solutions, the period
U	lower order moments: the macroscopic variables
V	higher order moments
$\mathcal{U}$	low-dimensional dominant subspace for Newton iterations
$\mathcal{U}^{\perp}$	high-dimensional subspace for Picard iterations

Chapter 1

Introduction

1.1 Motivation

Historically, dynamical systems were first studied phenomenologically by observation-based experiments. Famous examples are Tycho Brahe's accurate observations of stellar and planetary positions and Foucault's pendulum to visualize the earth's rotation. Subsequently, researchers tried to fit analytical models to their observations to make general statements about future experiments. These models can be seen as a *top-down* phenomenological approach to modeling. They describe the relations between the quantities of interest, i.e. the macroscopically observable variables. E.g. Kepler's laws of planetary motion and the Coriolis effect (describing the apparent deflection of a moving object in a rotating frame of reference) were derived from the above experiments. The resulting models are necessarily simple and in most cases their solutions can be calculated analytically.

With the advent of computers, these macroscopic and mostly continuous models became more complicated. By using appropriate discretization techniques, the models can be simulated numerically on a computer. A classical example are the Navier-Stokes equations that describe the relations between the density and flow velocity of a fluid. Over the years, a whole range of numerical tools were (and are still being) developed to accelerate the numerical computations and to study the macroscale behavior of these macroscopic models. E.g. in a bifurcation analysis, one seeks for parameter values where the behavior of the macroscopic model changes (either the stability or the nature of the solutions).

With the progress in scientific research and increased computing power, more and more details of the systems studied in various application fields like biology, physics, chemistry and material science, could be studied at smaller

and smaller scales. To describe the evolution of the individual particles (atoms, molecules, agents, biological cells) and their interactions, models at finer space and time scales needed to be developed. Widely used examples of such microscopic models are molecular dynamics methods and kinetic Monte Carlo methods. E.g. the fluid that was previously described at the macroscopic scale by the Navier-Stokes equations can also be described by the Boltzmann equation for the one-particle distribution function at the scale of the mean free path length between the particles. In many applications, one is primarily interested in these small scale changes of the microscopic system. Here, modeling with a fully detailed microscopic model over a short time interval is the ideal approach to describe the dynamics.

When the atomistic simulations are confined to small domains, the microscopic models can be used for relatively long time intervals (depending on the application). Macroscopic quantities of interest can then be computed by averaging over the particles. This can be seen as a *bottom-up* approach to model the dynamical system at the macroscopic level. Often however, simulating these microscale models for large spatial domains and long time intervals becomes prohibitively expensive due to the enormous computational cost of simulating all microscopic details.

These computational issues motivated the development of models in between the micro- and macroscale, the so-called pseudo-particle or mesoscopic models. These models keep some of the advantages of the atomistic models like the physically inspired particle character, while using larger space and time scales at the same time, thereby reducing computational complexity. Examples are cellular automata, lattice Boltzmann and dissipative particle dynamics models.

In various sorts of applications ranging from spacecraft reentry in the earth's atmosphere, to weather prediction, flame combustion, crack propagation and polymeric flow, the system dynamics is made up of complicated microscopic interactions (which warrants a description at the microscopic level), but the emergent macroscopic behavior is slow and governed by only a few macroscale quantities (possibly only on certain parts of the domain, see below). Nonetheless, a valid description on the macroscopic level only is difficult and often unavailable. Certain closure relations for the macroscopic variables are simply not available because unrealistic simplifying assumptions are needed.

Nowadays, there lies a big challenge in uniting the top-down and bottom-up modeling approaches efficiently. By identifying the slower emergent macroscale phenomena from the faster microscale behavior, coarse-grained reduced models for the slow processes can be constructed either analytically or computationally with the promise of large gains in efficiency. In many cases, the microscopic or mesoscopic simulations can be confined to small subdomains where the system changes at a more complex atomistic level.

Elsewhere, evolution is slow and continuum models can be used. Seamlessly coupling these different models into a multiscale or hybrid model is increasingly attracting the attention of the scientific community. A clear example of the benefit of a multiscale approach to modeling is the simulation of cracks, defects and dislocations. Near the defects, the system can only be described at a microscopic level. However, performing these atomistic simulations on the full spatial domain leads to a huge number of redundant degrees of freedom away from the defects, resulting in an enormous waste of computational resources.

Finally, a related challenge lies in adapting traditional numerical tools that were developed for continuum models to accelerate the simulation of their macroscale evolution or to study their macroscale behavior, to microscopic or mesoscopic models or to the new breed of multiscale models.

1.2 Aims

Within the setting of scale separation, Kevrekidis and coworkers [108] developed the so-called equation-free framework. Their coarse equation-free time stepper (or coarse time stepper in short) evolves the macroscopic observables using only microscopic simulations. This circumvents the need for a closed macroscopic equation that can be written in terms of the macroscopic variables only. Given a macroscopic initial condition, initial conditions for the microscopic variables are generated in the *lifting* step to start the microscopic simulation over a macroscopic time interval. Afterwards, the macroscopic variables are computed by appropriate averaging in the *restriction* step. This time stepper can then used in combination with existing or special purpose numerical methods to increase the overall efficiency or to study the macroscale dynamical behavior.

Our aim is a thorough analysis of the basic components of the coarse time stepper both in their own right and in the context of a macroscale numerical bifurcation analysis. We will show that traditional tools for time stepper (or time simulation) based numerical bifurcation analysis, developed for partial differential equations, can be used for mesoscopic models as well, using either the mesoscopic model itself or the coarse time stepper wrapped around the mesoscopic model. We will show that the degrees of freedom present in the lifting (initialization) phase need to be resolved carefully to avoid large macroscopic errors. Based on these results, we analyze the stability and convergence of the recently developed 'constrained runs' initialization schemes.

Instead of using a truly microscopic (and possibly stochastic) model in the equation-free framework, we use mesoscopic lattice Boltzmann models (LBMs) for reaction-diffusion problems. This has two advantages related to

the deterministic nature of the LBM. First, the components of the equation-free framework can be studied *an sich* without interference of stochastic effects. Second, most of these concepts can be applied to the LBM directly outside the context of equation-free computing.

The same concept underpinning lifting, namely mapping the macroscopic to the microscopic variables, also appears as the interfacing problem in hybrid spatial coupling. We study the coupling of a LBM and discretized PDE and analyze the behavior of the resulting spatial discretization error of the hybrid model.

1.3 Outline

Chapter 2. Modeling across the scales. A dynamical system can be modeled at different levels of abstraction. We consider macroscopic, mesoscopic and microscopic models. For a large class of multiscale problems, a separation of time scales exists such that after some time, evolution takes place on a lower-dimensional manifold. We introduce the equation-free framework developed by Kevrekidis *et al.*, which enables a macroscopic time evolution using only microscopic simulations. Special attention is paid to the multiscale interfacing problem where we have to map a few macroscopic initial conditions to meaningful values for a larger set of microscopic variables.

Chapter 3. Lattice Boltzmann models. In this chapter, we introduce the mesoscopic lattice Boltzmann models (LBMs) used throughout the text. A LBM tracks the evolution of distributions of particles that move on a grid with certain discrete velocities. Specifically, we consider the LBM with Bhatnagar-Gross-Krook (BGK) collision model for reaction-diffusion systems on a one-dimensional domain. We define a full set of moments for the mesoscopic distribution functions and derive the relations between the two using the Chapman-Enskog expansion. We argue that this LBM serves as an excellent model problem to test the concepts developed in the equation-free framework. We also present a class of LBMs with distribution dependent reaction terms.

Chapter 4. Time stepper based bifurcation analysis. We study two strategies to perform a time stepper based numerical bifurcation analysis of systems described by LBMs. The first strategy uses the LBM as the time stepper directly while the other is based on the coarse equation-free time stepper wrapped around the LBM. We show that techniques developed for time stepper based numerical bifurcation analysis of both steady states and periodic solutions of partial differential equations (PDEs) can be used for

LBMs as well, using either of the above time steppers. The results for both approaches are also compared to those for an equivalent macroscopic PDE description.

Chapter 5. Initialization (lifting or reconstruction). We perform an extensive study of the influence of the lifting or reconstruction step on the minimal time step of the coarse time stepper and the accuracy of the results. It is shown experimentally that this time step must often be much larger than the time it takes for the higher order moments to become slaved by the lowest order moment, which somewhat contradicts earlier claims. In this chapter, we make frequent use of the bifurcation analysis tools from Chapter 4.

Chapter 6. Analysis of the constrained runs scheme. We perform a numerical stability and convergence analysis of the constrained runs initialization scheme for the LBM from Chapter 3. Gear and Kevrekidis introduced this scheme in the context of equation-free computing. Given the macroscopic initial fields, we study the mapping of these variables to the higher-dimensional space of LBM variables. We prove that the constrained runs scheme is unconditionally stable and that it converges to an approximation of the slaved state, i.e. the microscopic state consistent with the macroscopic initial condition. This approximation is correct up to first order in the Chapman-Enskog expansion of the LBM. The asymptotic convergence factor is $|1-\omega|$ with ω the BGK relaxation parameter. We argue that at least for our model problem, the numerical analysis also holds for the recently developed initialization scheme of Mei *et al.*

Chapter 7. Constrained runs: Applications and extensions. In this chapter, we study several applications and extensions of both the constrained runs scheme itself and the analysis in Chapter 6. First, using the constrained runs initialization scheme as the lifting step in equation-free computing, we perform a coarse-grained bifurcation analysis of the LBM. Second, we extend the analysis of Chapter 6 to LBMs with distribution dependent reaction terms. Finally, we implement some higher order constrained runs schemes for the LBM that use interpolation techniques to obtain a higher accuracy.

Chapter 8. Hybrid spatial coupling. We construct a hybrid model by spatially coupling a LBM to a finite difference discretization of the PDE for reaction-diffusion systems. Because the LBM has more variables (the particle distribution functions) than the PDE (only the particle density), we have a one-to-many mapping problem from the PDE to the LBM domain

at the interface. Conceptually, this is related to the initialization problem. We perform this mapping using either results from the Chapman-Enskog expansion or the point-wise iterative constrained runs scheme that approximates these analytical relations numerically. Most importantly, we show that the global spatial discretization error of the hybrid model is one order less accurate than the local error made at the interface. We derive closed expressions for the spatial discretization error at steady state and verify them numerically for several examples on the one-dimensional domain.

Chapter 9. Conclusions. We summarize the main conclusions and contributions of the research presented in this manuscript. We acknowledge our collaborators and present guidelines for further research.

Chapter 2

Modeling Across the Scales

2.1 Introduction

When given the task of simulating a dynamical system, one has a variety of models to choose from, each operating on a different level of abstraction. It depends both on the complexity of particle interactions (atoms or molecules) and the corresponding level of detail required (either for correct simulation or the detail of interest to the user) which model is appropriate.

On the microscopic level, one has molecular dynamics methods [59] that monitor the individual particles. Kinetic Monte Carlo methods [70] provide a higher level of abstraction by modeling the statistics of the particle interactions. Even more coarse-grained are mesoscopic or pseudo-particle models, like lattice gas cellular automata models [33] and lattice Boltzmann models (LBMs) [194]. The latter describe the system's evolution through generalized distributions of particles that are limited to move on a grid with particular velocities only. Finally, on the macroscopic continuum level, one has ordinary or partial differential equations (ODEs or PDEs) in terms of a few macroscopic variables. These macroscopic observables are typically the density, flow velocity, pressure, etc, i.e. the low order moments of the microscopic variables of the underlying more detailed microscopic processes.

The choice for a particular model depends on several criteria. Typically, the solutions of macroscopic-level models like PDEs exhibit a smooth local behavior and in general allow for large time steps during simulation. In many cases however, a macroscopic model is not applicable because e.g. the Knudsen number (i.e. the ratio between the mean free path length and a characteristic length scale of the system) is too large and the detailed atomistic particle interactions need to be taken into account. When a macroscopic description for the system's evolution cannot be derived in terms

of the macroscopic variables only, i.e. when the macroscopic model does not close, a more microscopic model describing the same physics in more detail should be used. Because of their notion of, albeit idealized, particles, mesoscopic models like LBMs allow the incorporation of complicated physics in a more bottom-up way than macroscopic models. The LBM variables (the particle distribution functions) also contain extra information on the spatial derivatives of the macroscopic variables because they are linked to the particle velocities. However, these models typically require more variables and smaller time steps. Similar advantages apply to microscopic models. However, because they act on fine space and time scales to capture all microscopic phenomena and typically involve very large sets of variables, microscopic models have a significant computational complexity. Therefore, simulation with these models can be very expensive.

This chapter is organized as follows. In Sect. 2.2 and 2.3, we discuss, quite generally, macroscopic continuum models and microscopic and mesoscopic models. Section 2.4 introduces the concepts of analytical and computational coarse-graining and model reduction under the assumption of a separation of time scales. Finally, in Sect. 2.5, we present the equation-free framework of Kevrekidis and coworkers.

2.2 Macroscopic Continuum Description

2.2.1 Differential Equations

Arguably the most common approach to study the evolution of a dynamical system starts with the derivation of some sort of macroscopic description of the physical system. Such a macroscopic model is typically a set of ODEs or PDEs in terms of the macroscopic variables U of interest,

$$\frac{\mathrm{d}U(t)}{\mathrm{d}t} = P(U(t)) \quad \text{or} \quad \frac{\partial U(x,t)}{\partial t} = P(U(x,t)) \,, \tag{2.1}$$

where the derivatives $\mathrm{d}/\mathrm{d}t$ and $\partial/\partial t$ denote changes of U with respect to time t. The coordinate x denotes space and P is a model-dependent functional of U. A set of ODEs typically describes a spatially lumped system, i.e. the system is spatially homogeneous and only the evolution in time matters. When $U(x,t)$ is also distributed in space, we typically have a set of PDEs, where P in (2.1) contains spatial derivatives of $U(x,t)$.

As mentioned in the introduction, the macroscopic variables U are quantities like the density, the macroscopic (flow) velocity or the pressure of the various species present in the system. Typically, these variables are defined as the lower order velocity moments of more microscopic quantities derived from the underlying microscopic processes. To complete the model (2.1),

we impose an initial condition $U(x, t = 0)$ and suitable spatial boundary conditions.

To solve the continuous model (2.1), one typically discretizes the space and time derivatives with finite difference, finite volume or finite element schemes. When we use e.g. a simple forward Euler time discretization with time step ΔT to approximate the continuous time derivative, i.e.

$$\frac{\partial U(x,t)}{\partial t} \approx \frac{U(x, t + \Delta T) - U(x,t)}{\Delta T} ,$$

the value of U at the next time step can be computed from the previous one as

$$U(x, t + \Delta T) = U(x,t) + \Delta T \, P_d(U(x,t)) . \tag{2.2}$$

For the PDE, the notation P_d conceals the discretized spatial derivatives.

Next, we impose a grid in both time and space. On the grid, we define grid points characterized by discrete coordinates t_k in time and x_j in space. For one-dimensional spatial domains, we have

$$t_k = k\Delta T \; ; \; k = 0, 1, \ldots, T/\Delta T \; , \quad x_j = x_0 + j\Delta x \; ; \; j = 1, \ldots, N \; .$$

Here we assume a simulation for $t \in [0, T]$. The grid spacing in x is denoted by Δx with N the number of spatial grid points. The spatial boundaries are positioned at x_0 and x_{N+1}.

The continuous macroscopic quantities in (2.2) can be approximated by the discrete variables $U_j^{(k)}$ in the grid points (x_j, t_k), i.e.

$$U_j^{(k)} \approx U(x_j, t_k) .$$

The state at time t_k is fully described by the discrete state vector $U^{(k)}$, i.e.

$$U^{(k)} = [U_0^{(k)} \; U_1^{(k)} \; \ldots \; U_j^{(k)} \ldots \; U_N^{(k)} \; U_{N+1}^{(k)}]' .$$

Putting all of this together, one obtains the following large system of discrete equations to be solved

$$U^{(k+1)} = U^{(k)} + \Delta T \, P_d(U^{(k)}) = \hat{P}_d(U^{(k)}) . \tag{2.3}$$

We thus have a mapping $\hat{P}_d$ of the discrete state $U^{(k)}$ at time t_k to the next $U^{(k+1)}$ at time t_{k+1}.

2.2.2 PDE for Reaction-Diffusion Systems

In this manuscript, we concentrate on reaction-diffusion systems on a one-dimensional domain. The macroscopic fields $U(x,t)$ are the concentrations

or the particle densities $\rho^s(x,t)$ of the various species $s \in \{a, b, \ldots\}$ present in the system. For space-independent isotropic diffusion, the set of PDEs (2.1) consists of PDEs of the form

$$\frac{\partial \rho^s(x,t)}{\partial t} = D^s \frac{\partial^2 \rho^s(x,t)}{\partial x^2} + F^s(\rho^a(x,t), \rho^b(x,t), \ldots) \,, \tag{2.4}$$

where D^s is the diffusion coefficient and F^s a macroscopic reaction force term that depends on the densities of the species. From now on, we drop the superscript s, unless a value is specific for one species.

In the previous section, we showed that equations like (2.4) are discretized with e.g. finite differences for practical computations. For the PDE (2.4), we use second order central differences in space and either the trapezoidal rule (in Chapter 4 and 5) or an explicit forward difference scheme (in Chapter 8) for the time derivative.

2.3 Microscopic and Mesoscopic Models

In many physical and chemical processes, the system's evolution needs to be described at fine space and time scales because the overall dynamics is governed by the complex interactions between the individual particles, typically molecules or atoms. The microscopic model is the set of rules, which describe these fine-scale interactions, and can be chaotic or stochastic. Note that the derivation of a suitable microscopic model to describe a specific dynamical system can be a highly non-trivial task. Once such a model is found, there is some interest in reusing this model for other purposes.

At the most detailed level one has molecular dynamics simulations [59] that model all interactions between all individual particles (atoms or molecules), which are characterized by their positions and momenta. The forces between the particles are controlled by an interparticle potential and the time evolution of each individual particle is described by integrating Newton's equations of motion. Kinetic or direct simulation Monte Carlo methods [19, 156] provide a higher level of abstraction by modeling the statistics of the various interactions between particles. First, the particles move deterministically in continuous space as if they do not interact. Afterwards, a fixed number of particles are randomly selected for collisions. The probability that particles collide only depends on their relative velocity.

Even more coarse-grained are the pseudo-particle or mesoscopic methods like lattice gas cellular automata [33, 60, 61] and lattice Boltzmann models (LBMs) [194, 228]. These models do no longer model individual microscopic particles. Instead, they model the behavior of idealized particles limited to move in certain directions on a grid with particular velocities only. While lattice gas cellular automata track the evolution of individual

(boolean) particles and use simple local update rules for their interactions, LBMs evolve the distributions of such particles characterized by position and speed. The use of particle distributions removes much of the statistical noise that plagues cellular automata. Note that although historically the LBM was derived by averaging the boolean variables in lattice gas cellular automata [91, 92, 143], the LBM can also be seen as a particular discretization of the continuous Boltzmann equation [87, 88, 182].

Other mesoscopic methods are dissipative particle dynamics (DPD) [96, 55] and smoothed particle hydrodynamics (SPH) [147] methods that use aggregates of truly microscopic particles. These coarse-grained particles can move freely in continuous space at discrete time steps. In DPD methods, the coarse particles experience short-range interparticle forces and evolve according to Newton's laws of motion. In SPH methods, the macroscopic observables are represented as integral interpolants evaluated in the coarse-grained particles with suitable kernels to represent the influence of the neighboring microscale particles. In this thesis, we use the terms microscopic and mesoscopic interchangeably for reasons explained at the end of this chapter.

In the most general case, the microscopic or mesoscopic model is defined as a functional iteration or a so-called 'time stepper' defined by

$$u^{(k+1)} = \hat{p}(u^{(k)}) \; . \tag{2.5}$$

Equation (2.5) maps the discrete microscopic variables $u^{(k)}$ at time t_k to the next state $u^{(k+1)}$. The functional $\hat{p}$ can be a mathematical expression, but also a set of rules describing the microscopic behavior. Using a microscopic time step Δt, $u^{(k)}$ can be seen as the discretization of the continuous state $u(x, t_k)$ at time $t = k\Delta t$. The analogy to an ODE or spatially discretized PDE for the microscopic variables is conceptually the same as in Sect. 2.2.1. If such a system of continuous differential equations for u would be available, it can be formulated as

$$\frac{\mathrm{d}u(t)}{\mathrm{d}t} = p(u(t)) \quad \text{or} \quad \frac{\partial u(x,t)}{\partial t} = p(u(x,t)) \; . \tag{2.6}$$

The right hand side p of the PDE contains spatial derivatives of $u(x, t)$. To start a microscopic simulation, the system (2.5) or (2.6) must be augmented with initial conditions $u^{(0)} \approx u(x, 0)$ for the microscopic variables. When the system is spatially distributed, boundary conditions are needed too.

2.4 Coarse-Graining and Model Reduction

2.4.1 Separation of Time Scales

The process of representing a system with fewer degrees of freedom than those actually present in the system is called coarse-graining. By coarse-

graining, one eliminates the "less interesting" fast variables that evolve on a fast time scale (e.g. a molecular scale) while keeping the coarser slow variables evolving on much larger time scales. It is vital that we have some notion of the separation of time scales between the coarse slow and the other fast variables. The ultimate goal of coarse-graining techniques is a reduction of computational complexity: the dimension of the state space is smaller and the space and time scales considered are larger. One example of the coarse-graining approach is the hierarchy of coarse-grained mesoscopic models derived from molecular dynamics described in the previous section.

In many microscopic simulations, one observes an evolution of the long term dynamics that is attracted to a lower dimensional part of phase space. We call this attractor the slow manifold [75]. This slow manifold can be described adequately by, typically a few, low order modes of the microscopic variables called the coarse slow variables. The system's evolution on the manifold is then — at least conceptually — described by a coarser-level equation that can be written in terms of these slow variables only. In other words, using certain projection techniques for the microscopic equations governing the atomistic variables, one can reduce the model complexity and derive closed equations of motion of appropriately defined coarse-grained variables that evolve on distinctly slower time scales from the rest of the variables in the system. We refer to e.g. [78, 149, 238] for the mathematical foundations and the recent reviews in [54, 72, 74] and references therein. Further methods to obtain a coarse reduced description at the macroscale are the theory of Inertial Manifolds and Approximate Inertial Manifolds [39] and the Chapman-Enskog expansion [60]. One interesting application is stochastic climate modeling [137].

Sometimes the coarser-level equations do not close, i.e. the process cannot be described using the coarse variables only. Computational coarse-graining circumvents the derivation of closed equations for the coarse-grained variables or the explicit computation of the slow manifold. Instead, the microscopic model is used to compute the values of the coarser-level variables in an efficient way during simulation. To date, there are many multiscale models that pertain to this category. In equation-free modeling [108], the microscopic model is considered more or less as a black-box code. Short bursts of the microscopic simulator are used to predict the values of the coarse variables. These values are then combined with a coarse-level numerical scheme to increase the computational efficiency. In the heterogeneous multiscale method [48, 49] the starting point is different. Here, the evolution equations for the coarse variables are known although for some terms like fluxes or stresses, there are no closures available. These terms are computed using the underlying microscopic simulator. In the context of viscoelastic polymer flows, the CONNFFESSIT framework [98, 121] computes the stresses in the constitutive equation from molecular simulations. In the

gas-kinetic scheme [159, 229], the macroscale solver for the hydrodynamic variables is the finite volume method for which the fluxes are computed from the kinetic Boltzmann BGK equation. The optimal prediction methods [36, 37] estimate the average solution of underresolved systems using additional stochastic information. In the quasicontinuum method [183], atomistic computations are sampled to compute the quantities needed in a macroscale finite element method. In the transfer operator approach, a reduced model of metastable states is extracted from a Markov chain [97]. The stable computation of a few metastable macroscale states from an underlying stochastic system using the moment map is described in [11]. In chemical kinetics applications, slow manifolds are computed using either an eigenvalue decomposition [136] or the computational singular perturbation technique [119, 120] (see also [236, 237] for the use of the latter method in the context of model reduction for ODEs). We also mention the work described in [74, 75, 76, 77] centered around the computation of quasi-equilibrium manifolds. Finally, there are the hybrid modeling approaches where an atomistic and a continuum model are used on different parts of the domain (see Sect. 8.1 for a non-exhaustive overview).

2.4.2 A More Mathematical View

In case a time scale separation exists in the microscopic system (2.5), one observes that after a while, the microscopic variables u become functionals of (we say that they get slaved to) the governing macroscopic variables U describing the evolution on the slow manifold. The time this takes is called the healing time in [139] and is typically small compared to the relevant macroscopic time scales. Mathematically, this reduction in complexity can be expressed as

$$u = s(U) \,, \tag{2.7}$$

where the functionals s are called the slaving relations. These relations are of course model-specific.

As the variables U are typically the lower order velocity moments of u, it makes sense to consider the higher order moments V of u too. When we define a full set of moments $[U\,V]$' with the same dimension as the microscopic state space, we can define a conversion mapping M as

$$\begin{bmatrix} U \\ V \end{bmatrix} = M(u) \,, \tag{2.8}$$

and similarly $u = M^{-1}\big([U\ V]'\big)$ if the mapping M is invertible. Note that M might exist only conceptually. The exact relations might not be known for

certain microscopic models. If the relations are known, one can in principle derive a set of equations describing the evolution of the full system over the entire time span, but now in terms of U and V,

$$\frac{\mathrm{d}U}{\mathrm{d}t} = \bar{P}(U,V) \;, \tag{2.9}$$

$$\frac{\mathrm{d}V}{\mathrm{d}t} = \bar{Q}(U,V) \;. \tag{2.10}$$

The above system has the same dimension as the full microscopic model (2.5). The functionals $\bar{P}$, $\bar{Q}$ may contain spatial derivatives if the variables U, V are spatially distributed.

The separation of time scales can now clearly be observed between the macroscopic variables U and the higher order moments V, such that, when simulating with the full system (2.9)–(2.10), the higher order moments quickly evolve to functionals S of the lower order ones, i.e.

$$V = S(U) \;. \tag{2.11}$$

In principle, the slaving relations S can be derived from (2.7) using (2.8).

As discussed previously, after the relatively short healing or slaving process, the macroscopic variables U govern the system's evolution. By substituting (2.11) into (2.9), we obtain the following equation

$$\frac{\mathrm{d}U}{\mathrm{d}t} = \bar{P}(U, S(U)) = P(U) \;, \tag{2.12}$$

in terms of U only. Equation (2.12) is called the reduced equation on the slow manifold. This coarse macroscale equation only needs an initial condition $U(t=0)$ for the macroscopic variables to start the simulation. On the other hand, the microscopic model (2.5) as well as its equivalent in moment space (2.9)–(2.10) needs more initial information, either $u(t=0)$, or equivalently $U(t=0)$ supplemented with values for $V(t=0)$. Yet in most coarse-grained macroscale computations, only the macroscopic initial data $U(t=0)$ is given. The difficulty is how to initialize the microscopic model with typically many variables, consistently with only these few macroscopic initial quantities. This issue will be thoroughly discussed in this text for the LBMs under consideration in the context of equation-free computing.

In Fig. 2.1, we present a graphical impression of the above concepts. The figure shows an attracting manifold described by the macroscopic variables U in phase space. The phase space is described[1] by either u or $[U\ V]'$. Starting from an initial condition for the full state consistent with the given

[1]Note that these are actually discrete state vectors in space, making the state space much higher dimensional than Fig. 2.1 suggests.

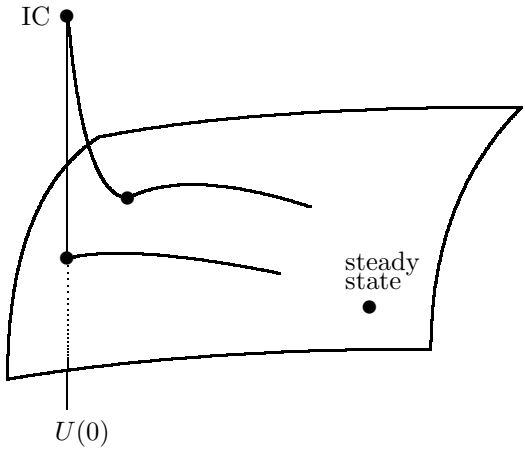


Figure 2.1: Sketch of a slow attracting manifold in phase space. Starting from an initial condition (IC) away from the manifold, the system's evolution can be described in terms of the macroscopic variables $U(t)$ on the manifold after a short healing phase. Here we assume that a stable steady state exists.

macroscopic initial condition $U(t = 0)$, the system evolves as described by (2.5) or (2.9)–(2.10). After the healing time (typically a fast process), the slaving relations (2.7) or (2.11) are attained and the dynamics is described by a slow transient trajectory according to the reduced equation (2.12) on the manifold. In Fig. 2.1, we assume that a long-term attractor, in this case a stable steady state, exists on the manifold, which attracts all trajectories. If the initialization is not performed carefully, deviations may occur, resulting in erroneous trajectories on the slow manifold (see Chapter 5).

In the context of equation-free computing, neither the reduced equation (2.12), nor the full system (2.9)–(2.10) in moment space are available. The slaving relations (2.11), being the link between the two, are not available either. Instead we only have the microscopic simulator (2.5) available. We assume that both the slaving relations and the reduced equation exist, but are (as yet) unavailable or difficult to obtain analytically.

2.5 Equation-Free Computing

2.5.1 Equation-Free Framework

In many applications, one is not interested in the detailed microscopic behavior of a system but only in its macroscopic behavior, i.e. the evolution of macroscopic variables over a large domain and relatively long time inter-

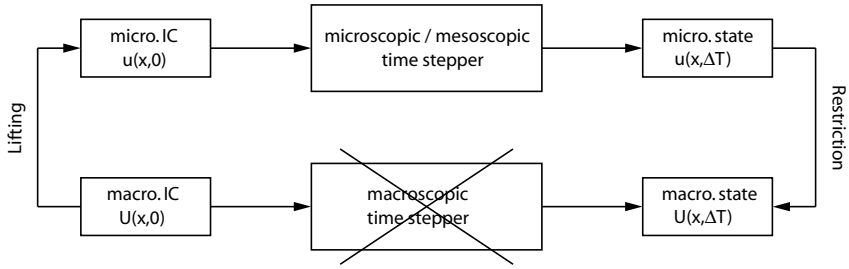


Figure 2.2: The coarse equation-free time stepper for a single time step ΔT. A traditional macroscopic (PDE-based) time stepper is replaced by appropriately initialized (lifted) microscopic or mesoscopic simulations from which the macroscopic quantities are computed (restriction). The resulting coarse time stepper can be used for traditional macroscopic-level tasks, like bifurcation analysis.

val. These variables U are typically the first few moments of a microscopic distribution u, like the concentration or flow speed of the various species. In [108, 199], Kevrekidis *et al.* proposed the equation-free framework: an approach to realize a macroscopic time step for a system for which only a microscopic description is available. The crucial assumption is that a closed macroscopic description in terms of those variables U exists, but is unavailable. A macroscopic time step is performed by first constructing one or more microscopic initial states corresponding to the macroscopic initial condition, then evolving those microscopic initial states using the microscopic evolution laws and finally computing a new macroscopic state. These steps are depicted in Fig. 2.2 and discussed in more detail in the next section. The resulting coarse time stepper (or coarse time integrator) can then replace traditional macroscopic (PDE-based) time integrators in conventional numerical methods to perform so-called system-level tasks such as bifurcation analysis and control at the macroscopic level for systems described by microscopic evolution laws. We refer to [138, 139, 146, 167, 199, 200] and Chapter 4 for coarse-grained numerical bifurcation analysis results, to [11] for an equation-free stabilization of metastable states and to [129, 186, 187, 188] for equation-free control applications.

2.5.2 Coarse Time Stepper

Before time integration can commence, an appropriate set of macroscopic variables U must be selected, which can be a highly nontrivial task. For the procedure to work well, the macroscopic description must, at least conceptually, exist and close using only those variables. I.e. in principle it should be possible to write down an evolution equation for U in which all terms can be expressed in function of U only, though the precise relationships

may not yet be known. This also implies that the chosen macroscopic variables should be a suitable parameterization of the slow manifold to which all initial states are quickly attracted. When using too few variables, the procedure would very likely fail or produce wrong results. On the other hand, using too many moments of the microscopic distribution might reveal too much of the microscopic behavior, and our coarse-grained macroscopic model might no longer exhibit the steady states or periodic solutions that we expect to find, but much more complicated dynamics. This is not an issue in this text since the microscopic models used (here mesoscopic LBMs) have well-defined steady states and periodic solutions.

A coarse macroscopic time step of length ΔT with the coarse time stepper consists of three substeps as depicted in Fig. 2.2. First, one needs to construct an initial condition $u(x,0)$ for the microscopic simulator that corresponds to the initial macroscopic state $U(x,0)$. This step is called the *lifting* (in [108]) or *reconstruction* step (in [48]). Defining a lifting operator μ, we have

$$u(x,0) = \mu\big(U(x,0)\big) \; . \tag{2.13}$$

This initialization process leads to a one-to-many mapping problem because the microscopic simulator needs more information than provided by the macroscopic initial variables $U(x,0)$. The missing information needs to be reconstructed. Because a macroscopic model is really a description for the dynamics on the lower-dimensional slow manifold, it is clear that the best initial condition for the microscopic simulator is the point on the manifold corresponding to the particular initial values of the macroscopic variables (in Fig. 2.1 geometrically the intersection of the "line" of constant $U(t=0)$ with the slow manifold or equivalently with the trajectory described by the reduced equation (2.12)).

Based on the separation of time scales between U and V, Kevrekidis *et al.* argued in [69, 108, 199] that the errors caused by the initialization of the missing higher order moments away from this manifold disappear as the higher order moments get slaved. According to this argument, the initialization should not matter too much. However, we will show in Chapter 5 that the fast slaving of the higher order moments does not imply that all influences of an inaccurately reconstructed initial condition disappear quickly (as depicted in Fig. 2.1, deviations at the macroscopic slow level may occur), and that a good reconstruction scheme is important.

In the second step, the microscopic initial condition $u(x,0)$ is evolved over the macroscopic coarse time step ΔT using the microscopic simulator (2.5). We use the LBM described in Chapter 3 as the "microscopic" simulator.

In the third step, called *restriction* (in [108]) or *compression* (in [48]), the macroscopic variables at the end of the time step are computed from

the final microscopic state. Conceptually, we have a restriction operator $\mathcal{M}$ defined by

$$U(x, \Delta T) = \mathcal{M}\big(u(x, \Delta T)\big) \ . \tag{2.14}$$

The restriction consists of an averaging operation of the microscopic variables $u(x, T)$ and is a fairly easy task in comparison to the inverse reconstruction problem (2.13). Note that lifting immediately followed by restriction should result in the identity operation, i.e.

$$\mathcal{M}(\mu(U(x, 0))) = U(x, 0) \ .$$

In its simplest form, the coarse time stepper is defined by the sequence

$$U(x, \Delta T) = \mathcal{M}\big(\hat{p}\big(\mu\big(U(x, 0)\big)\big)\big) \ ,$$

with ΔT the macroscopic coarse time step.

In case the microscopic model is stochastic or chaotic, there are additional issues. Multiple initializations (2.13) and/or multiple microscopic simulations and appropriate averaging in (2.14) may be needed to get sufficiently accurate results with small enough variance. In this text, we apply the coarse equation-free integrator to a LBM, which is fully deterministic. Multiple realizations and averaging are therefore unnecessary.

In applications, one often has to integrate over a time interval T much larger than the coarse time step ΔT. The above scheme can then be repeated until the end time T is reached. Typically, the time integrator for $t \in [0, T]$ is also referred to as the coarse time stepper. In this procedure, the restriction followed immediately by lifting from the end point to generate microscopic initial conditions for the next integrations is essential. Since we remove state information at every restriction step and add slightly different information again to the system in the following reconstruction step, performing k coarse time steps with time step ΔT is not equivalent to performing a single coarse time step with time step $k\Delta T$, in particular when there is an upper limit to ΔT. Though it is not needed to use multiple coarse time steps in the (deterministic) case discussed in this text, since there is no maximum to the allowable time step contrary to the stochastic problems in [138, 139], we will still use this procedure to experiment with small macroscopic time steps and to test the concept. We believe that many of the conclusions we draw will carry over to systems where the maximal successful macroscopic time step is limited.

2.5.3 Increasing Efficiency

The efficiency of the coarse time stepper can be increased in time by combining a few short coarse time integrations to estimate the time derivative

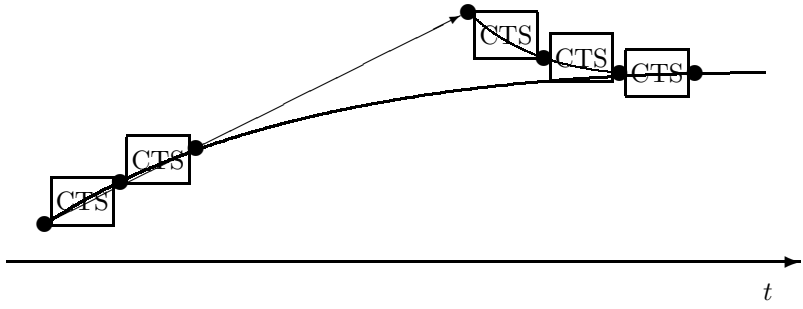


Figure 2.3: Short time simulations with the coarse time stepper (CTS) from Fig. 2.2 are combined with an extrapolation routine to increase the overall CTS efficiency in time. The dots represent the macroscopic data along the trajectory which serve as in- and output to the CTS.

with an extrapolation routine to compute the macroscopic state further ahead (see Fig. 2.3). Examples of such time acceleration schemes in the context of equation-free computing are the projective integration method [65, 66, 67, 124, 165] (see also [47, 50]) and the multistep state extrapolation method [218, 217] (the latter is related to the method described in [190]). Here, it is important that the coarse time step ΔT can be small to allow for a large gain in efficiency. As we will show in Chapter 5, this requires a good lifting strategy.

The efficiency can also be increased spatially (see Fig. 2.4). To this end,

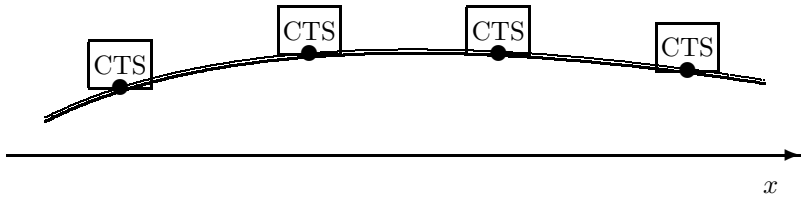


Figure 2.4: The coarse time stepper (CTS) from Fig. 2.2 is used on small parts of the domain and the results are interpolated to increase the overall CTS efficiency in space.

methods like the gap-tooth scheme and patch dynamics (a combination of the gap-tooth and projective integration method) were developed [108, 172, 173, 174]. Here, microscopic simulations are performed only in small parts (the "teeth") of the domain around the macroscopic grid points. The microscopic results are then averaged over the "teeth" to obtain macroscopic data. This macroscale data is combined over the spatial 'gaps' with an interpolation method.

In this thesis, we will only use the most basic variant of the coarse time stepper and concentrate on the main parts of the equation-free framework, most notably the lifting phase. I.e. we simulate over the full physical space.

2.5.4 This Thesis in the Equation-Free Context

From the previous discussion, we learn that the coarse time stepper (i.e. the lift-run-restrict cycle) constitutes the heart of the equation-free framework. A large portion of this text is concerned with analyzing the behavior of the coarse time stepper both in the context of time simulation and bifurcation analysis. In particular, we focus on the lifting phase. To this end, we have put together a mesoscopic test case that is ideally suited to test many of the equation-free concepts. In Chapter 3, we will show that LBMs can be represented fully in both mesoscopic and moment space by different sets of variables and that the slaving relations and the reduced equation are explicitly available. This allows for a comprehensive mathematical analysis of the equation-free framework. Furthermore, a LBM is a deterministic model, which allows us to study the coarse equation-free time stepper itself, without interference of stochastic effects. When exactly the influence of these stochastic effects is under investigation, other model problems need to be developed (see e.g. [72]). Because the mesoscopic LBM is really a substitute for a truly microscopic model in the coarse time stepper, we use the terms microscopic and mesoscopic models interchangeably in this text.

Note that, because of the deterministic nature of a LBM, many of the tools developed within the equation-free framework can be used directly on the LBM also, i.e. generally speaking, the equation-free modeling paradigm is not a requirement to study the behavior of dynamical systems described by a LBM. Examples in this manuscript are the direct application of bifurcation analysis tools to LBM (Chapter 4) and initialization routines like the constrained runs schemes (Chapters 6 and 7). Another example is the direct application of the projective integration method and the multistep extrapolation method to the LBM [219].

Chapter 3

Lattice Boltzmann Models

3.1 Introduction

In the past decades, mesoscopic lattice Boltzmann models have become a powerful tool for the simulation of dynamical systems that are traditionally described by macroscopic models like the Navier-Stokes equations. Below, we list a few application fields in which the LBM has proven to be very successful. First, one has the LBMs for multiphase and multicomponent flows. We list, in chronological order, the different approaches taken: i) the chromodynamic models [79, 80, 81], ii) the pseudo-potential method [179, 180, 181], iii) the free energy models [157, 196, 197] and iv) the methods based on kinetic theory [89, 130, 131]. Second, LBMs are particularly useful to model flows in complex geometries like porous media [23, 195] and permeable textiles [12, 112] because of their natural ability to handle complicated boundaries. Third, LBMs can also be used to model colloidal suspensions [113, 114, 115] and, fourth, turbulent flow regimes [13, 27, 28, 233]. Fifth, LBMs are also used with some success for thermohydrodynamical systems. Here, the energy is either manipulated by the LBM [6, 32, 86] or in more recent work, an athermal LBM is combined[1] with a separate finite difference equation for the temperature [117, 118, 145]. For further applications, we refer the interested reader to the review papers [14, 31, 34, 163] and books [33, 194, 228] on the matter.

In this chapter, we focus on the LBM for reaction-diffusion systems on the one-dimensional domain. These LBMs will be used throughout the text as model problems. Like in the first papers on equation-free computing [69, 108, 199], we use these models as a substitute for truly microscopic (and

[1] The latter type of models are also called 'hybrid' models; a terminology that should not be confused with the spatially hybrid models described in Chapter 8.

possibly stochastic) models for which equation-free computing has most potential. We will show how these models fully fit the equation-free framework. Specifically, a time scale separation and the resulting separation of variables, the reduced equation, the slaving relations, etc. are all explicitly available. This allows for a thorough mathematical analysis later on in the text.

The developments in LBMs for reaction-diffusion systems can be summarized as follows. Much of the early work on diffusive LBM has been done by Qian and Orszag [162], Chen, Dawson and Doolen [30, 41], Wolf-Gladrow [227, 228] and more recently by van der Sman [205, 206, 208, 209]. Subsequently, these models have been used to compute e.g. Turing patterns [20, 128] and the Lorenz attractor [230] and in applications like the cell division in E. coli [152] and the Belousov-Zhabotinskii reaction [231].

This chapter is organized as follows. In Sect. 3.2, we present the LBM with BGK collision model for one-dimensional reaction-diffusion systems. In Sect. 3.3 we perform a Chapman-Enskog expansion of the LBM and describe the relations between the LBM and the corresponding macroscopic PDE from Sect. 2.2.2. These relations allow different representations of the LBM state as described in Sect. 3.4. We derive the equations describing the evolution of the LBM in moment space in Sect. 3.5. We show the equivalence to Fick's laws in Sect. 3.6. The FitzHugh-Nagumo system from Sect. 3.7 will be used as an example throughout this text. In Sect. 3.8, we extend the previously discussed LBMs to models with distribution dependent reaction terms.

3.2 LBM for Reaction-Diffusion Systems

Lattice Boltzmann models (LBM) [34, 194, 228] describe the evolution of particle distribution functions $f_i(x,t)$ discretized[2] in space x, time t and velocity v_i. These distributions are defined on a space-time grid with lattice spacing Δx in space and Δt in time. We use the D1Q3 model, i.e. only three values are considered for the velocity v_i on the one-dimensional domain

$$v_i = c_i \frac{\Delta x}{\Delta t}, \quad c_i = i \in \{-1, 0, 1\} \,, \tag{3.1}$$

with c_i the dimensionless lattice velocity. This corresponds to particles moving to the left (with $c_{-1} = -1$), particles moving to the right ($c_1 = 1$) and particles at rest ($c_0 = 0$).

The lattice Boltzmann equation (LBE) describing the evolution of the distribution functions is

$$f_i(x + c_i \Delta x, t + \Delta t) = f_i^\star(x, t^\star) = f_i(x,t) + \Omega_i(x,t) + R_i(x,t) \,, \tag{3.2}$$

[2]Note that we use (x,t) instead of (x_j, t_k) to denote the discrete space and time variables (which is common in LBM literature).

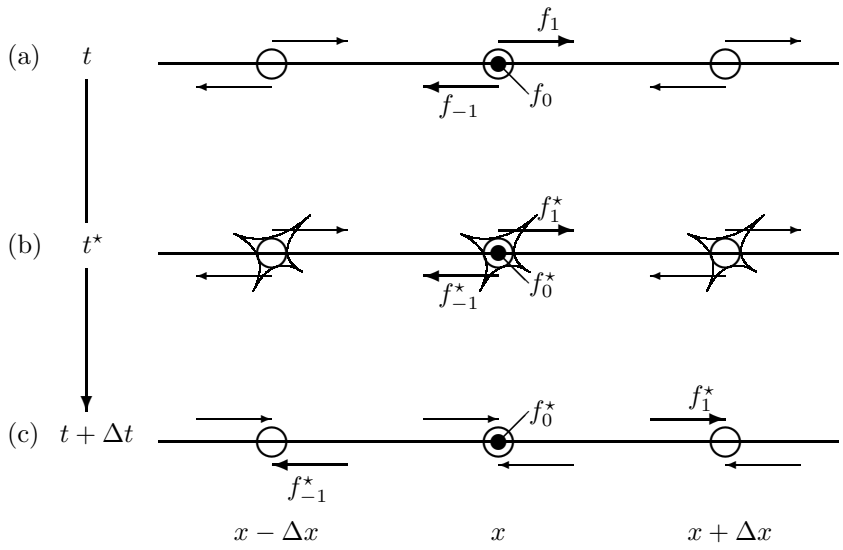


Figure 3.1: Evolution of the D1Q3 LBM for one time step Δt at lattice site x on a one-dimensional domain. (a) The distributions $f_i(x,t)$. (b) These variables undergo local collisions and reactions. As a result, we obtain post-collision values $f_i^\star(x,t^\star)$. (c) Subsequently, these values propagate to adjacent lattice sites according to their velocity $c_i = i$. We obtain the values $f_i(x + c_i\Delta x, t + \Delta t) = f_i^\star(x,t^\star)$.

for $i \in \{-1,0,1\}$. The collision term Ω_i models the diffusion while the reaction term R_i models the (chemical or physical) reactions. A LBM time step is then executed in two phases. First, the terms Ω_i and R_i are evaluated and used to update the value of $f_i(x,t)$ to *post-collision* values $f_i^\star(x,t^\star)$, with $t < t^\star < t + \Delta t$ (right hand side of (3.2)). Afterwards, these values propagate (or stream) to a neighboring site according to their velocity direction (left hand side of (3.2)). The LBE evolution (3.2) for one time step Δt is illustrated in Fig. 3.1.

The particle density $\rho(x,t)$, i.e. the macroscopic variable (cf. (2.4)), is defined as the zeroth order velocity moment of the distribution functions

$$\rho(x,t) = \sum_{i=-1}^{1} f_i(x,t) = \sum_{i=-1}^{1} f_i^{eq}(x,t)\ . \tag{3.3}$$

The second equality is explained below by (3.5).

3.2.1 Collision Term

The diffusive collisions are modeled by the Bhatnagar-Gross-Krook (BGK) collision model [18]. The collision operator Ω_i is defined as [26, 29, 110, 161]

$$\Omega_i(x,t) = -\omega \left(f_i(x,t) - f_i^{eq}(x,t) \right) , \tag{3.4}$$

and models the collisions as a relaxation to a local diffusive equilibrium distribution $f_i^{eq}(x,t)$. The relaxation rate is determined by the parameter ω (see below). Since no particles are created or destroyed during diffusive collisions, we have

$$\sum_{i=-1}^{1} \Omega_i(x,t) = 0 \quad \Leftrightarrow \quad \sum_{i=-1}^{1} f_i^{eq}(x,t) = \sum_{i=-1}^{1} f_i(x,t) = \rho(x,t) . \tag{3.5}$$

The latter expresses that the density ρ is a locally conserved quantity during the BGK diffusive collisions.

In turn, the equilibrium distribution $f_i^{eq}(x,t)$ is a functional of the conserved variable ρ and is defined as [34, 162, 205, 228]

$$f_i^{eq}(x,t) = \nu_i \, \rho(x,t) , \tag{3.6}$$

with ν_i satisfying the constraints (compare (3.5))

$$\sum_{i=-1}^{1} \nu_i = 1 \quad \text{and} \quad \nu_{-1} = \nu_1 .$$

This still leaves one degree of freedom for the choice of ν_i. For reaction-diffusion systems, all equilibrium weights are chosen equal [162, 41], i.e.

$$\nu_i = \frac{1}{3} . \tag{3.7}$$

The BGK relaxation coefficient ω in (3.4) is defined as

$$\omega = \frac{2}{1 + \frac{2D}{\sum_i c_i^2 \nu_i} \frac{\Delta t}{\Delta x^2}} , \tag{3.8}$$

with D the macroscopic diffusion coefficient from (2.4). In Sect. 3.3, we will derive this formula when $\nu_i = 1/3$. Note that in literature, the inverse $\tau = 1/\omega$ with τ a characteristic relaxation time is also frequently used. This single local BGK time scale τ should not be confused with the global time scales that are important for equation-free computing and bifurcation analysis. The large range of global time scales results from the coupling of

all lattice points. The slowest modes in the global behavior of the system evolve at much slower time scales than the local relaxation time scale.

For later use, we rewrite the LBE (3.2) with BGK collision model (3.4) as

$$f_i(x + c_i\Delta x, t + \Delta t) = (1 - \omega)f_i(x, t) + \omega f_i^{eq}(x, t) + R_i(x, t) \ , \quad (3.9)$$

If the reaction term $R_i(x, t)$ has a moderate value[3], the LBE (3.2) or (3.9) is linearly stable if $0 < \omega < 2$ [161, 192, 194].

3.2.2 Reaction Term

Reactions are modeled by the term $R_i(x, t)$ in (3.2) as [160, 162, 41]

$$R_i(x, t) = \frac{\Delta t}{3} F(\rho(x, t)) \ , \quad (3.10)$$

with $F(\rho(x, t))$ defined in (2.4). Here, it is assumed that reactions occur at the local diffusive equilibrium [40]. Hence the weights are the same as (3.7) for the equilibrium distribution.

3.3 Chapman-Enskog Expansion

When the system's solution varies slowly on a macroscopic length and time scale, both the LBM and PDE can be used to describe its evolution. Under this condition, the LBM from Sect. 3.2 can be reduced to the PDE from Sect. 2.2.2 using a multiscale Chapman-Enskog expansion [60]. Here, we perform a detailed derivation for the LBM from the previous section. First, we assume the diffusive scaling $x_\epsilon = \epsilon x$, $t_\epsilon = \epsilon^2 t$, with ϵ a small tracer parameter, such that the space and time derivatives are scaled as

$$\frac{\partial}{\partial x} = \epsilon \frac{\partial}{\partial x_\epsilon} \quad \text{and} \quad \frac{\partial}{\partial t} = \epsilon^2 \frac{\partial}{\partial t_\epsilon} \ . \quad (3.11)$$

For reaction-diffusion problems, we further assume that the reaction term $R_i(x, t)$ is of second order, i.e. $R_i = \epsilon^2 R_{i,\epsilon}$ [34, 41, 162]. This explains the choice in (3.10) and assures that the reactions only act on the scale of the second order terms in ϵ, which results in a direct appearance of the reaction forces in the reduced PDE (see below).

A second order Taylor expansion of the term $f_i(x + c_i\Delta x, t + \Delta t)$ in (3.9) around $f_i(x, t)$ leads to

$$\begin{aligned} &c_i\Delta x \frac{\partial f_i}{\partial x} + \Delta t \frac{\partial f_i}{\partial t} + \frac{c_i^2 \Delta x^2}{2} \frac{\partial^2 f_i}{\partial x^2} + c_i \Delta x \Delta t \frac{\partial^2 f_i}{\partial x \partial t} + \frac{\Delta t^2}{2} \frac{\partial^2 f_i}{\partial t^2} \\ &= -\omega(f_i - f_i^{eq}) + R_i \ . \end{aligned} \quad (3.12)$$

[3]Note the Δt scaling in (3.10).

Introducing the tracer scaling (3.11) and dropping the subscript ϵ notation, we obtain

$$\begin{aligned}&\epsilon c_i \Delta x \frac{\partial f_i}{\partial x} + \epsilon^2 \Delta t \frac{\partial f_i}{\partial t} + \epsilon^2 \frac{c_i^2 \Delta x^2}{2} \frac{\partial^2 f_i}{\partial x^2} + \epsilon^3 c_i \Delta x \Delta t \frac{\partial^2 f_i}{\partial x \partial t} \\ &+ \epsilon^4 \frac{\Delta t^2}{2} \frac{\partial^2 f_i}{\partial t^2} = -\omega (f_i - f_i^{eq}) + \epsilon^2 R_i \, .\end{aligned} \tag{3.13}$$

The distribution functions $f_i(x,t)$ are expanded in terms of increasingly higher order contributions $f_i^{[0]}$, $f_i^{[1]}$, ... as follows

$$f_i = f_i^{[0]} + \epsilon f_i^{[1]} + \epsilon^2 f_i^{[2]} + \epsilon^3 f_i^{[3]} + \mathcal{O}(\epsilon^4) \, . \tag{3.14}$$

We substitute (3.14) in (3.13) and keep only terms up to second order to obtain

$$\begin{aligned}&\epsilon c_i \Delta x \frac{\partial f_i^{[0]}}{\partial x} + \epsilon^2 c_i \Delta x \frac{\partial f_i^{[1]}}{\partial x} + \epsilon^2 \Delta t \frac{\partial f_i^{[0]}}{\partial t} + \epsilon^2 \frac{c_i^2 \Delta x^2}{2} \frac{\partial^2 f_i^{[0]}}{\partial x^2} \\ &= -\omega (f_i^{[0]} + \epsilon f_i^{[1]} + \epsilon^2 f_i^{[2]} - f_i^{eq}) + \epsilon^2 R_i \, .\end{aligned} \tag{3.15}$$

This equation should hold for each order separately. Equating the zeroth order terms leads to (cf. (3.6) and (3.7))

$$f_i^{[0]} = f_i^{eq} = \frac{1}{3} \rho \, . \tag{3.16}$$

The part of order ϵ leads to the following expression for the first order correction $f_i^{[1]}(x,t)$

$$f_i^{[1]} = -\frac{c_i \Delta x}{\omega} \frac{\partial f_i^{[0]}}{\partial x} = -\frac{c_i \Delta x}{3\omega} \frac{\partial \rho}{\partial x} \, . \tag{3.17}$$

Gathering the terms of order ϵ^2 in (3.15), we have

$$c_i \Delta x \frac{\partial f_i^{[1]}}{\partial x} + \frac{c_i^2 \Delta x^2}{2} \frac{\partial^2 f_i^{[0]}}{\partial x^2} + \Delta t \frac{\partial f_i^{[0]}}{\partial t} = -\omega f_i^{[2]} + R_i \, . \tag{3.18}$$

Substitution of (3.16), (3.17) and (3.10) results in the following expression for the second order contribution $f_i^{[2]}(x,t)$

$$f_i^{[2]} = -\frac{c_i^2 \Delta x^2}{6\omega^2} (\omega - 2) \frac{\partial^2 \rho}{\partial x^2} + \frac{\Delta t}{3\omega} \left(F(\rho) - \frac{\partial \rho}{\partial t} \right) \, . \tag{3.19}$$

When we sum (3.19) over all velocities, we obtain

$$\frac{\partial \rho}{\partial t} = -\frac{\Delta x^2}{3\omega \Delta t} (\omega - 2) \frac{\partial^2 \rho}{\partial x^2} + F(\rho) \, , \tag{3.20}$$

where we used the fact that $\sum_i f_i^{[2]} = 0$ (sum up (3.14) and use (3.3)). Comparing (3.20) to (2.4), we obtain the relation between D and ω (cf. [162])

$$\omega = \frac{2}{1 + 3\,D\frac{\Delta t}{\Delta x^2}}\ . \tag{3.21}$$

For a given diffusion coefficient D and for any space-time grid, there will always exists a value of $\omega \in (0, 2)$. Once a spatial grid has been chosen, the choice of the LBM time step Δt is therefore only subject to accuracy and efficiency considerations [208, 228]. This is different from a finite difference discretization for the same reaction-diffusion system, where we have a strong stability restriction on Δt (e.g. see Sect. 8.2). As mentioned in [228], this is what we gain from using more unknown variables in each lattice point. It can be shown [102, 95] that the LBM is of second order in space and first order in time[4].

Using the PDE (3.20) itself, (3.19) can be rewritten as

$$f_i^{[2]} = -\frac{\Delta t}{6\omega}(3c_i^2 - 2)\left(F(\rho) - \frac{\partial \rho}{\partial t}\right) = -\frac{\Delta x^2}{18\omega^2}(\omega - 2)(3c_i^2 - 2)\frac{\partial^2 \rho}{\partial x^2}\ . \tag{3.22}$$

One can use the Chapman-Enskog expansion to compute even higher order contributions to the state. These higher order expansions model the deviations from the second order LBM and PDE model. Extending the methodology described in this section to third order, the third order contribution $f_i^{[3]}$ can be obtained as

$$f_i^{[3]} = -\frac{c_i^3 \Delta x^3}{18\omega^3}(\omega^2 - 6\omega + 6)\frac{\partial^3 \rho}{\partial x^3} - \frac{c_i \Delta x \Delta t}{3\omega^2}\frac{\partial F(\rho)}{\partial x} - \frac{c_i \Delta x \Delta t}{3\omega^2}(\omega - 2)\frac{\partial^2 \rho}{\partial x \partial t}\ . \tag{3.23}$$

Again the PDE (3.20) can be used to translate time derivatives of ρ into second order spatial derivatives and vice versa.

3.4 Representation of the LBM State

Lattice Boltzmann models are often specified using the dimensionless variables for space, time and velocity obtained by rescaling space and time in units of grid spacing Δx and Δt respectively. To avoid confusion in our notation when moving between the mesoscopic and macroscopic space, we

[4]Note that $\mathcal{O}(\Delta t) \sim \mathcal{O}(\Delta x^2) \sim \mathcal{O}(\epsilon^2)$ because of the diffusive scaling and that, in our opinion, the value of ω must be kept constant in a stability analysis w.r.t. Δx and Δt.

will only express the higher order moments in dimensionless form. The dimensionless first and second order velocity moments (up to the factor 1/2 for the second order moment) of the distribution functions are

$$\phi(x,t) = \sum_{i=-1}^{1} c_i\, f_i(x,t) \quad , \quad \xi(x,t) = \frac{1}{2}\sum_{i=-1}^{1} c_i^2\, f_i(x,t)\ . \tag{3.24}$$

We will refer to these moments as the "momentum" ϕ and (kinetic) "energy" ξ (although these are non-conserved quantities in a diffusive system). The state of the LBM at time t and position x is then fully determined by either the distribution functions $\mathbf{f} = [f_{-1}\ f_0\ f_1]'$ or the moments $\boldsymbol{\varrho} = [\rho\ \phi\ \xi]'$. One can easily switch from one representation to the other by

$$\boldsymbol{\varrho} = \begin{bmatrix} \rho \\ \phi \\ \xi \end{bmatrix} = \begin{bmatrix} 1 & 1 & 1 \\ -1 & 0 & 1 \\ \frac{1}{2} & 0 & \frac{1}{2} \end{bmatrix} \begin{bmatrix} f_{-1} \\ f_0 \\ f_1 \end{bmatrix} = M\,\mathbf{f} \tag{3.25}$$

and vice versa $\mathbf{f} = M^{-1}\boldsymbol{\varrho}$ (one-to-one relationship).

As a by-product of the Chapman-Enskog expansion in Sect. 3.3, we derived slaving relations for the distribution functions f_i in terms of the macroscopic variable ρ on the slow manifold. Since we dropped the index ϵ notation in the derivation in Sect. 3.3, the actual macroscopic derivatives are obtained by combining (3.11) with (3.14). Up to second order, we have

$$f_i(x,t) = f_i^{[0]}(x,t) + f_i^{[1]}(x,t) + f_i^{[2]}(x,t) + \mathcal{O}(\Delta x^3)\ , \tag{3.26}$$

with the zeroth and first order contribution $f_i^{[0]}$ and $f_i^{[1]}$ given by (3.16) and (3.17), i.e.

$$f_i^{[0]} = f_i^{eq} = \frac{1}{3}\rho\ , \quad f_i^{[1]} = -\frac{\Delta x}{\omega} c_i \cdot \nabla f_i^{[0]} = -\frac{c_i \Delta x}{3\omega}\frac{\partial \rho}{\partial x}\ , \tag{3.27}$$

while the second order contribution $f_i^{[2]}$ was derived as (3.19) or (3.22)

$$f_i^{[2]} = -\frac{\Delta t}{6\omega}(3c_i^2 - 2)\left(F(\rho) - \frac{\partial \rho}{\partial t}\right) = -\frac{\Delta x^2}{18\omega^2}(\omega - 2)(3c_i^2 - 2)\frac{\partial^2 \rho}{\partial x^2}\ . \tag{3.28}$$

From (3.23)–(3.28) the equivalent slaving relations for the higher order moments $\phi(x,t)$ and $\xi(x,t)$ can be derived. Up to and including third order terms, we have (see also Appendix A)

$$\begin{aligned} \phi &= -\frac{2\Delta x}{3\,\omega}\frac{\partial \rho}{\partial x} + \frac{\Delta x \Delta t}{3\omega^2}\frac{(4\omega - 2)}{(\omega - 2)}\frac{\partial F(\rho)}{\partial x} + \frac{\Delta x \Delta t}{3\omega^2}\frac{(-2\omega^2 + 2\omega - 2)}{(\omega - 2)}\frac{\partial^2 \rho}{\partial x \partial t}\ , \\ \xi &= \frac{1}{3}\rho - \frac{\Delta t}{6\,\omega}\left(F(\rho) - \frac{\partial \rho}{\partial t}\right) + \mathcal{O}(\Delta x^4)\ . \end{aligned} \tag{3.29}$$

As in Sect. 3.3, we consider $\partial/\partial x$ to be a first order operator, while $\partial/\partial t$ and $F(\rho)$ are second order contributions (compare to the PDE (2.4)). In this way, the above expression for ϕ has a first and third order contribution, while ξ is written as a combination of zeroth and second order terms. Alternatively, relations (3.29) can be written in terms of spatial derivatives of ρ only using (3.20). Because of the discrete LBE propagation in (3.9), the continuous spatial derivatives in (3.29) can be seen as a shorthand notation for the appropriate central finite difference scheme corresponding to the D1Q3 stencil with according discretization (cf. Appendices A and B and [100, 101]).

The analogy with the notation of Chapter 2 is as follows. For the variables, $U = \rho$, $V = [\phi\ \xi]'$ and $u = f_i$. For the evolution, the LBE (3.9) stands in for the "microscopic" time stepper (2.5); the equations in moments space (2.9)–(2.10) are derived in Sect. 3.5. The slaving relations (2.7) or (2.11) are given by respectively (3.27)–(3.28) or (3.29) up to respective orders. Finally, the reduced equation (2.12) is the corresponding reaction-diffusion PDE (3.20) or equivalently (2.4).

3.5 Evolution Equations in Moment Space

To obtain a time stepper for the distribution functions $f_i(x,t)$ evaluated at the current position x, we write the standard LBE (3.9) alternatively as

$$f_i(x,t+\Delta t) = (1-\omega)\, f_i(x-c_i\Delta x,t)+\omega f_i^{eq}(x-c_i\Delta x,t)+R_i(x-c_i\Delta x,t)\ . \tag{3.30}$$

Expanding the terms in the right hand side of (3.30) up to second order around respectively $f_i(x,t)$, $f_i^{eq}(x,t)$ and $R_i(x,t)$, we obtain

$$\begin{aligned} f_i(x,t\ +\ \Delta t) = (1-\omega)&\left(f_i(x,t) - c_i\Delta x\frac{\partial f_i(x,t)}{\partial x} + \frac{c_i^2\Delta x^2}{2}\frac{\partial^2 f_i(x,t)}{\partial x^2}\right) \\ +\ \omega&\left(f_i^{eq}(x,t) - c_i\Delta x\frac{\partial f_i^{eq}(x,t)}{\partial x} + \frac{c_i^2\Delta x^2}{2}\frac{\partial^2 f_i^{eq}(x,t)}{\partial x^2}\right) \\ +\ &R_i(x,t) - c_i\Delta x\frac{\partial R_i(x,t)}{\partial x} + \frac{c_i^2\Delta x^2}{2}\frac{\partial^2 R_i(x,t)}{\partial x^2}\ . \end{aligned} \tag{3.31}$$

We now transform (3.31) to the space of moments. First, we sum over all distributions. Using definitions (3.25), we then get the equation for the macroscopic variables ρ

$$\begin{aligned} \rho(x,t+\Delta t) = \rho(x,t) &+ (1-\omega)\left(-\Delta x\frac{\partial\phi(x,t)}{\partial x} + \Delta x^2\frac{\partial^2\xi(x,t)}{\partial x^2}\right) \\ &+ \frac{\omega\Delta x^2}{3}\frac{\partial^2\rho(x,t)}{\partial x^2} + \Delta t F(\rho(x,t)) + \frac{\Delta t\Delta x^2}{3}\frac{\partial^2 F(\rho(x,t))}{\partial x^2}\ , \end{aligned} \tag{3.32}$$

where we used property (3.3) (local conservation of density), definitions (3.6) and (3.10) and $c_1^2 = c_{-1}^2 = 1$. The evolution equation for momentum ϕ is derived by multiplying (3.31) with c_i and summing over all i

$$\begin{aligned}\phi(x,t+\Delta t) = (1-\omega)\left(\phi(x,t) - 2\,\Delta x\,\frac{\partial \xi(x,t)}{\partial x} + \frac{\Delta x^2}{2}\frac{\partial^2 \phi(x,t)}{\partial x^2}\right) \\ - \frac{2\,\omega \Delta x}{3}\frac{\partial \rho(x,t)}{\partial x} - \frac{2\,\Delta x \Delta t}{3}\frac{\partial F(\rho(x,t))}{\partial x}\,.\end{aligned} \tag{3.33}$$

If we multiply (3.31) by $c_i^2/2$ and sum afterwards, we get the following equation for energy ξ

$$\begin{aligned}\xi(x,t+\Delta t) = (1-\omega)\left(\xi(x,t) - \frac{\Delta x}{2}\frac{\partial \phi(x,t)}{\partial x} + \frac{\Delta x^2}{2}\frac{\partial^2 \xi(x,t)}{\partial x^2}\right) + \frac{\omega}{3}\rho(x,t) \\ + \frac{\omega \Delta x^2}{6}\frac{\partial^2 \rho(x,t)}{\partial x^2} + \frac{\Delta t}{3}F(\rho(x,t)) + \frac{\Delta t \Delta x^2}{6}\frac{\partial^2 F(\rho(x,t))}{\partial x^2}\,.\end{aligned} \tag{3.34}$$

Obviously, the explicit time stepping in the above equations can be seen as a forward finite difference discretization of the corresponding continuous time derivative. Therefore, substituting $\boldsymbol{\varrho}(x,t+\Delta t) - \boldsymbol{\varrho}(x,t) = \Delta t\ \partial \boldsymbol{\varrho}(x,t)/\partial t$ in (3.32)–(3.34) leads to the fully continuous versions (in x and t) of these equations. In Appendix B.1, we present an alternative derivation of (3.32)–(3.34) based on the discrete nature of the LBM. Furthermore, we show in Appendix B.2 that the reduced PDE (2.4) can be obtained by substituting the slaving relations (3.29) for ϕ and ξ up to first order into (3.32) and retaining only the terms up to second order. As such, the derivation of the moment equations can be seen as an alternative to the Chapman-Enskog expansion. We refer to related work on the derivation of the LBM moment equations for the incompressible Navier-Stokes equations in two dimensions using either six velocities [109] or nine velocities [101] (where the conserved variables are ρ and ϕ) and to [43] for the moment equations for a thermal LBM with nine velocities in two dimensions (the conserved variables are now ρ, ϕ and ξ).

3.6 Fick's Laws and the Particle Flux

In this section, we show how the LBM from Sect. 3.2 for purely diffusive systems relates to classical Fickian diffusion.

The mass flux j is generally defined as the amount of particles that cross an interface at a given time instance. For the LBM from Sect. 3.2, the flux

can be defined at the boundary between lattice points x and $x + \Delta x$ as[5,6]

$$j(x + \frac{\Delta x}{2}, t + \Delta t) = v_1 f_1(x + \Delta x, t + \Delta t) + v_{-1} f_{-1}(x, t + \Delta t) \quad (3.35)$$

$$= v_1 f_1^\star(x, t^\star) + v_{-1} f_{-1}^\star(x + \Delta x, t^\star) \,, \quad (3.36)$$

with $f_i^\star$ the propagating (post-collision) distributions defined in Sect. 3.2.

Note that there is a subtle difference between the momentum ϕ (3.24) and the flux j (3.35) of the particles. The momentum is computed in the lattice nodes x while the flux is computed in between consecutive lattice nodes (at the boundary of the control volumes). Therefore, the flux effectively uses distributions from two different nodes.

Using (3.1) and (3.9), the flux (3.36) can be written as

$$j(x + \frac{\Delta x}{2}, t + \Delta t) = \frac{\Delta x}{\Delta t}\Big((1-\omega)\big(f_1(x,t) - f_{-1}(x + \Delta x, t)\big) + \frac{\omega}{3}\big(\rho(x,t) - \rho(x + \Delta x, t)\big)\Big) \,. \quad (3.37)$$

When we substitute the slaving relations up to first order (3.27), i.e. the equilibrium and the dominant non-equilibrium components of f_i, we obtain

$$j(x + \frac{\Delta x}{2}, t + \Delta t) = \frac{\Delta x}{\Delta t}\Big(\frac{1}{3}\big(\rho(x,t) - \rho(x + \Delta x, t)\big) - (1-\omega)\frac{\Delta x}{3\omega}\Big(\frac{\partial \rho(x,t)}{\partial x} + \frac{\partial \rho(x + \Delta x, t)}{\partial x}\Big)\Big) \,. \quad (3.38)$$

Expressing (3.38) w.r.t. $x + \Delta x/2$, we have

$$j(x + \frac{\Delta x}{2}, t + \Delta t) = -\frac{\Delta x}{\Delta t}\left(\frac{\Delta x}{3} + (1-\omega)\frac{2\Delta x}{3\omega}\right)\frac{\partial \rho(x + \Delta x/2, t)}{\partial x} \,. \quad (3.39)$$

Using (3.21), we obtain

$$j(x + \frac{\Delta x}{2}, t + \Delta t) = -D\frac{\partial \rho(x + \Delta x/2, t)}{\partial x} \,, \quad (3.40)$$

which states that the flux is proportional to the density gradient. Equation (3.40) is known as Fick's first law of diffusion [150]. The minus sign indicates that diffusion transports particles from regions of high density to regions of low density.

[5] We use the dimensioned formulation here, i.e. we use the speeds v_i rather than c_i.

[6] For multispeed models like the D1Q5R model in Sect. 3.8.3, this definition is not entirely accurate. As the flux counts the number of particles, the magnitude of the lattice speeds c_i (in casu 2) should not be taken into account.

To obtain Fick's second law of diffusion, i.e. the standard diffusion equation (2.4), we write down a conservation law that states that the rate of change in the amount of particles in a region is equal to the flow of particles that move in, minus those that move out across the boundaries. Here, we assume that no particles are created within the region. For the region $x - \Delta x/2 < x < x + \Delta x/2$ around node x, we have

$$\int_{x-\Delta x/2}^{x+\Delta x/2} \frac{\rho(x, t+\Delta t) - \rho(x,t)}{\Delta t} \, \mathrm{d}x = j(x - \frac{\Delta x}{2}, t) - j(x + \frac{\Delta x}{2}, t) \; .$$

For $\Delta t \to 0$ and $\Delta x \to 0$, we obtain Fick's second law of diffusion, i.e. the PDE for pure diffusion (2.4)

$$\frac{\partial \rho(x,t)}{\partial t} = -\frac{\partial j(x,t)}{\partial x} = D \frac{\partial^2 \rho(x,t)}{\partial x^2} \; , \tag{3.41}$$

where we used Fick's first law (3.40). Note that the last equality in (3.41) only holds if and only if D is independent of x.

3.7 FitzHugh-Nagumo Example

The FitzHugh-Nagumo (FHN) system [58, 151] is a reduced mathematical model for the more realistic Hodgkin and Huxley model [94]. The latter describes the excitable behavior of the nerve membrane of the giant squid due to the firing of electrical pulses of its nerve cells or neurons. The FHN model has been widely used as a generic model exhibiting rich bifurcation behavior, moving fronts, pattern formation and spiral wave phenomena, see e.g. [52, 73, 85, 155, 158, 226]. We will use the FHN model as our primary example throughout this thesis.

In Sect. 3.7.1, we define the PDE reaction-diffusion model for the FHN system. Section 3.7.2 describes the corresponding LBM. The reactive lattice gas cellular automata described in [140, 141] are another type of mesoscopic models for the FHN system.

3.7.1 Macroscopic PDE Model

At the macroscopic level, the FHN system is described by two reaction-diffusion PDEs for an activator and inhibitor species (denoted by the superscripts ac and in respectively). On the one-dimensional domain, we have

$$\begin{aligned} \frac{\partial \rho^{ac}}{\partial t} &= D^{ac} \frac{\partial^2 \rho^{ac}}{\partial x^2} + \rho^{ac} - (\rho^{ac})^3 - \rho^{in} \; , \\ \frac{\partial \rho^{in}}{\partial t} &= D^{in} \frac{\partial^2 \rho^{in}}{\partial x^2} + \varepsilon(\rho^{ac} - a_1 \rho^{in} - a_0) \; . \end{aligned} \tag{3.42}$$

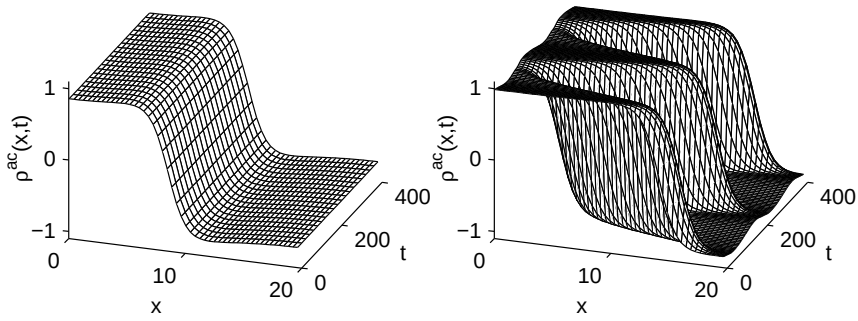


Figure 3.2: Stable steady state at $\varepsilon = 0.05$ (left) and stable periodic solution at $\varepsilon = 0.006$ (right) of the FHN LBM.

The variables $\rho^{ac}(x,t)$ and $\rho^{in}(x,t)$ are the activator and inhibitor particle densities (concentrations) respectively[7]. In all our computations, we fix the FHN parameters to the values $D^{ac} = 1$, $D^{in} = 4$, $a_0 = -0.03$ and $a_1 = 2$. The parameter ε serves as our bifurcation parameter in Chapter 4 and is varied between 0 and 1. Outside the context of bifurcation analysis, ϵ has the value 0.05 for steady state simulations. At the boundaries, we impose homogeneous Neumann (i.e. no-flux) boundary conditions on the one-dimensional domain $[0, L]$ of length $L = 20$. A typical steady state (here, for $\varepsilon = 0.05$) and periodic solution (here, for $\varepsilon = 0.006$) are shown in Fig. 3.2.

3.7.2 Mesoscopic Model

For each species, the LBM is described in Sect. 3.2. The evolution of the species is coupled through the reaction terms $R_i(x,t)$ only. These terms can be derived from (3.42) as (3.10), i.e.

$$\begin{aligned} R_i^{ac} &= \frac{\Delta t}{3} \left(\rho^{ac} - (\rho^{ac})^3 - \rho^{in} \right) , \\ R_i^{in} &= \frac{\Delta t}{3} \, \varepsilon \left(\rho^{ac} - a_1 \rho^{in} - a_0 \right) . \end{aligned} \tag{3.43}$$

We choose a LBM time step $\Delta t = 0.001$ (see Sect. 4.4).

The no-flux boundary conditions are implemented using the halfway bounce-back scheme [71, 90]. This puts the LBM variables at the midpoints of $N = 200$ lattice intervals (the same location as in the PDE discretization, see Sect. 2.2.2). The lattice size equals $\Delta x = 0.1$. Consider the left

[7] Strictly speaking, these are no concentrations in the physical sense because the values can also be negative depending on the choice of parameter values (cf. [85]).

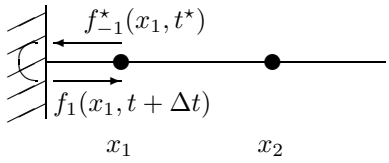


Figure 3.3: Mechanics of the halfway bounce-back scheme at the left boundary.

boundary that is a distance $\Delta x/2$ away from the nearest internal site x_1. The unknown incoming (out-of-wall) distribution f_1 is given by

$$f_1(x_1, t + \Delta t) = f^\star_{-1}(x_1, t^\star) \,, \tag{3.44}$$

a condition that is imposed during propagation. Here, $f^\star_{-1}$ denotes the post-collision value of f_1 (cf. Sect. 3.2). Figure 3.3 sketches the procedure. Similarly, we have $f_{-1}(x_N, t + \Delta t) = f^\star_1(x_N, t^\star)$ at the right wall.

3.8 Distribution Dependent Reaction Term

3.8.1 Planar Streamer Fronts

Many microscopic systems have reaction rates that depend on the velocities of the colliding particles. We consider the ionization reaction of moving electrons in a molecular gas under the influence of a strong electrical field. The electrical field accelerates the electrons. As a result, an ionization reaction occurs when the electrons collide with the neutral gas molecules. Hereby, the electrons transfer part of their energy. Slow electrons collide elastically and only change their direction. Fast electrons slow down by kicking additional electrons out of the molecule. In turn, these additional electrons are accelerated by the electrical field. The net result is a sharp, non-linear wave of electrons that propagates through the gas, called a streamer front of electrons. Under extreme conditions, an electron avalanche occurs at the tip of the front that can cause a disruptive discharge or lightning sparks.

Because of the computational complexity of such systems, most analysis of streamer fronts is based on a Townsend approximation of the microscopic ionization reaction that appears at the tip of the front [51]. The reaction term is described by $F(\rho(x,t)) = \rho(x,t)|E| \exp(-1/|E|)$ and depends on the electron density only. Here $E(x,t)$ represents the electrical field.

Ideally, the reactions should be modeled on a microscopic or mesoscopic level to capture the complex collision process. In [222], a LBM for the elec-

tron distributions $f_i(x,t)$ is derived. This model was used to compute the planar streamer front solutions numerically in [175]. This LBM is coupled to a PDE that describes the evolution of the electrical field $E(x,t)$ through the macroscopic electron density field $\rho(x,t)$. The coupled equations are

$$f_i(x+c_i\Delta x, t+\Delta t) = (1-\omega)f_i(x,t) + \omega f_i^{eq}(x,t) + \Delta t \sum_j R_{ij} f_j(x,t) \\ -\frac{\Delta t}{2}\big(E(x-\frac{\Delta x}{2},t) + E(x+\frac{\Delta x}{2},t)\big)\sum_j V_{ij} f_j(x,t)\ , \qquad (3.45)$$

$$E(x+\frac{\Delta x}{2}, t+\Delta t) = E(x+\frac{\Delta x}{2},t) - \Delta t\, j(x+\frac{\Delta x}{2},t)\ , \qquad (3.46)$$

where the sums are taken over all velocity indexes j, e.g. $j \in \{-1,0,1\}$ for the D1Q3 model from Sect. 3.2. The flux $j(x+\Delta x/2,t)$ is calculated from (3.36). The definition of V_{ij} as well as all the details for the derivation of (3.45)–(3.46) can be found in [222]. Note that the reaction term $\Delta t \sum_j R_{ij} f_j(x,t)$ explicitly depends on the particle velocities through the distribution functions. The reaction rates R_{ij} will be defined below.

In Chapter 7, we will extend the analysis of Chapter 6 for a simplified version of (3.45)–(3.46). We leave the evolution of $E(x,t)$ aside and only consider the reaction terms depending on the distributions, i.e.

$$f_i(x+c_i\Delta x, t+\Delta t) = (1-\omega)f_i(x,t) + \omega f_i^{eq}(x,t) + \Delta t \sum_j R_{ij} f_j(x,t)\ . \qquad (3.47)$$

3.8.2 D1Q3R Model

First, we consider the D1Q3 model with speeds (3.1). The reaction term in (3.47) can be modeled as

$$\Delta t\ R\,\mathbf{f} = \Delta t \begin{bmatrix} -\alpha_1 & 0 & 0 \\ \alpha_2 & 0 & \alpha_2 \\ 0 & 0 & -\alpha_1 \end{bmatrix} \begin{bmatrix} f_{-1} \\ f_0 \\ f_1 \end{bmatrix}\ , \qquad (3.48)$$

i.e. particles with (dimensionless) speed ± 1 "slow down" at a rate α_1 to become particles with speed $c_0 = 0$. The latter are created at a rate α_2. When $\alpha_2 > \alpha_1$ we have a growth-diffusion type system as used in [215]. When $\alpha_1 = \alpha_2 = \alpha$, no particles are created in the system; as $\sum_i R_i = 0$. In the latter case, the model has a clear steady state. The BGK equilibrium $f_i^{eq}(x,t)$ is again defined by (3.6). We will refer to the D1Q3 model with reaction term (3.48) and constant $\alpha_1 = \alpha_2 = \alpha$ as the D1Q3R model.

3.8.3 D1Q5R Multispeed Model

Second, we consider the one-dimensional model with five speeds used in [175, 222] to model the ionization process discussed in Sect. 3.8.1. The speeds are

$$v_i = c_i \frac{\Delta x}{\Delta t}, \quad c_i = i \in \{-2, -1, 0, 1, 2\} \; . \tag{3.49}$$

Here, the distributions $f_{\pm 2}$ model the fast particles (electrons) with speeds ± 2 while $f_{\pm 1}$ represents the electrons with speed ± 1.

The reaction term in (3.47) is defined as

$$\Delta t \; R \, \mathbf{f} = \Delta t \begin{bmatrix} -\alpha & 0 & 0 & 0 & 0 \\ \alpha & 0 & 0 & 0 & \alpha \\ 0 & 0 & 0 & 0 & 0 \\ \alpha & 0 & 0 & 0 & \alpha \\ 0 & 0 & 0 & 0 & -\alpha \end{bmatrix} \begin{bmatrix} f_{-2} \\ f_{-1} \\ f_0 \\ f_1 \\ f_2 \end{bmatrix} \; , \tag{3.50}$$

i.e. during the ionization reaction, a particle with (dimensionless) speed ± 2 slows down to speed ± 1 and kicks another particle with opposite speed ∓ 1 out of the molecule at a constant rate α.

The BGK diffusive equilibrium is defined similarly to (3.6) as

$$f_i^{eq}(x,t) = \nu_i \rho(x,t) \quad \text{with} \quad \nu_i = \{0, 1/4, 2/4, 1/4, 0\} \; . \tag{3.51}$$

For this choice of weights, there are no fast particles under diffusive equilibrium. The number of electrons is conserved in (3.4), but not the momentum. According to [222], the latter is because, during diffusion, the electrons randomly change their direction when they collide elastically with the much heavier neutral molecules. Note that the relaxation parameter ω is now defined by (3.8) as $\omega = 2/(1 + 4D\Delta t/\Delta x^2)$. We will refer to this model as the D1Q5R model.

3.8.4 Chapman-Enskog Expansion for D1Q3R

In this section, we perform a Chapman-Enskog expansion for the D1Q3R model from Sect. 3.8.2. The derivation is very similar to the one in Sect. 3.3. Using the tracer ϵ, we define the diffusive coordinate scaling (3.11) and expand the distribution functions as in (3.14). Substituting these relations in a second order Taylor expansion of (3.47), we obtain

$$\begin{aligned} &\epsilon c_i \Delta x \frac{\partial f_i^{[0]}}{\partial x} + \epsilon^2 c_i \Delta x \frac{\partial f_i^{[1]}}{\partial x} + \epsilon^2 \Delta t \frac{\partial f_i^{[0]}}{\partial t} + \epsilon^2 \frac{c_i^2 \Delta x^2}{2} \frac{\partial^2 f_i^{[0]}}{\partial x^2} = \\ &- \omega \big(f_i^{[0]} + \epsilon f_i^{[1]} + \epsilon^2 f_i^{[2]} - f_i^{eq} \big) + \Delta t \sum_j R_{ij} \big(f_j^{[0]} + \epsilon f_j^{[1]} + \epsilon^2 f_j^{[2]} \big) \; . \end{aligned} \tag{3.52}$$

The difference between (3.52) and (3.15) in Sect. 3.3 is clearly the expansion of the reaction term. Because the reactions depend on the distributions directly instead of just the macroscopic density, the reaction term is not exclusively of second order anymore.

Equation (3.52) should hold for each order separately. When we gather all ϵ^0 terms, we obtain the zeroth order contribution

$$f_i^{[0]} = f_i^{eq} + \frac{\Delta t}{\omega} \sum_j R_{ij} f_j^{[0]} \,. \tag{3.53}$$

Specifically for the reaction term (3.48), we have

$$f_{\pm 1}^{[0]} = \frac{\omega}{\omega + \alpha \Delta t} f_{\pm 1}^{eq} \quad \text{and} \quad f_0^{[0]} = f_0^{eq} + \frac{\alpha \Delta t}{\omega + \alpha \Delta t} \big(f_1^{eq} + f_{-1}^{eq} \big) \,. \tag{3.54}$$

Gathering all ϵ terms from (3.52), we obtain

$$f_i^{[1]} = -\frac{c_i \Delta x}{\omega} \frac{\partial f_i^{[0]}}{\partial x} + \frac{\Delta t}{\omega} \sum_j R_{ij} f_j^{[1]} \,. \tag{3.55}$$

For the reaction term (3.48), we obtain

$$f_{\pm 1}^{[1]} = -\frac{(\pm 1)\omega \Delta x}{(\omega + \alpha \Delta t)^2} \frac{\partial f_{\pm 1}^{eq}}{\partial x} \quad \text{and} \quad f_0^{[1]} = \frac{\alpha \Delta t}{\omega} \big(f_1^{[1]} + f_{-1}^{[1]} \big) \,. \tag{3.56}$$

When we gather all ϵ^2 terms, we obtain the following expression for $f_i^{[2]}$

$$f_i^{[2]} = -\frac{c_i \Delta x}{\omega} \frac{\partial f_i^{[1]}}{\partial x} - \frac{\Delta t}{\omega} \frac{\partial f_i^{[0]}}{\partial t} - \frac{c_i^2 \Delta x^2}{2\omega} \frac{\partial^2 f_i^{[0]}}{\partial x^2} + \frac{\Delta t}{\omega} \sum_j R_{ij} f_j^{[2]} \,. \tag{3.57}$$

By substituting (3.54) and (3.56), relations for $f_i^{[2]}$ in terms of f_i^{eq} can be obtained.

It can be checked that $\sum_i f_i^{[0]} = \sum_i f_i^{eq}$. This holds because $\sum_{ij} R_{ij} f_j = 0$, i.e. because there are no particle injected or created in the system. Because the diffusive BGK collision term (3.4) locally conserves density (3.5), we have $\sum_i f_i^{[0]} = \rho$ and $\sum_i f_i^{[1]} = \sum_i f_i^{[2]} = 0$ (sum up (3.14)). By summing (3.57) over all velocities, we obtain, after some calculations, a PDE for the density

$$\frac{\partial \rho}{\partial t} = \frac{\Delta x^2}{\Delta t} \frac{\omega(2 - \omega - \alpha \Delta t)}{3(\omega + \alpha \Delta t)^2} \frac{\partial^2 \rho}{\partial x^2} = \bar{D} \frac{\partial^2 \rho}{\partial x^2} \,, \tag{3.58}$$

or equivalently

$$\frac{\partial \rho}{\partial t} = D \frac{\omega^2}{(\omega + \alpha \Delta t)^2} \frac{\partial^2 \rho}{\partial x^2} - \frac{\Delta x^2 \omega \alpha}{3(\omega + \alpha \Delta t)^2} \frac{\partial^2 \rho}{\partial x^2} \,, \tag{3.59}$$

with $\bar{D}$ the resulting macroscopic diffusion coefficient and D the diffusion coefficient defined by (3.21) that would be obtained when $\alpha = 0$. The altered diffusion can be explained because mesoscopically there is no particle creation, only a change in speed of particles according to the reactions (3.48). As a result, the macroscopic diffusion behavior changes.

The slaving relations for momentum and energy can be computed from the Chapman-Enskog relations (3.53)–(3.57) for $f_i^{[0]}$, $f_i^{[1]}$ and $f_i^{[2]}$ using definition (3.24). After some tedious calculations, we obtain the slaving relations up to second order for momentum

$$\phi = -\frac{2\Delta x\omega}{3(\omega + \alpha\Delta t)^2}\frac{\partial \rho}{\partial x} + \mathcal{O}(\Delta x^3) \,, \tag{3.60}$$

and energy

$$\xi = \frac{\omega}{3(\omega + \alpha\Delta t)}\rho + \frac{\Delta t(\omega + 3\alpha\Delta t)}{6(\omega + \alpha\Delta t)^2}\frac{\partial \rho}{\partial t} + \mathcal{O}(\Delta x^4) \,, \tag{3.61}$$

where the factor $\partial\rho/\partial t$ in (3.61) can be substituted for $\bar{D}\partial^2\rho/\partial x^2$ using the PDE (3.58). Note that a sanity check shows that for $\alpha = 0$, (3.60)–(3.61) is equivalent to (3.29) for pure diffusion.

Chapter 4

Time Stepper Based Bifurcation Analysis

4.1 Introduction

Direct time simulation is a popular method to study the influence of varying parameters in a parameter-dependent dynamical system. However, comparing the simulation results for many different fixed parameter values is tedious. Also, only stable solutions can be explored in this way. Bifurcation theory offers a more systematic way to study the asymptotic behavior of a parameter-dependent system by examining the possible transitions between various stable and unstable static and dynamic equilibria as the parameters are varied. In a numerical bifurcation analysis, one computes branches of solutions of some type (steady states, periodic solutions or a particular type of critical points) by varying one or — for branches of critical points — more parameters. Along the branch, the stability information is monitored and the critical (or *bifurcation*) points where stability changes occur are detected and often computed. In these bifurcation points, other branches of solutions usually intersect or branches of solutions of a different type emerge or end.

Numerical bifurcation analysis is well established for small ODE/PDE systems [178, 193] with several software packages available, e.g. AUTO [45] and MATCONT [42]. For systems with a small dimensional state space, the Jacobian matrix of the linearized system can be computed. Its eigenvalues determine the stability of a solution. More recently, various so-called 'matrix-free' bifurcation analysis methods have been proposed for large-scale systems. Here, the state space dimension is so large that a direct computation of the Jacobian matrix becomes nearly impossible. Of partic-

ular interest are methods that operate on top of an existing time simulation code [204]. In this chapter, we show that such techniques can be used for the bifurcation analysis of LBMs also. Examples of these *time stepper* or *time simulation based* bifurcation codes are the Recursive Projection Method [184] and the Newton-Picard method [133, 134, 135]. These methods exploit a spectral property of the time integration operator that is typical of systems with a dissipative operator: the time integration operator has only few large eigenvalues, i.e. eigenvalues close to or outside the unit circle. In other words, the system's long-term behavior is governed by only a small number of slow modes. This is an inherent property of the physics of the system and is independent of the mathematical model. We use the Newton-Picard method rather than the Recursive Projection Method because it is more robust and better suited to compute branches of periodic solutions.

We will discuss two strategies for the bifurcation analysis of LBM. One approach is to use the LBM time stepper directly as the time stepper in the bifurcation code. The state can be expressed completely either by the distribution functions or by the set of corresponding velocity moments (cf. Sect. 3.4). We will also make a slight extension of the LBM time stepper to compute periodic solutions. The second approach is based on the coarse equation-free time stepper proposed by Kevrekidis *et al.* [108, 199]. It performs a time integration for the macroscopic variables (a subset of the velocity moments in a LBM) using only microscopic or mesoscopic simulations. Recall from Sect. 2.5 that a coarse time step ΔT is carried out in three parts. First, the mesoscopic state is initialized from the macroscopic one. The system is then evolved in time using the LBM time stepper. Finally, the macroscopic state is computed from the mesoscopic one. This strategy is applicable to many microscopic or mesoscopic models. Whereas our numerical bifurcation analysis techniques rely on a separation of time scales at the macroscopic level, the coarse time stepper relies on a time scale separation between the macroscopically relevant variables, i.e. the lower order moments of the distribution functions in a LBM, and the other variables that are only relevant at the microscopic or mesoscopic scales.

We use the FitzHugh-Nagumo reaction-diffusion system from Sect. 3.7 as our test example. Because the macroscopic PDE is known in this case, we will also perform a bifurcation analysis on the latter model to compare the LBM and coarse equation-free LBM results with. However, it should be noted that the full LBM is the ideal benchmark to compare the equation-free LBM bifurcation results with. Indeed, as we shall argue later, if the microscopic model has a steady state, the best one can hope for is to compute the same steady state using the coarse equation-free time stepper (and similarly for periodic solutions). These states may be slightly different from those of an equivalent macroscopic model since every macroscopic model is only an approximation and thus involves modeling errors. Our LBM is fully

deterministic and has no chaotic dynamics. Our initialization of the LBM at each coarse time step is also fully deterministic. Therefore this model is an ideal example to study the errors caused by the imperfect initialization (lifting) of the "microscopic" state in the coarse time stepper, see Chapter 5.

A coarse-grained bifurcation analysis for the steady solutions of the FHN example has previously been performed by Theodoropoulos *et al.* in [199]. In this and the next chapter, we extend the results obtained in that paper in several ways. First, we extend the coarse time stepper concept to enable the computation of periodic solutions and we use the more versatile Newton-Picard method rather than the Recursive Projection Method for the numerical bifurcation analysis. Second, we compare the obtained bifurcation diagram with the bifurcation diagrams of the corresponding macroscopic PDE and the full LBM. Finally, in Chapter 5, we perform an extensive study of the influence of the lifting or reconstruction step on the minimal successful time step of the coarse time stepper and the accuracy of the results. It is shown experimentally that this time step must often be much larger than the time it takes for the higher order moments to become slaved by the lowest order moment, which somewhat contradicts earlier claims.

The plan of this chapter is as follows. We discuss the specifics of the macroscopic PDE model, the LBM and the equation-free LBM time integrator in Sect. 4.2. The Newton-Picard scheme is discussed in Sect. 4.3. In Sect. 4.4, we compute the bifurcation diagram for steady states and periodic solutions of the PDE, the LBM and the coarse equation-free time stepper for the LBM. A careful study of the effects of the initialization of the microscopic simulator and the size of the macroscopic time step on the results is deferred to the next chapter. We also study the dominant eigenvalues that determine stability in Sect. 4.5 and their effect on the number of calls to the time stepper in Sect. 4.6. In Sect. 4.7, we summarize the main conclusions.

4.2 System Descriptions

The FitzHugh-Nagumo reaction-diffusion system of two interacting species on the one-dimensional domain is described in Sect. 3.7. The PDE and corresponding LBM are already discussed there, but we go into some application specific details of these models in Sect. 4.2.1 and 4.2.2 respectively. In Sect. 4.2.3, we present the coarse time stepper as defined in Sect. 2.5 with our LBM as the "microscopic" model.

4.2.1 Macroscopic PDE Description

In our numerical bifurcation analysis experiments in Chapter 4 and 5, we used a method of lines discretization of (3.42) with central finite differences

(FD) in space at the midpoints of $N = 200$ grid intervals and the trapezoidal rule for time integration. The FD time step is fixed during the computation of a single trajectory but varied between 0.02 and 0.47 for different computations in these chapters.

4.2.2 Mesoscopic LBM Description

The LBM is discussed in Sect. 3.2. In Sect. 4.4, we will compute a branch of periodic solutions of the LBM. Strictly speaking, a periodic orbit is a phenomenon in a continuous time model while an invariant circle is the corresponding phenomenon in maps and thus in discrete time systems. However, since the (discrete time) LBM clearly models a continuous time system and since the LBM time step is so small compared to the period of the limit cycle, it makes sense to consider a continuous time extension of the LBM and to use numerical techniques developed for such models.

When integrating over a time interval $[0, T]$, the end time T can be arbitrary. To evaluate the LBM state at arbitrary T, we use the same strategy as many time integration codes for ODEs, e.g. LSODE [93]. We first determine the positive integer k such that $(k-1)\Delta t < T \leq k\Delta t$ and then use a linear interpolation between the results at the discrete time steps $k-1$ and k. Because there is a linear transformation (3.25) between the distribution functions and the moments, it does not matter whether we interpolate the distribution functions or corresponding moments.

4.2.3 Coarse Equation-Free LBM Description

4.2.3.1 Performing a Single Coarse Time Step

In this section, we apply the equation-free modeling approach from Sect. 2.5 to the LBM for one-dimensional reaction-diffusion systems from Sect. 3.2. In this case, the existence of a macroscopic PDE confirms that a macroscale equation-free computational description using only the zeroth order moment $\rho(x,t)$ of the LBM distributions is feasible. The resulting coarse equation-free time integrator evolves the density $\rho(x,t)$.

Recall that a coarse time step ΔT consists of three basic steps. First, meaningful initial values for the distribution functions have to be derived that are consistent with the macroscopic variable $\rho^{(0)} = \rho(x,0)$. To start with, we will use the lifting scheme proposed in [199]

$$f_i(x,0) = w_i\,\rho(x,0) \quad \text{with} \quad \sum_{i=-1}^{1} w_i = 1\,. \tag{4.1}$$

The constraint on the reconstruction or lifting weights w_i follows from the correspondence of the LBM state with the macroscopic state, see (3.3). A

first choice for the weights w_i are those for the local diffusive equilibrium distribution (3.7), i.e.

$$w_i = \nu_i = \frac{1}{3} \,. \tag{4.2}$$

In Chapter 5, we will consider other choices for the weights w_i and investigate the influence of the lifting operation on the accuracy of the time integration and bifurcation analysis.

Because the LBM state is described completely by either the distributions $\mathbf{f}$ or the moments $\boldsymbol{\varrho}$ (see Sect. 3.4), with a linear transformation between both spaces: $\boldsymbol{\varrho} = M\mathbf{f}$ (3.25), we see that the lifting problem amounts to the initialization of the missing higher order moments: momentum $\phi(x,0)$ and energy $\xi(x,0)$ (3.24). For the reconstruction scheme (4.1) with the weights (4.2), we have $\phi(x,0) = 0$ and $\xi(x,0) = \nu_i\rho(x,0) = (1/3)\rho(x,0)$. This is only a rough approximation of the true slaved state (3.29) with respect to the initial $\rho(x,0)$ on the manifold.

In the second step, the LBM is used to evolve the distribution functions from (4.1) over a coarse time step ΔT. Finally, in the restriction step, the densities $\rho(x,\Delta T)$ are computed from the final LBM state using (3.3).

When the underlying microscopic model is a stochastic model or when the lifting scheme is stochastic, the result of a coarse time step is again a stochastic variable, characterized by an average, a variance, etc. To get a sufficiently small variance, which is needed for the numerical bifurcation analysis techniques but also for other methods such as the projective integration method mentioned in Chapter 2, one should run many microscopic simulations from the same (if the simulator itself is stochastic) or equivalent initial conditions. In the restriction step, the result for all the simulations must then be averaged. A similar problem occurs for deterministic microscopic models with chaotic dynamics. In this case, a lot of nearby initial conditions have to be used. These difficulties do not occur for LBMs. It is sufficient to evolve a single initial condition once, interpolating as explained before between two LBM time steps at the end if ΔT is not a multiple of the LBM time step Δt.

The last difficulty is the choice of the macroscopic time step ΔT. According to [108, 138], this time step should be larger than the time it takes for the higher order moments to become slaved by the lower order ones, i.e. the time that the solution takes to approach the lower-dimensional "slow" manifold mentioned before. The latter time interval is also called the *healing time* in [139] and is typically small compared to the relevant macroscopic time scales. On the other hand, as is clearly demonstrated in [138], ΔT should not be too large either, in particular in the case of a stochastic or chaotic microscopic model because the various realizations might diffuse irreparably over a large part of the attractor, losing phase information. The

latter is not a problem for LBMs because of their deterministic nature.

In Chapter 5 we will show that the claim made in the early papers [69, 108, 199] that the initialization of the higher order moments does not matter much, is not always right. Our numerical experiments will demonstrate that if the initialization of the higher order moments is too far from the unknown correctly slaved state, the effects of this deviation might decay very slowly (on a much longer time scale than the healing time, in fact, on a time scale comparable to the slowest macroscopic time scales) and sufficiently accurate results might only be obtained using a coarse time step that is several orders of magnitude larger than the healing time.

4.2.3.2 Extension to Continuous Time

If the end time T is not a multiple of the coarse time step ΔT, we have two choices. If ΔT is small compared to the dominant time scales of the macroscopic dynamics, i.e. if ΔT is comparable to what a time step would be in a typical numerical integrator for the macroscopic model if the latter were known explicitly, we can use the same approach as for the LBM and interpolate between the two last states. If ΔT is larger, we need another approach. Let ΔT_{min} and ΔT_{max} be the minimum and maximum allowed macroscopic time step, estimated according to the criteria specified in Sect. 4.2.3.1. Varying ΔT between these limits should have very little influence on the result at time T. Therefore we change ΔT such that T is an integer multiple of ΔT. This approach may fail however if T is not sufficiently larger than ΔT_{max} and the time step limits are too close to each other. We used the second approach in our experiments.

4.3 Numerical Bifurcation Analysis

To perform a numerical bifurcation analysis of a system of autonomous parameter-dependent PDEs, the PDEs are first space-discretized. In many cases, this leads to a large system of ODEs

$$\frac{\mathrm{d}y}{\mathrm{d}t} = g(y,\gamma)\ , \quad g : \mathbb{R}^n \times \mathbb{R}^\Gamma \mapsto \mathbb{R}^n\ , \tag{4.3}$$

though in some cases, a system of differential-algebraic equations is obtained. In (4.3), y is the state vector with dimension n while γ denotes the parameters of the system (dimension Γ). For most discretization schemes, the Jacobian matrix $\partial g(y,\gamma)/\partial y$ is a large but very sparse matrix. In bifurcation analysis, steady states are usually computed by applying some version of Newton's method to $g(y,\gamma) = 0$. The stability of the resulting steady state is determined by the eigenvalues λ_l of $\partial g(y,\gamma)/\partial y$. A steady

state is asymptotically stable if

$$\mathrm{Re}(\lambda_l) < 0 \,, \quad l = 1, \ldots, n \,.$$

For a discretized PDE, only the rightmost eigenvalues will be good approximations to the true eigenvalues of the continuous PDE problem, but these are precisely the eigenvalues that determine stability. Bifurcations occur when one or more eigenvalues cross the imaginary axis as the parameter is changed.

Let $\psi_T(y(0), \gamma)$ denote the solution $y(T)$ at time T of (4.3) with initial condition $y(0)$ at the parameter values γ. A steady state of (4.3) is also a fixed point of the map

$$y \mapsto \psi_T(y, \gamma) \tag{4.4}$$

for any value of T. A periodic solution of (4.3) is a fixed point of (4.4) only when T is a multiple of the (unknown) period. Solutions of (4.3) can therefore be studied by analyzing fixed points of (4.4) instead. The stability of a fixed point of (4.4) is determined by the eigenvalues μ_l of

$$\Pi := \frac{\partial \psi_T(y, \gamma)}{\partial y} \,.$$

The fixed point is stable if all eigenvalues have modulus smaller than one. If y is a steady state of (4.3) then

$$\Pi = \frac{\partial \psi_T(y, \gamma)}{\partial y} = \exp\left(T \frac{\partial g(y, \gamma)}{\partial y}\right)$$

and hence

$$\mu_l = \exp(\lambda_l T) \,. \tag{4.5}$$

Thus $|\mu_j| < 1 \Leftrightarrow \mathrm{Re}(\lambda_j) < 0$ and consequently, the stability information obtained with both approaches is equivalent. In practice, we have to use a numerical time integrator. Most classical time integration schemes preserve steady states of (4.3). However, (4.5) will only be satisfied approximately. If the step size is sufficiently small, the dominant eigenvalues of the numerical time integrator will be very good approximations to the eigenvalues μ_l of the exact time integrator and can be used to judge the stability of the computed fixed points. One can then still use (4.5) to compute approximations to the eigenvalues λ_l.

A LBM defines a map. Since a LBM is deterministic, one can use the same techniques to analyze this map as for the time integrator map. If the

dynamics of the LBM are equivalent to those of a PDE, the dominant eigenvalues μ_l computed from the LBM and the rightmost eigenvalues λ_l computed from the equivalent PDE will also approximately satisfy (4.5). The same framework can also be used in combination with the coarse equation-free time integrator to compute steady states of the unknown but assumed to exist macroscopic description and to analyze their stability.

In numerical bifurcation analysis, one typically computes a discrete set of points on a branch of steady states or fixed points obtained by varying one parameter of the ODE system (4.3) or map (4.4) while monitoring the stability-determining eigenvalues along the branch to detect bifurcation points. The tool for this is a continuation method. Given the already computed points on a branch, a prediction is made for the position of the next point and that point is then computed by solving the nonlinear system

$$\begin{cases} \psi_T(y,\gamma) - y = 0 \,, \\ n(y,\gamma;\zeta) = 0 \,. \end{cases} \tag{4.6}$$

The vector y and one of the components of the parameter vector γ, i.e. the bifurcation parameter, are the unknowns. The last equation, $n(y,\gamma;\zeta) = 0$ is a scalar equation that determines the position of the point along the branch through a reparameterization with parameter ζ. In our experiments we used pseudo-arclength continuation [107].

When computing a branch of isolated periodic solutions, the period T is also unknown. We use single shooting to compute a point on the branch. This point is computed by adding a phase condition $q(y,T,\gamma) = 0$ to (4.6), which fixes the starting point for integration along the periodic orbit, i.e. the phase condition effectively defines a Poincaré section. The resulting system

$$\begin{cases} \psi_T(y,\gamma) - y = 0 \,, \\ q(y,T,\gamma) = 0 \,, \\ n(y,T,\gamma;\zeta) = 0 \,, \end{cases} \tag{4.7}$$

is solved for the vector y, T and one component of γ. For a periodic solution, Π is called the *monodromy matrix* and its eigenvalues the *Floquet multipliers*. These eigenvalues determine the stability of the periodic orbit. One of the multipliers will be one and should not be taken into account. The others determine the stability of the periodic orbit. Instead of a numerical time integrator for (4.3), we can also use the coarse time integrator or the LBM (with the extension to a continuous time variable). This approach to bifurcation analysis, using the time integrator map, can also be extended to compute periodic solutions of a Hamiltonian system or to compute traveling waves etc. The problems that arise in those computations are similar to those that arise in other continuation methods.

In [184], Shroff and Keller proposed the Recursive Projection Method to compute solutions of (4.6). This procedure is essentially a stabilization and acceleration procedure for iterating with the map. This method was used in [199]. Though it is possible to extend the Recursive Projection Method to compute periodic solutions also, we used the Newton-Picard method [133, 134, 135]. This method tends to be more robust and was originally developed for bifurcation analysis of periodic solutions of large systems. Both methods are based on the assumption that Π has only few eigenvalues close to or outside the unit circle. The Newton-Picard method starts from Newton's method, but computes only an approximate solution to each linearized system. At each step, the low-dimensional dominant subspace $\mathcal{U}$ of Π (i.e. the subspace of all eigenvalues larger than some user-determined threshold θ, with $0 < \theta < 1$) is determined using orthogonal subspace iteration [169], the linearized system is projected on this space and its orthogonal complement $\mathcal{U}^\perp$, and the resulting system is solved approximately by combining fixed-point (or Picard) iterations in $\mathcal{U}^\perp$ with a direct solver in $\mathcal{U}$. The dominant eigenvalues are easily computed from the projection of Π onto $\mathcal{U}$.

The total number of time integrations needed to converge to a given accuracy is mostly determined by these dominant eigenvalues. Since the dominant eigenvalues depend on the physics of the dynamical system and not on the particular mathematical model or its discretization, the same is true for the number of time integrations. Indeed, we expect that a similar number of time integrations will be needed for the PDE model, the LBM and the equation-free LBM description. Some differences are possible of course, e.g. because the different approaches use a different number of variables. Differences can also occur when the nonlinearity becomes too strong and Newton has difficulties converging.

When using time stepper based bifurcation analysis to compute steady state solutions, T can be chosen freely. However, T should not be too large since the nonlinear behavior of the map (4.4) may become more pronounced, causing trouble when solving the nonlinear system (4.6). This is especially the case when computing unstable steady states and is essentially the same problem as encountered in single shooting methods for computing periodic solutions [10, 106]. As can be seen from (4.5), T also influences the eigenvalues of Π and thus the convergence of the Newton-Picard method. Assuming the threshold θ is squared so that the dimension of the subspace $\mathcal{U}$ remains the same, doubling T will roughly halve the number of orthogonal subspace iteration and Picard iteration steps, but each step will be twice as expensive. The overall computational cost remains roughly the same. The value of T is not critical for the Newton-Picard method, although we did observe some problems with the subspace convergence criterion we used if T becomes too small.

Both the Recursive Projection Method and the Newton-Picard method

need matrix-vector products with Π. These can be computed using finite difference methods. These matrix-vector products must be accurate enough, otherwise it will be impossible to compute a basis for $\mathcal{U}$ with enough accuracy. Note that the subspace $\mathcal{U}$ may be better conditioned than individual eigenvalues associated with that subspace. Therefore, in order to compute the eigenvalues with enough accuracy to reliably determine the stability and bifurcation points, even higher accuracy of the matrix-vector products may be required. Problems are possible with the coarse time stepper if the underlying microscopic model is stochastic or has chaotic dynamics. Since differentiation is by itself an ill-conditioned operation, we will need a very low variance of the result of the coarse time stepper to compute the matrix-vector products accurately enough. This may require a lot of microscopic simulations at each time step as was experienced in [138] for a system with an ODE-like one- to three-dimensional macroscopic state. If too many simulations are needed to obtain a low enough variance, the numerical bifurcation analysis using the coarse time stepper may be too expensive and thus unfeasible. However, in our test case, the "microscopic" model (the LBM) has clear steady states and periodic solutions.

We use only a single LBM simulation at each coarse time step, and the initial conditions are prescribed in a deterministic way. Therefore we have no problems computing the matrix-vector products. A stochastic microscopic simulator would be a better choice to study this aspect of coarse-grained bifurcation analysis. However, by avoiding this problem in our test case, we are in a much better position to study the influence of the initialization of the microscopic simulator and the macroscopic time step ΔT, which is the subject of Chapter 5.

4.4 Bifurcation Diagrams

For the choice of FHN parameters in Sect. 3.7, we computed a branch of steady states and a branch of periodic solutions. The top panels in Fig. 4.1 present the steady state bifurcation diagram for the LBM, the coarse LBM time stepper (CTS) and the PDE model. On the vertical axis, we show $\int_0^L \rho^{ac}(x)\,dx$, computed using the midpoint quadrature rule. This quantity should be essentially the same for all three models and is also, up to discretization errors, independent of the grid size. For all computations, we used a grid with $N = 200$ grid cells ($\Delta x = L/N = 0.1$). All branches, also the branch for the PDE model, were computed using the time stepper based bifurcation approach explained in Sect. 4.3 with the publicly available package PDEcont [132]. We set $T = 5$. For this value of T, we had no difficulties computing the unstable solutions. Also, for this T, the eigenvalues are well enough separated for the robust operation of the Newton-Picard implemen-

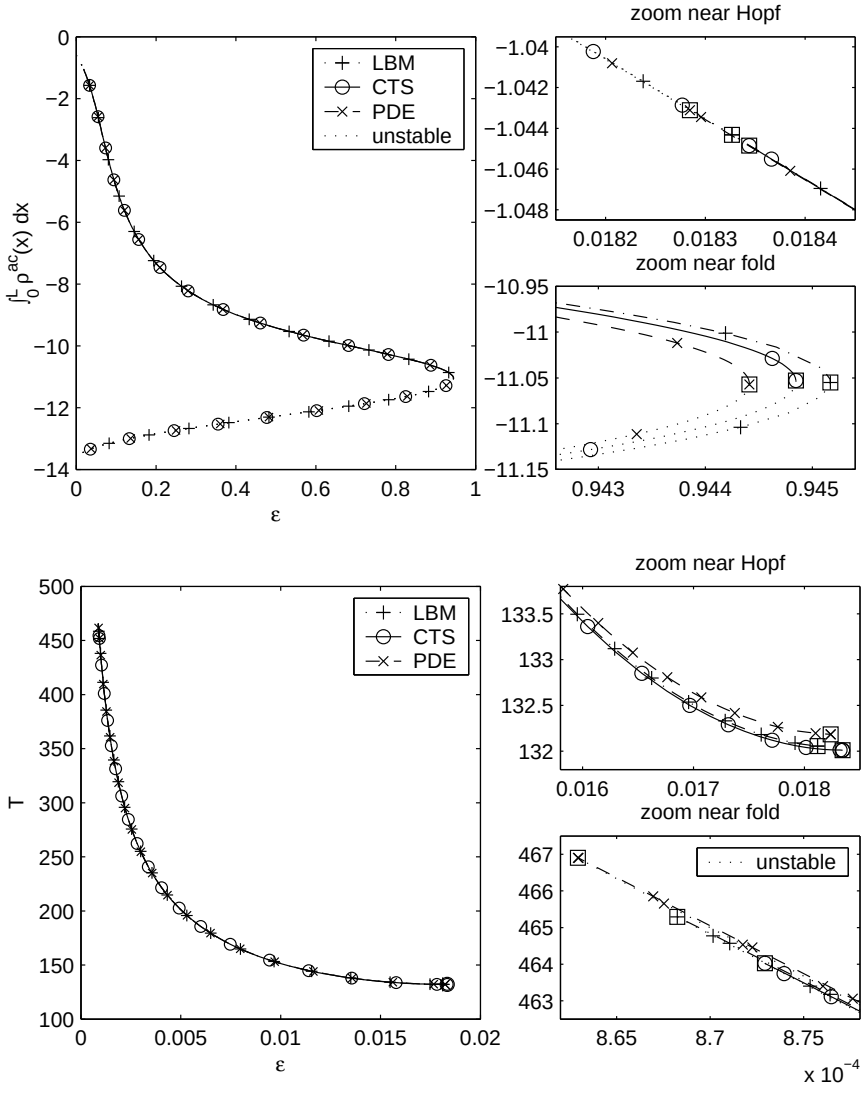


Figure 4.1: Bifurcation diagram for steady state (top) and periodic solutions (bottom) obtained with each of the three models. The coarse time step $\Delta T = 5 = 5000\Delta t$. Unstable solutions are plotted using a dotted line. The markers represent only a subset of the points computed by the continuation code. The two figures on the right zoom in on the Hopf and the fold point. The bifurcation points are marked with a square.

tation. Note also that the computed steady states do not depend on the value of T. The LBM time step Δt was set equal to 0.001. The time step for the trapezoidal rule was 0.02. Smaller values of Δt only led to minor changes (on the order of the spatial discretization error) in the bifurcation diagram, while the bifurcation diagram changed considerably for larger values of Δt. In other words, the LBM bifurcation diagram has converged for $\Delta t = 0.001$. Also, the correspondence with the PDE bifurcation diagram is very good. In [219], we show with several other experiments that the choice of $\Delta t = 0.001$ is optimal. To compute the fixed points of the coarse integrator, we used a fairly large macroscopic time step $\Delta T = 5$ and the weights (4.2) in the reconstruction operator. Note that the results do depend on the choice of ΔT, see Chapter 5. With this choice of parameters, the difference with the PDE results is also of the order of the discretization error[1]. We will study the influence of these parameters in more detail in Chapter 5. There is a fold point at $\varepsilon \approx 0.945$ and a supercritical Hopf bifurcation at $\varepsilon \approx 0.0183$ giving rise to stable periodic orbits at smaller parameter values. The location of the bifurcation points corresponds very well for all three approaches.

In Fig. 4.1 (bottom), we show the branch of periodic solutions emanating from the Hopf point. Since the phase condition was not the same for all simulations, it is impossible to compare the computed point on the orbit for all three models. Therefore we now plot the period T on the vertical axis. To compute periodic solutions using the coarse integrator, we set $\Delta T \approx 5$, cf. the second approach in Sect. 4.2.3.2. For the trapezoidal rule, we used 1000 time steps per period. There is a fold point at $\varepsilon \approx 0.00087$. Solutions on the unstable part of the branch have (at least initially) almost the same parameter-period dependence as on the stable part, but the periodic orbit is slightly different. The amplitude of the temporal oscillations of the inhibitor is larger for the unstable periodic solution than for the stable one at the same parameter value. We did not succeed in computing the unstable branches far past the fold point. This demonstrates the lack of robustness of single shooting methods, in particular when computing unstable solutions [10, 106]. The Hopf points for the three methods are slightly different from those in Fig. 4.1 (top) because they are computed from a different eigenvalue problem. The results in Fig. 4.1 (bottom) are less accurate since the location of the Hopf point is determined by detecting an ill-conditioned algebraically double eigenvalue at 1.

We can draw two conclusions from this section. First, the steady states and periodic solutions of the LBM correspond very well to those of the macroscopic PDE. Second, computing a bifurcation diagram for the coarse

[1]Note that our numerical bifurcation results are much more accurate than those reported in [69, 108, 199] because of an unfortunate error in the implementation of the FHN LBM boundary conditions in the latter papers.

Table 4.1: Dominant eigenvalues (largest exponents) corresponding to the unstable steady state solution at $\varepsilon = 0.01$ (with $T = 5$ and, for the CTS, $\Delta T = 5$).

Exponents:	$\lambda_{1,2}$	λ_3	λ_4
LBM	$0.002010 \pm 0.039461i$	-0.124867	-0.411364
CTS	$0.002012 \pm 0.039463i$	-0.124863	-0.411348
PDE	$0.001999 \pm 0.039446i$	-0.124861	-0.411288

Table 4.2: Dominant Floquet multipliers for the stable periodic solution at $\varepsilon = 0.01$ (with $\Delta T = 5$ for the CTS).

Multipliers:	trivial μ_1	μ_2
LBM	1.000000	0.514888
CTS	1.000000	0.514452
PDE	1.000000	0.516712

equation-free time integrator does work and produces the expected results (at least for this choice of ΔT and reconstruction scheme).

4.5 Dominant Eigenvalues and Stability

In Sect. 4.4, we noticed that the bifurcation diagrams for the PDE model, LBM and coarse LBM time stepper (CTS) are virtually the same, including the location of the bifurcation points. The latter fact indicates that the dominant, stability-determining eigenvalues will match very well also. We will now study this in more detail.

The dominant eigenvalues are computed in the Newton-Picard code by performing a number of additional orthogonal subspace iteration steps after the computation of the fixed point. In Table 4.1, we list the dominant eigenvalues for the unstable steady state at $\varepsilon = 0.01$ on the upper part of the branch in Fig. 4.1 (top). We used $T = \Delta T = 5$ and transformed the eigenvalues to exponent form using (4.5). Table 4.2 lists the trivial Floquet multiplier and the most dominant non-trivial multiplier for the stable periodic solution at the same parameter value. All other Floquet multipliers were considerably smaller, which confirms our assumption about the spectrum. The existence of a trivial multiplier at one is a general property of autonomous systems. Its computational accuracy is independent of the spatial discretization error. The remarkable precision of the computed value indicates that the time integration and eigenvalue computation are very

Table 4.3: Total number of time integrations, the number of fixed points computed and the average number of time integrations needed for the continuation of part of the stable branches of steady states for $\varepsilon \in [0.05, 0.55]$ and periodic solutions for $\varepsilon \in [0.006, 0.016]$. For the CTS, the coarse time step equals $\Delta T = 5$.

	steady state			periodic		
	total	nb. pts	avg.	total	nb. pts	avg.
LBM	1352	20	67.600	1611	25	64.440
CTS	1419	21	67.571	1623	25	64.920
PDE	1420	21	67.619	1621	25	64.840

accurate. Clearly, the eigenvalues and also the corresponding eigenvectors (not shown) correspond very well for all three models and thus provide the same stability information.

4.6 Time Stepper Calls

For each of the three approaches, we list the number of time integrations needed to continue part of the branch of stable steady state solutions for $\varepsilon \in [0.05, 0.55]$ and part of the branch of stable periodic solutions for $\varepsilon \in [0.006, 0.016]$ in Table 4.3. For the steady state computations, we used the same time interval $T = 5$ again for all time integrators. The work for the accurate computation of the dominant eigenvalues at the end of a Newton-Picard step is not included in Table 4.3. Note that the LBM uses a different set of variables from the other two approaches and hence another measure for the distance. In these experiments, we chose the maximal step size in our variable step size continuation code for the different schemes in such a way that the number of points computed along the branch is approximately the same. As expected, the average number of time integrations needed for each point is almost the same. In our case however, the computing time for the PDE based model is much lower since the implicit time stepper uses much larger steps than the LBM. The computing time for the LBM based continuations is dominated by the LBM simulations and virtually the same for both approaches.

4.7 Conclusions

In this chapter, we have demonstrated that algorithms developed for time stepper based numerical bifurcation analysis of PDEs can be used for bifurcation analysis of steady states and periodic solutions of LBMs as well in

two different ways. It is possible to use either the LBM itself or the coarse equation-free time integrator wrapped around the LBM as the time stepper in a bifurcation code.

The coarse-grained bifurcation analysis procedure has been proposed in [199], using the same test case, a FitzHugh-Nagumo LBM. We have extended the work of [199] in several ways. We compared the results of a numerical bifurcation analysis using the coarse equation-free time integrator not only with results for an equivalent PDE, but also with the bifurcation diagram for the full LBM used in the coarse time stepper. The results for all three approaches corresponded very well. We have also extended the coarse integrator to produce results at an (almost) arbitrary time T. This enabled the computation of periodic solutions. Instead of the Recursive Projection Method used in [199], we used the Newton-Picard method [133, 134, 135]. Though our results show that the coarse equation-free time stepper is not really needed to perform a numerical bifurcation analysis of the LBM (because of its deterministic nature), this test case did enable us to thoroughly study the effects of the reconstruction scheme in the next chapter.

For our test case, we showed that the amount of work when using the Newton-Picard method is roughly the same for all approaches. This is mostly determined by the dominant eigenvalues, which are the same in all representations. We have also demonstrated that the bifurcation information obtained from a LBM is the same as the information obtained from a PDE model. However, time integration of the PDE was much faster, resulting in much lower computing times for the bifurcation diagram of the PDE model.

The two approaches for bifurcation analysis of LBMs have distinct advantages and disadvantages. The coarse equation-free integrator has several parameters that need to be chosen carefully. We will discuss these issues in the next chapter. On the other hand, the dimension of the state vector is lower (only one third of the number of components in our case), resulting in a proportionally lower memory consumption of the Newton-Picard method for the coarse time integrator. In some cases, this can be an issue and thus possibly an advantage of the equation-free approach.

This chapter does not claim that numerical bifurcation analysis based on the coarse equation-free time stepper of [108, 199] will always work. Indeed, microscopic or mesoscopic simulations based on stochastic models or models with chaotic behavior, may (and likely will) pose additional numerical problems that cannot be studied with this simple test case. Further research is needed in this area.

A possible extension of this work is the combination with more efficient multiscale simulation techniques proposed in [108, 48]. To accelerate the time integration, we have projective integration [65, 66, 67, 124], the multistep state extrapolation method [217, 218, 219] and the acceleration tech-

niques based on the heterogenous multiscale method described in [47, 50]. To increase the spatial efficiency, we have the gap-tooth and patch dynamics scheme [108, 172, 173, 174] or a hybrid approach [3, 4, 213, 215].

Chapter 5

Initialization (Lifting or Reconstruction)

5.1 Introduction

In general, starting a microscopic simulator from given macroscopic initial conditions includes some arbitrariness because there are, typically, a large set of microscopic variables and only a few macroscopic variables given. Because the macroscopic initial state does not contain enough information to initialize the microscopic simulator, the missing information has to be filled in. In molecular dynamics, for example, the initial positions and velocities of all the particles have to be computed from the given temperature and density profile. Typically, the particles are positioned on a square lattice while the velocities are drawn from a Maxwellian distribution. In a similar way, LBM simulations are traditionally bootstrapped from the initial macroscopic fields by setting the distribution functions in each point to the local BGK equilibrium. For steady state calculations, one then relies on the subsequent time simulation to damp any initialization errors likely to occur. We will show in this chapter that such careless initialization can lead to significant initialization errors with considerable effects on the computed solution (see also [189, 144]).

The same initialization problem occurs in the lifting or reconstruction phase of the equation-free framework. Using a multiple time scales argument, Kevrekidis *et al.* argued in [69, 108, 199] that the effect of the errors from the initializations will disappear very fast (compared to the macroscopic time step) as the higher order moments of the microscopic distribution quickly become slaved by (or equivalently, become functionals of) the lower order ones (corresponding to the macroscopic variables). I.e. it is as-

sumed that the long-term dynamics of the microscopic model take place on or very near to a lower-dimensional slow manifold, which can be parameterized adequately by the macroscopic variables, and that any orbit started away from this manifold is very quickly attracted to it (at a time scale much smaller than the typical macroscopic time scales). However, we will show in this chapter that this fast slaving process does not imply that all influences of an inaccurately reconstructed initial state disappear quickly. The initialization can have a significant impact on the value of the minimal successful coarse time step and the accuracy of the solution. As such, the lifting phase can be considered the most critical component of the coarse equation-free time stepper.

We will use the FitzHugh-Nagumo (FHN) system from Sect. 3.7 as our test case again. Because we are not only interested in the influence of the initialization on the actual microscopic time simulation, but also in the behavior of the lifting step in a coarse-grained bifurcation analysis, we rely heavily on the results and theory from the previous chapter.

This chapter is structured as follows. In Sect. 5.2, we calculate the slaving relations for the FHN LBM and discuss their use in the initialization phase. Section 5.3 describes the lifting or reconstruction problem for our LBM. In Sect. 5.4, we discuss the healing or slaving process, while Sect. 5.5 describes the influence of the lifting on the bifurcation analysis. Finally, in Sect. 5.6, we look for slaving relations in the eigenvectors of the LBM time stepper. Section 5.7 ends this chapter with a discussion and conclusions.

5.2 Slaved State

In Sect. 3.4, we derived the slaving relations (3.29) for momentum $\phi(x,t)$ and energy $\xi(x,t)$ in analytical form. These relations are valid on the slow manifold described by the macroscopic density variable $\rho(x,t)$. Up to first order, the relations are

$$\phi(x,t) = -\frac{2\Delta x}{3\omega}\frac{\partial \rho(x,t)}{\partial x} \quad \text{and} \quad \xi(x,t) = \frac{1}{3}\rho(x,t) \; .$$

In an equation-free context, the slaving relations are unknown. However, one can always try and estimate them numerically. We illustrate this for the FHN LBM. When plotting the moments of the activator and inhibitor species (the latter are not shown) for the stable steady state at $\varepsilon = 0.05$ in Fig. 5.1 (top), it is immediately clear that $\xi(x)$ is almost perfectly one third of $\rho(x)$. This is conform (3.29), which states that the next term in the slaving relation for the energy is of second order. Numerically checking the relation between $\phi(x)$ and $\rho(x)$ is less straightforward, but the fact that $\phi(x)$ is relatively large where $\rho(x)$ changes most, suggests that $\phi(x)$ is

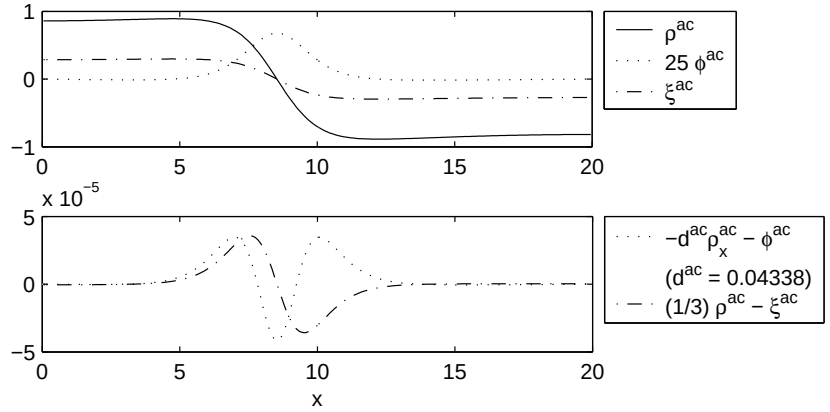


Figure 5.1: Slaving of the activator higher order moments for the stable LBM steady state at $\varepsilon = 0.05$. We plotted $25\phi^{ac}$ rather than ϕ^{ac} in the top panel.

related to the gradient of $\rho(x)$, i.e. that $\phi(x) \sim -d\,\partial\rho(x)/\partial x$. Approximating the density gradient with finite differences, we compute the coefficient as $d = \|\phi(x)\| \,/\, \|\partial\rho(x)/\partial x\|$ (with $\|\cdot\|$ the two-norm of the discrete state vector). We obtain the values $d^{ac} = 0.04338$ and $d^{in} = 0.07334$, which are in good accordance with the theoretical values $2\Delta x/(3\omega^{ac}) = 0.04333$ and $2\Delta x/(3\omega^{in}) = 0.0733$. The bottom panel of Fig. 5.1 illustrates the difference w.r.t. the analytical slaving relations up to first order.

The slaving relations derived from the Chapman-Enskog expansion enable us to develop an almost perfect reconstruction scheme by first computing $\phi(x,0)$ and $\xi(x,0)$ from $\rho(x,0)$ using (3.29). The corresponding distributions $f_i(x,0)$ can then be obtained as $\mathbf{f}(x,0) = M^{-1}\boldsymbol{\varrho}(x,0)$ (3.25). The spatial derivatives in the analytical slaving relations (3.29) are approximated numerically by finite differences[1]. For the time derivatives, the macroscopic reduced equation can be used, if available. Some of these derivatives might be available directly from simulation. For systems not governed by diffusion, initialization with the Chapman-Enskog relations has additional issues. For e.g. flow problems described macroscopically by the Navier-Stokes equation, the macroscopic variables are the density ρ and the flow velocity v (i.e. v_x and v_y in two dimensions) or equivalently the momentum $\phi = \rho v$ (3.24). For such systems, the first order Chapman-Enskog relations do not conserve momentum, which means that the velocity field that results from initialization is different from the original velocity field. Additional terms

[1] It is interesting to note the parallel line of thought in [229]. There, the authors also improve their initialization scheme by including appropriately discretized spatial derivatives of the initial macroscopic variables.

must be added to ensure a correct initialization, see [189]. The resulting computations can become cumbersome and impractical (mostly due to the discretization of many continuous derivatives). Another difficulty might be the occurrence of complex local interaction force terms, which makes the Chapman-Enskog derivation highly non-trivial. Finally, in applications like decaying homogeneous isotropic turbulence [232, 233, 234], the initial velocity field $v(x,0)$ is a random field and the computation of derivatives of $v(x,0)$ is meaningless. From now on, we assume that slaving relations like (3.29) are unavailable or difficult to obtain analytically and we focus on the behavior of the coarse equation-free time stepper using initializations away from the slow manifold.

5.3 Lifting (Reconstruction)

We study several reconstruction schemes in our experiments. Three schemes are based on the scheme from [199] given by (4.1)

$$f_i(x,0) = w_i\,\rho(x,0) \quad \text{with} \quad \sum_{i=-1}^{1} w_i = 1\ ,$$

with different sets of weights w_i. Initialization with the local diffusive equilibrium distribution, i.e.

$$w_{-1} = w_0 = w_1 = \frac{1}{3} \tag{5.1}$$

in (4.1) is a straightforward choice. For this choice, the kinetic energy is almost perfectly slaved. The momentum is identically zero. Though the momentum is small in the correctly slaved state also, this reconstruction scheme – as all others based on (4.1) – does not satisfy (3.29). For the second reconstruction scheme, we chose the symmetric set of weights

$$w_{-1} = w_1 = 0.01,\ w_0 = 0.98\ . \tag{5.2}$$

The momentum is still zero and thus "close" to the correctly slaved state, but the kinetic energy (the second order velocity moment) is very different from the correctly slaved state. Our third scheme uses the asymmetric weights

$$w_{-1} = 0.75,\ w_0 = 0.24,\ w_1 = 0.01\ . \tag{5.3}$$

For this choice, both the first order and second order velocity moments, i.e. both momentum and kinetic energy, differ significantly from the correctly slaved state.

Though we can initialize the kinetic energy very well with reconstruction scheme (4.1), the momentum cannot be initialized correctly unless a more complicated scheme such as (3.29) is used. To overcome this problem, we also performed experiments with a coarse time stepper using both concentration and momentum as the macroscopic variables. This leaves only one degree of freedom per species and per lattice point for the initial state of the LBM. Using $\mathbf{f} = M^{-1}\boldsymbol{\varrho}$ (3.25), the reconstruction scheme can be defined as

$$f_{-1} = \frac{1}{2}(1 - w_0^*)\rho - \frac{1}{2}\phi \;,\; f_0 = w_0^*\rho \;\text{ and }\; f_1 = \frac{1}{2}(1 - w_0^*)\rho + \frac{1}{2}\phi \;, \quad (5.4)$$

where ρ and ϕ denote $\rho(x,0)$ respectively $\phi(x,0)$ and w_0^* can be chosen freely. For this initialization, the initial energy is

$$\xi(x,0) = \frac{1}{2}(1 - w_0^*)\rho(x,0) \;.$$

We considered two choices for the parameter w_0^*. For the first choice,

$$w_0^* = 0.98 \;, \quad (5.5)$$

the energy differs significantly from the correctly slaved state. The second choice,

$$w_0^* = \frac{1}{3} \;, \quad (5.6)$$

provides an (almost) perfect initialization of all velocity moments.

5.4 Healing Process

In Fig. 5.2, we study the healing process. Diagram (a) shows the difference between the momentum and the scaled concentration gradient while diagram (b) shows the difference between the kinetic energy and one third of the concentration for the activator at the lattice point $x = 9.95$ in the first few LBM time steps using the three reconstructions based on (4.1). Both diagrams show the deviation from the best available approximation of the correctly slaved state. The macroscopic initial state is the stable steady state of the LBM at $\varepsilon = 0.05$. From this state, we generated microscopic initial conditions using (4.1) with weights (5.1), (5.2) and (5.3). The figures show that both the momentum and kinetic energy become slaved in about 10 to 15 LBM time steps of $\Delta t = 0.001$. This claim is further verified by the experiment in Fig. 5.3. If the higher order moments are correctly slaved for a given state, the evolution from then on could be described by a macroscopic model with the lower order moments as the unknowns. Since our LBM is

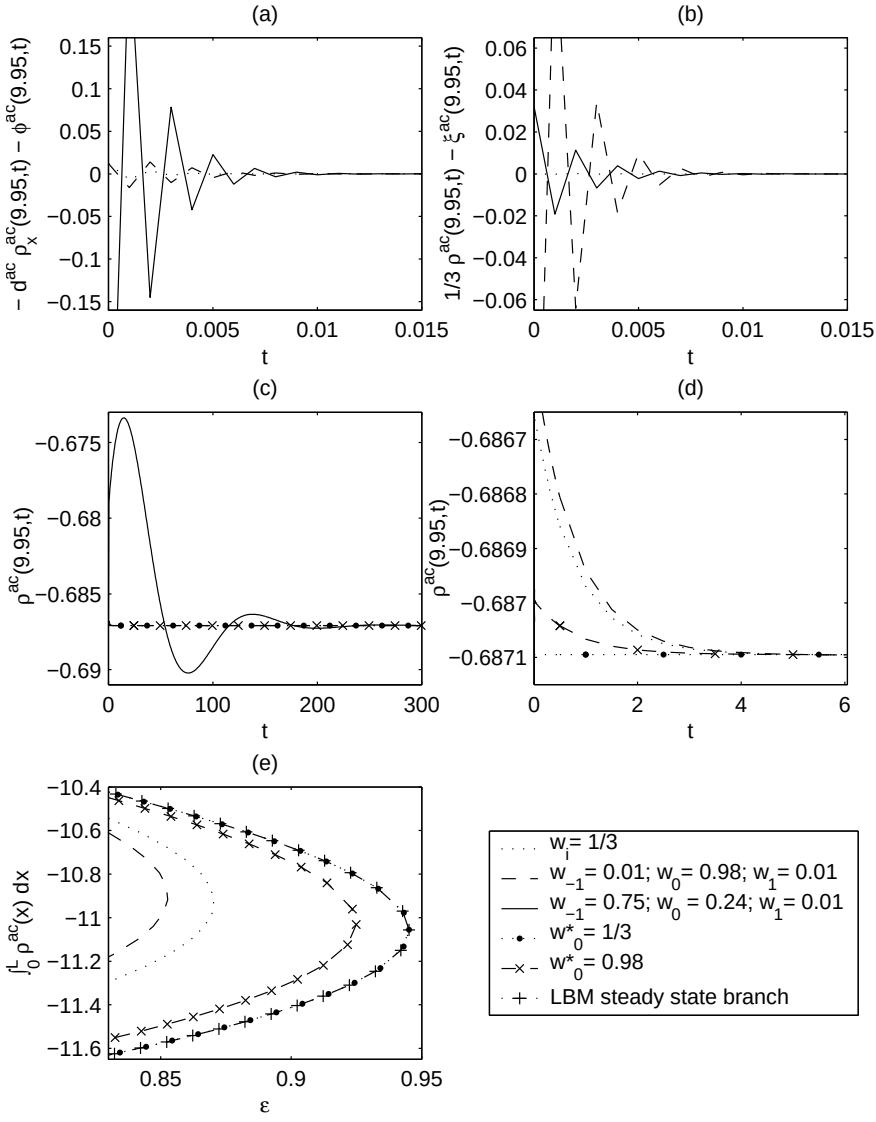


Figure 5.2: Healing of the lifting error. Evolution of (a) $-d^{ac}\rho_x^{ac}(x,t) - \phi^{ac}(x,t)$, (b) $(1/3)\rho^{ac}(x,t) - \xi^{ac}(x,t)$ and (c) concentration $\rho^{ac}(x,t)$ at lattice site $x = 9.95$ for the LBM trajectories started from the stable steady state at $\varepsilon = 0.05$ using the reconstruction schemes (4.1) and (5.4). (d) is a close-up of (c). (e) Steady state bifurcation diagrams for the coarse time stepper using $\Delta T = 0.02$. The steady state bifurcation diagram for the full LBM from Fig. 4.1 is also shown for comparison.

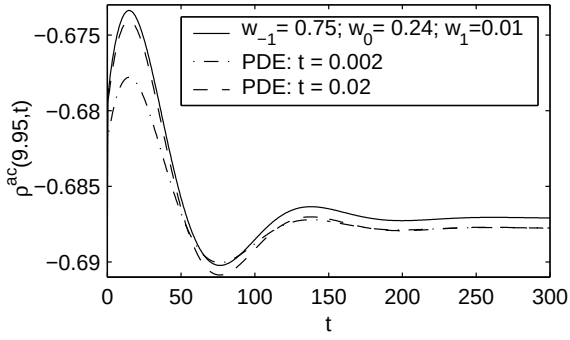


Figure 5.3: Trajectory of $\rho(9.95, t)$ for a LBM simulation started from the initial condition obtained by reconstruction using the asymmetric reconstruction scheme, and for two PDE simulations started from the LBM trajectory at $t = 0.002$ and $t = 0.02$.

designed to correspond to the macroscopic FitzHugh-Nagumo PDE model (3.42), it is clear what the macroscopic model should be in this case. Hence we started time integration of the PDE model from the LBM trajectory obtained for initialization (4.1) with weights (5.3), at $t = 0.002 = 2\Delta t$ (i.e. before slaving is obtained) and at $t = 0.02 = 20\Delta t$ (after obtaining slaving). The PDE trajectory started from the LBM trajectory at $t = 0.002$ differs significantly from the LBM trajectory, while the PDE trajectory started at $t = 0.02$ follows the LBM trajectory more closely. Note that the LBM and PDE trajectories converge to a slightly different steady state as discussed in Chapter 4. This experiment confirms that after 20 time steps, the higher order moments are slaved by the lower order ones, while this is not yet the case after 2 time steps.

5.5 Bifurcation Diagram

The fact that slaving is obtained so quickly, suggests that a coarse time step $\Delta T = 20\Delta t = 0.02$ would be sufficient to compute the bifurcation diagram accurately. Diagram (e) in Fig. 5.2 shows the bifurcation diagrams near the fold point computed with this time step. The results for all reconstructions except (5.4) with (5.6) have an unacceptably large error. In fact, the line for (4.1) with weights (5.3) even falls off the figure. This can be explained with the help of Fig. 5.2, diagrams (c) and (d). Although slaving is obtained quickly, the LBM simulation does not follow the intended trajectory, i.e. the trajectory that would be followed by a macroscopic model using the same macroscopic initial condition. Note that we initialized from

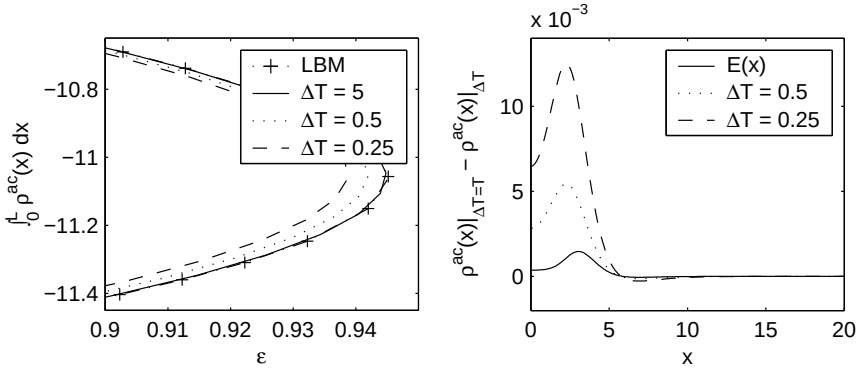


Figure 5.4: Left: Steady state solution branches for the coarse time stepper with reconstruction scheme (4.1) and equilibrium weights, for different values of ΔT. Right: The difference between the coarse steady state using $\Delta T = T = 5$ and the corresponding states using $\Delta T = 0.5$ or $\Delta T = 0.25$, is compared to the discretization error $E(x)$ of the coarse time stepper with $\Delta T = T = 5$ for the stable steady state at $\varepsilon = 0.93$.

a steady state in this experiment, so the correct trajectory is constant. In the healing process, the lower order moments change also and even at a fairly fast time scale[2]. At the end of the healing process, these lower order moments are different from what they would have been for a "perfect" initialization, and so the trajectories differ. In [220], it was shown that the reduced equation describing this deviating trajectory is different from the reduced PDE (2.4) corresponding to the LBM considered in Sect. 3.2. Apparently, the initialization triggers a slow eigenmode in the system. Similar observations in the context of LBM initialization with the local equilibrium f_i^{eq} were made in [189, 144]. Since we are in the neighborhood of a stable steady state, all trajectories ultimately converge to the steady state. However, it takes about 5 macroscopic time units (5000 LBM time steps) with most reconstruction schemes to return to the steady state, while with the reconstruction scheme (4.1) with the asymmetric weight choice (5.3) (i.e. both momentum and kinetic energy are badly initialized), it even takes on the order of 300 macroscopic time units (300000 times Δt). Therefore the coarse time step ΔT must be much larger than the healing time unless an accurate reconstruction scheme is used.

In Fig. 5.4 we show the bifurcation diagram obtained with the initialization (4.1) with weights (5.1) (the diffusive equilibrium distribution). The

[2]This is different from systems with a larger gap in time scales like e.g. stiff singularly perturbed ODE systems [47, 64, 237] and the systems described in [119, 136, 137]. There, the macroscopic slow variables do not change much during the healing phase.

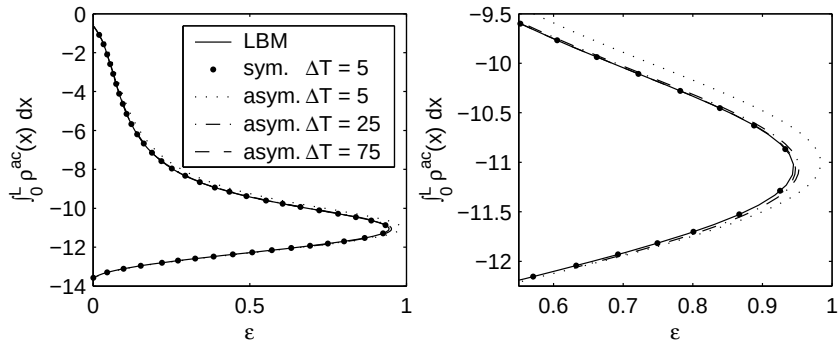


Figure 5.5: The steady state bifurcation diagram for the coarse time stepper with both a symmetric ($w_{-1} = 0.01$, $w_0 = 0.98$ and $w_1 = 0.01$) and asymmetric ($w_{-1} = 0.75$, $w_0 = 0.24$ and $w_1 = 0.01$) set of reconstruction weights. The diagram for the coarse time stepper with asymmetric reconstruction scheme is computed for three different macroscopic time steps. The steady state branch obtained with the LBM from Fig. 4.1 is also shown. The right figure zooms in on the area near the fold point.

left panel shows the bifurcation diagram near the fold point for different values of ΔT. In the right diagram, we plot the estimated discretization error $E(x)$ for the stable steady state at $\varepsilon = 0.93$, close to the fold point. The estimate $E(x)$ was obtained by comparing with a LBM steady state on a lattice with 16200 lattice points. As ΔT increases, the computed equilibria and bifurcation diagram become more accurate. For $\Delta T = 0.5$, the error of the activator concentration is on the order of four times the discretization error and the bifurcation diagram is also acceptable. For $\Delta T = 5$, the bifurcation diagram is virtually the same as for the LBM. This is in agreement with Fig. 5.2 (d), where it took about 5 time units for the LBM simulator to converge to the correct trajectory. However, near an unstable solution, the trajectories diverge and one would expect that the results only get worse as ΔT is increased. This is true when plotting the trajectories, but when computing fixed points, we still notice an improvement as ΔT is increased.

In Fig. 5.5 we show the bifurcation diagram obtained using (4.1) with the symmetric weight set (5.2) and the asymmetric one (5.3). With the symmetric weight set, we again obtain sufficiently accurate results for $\Delta T = 5$. For the asymmetric weight set, the results also get better as ΔT increases, but only become acceptable when $\Delta T = 75$. Though we can compute fairly accurate solutions even for this bad initialization, the coarse time step ΔT and hence the time integration interval T for the Newton-Picard method becomes so large that it is hard to compute the unstable solutions as we already pointed out in Sect. 4.3. The computations break down at $\varepsilon \approx 0.636$

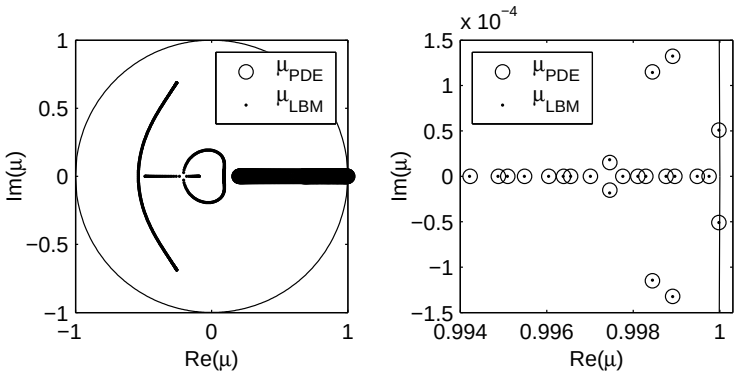


Figure 5.6: Left: The full spectrum for the LBM and discretized PDE model for the stable steady state at $\varepsilon = 0.05$. Right: Close-up of the most dominant eigenvalues.

for $\Delta T = 25$ and at $\varepsilon \approx 0.928$ for $\Delta T = 75$.

Clearly, obtaining a correctly slaved state by the end of the microscopic integration in the coarse time stepper is not sufficient to obtain accurate results. If the reconstruction is not very good, the microscopic simulator must be run over a much larger time interval ΔT. In this test case, there are no upper limits on this time interval other than those imposed by the Newton-Picard procedure. However, as we pointed out in Sect. 4.2.3, other microscopic models, and in particular stochastic simulations, may impose a more severe upper bound on ΔT. In these cases it may be impossible to compute an accurate bifurcation diagram unless a very good reconstruction scheme is used.

5.6 Slaving and the Spectrum of the LBM

To conclude, we study the full spectrum of the LBM and the discretized PDE model. We computed the Jacobian matrix analytically for both cases. To compare with the eigenvalues of the LBM, the eigenvalues λ_l obtained for the PDE were transformed to multiplier form using $\mu_l = \exp(\lambda_l T)$ (4.5) with $T = \Delta t = 0.001$, the LBM time step. The results for the stable steady state at $\varepsilon = 0.05$ are shown in Fig. 5.6. The LBM has 400 eigenvalues in the same zone along the real axis as the discretized PDE. However, only the dominant eigenvalues correspond well. This is not surprising. The less dominant eigenvalues depend very much on the discretization and have little relationship with the true eigenvalues of the continuous problem.

To study the slaving in the eigenvectors, they were split into parts cor-

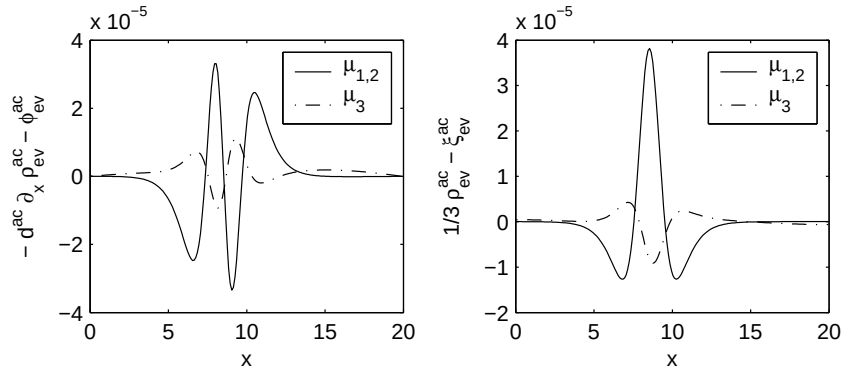


Figure 5.7: Slaving of the activator momentum and energy of the (real part of the) full LBM eigenvectors for the largest complex pair of eigenvalues and the first real eigenvalue from Fig. 5.6. Left: Difference between the eigenvector's momentum and its appropriately scaled concentration gradient. Right: Difference between the eigenvector's energy and one third of the concentration.

responding to each individual distribution function; converted to moment representation using (3.25) and mapped to the spatial domain. The relations between the resulting moments were tested using (3.29) up to first order. At first, one would expect to recognize slaving of the first and second order moment to the zeroth order moment of the eigenvectors of the 400 LBM eigenvalues along the real axis, while in the other eigenvectors there would clearly be no slaving. However, we only observed slaving in the eigenvectors for the most dominant eigenvalues that correspond very well to those of the discretized PDE. Figure 5.7 illustrates this slaving for the real part of the eigenvectors corresponding to the rightmost complex pair of eigenvalues and for the eigenvector corresponding to the largest real eigenvalue. The eigenvector's momentum is small compared to its concentration and proportional to its concentration gradient, and its second order moment, the energy, is very nearly one third of the concentration, so we note the same slaving relationships as for the state in Sect. 5.2. The discovery of such relationships between the higher order and lower order moments could be a step towards the development of some kind of constitutive equation or closure relation for the macroscopic model in terms of appropriate macroscopic variables.

5.7 Discussion and Conclusion

In this chapter, we studied the initialization of a LBM from given macroscopic initial conditions in the context of LBM time simulation, equation-free computing and coarse-grained bifurcation analysis. As we showed in

Chapter 4, the application of the coarse equation-free time stepper is not essential to study the macroscopic behavior of a LBM nor to perform a numerical bifurcation analysis, because a LBM is deterministic and its macroscopic state is unambiguously defined by the lowest order velocity moments. However, using the LBM as the "microscopic" model in the coarse equation-free time stepper did enable us to thoroughly study the effects of the reconstruction or lifting scheme.

Contrary to the claim made in the early papers [69, 108, 199] that the quality of the reconstruction step does not really matter, we have shown that this step is crucial to the accuracy and success of the method. Though slaving is obtained quickly irrespective of the reconstruction scheme, the trajectory of the microscopic simulator started from a bad initialization may be quite different from the intended one (the one that corresponds to the trajectory of a macroscopic model, if such a model would be known explicitly, started from the same initial macroscopic state), see also [220]. For the computation of steady states of a LBM, we showed that such a bad initialization can excite slow modes in the system. The macroscopic time step ΔT must then be unnecessary large to damp the resulting initialization error. This observation is definitely an issue when the microscopic simulator is stochastic or chaotic. In this case, Makeev *et al.* [138] show that a large ΔT leads to irreparable diffusion over a large part of the attractor, thereby losing phase information. In the context of time integration acceleration schemes such as projective integration [65, 66] and the multistep state extrapolation method [217, 218], where bursts of microscopic simulations are used to estimate the macroscopic time derivatives, this is also an issue, since an accurate initialization will limit the size of ΔT and efficient schemes can be developed. Furthermore, we showed that the computation of unstable equilibria becomes nearly impossible when ΔT is very large.

It can be checked that the same conclusions also apply when computing periodic solutions. Even more so, the effects of a careless initialization will not disappear when the stable solution is reached. Instead, the initialization will introduce a permanent phase shift in every computed trajectory, resulting in an error in the computed period. Note that the lifting problem also occurs in hybrid domain decomposition techniques where different models are spatially coupled. One example is the coupling of a PDE to a LBM (see Chapter 8 for details). At the boundary, the PDE will provide the macroscopic variables from which the LBM distribution functions have to be calculated. This can be seen as a localized initialization that needs to be implemented carefully to ensure smooth behavior of the solution at the interface between the models.

The fact that an initialization with the lifting scheme $f_i(x,0) = w_i\rho(x,0)$ from [199] (as we showed, with at best $f_i(x,0) = f_i^{eq}(x,0) = \rho(x,0)/3$), induces errors is not surprising since this initialization neglects the higher

order Chapman-Enskog contributions (3.27)–(3.28) to f_i related to the gradients of the macroscopic variables. As can be seen in Fig. 3.2, these are large near the front in the FHN model.

Clearly, good reconstruction schemes are problem-dependent and an interesting topic of further research, see e.g. [64, 68], [144, 189] and the next chapters.

We conclude with two other applications of coarse equation-free LBM computations. In Chapter 4, we argued that equation-free modeling has the benefit of a reduced dimension of the state vector (in our context, we have a reduction of one third of the number of variables). This can be an advantage for the time integration acceleration schemes described in [47, 65, 66, 217, 218], since the spectrum is also reduced and only contains coarse PDE-like eigenmodes instead of the full LBM spectrum (cf. Fig. 5.6), which can lead to a significant gain in efficiency. Like with bifurcation analysis techniques, these acceleration methods can also be applied directly to the LBM [219]. The resulting speedup is however less than the speedup obtained with the equation-free approach [216]. In [175, 222], the authors use coarse equation-free time steppers for the LBMs discussed in Sect. 3.8 to reduce the state space. This enabled their Newton-Krylov computations to be preconditioned with an approximate PDE.

Chapter 6

Analysis of the Constrained Runs Scheme

6.1 Introduction

In the previous chapter, we showed that an accurate initialization is an important issue, both in the context of equation-free computing and LBM simulation. Recall from Sect. 2.5 and Chapter 5 that the best initial condition for the microscopic variables is the one on the slow manifold corresponding to the macroscopic initial condition. In [68, 64], Gear *et al.* proposed the *constrained runs* (CR) scheme in the context of stiff singularly perturbed ODEs to consistently map macroscopic initial data to microscopic variables. The CR scheme performs a series of short microscopic simulations and resets the lowest moments of the microscopic variables to the macroscopic initial condition after each run while leaving the higher order moments unchanged. In this way, the scheme computes an approximation of the slaved state corresponding to the initial macroscopic data. As a result, the microscopic variables are initialized both consistent with the initial macroscopic state and close to the slow manifold described by the macroscopic variables. With such initialization, the subsequent microscopic simulation will approximate the "true" time trajectory on the manifold described by the reduced equation.

Zagaris *et al.* compare the CR scheme, which they call the *zero-derivative principle*, to the computational singular perturbation method [237] for stiff ODE systems. A similar initialization procedure for the computation of the full state constrained on the values of the initial variables has been suggested in the context of differential-algebraic equations [21]. Note that the CR scheme is reminiscent of the SHAKE [168] and RATTLE [9] algorithms for

molecular dynamics simulations of molecules with holonomic constraints on the atom bonds.

In this chapter, we perform an extensive analysis of the stability and convergence of the CR initialization scheme for the LBM with BGK collisions for one-dimensional reaction-diffusion problems (see Sect. 3.2). In this context, the initial density $\rho^{(0)}$ (the lowest moment) is given and we seek the values of the corresponding higher order moments, momentum and energy, (or equivalently, the values of the distribution functions consistent with $\rho^{(0)}$) to initialize the LBM with. We show that the CR scheme is unconditionally stable and convergent and that the resulting higher order moments correspond to the Chapman-Enskog slaving relations up to first order. The asymptotic convergence rate equals $|1 - \omega|$ with ω the BGK relaxation parameter.

After completing the research described in this chapter, we learned of the related work of Mei *et al.* [144] and Caiazzo [22]. In [144], the authors present a scheme for the initialization of the LBM with multiple relaxation time (MRT) collision model for the incompressible Navier-Stokes equations. For a given initial velocity field $v^{(0)}$, both the unknown initial pressure field (or equivalently the density field) and the higher order moments are computed using a modified LBM simulation where the velocity field in the equilibrium distribution is kept fixed to the value $v^{(0)}$. This effectively reduces the model to a convection-diffusion LBM with one conserved variable, the density. Caiazzo [22] analyzes this scheme for the LBM with BGK collisions for the same Navier-Stokes problem and shows that the resulting pressure (and density) is second order accurate. We have implemented the scheme of [144, 22] for one-dimensional reaction-diffusion systems. We show that it behaves similarly to the CR scheme and that the results of our numerical analysis also apply to this initialization procedure.

This chapter is organized as follows. In Sect. 6.2, we present the CR initialization scheme. In Sect. 6.3 and 6.4, we show that the scheme is unconditionally stable and convergent. These theoretical results are verified numerically in Sect. 6.5 for the FitzHugh-Nagumo system with no-flux boundary conditions. The related initialization scheme developed by Mei *et al.* is discussed in Sect. 6.6 for our model problem. In Sect. 6.7, we summarize the conclusions of this chapter.

6.2 Constrained Runs Scheme

The CR scheme [68, 64] is a fixed point iteration scheme that computes the full state of a microscopic time simulator corresponding to the given macroscopic variables. Using the CR procedure on the LBM from Sect. 3.2, we iterate upon the higher order moments ϕ and ξ, given $\rho^{(0)} = \rho(x, 0)$.

Algorithm 6.1 Constrained runs scheme for diffusive LBM

Require: $\rho^{(0)} = \rho(x,0)$ and a user-defined tolerance $\theta \ll 1$
  $f_i^{(0)} = w_i\,\rho^{(0)}$; $\sum_{i=-1}^{1} w_i = 1$, e.g. $w_i = \nu_i = 1/3$ — Choose $f_i^{(0)}$
  $\phi^{(0)} = (w_1 - w_{-1})\rho^{(0)}$ — Equivalent higher order moments
  $\xi^{(0)} = \frac{1}{2}(w_1 + w_{-1})\rho^{(0)}$
  repeat
    $\mathbf{f}^{(k+1)} = \mathrm{LBM}(\mathbf{f}^{(k)})$ — LBM simulation (3.9) over time δt
    $\boldsymbol{\varrho}^{(k+1)} = M\mathbf{f}^{(k+1)}$ — Corresponding $\phi^{(k+1)}$ and $\xi^{(k+1)}$ (3.25)
    $\rho^{(k+1)} = \rho^{(0)}$ — Reset macroscopic variables
    $\mathbf{f}^{(k+1)} = M^{-1}\boldsymbol{\varrho}^{(k+1)}$ — Map back (3.25)
  until convergence heuristic $< \theta$

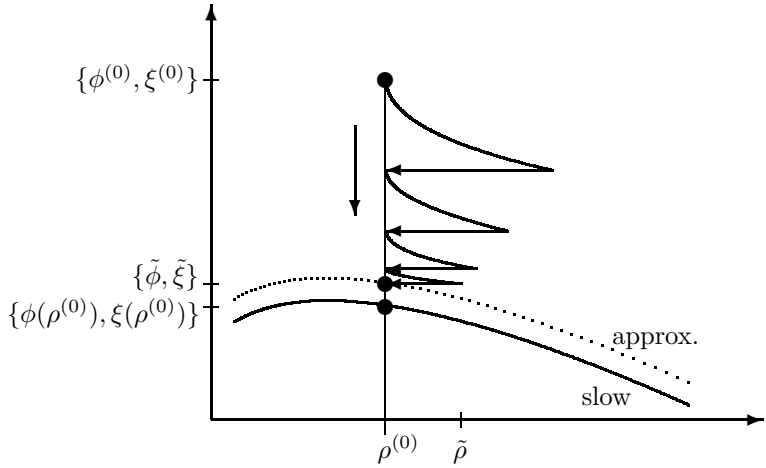


Figure 6.1: Sketch of the evolution of the constrained runs initialization procedure. The higher order moments ϕ and ξ are plotted with respect to the macroscopic variable ρ. The density ρ is reset to the given $\rho^{(0)}$ after each LBM simulation. The fixed point $\{\tilde{\phi}, \tilde{\xi}\}$ is an approximation to the slaved state $\{\phi(\rho^{(0)}), \xi(\rho^{(0)})\}$. The former lies on an "approximate" manifold while the latter lies on the slow manifold described by ρ. The value $\tilde{\rho}$ is the density corresponding to $\{\tilde{\phi}, \tilde{\xi}\}$ (before the final reset to $\rho^{(0)}$) and will be useful as an estimate for the error.

The CR scheme can be defined as a map

$$\boldsymbol{\varrho}^{(k+1)} = \mathcal{C}_{\delta t}(\boldsymbol{\varrho}^{(k)}) \; ; \quad k = 0, 1, 2, \ldots, K \tag{6.1}$$

with k the iteration number and δt the simulation time needed by the inner microscopic simulator. Although the value $\rho^{(k)} = \rho^{(0)}$ is kept constant (reset), we included ρ in the state vector $\boldsymbol{\varrho}^{(k)} = [\rho^{(k)} \; \phi^{(k)} \; \xi^{(k)}]'$.

The details for a one-dimensional diffusive LBM are given in Algorithm 6.1. For a given density profile $\rho^{(0)}$, a good initial guess for $f_i^{(0)}$ is the BGK equilibrium distribution (3.6), i.e. $w_i = \nu_i = 1/3$. The LBM is then repeatedly used to evolve the state for a short time δt. After each such simulation, the lowest moment of the distribution functions is reset to the initial density profile. A straightforward choice for the convergence heuristic is

$$||\phi^{(k+1)}(x) - \phi^{(k)}(x)|| < \theta \quad \text{and} \quad ||\xi^{(k+1)}(x) - \xi^{(k)}(x)|| < \theta \; , \tag{6.2}$$

with $||\cdot||$ and θ a norm and tolerance ($\theta \ll 1$) chosen by the user. Note that the computation of $\mathbf{f}^{(k+1)} = M^{-1}\boldsymbol{\varrho}^{(k+1)}$ in Algorithm 6.1 reduces to

$$f_0^{(k+1)} = \rho^{(0)} - f_{-1}^{(k+1)} - f_1^{(k+1)} \; , \tag{6.3}$$

since solely resetting the density changes the value of $f_0^{(k+1)}$ only.

Figure 6.1 sketches the procedure's evolution. We denote the fixed point of the CR scheme by $\{\tilde{\phi}, \tilde{\xi}\}$ and the corresponding density from the microscopic simulation by $\tilde{\rho}$. Due to the microscopic simulation, $\tilde{\rho}$ will be different from the $\rho^{(0)}$ to reset to (that is, unless the initial condition is a steady state of the microscopic model itself and $\tilde{\rho} = \rho^{(0)}$). The corresponding higher order moments $\{\tilde{\phi}, \tilde{\xi}\}$ are only approximations to the missing higher order moments $\{\phi(\rho^{(0)}), \xi(\rho^{(0)})\}$ of the slaved state. The values $\{\rho^{(0)}, \tilde{\phi}, \tilde{\xi}\}$ denote a point on an *"approximate" manifold* instead of the true slow manifold described by the density ρ (cf. Fig. 6.1). Since the approximation error is proportional to the microscopic simulation time δt, the latter should be chosen as small as possible. For a LBM, we thus choose $\delta t = \Delta t$ (one LBM time step).

6.3 Stability Analysis

The eigenvalues of the linearization (i.e. the Jacobian matrix) of the CR scheme (6.1) will determine its stability. Section 6.3.1 lists a few theorems about the eigenvalues of a certain class of matrices that will be needed further on. In Sect. 6.3.2 and 6.3.3, we derive the Jacobian matrix for the LBM under discussion with either periodic, no-flux or Dirichlet boundary conditions. Finally, we prove in Sect. 6.3.4 that the scheme is unconditionally stable for the type of systems considered.

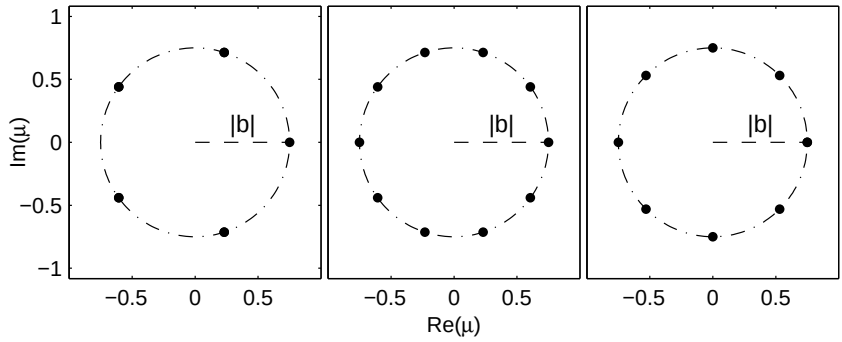


Figure 6.2: Eigenvalues μ_m of the 10×10 matrices with structure (6.4) (left), (6.6) (middle) or (6.7) (right) and relations (6.5) for $b = 0.75$.

6.3.1 Useful Matrix Lemmas

Here, we state a few general lemmas about the spectra of a class of matrices that will be needed in Sect. 6.3.4. The proofs are given in Appendix C. Figure 6.2 shows the numerically computed eigenvalues μ of matrices (6.4), (6.6) and (6.7). The matrix elements are related as in (6.5) with $b = 0.75$.

Lemma 6.1. *Define a square $2N \times 2N$ matrix A structured as follows (here given a small dimensional example with $2N = 10$):*

$$\begin{bmatrix}
 & & a & -b & & & & & a & b \\
 & & -c & a & & & & & c & a \\
a & b & & & a & -b & & & & \\
c & a & & & -c & a & & & & \\
 & & a & b & & & a & -b & & \\
 & & c & a & & & -c & a & & \\
 & & & & a & b & & & a & -b \\
 & & & & c & a & & & -c & a \\
a & -b & & & & & a & b & & \\
-c & a & & & & & c & a & &
\end{bmatrix} \tag{6.4}$$

(for clarity, we omitted zeros from our notation). When the elements of such a matrix are related as

$$a = \frac{b}{2} \quad ; \quad c = \frac{b}{4} \quad ; \quad b \in \mathbb{R}\,, \tag{6.5}$$

the matrix has N distinct eigenvalues $\mu_m = b\exp(i\,m\,2\pi/N)$; with $m = 0, 1, \ldots, N-1$ (each with multiplicity 2), lying on a circle with radius $r = |b|$.

Lemma 6.2. *Define the square $2N \times 2N$ matrix A (here for $2N = 10$):*

$$\begin{bmatrix}
-a & b & a & -b & & & & & & \\
-c & a & -c & a & & & & & & \\
a & b & & & a & -b & & & & \\
c & a & & & -c & a & & & & \\
& & a & b & & & a & -b & & \\
& & c & a & & & -c & a & & \\
& & & & a & b & & & a & -b \\
& & & & c & a & & & -c & a \\
& & & & & & a & b & -a & -b \\
& & & & & & c & a & c & a
\end{bmatrix} \tag{6.6}$$

When the elements are related as in (6.5), matrix (6.6) has $2N$ distinct eigenvalues $\mu_m = b\exp(i\,m\,\pi/N)$; $m = 0, 1, \ldots, 2N-1$. These eigenvalues lie on a circle with radius $r = |b|$.

Conjecture 6.3. *Define the square $2N \times 2N$ matrix A (here for $2N = 10$):*

$$\begin{bmatrix}
2b & b & -2b & & & & & & & \\
b & & & & & & & & & \\
a & b & & & a & -b & & & & \\
c & a & & & -c & a & & & & \\
& & a & b & & & a & -b & & \\
& & c & a & & & -c & a & & \\
& & & & a & b & & & a & -b \\
& & & & c & a & & & -c & a \\
& & & & & & b & 2b & & -2b \\
& & & & & & & & & b
\end{bmatrix} \tag{6.7}$$

When the elements are related as in (6.5), matrix (6.7) has $2N-2$ distinct eigenvalues $\mu_m = b\exp(i\,m\,2\pi/(2N-2))$; $m = 0, 1, \ldots, 2N-3$, lying on a circle with radius $r = |b|$. All eigenvalues have multiplicity 1, except $\mu_0 = b$, which has multiplicity 3.

6.3.2 Jacobian Matrix

In the CR procedure, we reset the density variable $\rho^{(k+1)} = \rho^{(k)} = \rho^{(0)}$ and retain only the evolution equations for the higher order moments (3.33) and

(3.34) as described in Sect. 3.5. These equations are coupled as follows

$$\begin{bmatrix} \phi^{(k+1)} \\ \xi^{(k+1)} \end{bmatrix} = (1-\omega) \left[\begin{array}{c|c} \left(1 + \frac{\Delta x^2}{2}\frac{\partial^2}{\partial x^2}\right) & -2\Delta x \frac{\partial}{\partial x} \\ \hline -\frac{\Delta x}{2}\frac{\partial}{\partial x} & \left(1 + \frac{\Delta x^2}{2}\frac{\partial^2}{\partial x^2}\right) \end{array}\right] \begin{bmatrix} \phi^{(k)} \\ \xi^{(k)} \end{bmatrix} + B_{cont}, \tag{6.8}$$

with

$$B_{cont} = \begin{bmatrix} -\frac{2\omega\Delta x}{3}\frac{\partial \rho^{(0)}}{\partial x} - \frac{2\Delta x \Delta t}{3}\frac{\partial F(\rho^{(0)})}{\partial x} \\ \frac{\omega}{3}\rho^{(0)} + \frac{\omega\Delta x^2}{6}\frac{\partial^2 \rho^{(0)}}{\partial x^2} + \frac{\Delta t}{3}F(\rho^{(0)}) + \frac{\Delta t \Delta x^2}{6}\frac{\partial^2 F(\rho^{(0)})}{\partial x^2} \end{bmatrix}, \tag{6.9}$$

where B_{cont} gathers the terms related to $f_i^{eq}(x - c_i\Delta x, t)$ and $R_i(x - c_i\Delta x, t)$ that depend upon the density $\rho^{(0)}$ only (see Sect. 3.5). Since these values are kept constant, they do not contribute to the Jacobian matrix.

Due to the local nearest-neighbor nature of the LBM equation (3.9) or (3.30), combining the *second order* Taylor expansion from Sect. 3.5 with a discretization of the corresponding spatial derivatives with standard *central* differences, ensures that the dynamics of the higher order moments is described correctly. Alternatively, as described in Appendix B.1, the equations for the moments (and the corresponding Jacobian) can be derived in discrete form from the LBM based on the propagation and the D1Q3 stencil only. The result is the central differences approximation of (3.32), (3.33) and (3.34).

If we write the discretized state vector in interwoven form as

$$\begin{aligned} \boldsymbol{\varphi}^{(k)} = [\ldots\ & \phi^{(k)}(x_{j-1})\ \ \xi^{(k)}(x_{j-1})\ \ \phi^{(k)}(x_j)\ \ \xi^{(k)}(x_j)\ \ \phi^{(k)}(x_{j+1}) \\ & \xi^{(k)}(x_{j+1})\ \ldots]', \end{aligned} \tag{6.10}$$

for $j = 2, \ldots, N-1$ and N the number of lattice points, the discretized system has the following structure

$$\boldsymbol{\varphi}^{(k+1)} = A\boldsymbol{\varphi}^{(k)} + B_{disc}\,, \tag{6.11}$$

with

$$A = \begin{bmatrix} \ddots & \ddots & \ddots & & & & & \\ & & a & -b & & & & \\ & & -c & a & & & & \\ a & b & & & a & -b & & \\ c & a & & & -c & a & & \\ & & a & b & & & a & -b \\ & & c & a & & & -c & a \\ & & & \ddots & \ddots & \ddots & & \ddots \end{bmatrix} \tag{6.12}$$

and B_{disc} the central difference discretization of B_{cont} (see (B.9)-(B.10) in Appendix B.1) and

$$a = \frac{1-\omega}{2} \quad , \quad b = 1-\omega \quad \text{and} \quad c = \frac{1-\omega}{4} \; . \tag{6.13}$$

Since the matrix shown in (6.12) is constant, it is also the Jacobian matrix. Its dimension equals $2N \times 2N$, i.e. two times the number of lattice points.

The top and bottom rows of the Jacobian matrix in (6.12) are determined by the boundary conditions imposed on the spatial domain. In Sect. 6.3.3, we derive these border elements for periodic, no-flux and Dirichlet boundary conditions. In all cases, we use N lattice sites.

6.3.3 A Note on Boundary Conditions

6.3.3.1 Periodic boundary conditions

The N lattice sites are positioned at the midpoints of N lattice intervals, such that all distributions, including the ones crossing the boundary, propagate over only one lattice distance Δx. The boundary conditions are

$$f_1(x_1, t+\Delta t) = f_1^\star(x_N, t^\star) \quad \text{and} \quad f_{-1}(x_N, t+\Delta t) = f_{-1}^\star(x_1, t^\star) \; , \tag{6.14}$$

where the value $f_i^\star$ denotes the post-collision (or pre-propagation) distribution with velocity c_i (see Sect. 3.2). When discretizing the spatial derivatives in (6.8) with central differences, the missing higher order moments at one side of the interval are just the higher order moments at the other side of the interval. We then obtain the recurring structure in the first and last two rows of matrix (6.4). Alternatively, the border elements of matrix (6.4) can be derived as in the paragraphs below.

6.3.3.2 No-flux boundary conditions

No-flux boundary conditions are best implemented using the halfway bounce-back scheme [71, 90]. This puts the LBM variables at the midpoints of N lattice intervals. The unknown (out-of-wall) distributions $f_1(x_1, t+\Delta t)$ and $f_{-1}(x_N, t+\Delta t)$ are obtained during propagation as (3.44), i.e.

$$f_1(x_1, t+\Delta t) = f_{-1}^\star(x_1, t^\star) \quad \text{and} \quad f_{-1}(x_N, t+\Delta t) = f_1^\star(x_N, t^\star) \; .$$

The discrete evolution equation for momentum at the left boundary site

x_1 can be written as

$$\begin{aligned}
\phi(x_1, t+\Delta t) &= f_1(x_1, t+\Delta t) - f_{-1}(x_1, t+\Delta t) && (6.15)\\
&= f^\star_{-1}(x_1, t^\star) - f^\star_{-1}(x_2, t^\star) && (6.16)\\
&= (1-\omega) f_{-1}(x_1, t) - (1-\omega) f_{-1}(x_2, t) + G(\rho(x_1, t); \rho(x_2, t)) && (6.17)\\
&= -\frac{(1-\omega)}{2}\phi(x_1, t) + (1-\omega)\xi(x_1, t) + \frac{(1-\omega)}{2}\phi(x_2, t)\\
&\quad - (1-\omega)\xi(x_2, t) + G(\rho(x_1, t); \rho(x_2, t)) && (6.18)\\
&= -a\phi(x_1, t) + b\xi(x_1, t) + a\phi(x_2, t) - b\xi(x_2, t) + G(\rho(x_1, t); \rho(x_2, t))\,. && (6.19)
\end{aligned}$$

Equation (6.15) defines the momentum (3.24) after propagation. Imposing propagation and the boundary condition (3.44), we obtain (6.16). Enforcing BGK collisions and reactions, (6.17) is obtained in terms of the pre-collision distributions. Substituting the corresponding pre-collision higher order moments using $\mathbf{f} = M^{-1}\boldsymbol{\varrho}$ (3.25), (6.18) and (6.19) are obtained, the latter using (6.13). The term G gathers the terms depending on ρ. This term winds up in the vector of constants (6.9) and does not contribute to the Jacobian matrix. The coefficients in (6.19) are precisely the elements in the first row of matrix (6.6). The second row follows from a similar derivation for the energy.

The same type of derivation can be done for the rightmost site x_N to obtain the coefficients in the last two rows of (6.6).

6.3.3.3 Dirichlet boundary conditions

To enforce Dirichlet boundary conditions, we put the N lattice points at the edges of $N-1$ intervals, such that the boundaries coincide with the outer lattice sites x_1 and x_N. Note that Δx is now $L/(N-1)$ with L the domain length. The unknown distributions at the boundaries are computed during propagation as

$$\begin{aligned}
f_1(x_1, t+\Delta t) &= \rho(x_1, t) - f^\star_0(x_1, t^\star) - f^\star_{-1}(x_2, t^\star)\,,\\
f_{-1}(x_N, t+\Delta t) &= \rho(x_N, t) - f^\star_0(x_N, t^\star) - f^\star_1(x_{N-1}, t^\star)\,,
\end{aligned} \qquad (6.20)$$

where $\rho(x_1, t)$ and $\rho(x_N, t)$ are the density values imposed by the Dirichlet condition at the boundary.

The discrete evolution equation for momentum at the left boundary site

x_1 can be written as

$$\phi(x_1, t+\Delta t) = f_1(x_1, t+\Delta t) - f_{-1}(x_1, t+\Delta t) \tag{6.21}$$
$$= \rho(x_1, t) - f_0^\star(x_1, t^\star) - 2\, f_{-1}^\star(x_2, t^\star) \tag{6.22}$$
$$= -(1-\omega) f_0(x_1, t) - 2(1-\omega) f_{-1}(x_2, t) + G(\rho(x_1, t); \rho(x_2, t)) \tag{6.23}$$
$$= -(1-\omega)\rho(x_1, t) + 2(1-\omega)\xi(x_1, t) + (1-\omega)\phi(x_2, t) - 2(1-\omega)\xi(x_2, t) + G(\rho(x_1, t); \rho(x_2, t)) \tag{6.24}$$
$$= 2(1-\omega)\xi(x_1, t) + (1-\omega)\phi(x_2, t) - 2(1-\omega)\xi(x_2, t) + G'(\rho(x_1, t); \rho(x_2, t)) \tag{6.25}$$
$$= 2b\xi(x_1, t) + b\phi(x_2, t) - 2b\xi(x_2, t) + G'(\rho(x_1, t); \rho(x_2, t))\ . \tag{6.26}$$

The reasoning is equivalent to the one for equations (6.15)–(6.19). Again, the terms G and G' gather the terms depending on ρ. The coefficients in (6.26) are the elements in the first row of matrix (6.7). The second row follows from a similar derivation for the energy. The last two rows are derived from the same type of derivation for the rightmost site x_N.

6.3.4 Stability Theorem

Theorem 6.4 (Stability theorem). *The constrained runs scheme for the lattice Boltzmann BGK model that describes a one-dimensional reaction-diffusion system with either periodic, no-flux or Dirichlet boundary conditions (and with the reaction term depending on ρ only* (3.10)*), is unconditionally stable.*

Proof. The eigenvalues μ_m of the linearization (the Jacobian matrix) of one iteration of the fixed point map $\mathcal{C}_{\Delta t}$ (6.1) determine the stability of the algorithm. If all eigenvalues in the spectrum $\sigma(\mathcal{C}_{\Delta t})$ lie within the unit circle, i.e. $\forall \mu_m \in \sigma(\mathcal{C}_{\Delta t}) : |\mu_m| < 1$, the iteration is stable.

Since (6.13) satisfies (6.5), the Jacobian matrix in (6.12) represents the bulk of the matrix A (except for the boundaries) from either Lemmas 6.1, 6.2 or 6.3. Depending on the type of boundary conditions (see Sect. 6.3.3), the full structure of A given in (6.4), (6.6) or (6.7) is obtained. These theorems state that all eigenvalues μ_m lie on a circle centered at the origin with radius $r = |b| = |1-\omega|$. The CR iteration is unconditionally stable because $0 < \omega < 2$ (see Sect. 3.2 and 3.3) and thus always $|\mu_m| = |b| < 1$. □

Theorem 6.5 (Asymptotic convergence factor). *The asymptotic convergence factor η of the constrained runs scheme for the LBM described in Theorem 6.4 equals $|1-\omega|$.*

Proof. The proof of Theorem 6.4 states that all eigenvalues μ_m lie on a circle with radius $r = |b| = |1 - \omega|$. Hence the spectral radius (or equivalently, the asymptotic convergence factor) is given by

$$\eta := \max_{\mu_m \in \sigma(\mathcal{C}_{\Delta t})} |\mu_m| = |b| = |1 - \omega| \; .$$

□

Note that this is the same rate at which the underlying LBM simulation relaxes towards the diffusive BGK equilibrium, cf. (3.9).

6.4 Convergence

Theorem 6.6 (Convergence theorem). *The constrained runs scheme for the LBM described in Theorem 6.4 converges to a first order correct approximation* $\{\tilde{\phi}, \tilde{\xi}\}$ *of the slaved state* (3.29)*. The approximation error depends on* $\tilde{\rho} - \rho^{(0)}$*, where* $\rho^{(0)}$ *is the initial density and* $\tilde{\rho}$ *is the internal simulated-upon density corresponding to* $\{\tilde{\phi}, \tilde{\xi}\}$ *(before the final reset to* $\rho^{(0)}$*).*

Proof. The unconditional stability of the CR algorithm (Theorem 6.4) implies that the scheme converges to a fixed point $\{\tilde{\phi}, \tilde{\xi}\}$. We will now prove that this is an approximation to the slaved state (3.29).

Since the macroscopic variable ρ is reset in each step of the algorithm, i.e. since $\boldsymbol{\varrho}^{(k+1)} = \mathcal{C}_{\Delta t}([\rho^{(0)} \; \phi^{(k)} \; \xi^{(k)}]')$, equation (3.32) becomes

$$\begin{aligned} \rho^{(k+1)} = \rho^{(0)} + (1-\omega)\left(-\Delta x \frac{\partial \phi^{(k)}}{\partial x} + \Delta x^2 \frac{\partial^2 \xi^{(k)}}{\partial x^2}\right) + \frac{\omega \Delta x^2}{3} \frac{\partial^2 \rho^{(0)}}{\partial x^2} \\ + \Delta t \, F(\rho^{(0)}) + \frac{\Delta t \Delta x^2}{3} \frac{\partial^2 F(\rho^{(0)})}{\partial x^2} \end{aligned} \tag{6.27}$$

after simulation in the $(k+1)^{th}$ step. Reordering terms in (6.27), we obtain an expression for the term between brackets. Substituting this expression in (3.34) results in the following equation for $\xi^{(k+1)}$:

$$\xi^{(k+1)} = \xi^{(k)} - \omega \xi^{(k)} + \frac{\omega}{3}\rho^{(0)} - \frac{\Delta t}{6} F(\rho^{(0)}) + \frac{1}{2}(\rho^{(k+1)} - \rho^{(0)}) \; . \tag{6.28}$$

The fixed point $\{(\rho^{(0)}), \tilde{\phi}, \tilde{\xi}\}$ of (6.1) is defined by $\tilde{\phi}^{(k+1)} = \tilde{\phi}^{(k)}$ and $\tilde{\xi}^{(k+1)} = \tilde{\xi}^{(k)}$. Denote the corresponding density from simulation by $\tilde{\rho}$ (cf. Fig. 6.1). At the fixed point, (6.28) equals

$$\tilde{\xi} = \frac{1}{3}\rho^{(0)} - \frac{\Delta t}{6\,\omega} F(\rho^{(0)}) + \frac{1}{2\omega}(\tilde{\rho} - \rho^{(0)}) \; . \tag{6.29}$$

When we substitute (6.29) in (3.33), the following equation for the fixed point value $\tilde{\phi}$ can be derived

$$\tilde{\phi} = -\frac{2\,\Delta x}{3\,\omega}\frac{\partial \rho^{(0)}}{\partial x} + (\frac{1}{3} - \omega)\frac{\Delta t \Delta x}{\omega^2}\frac{\partial F(\rho^{(0)})}{\partial x} - (1-\omega)\frac{\Delta x}{\omega^2}\frac{\partial(\tilde{\rho} - \rho^{(0)})}{\partial x} + (1-\omega)\frac{\Delta x^2}{2\omega}\frac{\partial^2 \tilde{\phi}}{\partial x^2}\,. \tag{6.30}$$

An expression for $\partial^2\tilde{\phi}/\partial x^2$ is obtained by taking the second derivative of (6.30) and keeping only the lowest (third) order terms. Using (2.4), this can be written as

$$\frac{\partial^2 \tilde{\phi}}{\partial x^2} = -\frac{2\Delta x}{3\,\omega}\frac{\partial^3 \rho^{(0)}}{\partial x^3} = \frac{2}{(\omega-2)\Delta x}\left(\frac{\partial(\tilde{\rho} - \rho^{(0)})}{\partial x} - \Delta t \frac{\partial F(\rho^{(0)})}{\partial x}\right)\,. \tag{6.31}$$

Substituting (6.31) in (6.30), we finally obtain

$$\tilde{\phi} = -\frac{2\Delta x}{3\,\omega}\frac{\partial \rho^{(0)}}{\partial x} + \frac{\Delta x \Delta t}{3\omega^2}\frac{(4\omega-2)}{(\omega-2)}\frac{\partial F(\rho^{(0)})}{\partial x} + \frac{\Delta x}{\omega^2}\frac{(-2\omega+2)}{(\omega-2)}\frac{\partial(\tilde{\rho} - \rho^{(0)})}{\partial x}\,. \tag{6.32}$$

Equivalently, the fixed point in moment space $\{(\rho^{(0)}), \tilde{\phi}, \tilde{\xi}\}$ can be written in terms of distribution functions as $\{\tilde{f}_{-1}, \tilde{f}_0, \tilde{f}_1\}$ using (3.25). Up to second order, we have

$$\tilde{f}_i = \frac{1}{3}\rho^{(0)} - \frac{c_i \Delta x}{3\omega}\frac{\partial \rho^{(0)}}{\partial x} - \frac{\Delta t}{6\omega}(3c_i^2 - 2)\left(F(\rho^{(0)}) - 3\frac{(\tilde{\rho} - \rho^{(0)})}{\Delta t}\right)\,. \tag{6.33}$$

When we compare (6.29) and (6.32) (or (6.33)) to the analytical slaving relations (3.29) (resp. (3.26)–3.28)), we see that the first two terms (resp. three) match, but not the third (fourth) one. Using the notion of order from Sect. 3.3 and 3.4, it follows that the CR fixed point matches the slaved state completely up to first order. The approximation error is proportional to the error made upon resetting the density, i.e. the value $\tilde{\rho} - \rho^{(0)}$ and the spatial derivative thereof. □

This value is thus a measure for the "difference" between the slow manifold and the actual approximate manifold converged upon (see Fig. 6.1). One can interpret this error as a crude approximation of the macroscopic time derivative

$$(\tilde{\rho} - \rho^{(0)}) \sim \Delta t \frac{\partial \rho^{(0)}}{\partial t}\,. \tag{6.34}$$

It then follows that choosing the smallest possible CR simulation time $\delta t = \Delta t$ ensures that the error in (6.29) and (6.32) is as small as possible, which

confirms our reasoning in Sect. 6.2. Also, the error is small when the density profile is smooth. Finally, note that in a full system steady state, i.e. a steady state of the LBM itself, the approximation error in (6.29) and (6.32) vanishes since all time derivatives (and thus also $\tilde{\rho} - \rho^{(0)}$) evaluate to zero. As already mentioned in [68], this means that full system steady states lie both on the approximate and the slow manifold.

Note that the continuous spatial derivatives in (6.32) are really a shorthand notation for the second order central finite difference scheme and need to be implemented accordingly (see also the discussion in Appendix A).

6.5 Numerical Results

In this section, we illustrate the theoretical results for the FHN reaction-diffusion system with no-flux boundary conditions. The details of this system are given in Sect. 3.7. We chose $\varepsilon = 0.05$ in the FHN reaction term (3.43) in all our numerical experiments.

First, we computed the Jacobian matrix J of the CR procedure numerically using a finite difference technique. Column l of J is obtained as the directional derivative of $\mathcal{C}_{\Delta t}(\boldsymbol{\varrho}^{(k)})$ (6.1) in the direction of the l^{th} unit vector e_l using

$$J[l] = Je_l = \frac{\mathcal{C}_{\Delta t}(\boldsymbol{\varrho}^{(k)} + \epsilon e_l) - \mathcal{C}_{\Delta t}(\boldsymbol{\varrho}^{(k)})}{\epsilon} , \tag{6.35}$$

where ϵ is a small parameter, typically the square root of the machine precision.

For the FHN model with two species, we use the following ordering of the state vector $\boldsymbol{\varrho}^{(k)} = [\rho^{ac}\ \rho^{in}\ \phi^{ac}\ \xi^{ac}\ \phi^{in}\ \xi^{in}]'$ (where we omitted the iteration index k). The resulting Jacobian matrix J has the following structure[1]

$$J = \begin{bmatrix} I & 0 & 0 \\ B^{ac} & A^{ac} & 0 \\ B^{in} & 0 & A^{in} \end{bmatrix} , \tag{6.36}$$

where each sparse submatrix is $2N \times 2N$ dimensional. The identity matrix I is related to both species' densities, while the submatrices A^{ac}, B^{ac} and A^{in}, B^{in} are associated with both ϕ and ξ for either the activator or inhibitor species. If the discretized state variables ϕ and ξ are written in an interwoven manner (6.10) or if permutations are done on the Jacobian, these matrices are banded (2×2 block tridiagonal) with bandwidth 6. The

[1] Note that the submatrices A and B are equal to the corresponding blocks from the LBM Jacobian matrix J_{LBM} (discussed in Sect. 5.6) transformed to moment space by $MJ_{LBM}M^{-1}$, with M derived from (3.25).

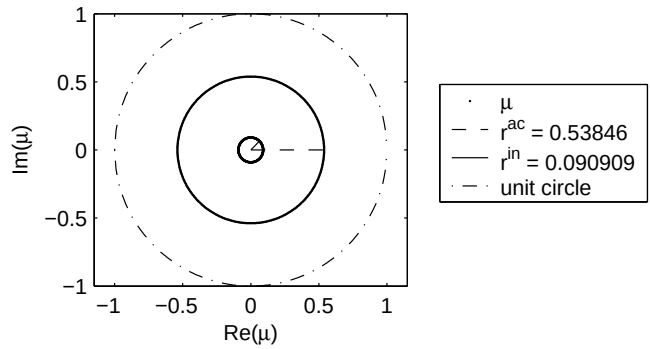


Figure 6.3: Eigenvalues μ of the Jacobian matrix of the CR scheme for the FHN LBM problem. The smallest circle of $2N = 400$ eigenvalues corresponds to the inhibitor species, while the larger circle of 400 eigenvalues is related to the activator species. The unit circle represents the stability boundary. The computed values for the circle radii r^{ac} and r^{in} are given also. The $2N$ "neutral" eigenvalues $\mu = 1$ corresponding to the density variables are not shown.

submatrices B^{ac} and B^{in} contain the derivatives of the ϕ- and ξ-equations with respect to ρ and can be worked out analytically from B_{cont} (6.9) or equivalently from B_{disc} (6.11).

Note that the marked submatrices in (6.36), which gather the derivatives that couple the higher order moments of the activator with the higher order moments of the inhibitor and vice versa, are zero matrices. This means that there is no extra coupling between the activator and inhibitor higher order moments other than the one induced by momentum and energy quickly becoming slaved with respect to their own species' density, which is in turn the only variable coupled to the other species. This is in agreement with (3.43) (and the corresponding force term in the reduced PDEs) where the species' densities are coupled through the reaction term only.

The eigenvalues of the block lower triangular matrix (6.36) are the eigenvalues of each diagonal block. The density-related identity matrix I accounts for $2N$ eigenvalues $\mu = 1$ that do not count for the stability/convergence analysis since ρ is kept constant by constraining (resetting) its value. Since ρ is not really a state variable, the corresponding eigenvalues are neglected.

Both submatrices A^{ac} and A^{in} are structured as in (6.6) (with relations (6.13)). Lemma 6.2 states that each matrix has $2N$ eigenvalues lying on a circle. Figure 6.3 shows the numerically computed eigenvalues of the Jacobian matrix of the CR procedure evaluated at the fixed point $\{(\rho^{(0)}), \tilde{\phi}, \tilde{\xi}\}$. The circles of eigenvalues have radius $r^{ac} = 0.53846 < 1$ and

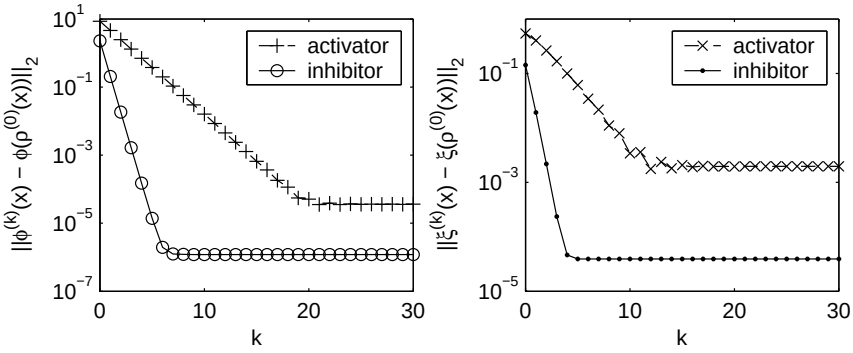


Figure 6.4: Convergence of the higher order moments $\phi^{(k)}$ and $\xi^{(k)}$ in the CR scheme with respect to the "unknown" slaved higher order moments $\phi(\rho^{(0)})$ and $\xi(\rho^{(0)})$. To better show linear convergence, we started Algorithm 6.1 with a bad choice for the higher order moments $\phi^{(0)} = -0.74\rho^{(0)}$ and $\xi^{(0)} = 0.38\rho^{(0)}$.

$r^{in} = 0.090909 < 1$ respectively. It can be checked that all eigenvalues lie at equi-angular distances π/N on the circle, which is conform Lemma 6.2. The CR iteration is stable because all eigenvalues lie within the unit circle.

Substituting the parameter values of our model problem in (3.21), we see that

$$\omega^{ac} = 1.53846 \qquad \text{and} \qquad \omega^{in} = 0.90909 \ ,$$

such that

$$b^{ac} = 1 - \omega^{ac} = -0.53846 \qquad \text{and} \qquad b^{in} = 1 - \omega^{in} = 0.090909 \ . \quad (6.37)$$

In absolute value, these are exactly the radii r^{ac} and r^{in} shown in Fig. 6.3.

Figure 6.4 shows the evolution of the higher order moments $\phi^{(k)}$ and $\xi^{(k)}$ computed in the CR runs procedure with respect to the "missing" higher order moments $\phi(\rho^{(0)})$ and $\xi(\rho^{(0)})$ of the starting point. The latter were obtained by first simulating with the LBM until slaving is obtained, i.e. over a time interval larger than the healing time, here $20\Delta t$ (cf. Chapter 5) and then computing the ϕ and ξ values (3.24) that correspond to the resulting $\rho^{(0)}$ (the starting point for this experiment). The asymptotic convergence factor η can be estimated as

$$\eta^{\kappa} = \frac{||e^{(k+\kappa)}||_2}{||e^{(k)}||_2} \ ; \quad \kappa = 1, 2, \dots \ , \qquad (6.38)$$

with $e^{(k)}$ the error at step k, i.e. either $e^{(k)} = \phi^{(k)} - \phi(\rho^{(0)})$ or $e^{(k)} = \xi^{(k)} - \xi(\rho^{(0)})$. Computing (6.38) for the momentum variables leads to values $\eta^{ac} \approx$

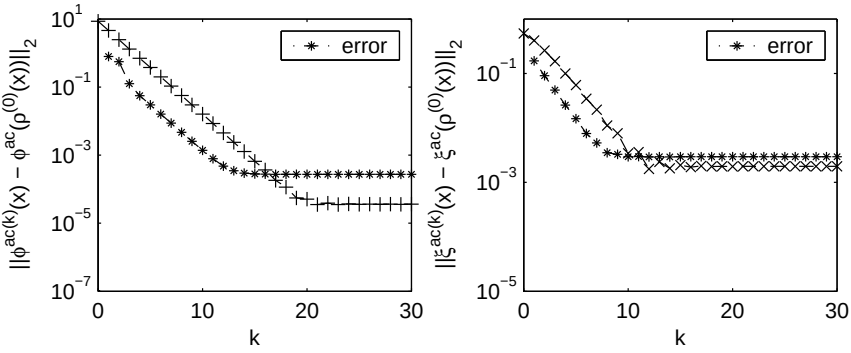


Figure 6.5: The CR convergence error for the activator $\phi^{ac(k)}$ and $\xi^{ac(k)}$ from Fig. 6.4 is compared to the theoretical CR approximation error, i.e. $||q\,\partial(\rho^{(k+1)} - \rho^{(0)})/\partial x||_2$ (left, with q the coefficient defined in (6.32)) and $||(\rho^{(k+1)} - \rho^{(0)})/(2\omega)||_2$ (right, cf. (6.29)). The latter term determines when the convergence error levels off.

0.53 and $\eta^{in} \approx 0.090$ (Fig. 6.4 left), while for the energy variables $\eta^{ac} \approx 0.60$ and $\eta^{in} \approx 0.11$ (Fig. 6.4 right). These values are approximations to the respective theoretical asymptotic convergence factors (circle radii) $|b^{ac}|$ and $|b^{in}|$ (6.37). Since $|b^{in}| < |b^{ac}|$, the inhibitor species converges faster. Even more so, we observe in Fig. 6.4 that this faster convergence leads to a fixed point that is more accurate. In phase space, we have a "steeper" attraction towards the manifold. This leads to a fixed point with a $\tilde{\rho}$ value closer to $\rho^{(0)}$ and thus a more accurate result. This is conform the results for the stiff singularly perturbed ODE systems in [68, 64]. In the latter context, the results become more accurate when the perturbation parameter approaches zero. In a LBM context, $1-\omega$ is related to this perturbation parameter. The closer $1-\omega$ is to zero, i.e. the more $\omega \approx 1$, the more we have a separation of time scales. This is conform Appendix B.2, where we show that for $\omega = 1$, the evolution can be described by the macroscopic reduced PDE.

To verify expressions (6.29) and (6.32) numerically, we computed the norm of the difference between $\tilde{\xi}$, respectively $\tilde{\phi}$, and the right hand side of (6.29) and (6.32) evaluated at the $\tilde{\rho}$ and $\rho^{(0)}$ values. We obtained values within machine precision.

The convergence plots in Fig. 6.4 level off because the fixed point $\{\tilde{\phi}, \tilde{\xi}\}$ ends up on the approximate manifold instead of the true slow manifold (cf. Sect. 6.2). The simple convergence heuristic (6.2) does not take this "leveling off" into account. On the other hand, the error terms in (6.29) and (6.32) suggest to monitor the differences $\rho^{(k+1)} - \rho^{(0)}$ and the spatial derivative thereof for $k = 0, 1, 2, \ldots$ and stop iterating when these values

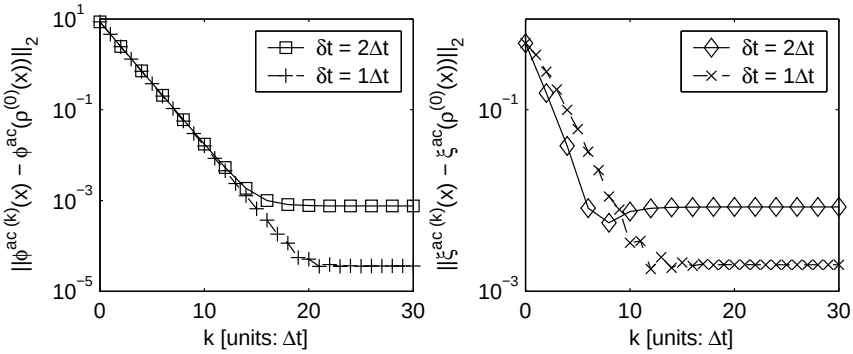


Figure 6.6: Convergence plots of the CR procedure for the activator species. The LBM simulation is performed for $\delta t = \Delta t$ or $\delta t = 2\Delta t$. The initial condition in Algorithm 6.1 is $\phi^{(0)} = -0.74\rho^{(0)}$ and $\xi^{(0)} = 0.38\rho^{(0)}$. The left panel shows the evolution of momentum $\phi^{ac\,(k)}$, while the right panel shows the evolution of energy $\xi^{ac\,(k)}$ with respect to the corresponding "unknown" slaved moments. Output is shown at the same absolute time, thus we slightly abuse the index k notation.

converge (since $\tilde{\rho} - \rho^{(0)}$ is a measure for the difference between the approximate manifold and the slow manifold at $\rho^{(0)}$). Figure 6.5 shows that about 20–25 iterations are sufficient if $\rho^{(k+1)} - \rho^{(0)}$ is monitored. Note that the simulation overhead incurred by the CR initialization comes at the benefit of a very accurate time simulation afterwards (see Sect. 7.2).

The absolute stability of the CR procedure implies that the scheme is always convergent, independent of the initial condition in Algorithm 6.1. A bad choice of $f_i^{(0)}$ (or equivalently $\phi^{(0)}$ and $\xi^{(0)}$) away from the slaving relations (3.29) leads to a larger initial error $e^{(0)}$ and thus a few more iterations necessary for convergence. The fixed point converged upon is however the same. To better show linear convergence in Fig. 6.4, we chose the initial distributions asymmetrically as $f_{-1}^{(0)} = 0.75\rho^{(0)}$, $f_0^{(0)} = 0.24\rho^{(0)}$, $f_1^{(0)} = 0.01\rho^{(0)}$ (or $\phi^{(0)} = -0.74\rho^{(0)}$ and $\xi^{(0)} = 0.38\rho^{(0)}$) instead of the better option of e.g. $f_i^{(0)} = \rho^{(0)}/3$ (or $\phi^{(0)} = 0$ and $\xi^{(0)} = \rho^{(0)}/3$), where the latter is closer to the slaved state (cf. Chapter 5).

Figure 6.6 illustrates that it is best to choose the simulation time δt of the microscopic simulator used in the CR scheme (6.1) as small as possible. In case of a LBM thus equal to one Δt. Results are shown for δt either equal to Δt or $2\Delta t$. Although the latter initially converges faster, the fixed point of the former is more accurate. As suggested in [64], one could first run the CR algorithm with a larger value of δt and switch to a smaller value later on for accuracy (although for our model problem, it is clear that not much would be gained).

6.6 Comparison to the Scheme of Mei *et al.*

Algorithm 6.2 Initialization scheme of Mei *et al.* for diffusive LBM

Require: $\rho^{(0)} = \rho(x,0)$ and a user-defined tolerance $\theta \ll 1$
$f_i^{(0)} = \rho^{(0)}/3$ — Initialize consistent with $\rho^{(0)}$
repeat
$\mathbf{f}^{(k+1)} = \mathrm{LBM}_{\mathrm{mod}}(\mathbf{f}^{(k)}, \rho^{(0)})$ — Run modified LBM over time Δt
until convergence heuristic $< \theta$
$\tilde{\boldsymbol{\varrho}} = M\tilde{\mathbf{f}}$ — Corresponding $\tilde{\phi}$ and $\tilde{\xi}$ (3.25)
$\tilde{\rho} = \rho^{(0)}$ — Use initial density
$\tilde{\mathbf{f}} = M^{-1}\tilde{\boldsymbol{\varrho}}$ — Corresponding distribution functions (3.25)

Mei *et al.* [144] proposed an initialization scheme for the LBM with multiple relaxation times (MRT) for the incompressible Navier-Stokes problem. Caiazzo [22] analyzes this scheme for the LBM BGK model for the same Navier-Stokes problem. We implement this initialization scheme for the LBM BGK model for one-dimensional diffusive problems. The LBM from Sect. 3.2 is then initialized with Algorithm 6.2. Here, evolution equation $\mathrm{LBM}_{\mathrm{mod}}(\mathbf{f}^{(k)}, \rho^{(0)})$ represents (3.9) with a fixed density value $\rho^{(0)}$ in both the equilibrium distribution and reaction term, i.e. (3.6) and (3.10) are replaced with

$$f_i^{eq}(x,t) = \frac{1}{3}\rho^{(0)}(x,t) \quad ; \quad R_i(x,t) = \frac{\Delta t}{3} F(\rho^{(0)}(x,t)) \,. \tag{6.39}$$

Note that for diffusion, this is not a LBM anymore, since density is not conserved by the BGK collisions, i.e. (3.5) does not hold. This implies that the converged distributions $\tilde{f}_i$ do not sum up to the correct initial density $\rho^{(0)}$. A small additional transformation is necessary (last lines of Algorithm 6.2).

We now compare Algorithms 6.1 and 6.2. The CR scheme uses the LBM itself and manipulates the distribution functions externally by resetting the macroscopic variables to the given initial fields. On the other hand, the scheme of Mei *et al.* modifies the LBM internally by fixing the macroscopic variables to the initial values in the equilibrium distribution and force terms. The resulting scheme relaxes towards the given macroscopic variables.

However, it can be checked that the evolution of ϕ and ξ (or equivalently f_1 and f_{-1}) is the same in both Algorithms 6.1 and 6.2. Indeed, in step k of Algorithm 6.1, we reset the density (6.3). In step $k+1$, the density – which is a conserved variable here – is computed (3.3) and used in the BGK equilibrium (3.6) and reaction term (3.10) in (3.9). The resulting iteration for f_1 and f_{-1} is equal to (3.9) with (6.39). Note that for f_0, the schemes

behave differently, which is the reason for the reset of density in the last lines of Algorithm 6.2. We can conclude that the higher order moments have the same convergence behavior (this can be checked numerically also). Thus the results of Theorems 6.4, 6.5 and 6.6 apply. As a consequence, the converged higher order moments $\tilde{\phi}$ and $\tilde{\xi}$ for our model problem in Algorithm 6.2 are first order accurate and their values are given by (6.29) and (6.32).

6.7 Conclusions

In this chapter, we analyzed the behavior of the constrained runs (CR) scheme [68, 64] for the initialization of a LBM from given macroscopic initial fields. The LBM considered is the BGK model for one-dimensional reaction-diffusion systems with either periodic, no-flux or Dirichlet boundary conditions. For such systems, we proved that the CR scheme is unconditionally stable and convergent. We showed that the scheme converges to a first order correct approximation of the slaved state, i.e. the state that is consistent with the macroscopic initial condition. Furthermore, we derived that the asymptotic convergence factor equals $|1-\omega|$, with ω the BGK relaxation coefficient. We used the FitzHugh-Nagumo reaction-diffusion system with no-flux boundary conditions to illustrate the theoretical results.

As an alternative to CR initialization, the initialization scheme of Mei *et al.* [144, 22] can be used. For the LBM BGK model for one-dimensional reaction-diffusion systems, we showed that this initialization procedure is very similar and that the results of our numerical analysis apply, yielding the same convergence and accuracy results.

Of course, these initialization schemes are only useful under the assumption that the slaving relations (3.27)–(3.28) or equivalently (3.29) are unavailable or difficult to compute (see also Sect. 5.2). If these relations are available, the most efficient approach is a direct initialization with these analytical relations, thereby approximating any derivatives with appropriate finite differences. Of course, with these relations available, one might also go one step further and derive the reduced PDE (cf. Sect. 3.3) and use it for the simulation instead of the LBM. When using the slaving relations is not feasible, we stress that a direct initialization with e.g. the local BGK equilibrium is not a good option because this can lead to significant macroscopic initialization errors as we have shown in Chapter 5. The initialization with the CR scheme requires some extra work but the benefits are clear. After initialization, the microscopic state is both consistent with the initial macroscopic state and close to the slow manifold described by the macroscopic variables. The microscopic time simulation started from the resulting microscopic initial state will be quite accurate (for quantitative results, we refer to Sect. 7.2 and 7.5.4).

Chapter 7

Constrained Runs: Applications and Extensions

7.1 Introduction

In this chapter, we discuss some applications and extensions of both the CR scheme and the analysis from the previous chapter.

First, we use the CR scheme as the lifting procedure in the coarse equation-free time stepper for the FHN LBM and perform a time stepper based numerical bifurcation analysis of the resulting system (see Sect. 7.2). As explained in Chapter 5, we show that, with a good lifting scheme like the CR scheme, the coarse time step ΔT can be chosen on the order of the healing time.

Second, we argue that our numerical analysis of the CR scheme can be further extended to lattice Boltzmann BGK models for systems other than reaction-diffusion as well as higher dimensional systems. Although it seems unlikely that the eigenvalues of the linearized CR scheme for a more general LBM lie on a circle, the factor $(1 - \omega)$ can still be expected to play an important role in the stability analysis.

The analysis can be generalized as follows. To begin with, a set of meaningful higher order moments must be defined, see e.g. [116]. The BGK collision term in the LBE can still be expanded in a Taylor series. For the derivation of the continuous evolution equations in the higher order moments, we refer to [43, 101, 109]. Note that the discretization of the spatial derivatives in these equations should be the natural one correspond-

ing to the nearest neighbor nature of the propagation (cf. Appendix B.1 and [100, 101]). This will result in a sparsity pattern of the corresponding Jacobian matrix comparable to the one in Chapter 6. Also, since the BGK equilibrium distribution only depends on the conserved macroscopic variables that are kept constant during the constrained iterations, this term will not contribute to the Jacobian matrix, i.e. it will have no influence on the stability of the method.

In Sect. 7.3, we extend our analysis for the regular CR scheme to the D1Q3R LBM with distribution dependent reaction terms described in Sect. 3.8.2. We prove that the CR iteration is stable and convergent when the underlying LBM is stable. The CR fixed point is a first order approximation of the Chapman-Enskog relations for this model. In Sect. 7.4, we prove that the CR algorithm is stable also for the D1Q5R LBM with distribution dependent reaction terms and multiple speeds from Sect. 3.8.3.

Third, we note that for some applications the accuracy of Algorithm 6.1 might not be enough (e.g. for mildly advective systems). Gear *et al.* [64] extended their basic CR scheme from [68] to CR schemes that use interpolation techniques to improve accuracy. For stiff ODE systems, they proved that these higher order CR schemes have a fixed point that approximates the slow manifold more closely. In Sect. 7.5, we implement the first order CR scheme proposed by the authors for our LBM. We show that the iteration can be unstable depending on the LBM parameters, in contrast to the basic CR scheme discussed in Chapter 6. A careful study of the time simulation after CR initialization leads us to the development of a novel CR based initialization scheme, coined the constrained runs scheme with manifold reconstruction, with improved accuracy and stability under reasonable system conditions.

Finally, Sect. 7.6 summarizes the conclusions of this chapter.

7.2 Coarse-Grained Bifurcation Analysis

In this section, we use the CR procedure in the lifting step of the coarse equation-free time stepper wrapped around the FHN LBM. We compare our results to those obtained with the reconstruction scheme $f_i(x,0) = w_i\rho(x,0)$ (4.1). As discussed in Chapter 5, the latter type of initialization does not attempt to approximate the slaving relations (3.29) for the higher order moments. This induces a significant macroscopic error, which leads to an unnecessary large value of ΔT. The best possible approximation to the slaving relations with (4.1) is the choice $w_i = 1/3$, i.e. initialization with the local diffusive BGK equilibrium (3.6). The corresponding initial higher order moments are correct up to zeroth order: $\xi = \rho/3$ (reasonable) and $\phi = 0$ (bad, although the numerical value is small also, see Fig. 5.1).

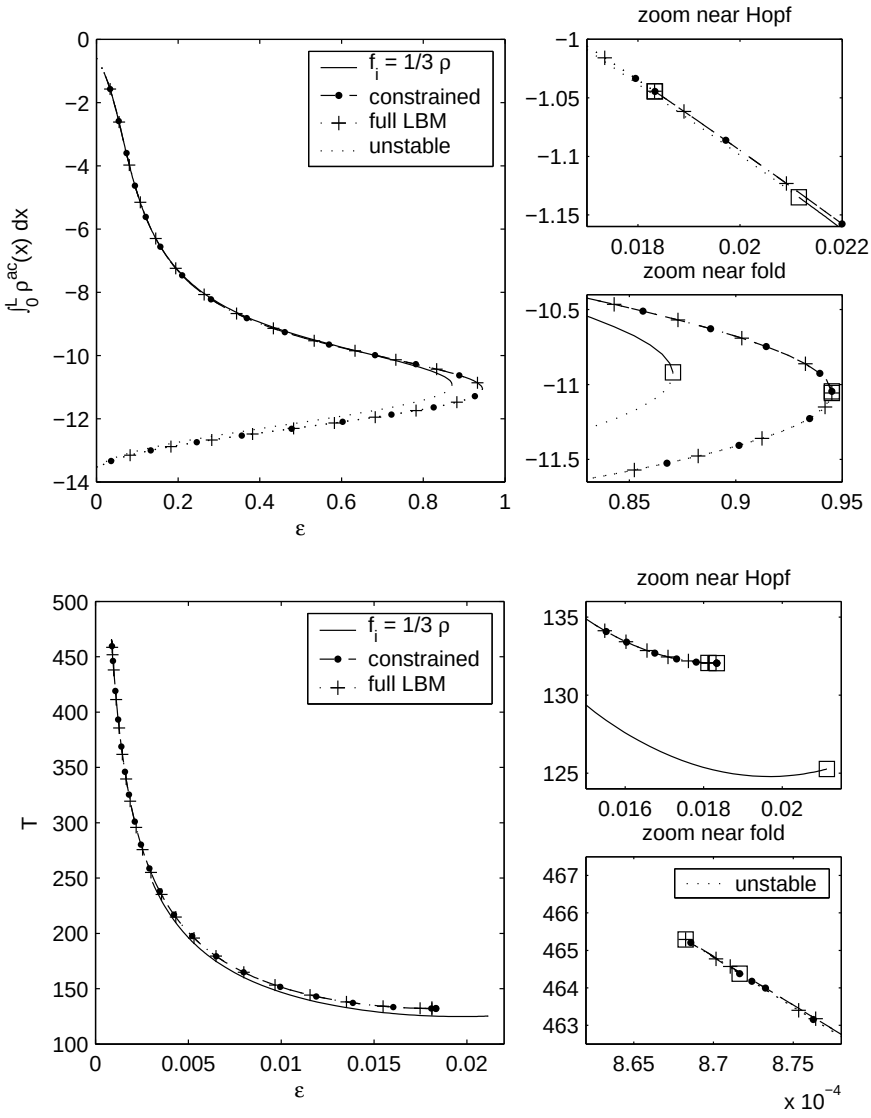


Figure 7.1: Bifurcation diagram for steady states (top) and periodic solutions (bottom). Time steppers are the coarse equation-free LBM with reconstruction scheme either $f_i(x,0) = (1/3)\,\rho(x,0)$ (4.1) or the constrained runs scheme (Algorithm 6.1) and the full LBM for reference. The coarse time step $\Delta T = 0.02 = 20\Delta t$. Unstable solutions are indicated by dotted lines and bifurcation points by boxed markers. The markers represent only a subset of the computed points.

After initialization, we simulate over a coarse time step ΔT using the LBM. Finally, the restriction computes $\rho(x, t + \Delta T)$ using (3.3). As in Chapters 4 and 5, we focus on the effect of the lifting only and successively repeat these ΔT-integrations within the time integration interval $[0, T]$, instead of using this basic time stepper in combination with the time integration acceleration techniques proposed in [47, 65, 218].

The setup is the same as in Chapter 4. We have used the coarse equation-free LBM in a time stepper based numerical bifurcation analysis using the Newton-Picard method. For the FHN model with the choice of parameters mentioned in Sect. 3.7, we compute a branch of steady states and a branch of periodic solutions for varying $\varepsilon \in [0, 1]$. Figure 7.1 shows the results for the coarse equation-free LBM time stepper with either the reconstruction scheme (4.1) with $w_i = 1/3$ or the CR procedure (Algorithm 6.1). We compare to the bifurcation diagram of the full LBM (without equation-free coarse-graining). For steady states, we set $T = 5$, while for periodic solutions, T is the period. We choose $\Delta T = 0.02 = 20\Delta t$ (on the order of the healing time, see Sect. 5.4). It is clear from Fig. 7.1 that, even for such small value of ΔT, the results for the lifting with the CR scheme compare well to those for the full LBM, which is not the case for the reconstruction with (4.1) and $w_i = 1/3$. Note that we failed to compute the complete periodic solution branch in the direction of the fold point for the reconstruction with $f_i(x, 0) = (1/3)\rho(x, 0)$. The resulting time stepper proved too inaccurate to compute solutions near the unstable ones beyond the fold point.

7.3 Analysis for the D1Q3R Model

In this section, we extend to results from Chapter 6 to the D1Q3R model described in Sect. 3.8.2. The model has reaction terms that depend linearly on the distributions instead of being (non-linear) functionals of the density.

7.3.1 Evolution Equations for the Moments

Following the methodology in Sect. 3.5, it can be checked that the evolution equations for the moments are given by

$$\begin{aligned}\rho(x, t + \Delta t) &= \rho + (1 - \omega)\left(-\Delta x \frac{\partial \phi}{\partial x} + \Delta x^2 \frac{\partial^2 \xi}{\partial x^2}\right) + \frac{\omega \Delta x^2}{3}\frac{\partial^2 \rho}{\partial x^2} \\ &\quad + \alpha \Delta x \Delta t \frac{\partial \phi}{\partial x} - \alpha \Delta x^2 \Delta t \frac{\partial^2 \xi}{\partial x^2}\,, \qquad (7.1)\\ \phi(x, t + \Delta t) &= (1 - \omega)\left(\phi - 2\,\Delta x\,\frac{\partial \xi}{\partial x} + \frac{\Delta x^2}{2}\frac{\partial^2 \phi}{\partial x^2}\right) - \frac{2\,\omega \Delta x}{3}\frac{\partial \rho}{\partial x} \\ &\quad - \alpha \Delta t \phi + 2\alpha \Delta x \Delta t \frac{\partial \xi}{\partial x} - \frac{\alpha \Delta x^2 \Delta t}{2}\frac{\partial^2 \phi}{\partial x^2}\,, \qquad (7.2)\end{aligned}$$

$$\xi(x,t+\Delta t) = (1-\omega)\left(\xi - \frac{\Delta x}{2}\frac{\partial\phi}{\partial x} + \frac{\Delta x^2}{2}\frac{\partial^2\xi}{\partial x^2}\right) + \frac{\omega}{3}\rho + \frac{\omega\Delta x^2}{6}\frac{\partial^2\rho}{\partial x^2} - \alpha\Delta t\xi + \frac{\alpha\Delta x\Delta t}{2}\frac{\partial\phi}{\partial x} - \frac{\alpha\Delta x^2\Delta t}{2}\frac{\partial^2\xi}{\partial x^2}\,. \tag{7.3}$$

The moments at the right hand side are evaluated at (x,t).

7.3.2 Jacobian Matrix and Stability

As explained in Sect. 6.3.2, the evolution equations for ϕ and ξ determine the stability of the CR scheme, because we reset the density variable $\rho^{(k+1)} = \rho^{(k)} = \rho^{(0)}$. We can rewrite equations (7.2) and (7.3) as

$$\begin{bmatrix}\phi^{(k+1)}\\ \xi^{(k+1)}\end{bmatrix} = (1-\omega-\alpha\Delta t)\left[\begin{array}{c|c}\left(1+\frac{\Delta x^2}{2}\frac{\partial^2}{\partial x^2}\right) & -2\Delta x\,\frac{\partial}{\partial x}\\ \hline -\frac{\Delta x}{2}\frac{\partial}{\partial x} & \left(1+\frac{\Delta x^2}{2}\frac{\partial^2}{\partial x^2}\right)\end{array}\right]\begin{bmatrix}\phi^{(k)}\\ \xi^{(k)}\end{bmatrix} + B_{cont}. \tag{7.4}$$

As before, B_{cont} gathers the terms that do not contribute to the Jacobian matrix because they depend on the constrained density variables (through the BGK equilibrium $f_i^{eq}(x - c_i\Delta x, t)$). This vector is defined as

$$B_{cont} = \begin{bmatrix} -\frac{2\omega\Delta x}{3}\frac{\partial\rho^{(0)}}{\partial x} \\ \frac{\omega}{3}\rho^{(0)} + \frac{\omega\Delta x^2}{6}\frac{\partial^2\rho^{(0)}}{\partial x^2}\end{bmatrix}\,. \tag{7.5}$$

We can now state the following theorem.

Theorem 7.1 (Stability theorem). *The constrained runs scheme for the one-dimensional lattice Boltzmann BGK model with the distribution dependent reaction term* (3.48) *and either periodic, no-flux or Dirichlet boundary conditions is stable if* $|1-\omega-\alpha\Delta t| < 1$, *i.e. if* $\alpha < (2-\omega)/\Delta t$. *The asymptotic convergence factor is* $\eta = |1-\omega-\alpha\Delta t|$.

Proof. When we compare (7.4) to (6.8), we see that we obtain a Jacobian matrix with exactly the same structure, only the multiplication factor differs ($1-\omega-\alpha\Delta t$ instead of $1-\omega$). Note that we can define $\bar{\omega} = \omega + \alpha\Delta t$ to highlight this equivalence. Consequently, the stability results of Chapter 6 apply to the model under consideration. It then follows that the eigenvalues of the CR time stepper lie on a circle with radius $|1-\omega-\alpha\Delta t|$. By definition, the asymptotic convergence factor η is equal to $\eta = |1-\omega-\alpha\Delta t|$. □

Note that the CR iteration is stable when the underlying LBM simulation is stable.

7.3.3 Convergence

Theorem 7.1 states that, if $|1-\omega-\alpha\Delta t|<1$, the CR algorithm for the LBE (3.47) with reaction term (3.48) is stable and thus convergent. The fixed point $\{(\rho^{(0)}),\tilde{\phi},\tilde{\xi}\}$ converged upon can be derived analytically as in Sect. 6.4. Below, we compute the fixed point energy $\tilde{\xi}$ analytically.

Because we reset the density to $\rho^{(0)}$ in each iteration, the density $\rho^{(k+1)}$ is obtained from (7.1) as

$$\rho^{(k+1)}=\rho^{(0)}+(1-\omega-\alpha\Delta t)\left(-\Delta x\frac{\partial\phi^{(k)}}{\partial x}+\Delta x^2\frac{\partial^2\xi^{(k)}}{\partial x^2}\right)+\frac{\omega\Delta x^2}{3}\frac{\partial^2\rho^{(0)}}{\partial x^2}\ . \tag{7.6}$$

Reordering terms in (7.6), we obtain an expression for the term between brackets. Substituting this expression in (7.3) results in the following equation for $\xi^{(k+1)}$:

$$\xi^{(k+1)}=(1-\omega-\alpha\Delta t)\xi^{(k)}+\frac{\omega}{3}\rho^{(0)}+\frac{1}{2}(\rho^{(k+1)}-\rho^{(0)})\ . \tag{7.7}$$

The fixed point $\{(\rho^{(0)}),\tilde{\phi},\tilde{\xi}\}$ is defined by $\tilde{\phi}^{(k+1)}=\tilde{\phi}^{(k)}$ and $\tilde{\xi}^{(k+1)}=\tilde{\xi}^{(k)}$ with the corresponding density from simulation being $\tilde{\rho}$ (cf. Fig. 6.1). The fixed point energy can be found from (6.28) as

$$\tilde{\xi}=\frac{\omega}{3\bar{\omega}}\rho^{(0)}+\frac{1}{2\bar{\omega}}(\tilde{\rho}-\rho^{(0)})\ , \tag{7.8}$$

with $\bar{\omega}=\omega+\alpha\Delta t$. Comparing (7.8) to the Chapman-Enskog slaving relation for $\xi(\rho^{(0)})$ given by (3.61), we again obtain a first order approximation of the slaving relations. As in Sect. 6.4 for the regular D1Q3 model, the approximation error is due to both a crude approximation of the time derivative and a difference in the analytical coefficients. An expression for $\tilde{\phi}$ can be obtained also with a derivation similar to the one in Sect. 6.4.

7.3.4 Numerical Verification

We will now test the behavior of the CR iteration for the D1Q3R model (3.47)–(3.48). We generate a suitable starting condition as follows. First, we simulate with the full LBM for a certain time interval larger than the healing time (e.g. $T=10$) and use (3.60)–(3.61) to initialize the model from an initial Gaussian density distribution. The full end state lies on the slow manifold and is perfectly slaved. Second, we compute all moments (3.25) from this end result and denote them by $\rho^{(0)}$, $\phi(\rho^{(0)})$ and $\xi(\rho^{(0)})$. The $\rho^{(0)}$ value serves as the macroscopic initial condition for the CR scheme, while $\phi(\rho^{(0)})$ and $\xi(\rho^{(0)})$ are supposedly unknown. Finally, we approximate these

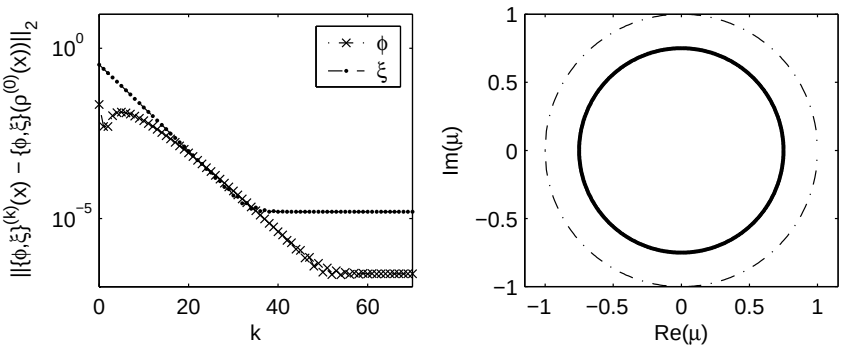


Figure 7.2: Left: Error of the higher order moments $\phi^{(k)}$ and $\xi^{(k)}$ in the constrained runs scheme w.r.t. the "unknown" slaved moments $\phi(\rho^{(0)})$ and $\xi(\rho^{(0)})$. The LBM is the D1Q3R model (3.47) with the f_i-dependent reaction term (3.48). Right: Eigenvalues μ of the Jacobian matrix of the constrained runs scheme. The unit circle marks the stability boundary.

"unknown" moments with the CR scheme (Algorithm 6.1). The parameters are chosen as $D = 2$, $L = 20$, $N = 200$ (and thus $\Delta x = 0.1$), $\Delta t = 0.001$, which corresponds to $\omega = 1.25$ (3.21). We use a reaction rate $\alpha = 500$ and no-flux boundary conditions (3.44).

Figure 7.2 (left) shows the error of the CR scheme in terms of the iterated $\phi^{(k)}$ and $\xi^{(k)}$ compared to the "unknown" moments $\phi(\rho^{(0)})$ and $\xi(\rho^{(0)})$. Again, the CR accuracy levels off because the approximate manifold — determined by $\tilde{\rho} - \rho^{(0)}$ in (7.8) and the spatial derivative(s) thereof — is reached, i.e. because of the first order accuracy of the CR scheme. We verified (7.8) numerically by explicitly evaluating this analytical expression for $\rho^{(0)}$ and $\tilde{\rho}$ and comparing to the computed fixed point energy $\tilde{\xi}$. The difference is within machine precision. The asymptotic convergence rate η can be estimated from (6.38). We find $\eta \approx 0.76$ from the momentum related error and $\eta \approx 0.74$ from the error related to energy, i.e. fairly good approximations of $|1 - \omega - \alpha\Delta t| = 0.75$.

The Jacobian matrix J of the CR iteration is computed numerically using (6.35). It has the same structure as (6.36), now for one species, i.e.

$$J = \begin{bmatrix} I & 0 \\ B & A \end{bmatrix} ,$$

with I the $N \times N$ identity matrix corresponding to the reset density and the $2N \times 2N$ matrix A and the $2N \times N$ matrix B the discretized versions of (7.4) and (7.5) respectively. Because of the no-flux boundary conditions, the relevant part A is structured as (6.6) with $b = 1 - \omega - \alpha\Delta t = -0.75$.

The eigenvalues μ of A are plotted in the right panel of Fig. 7.2. These $2N$ eigenvalues lie on a perfect circle with radius $r = |1 - \omega - \alpha\Delta t| = 0.75$ as predicted in Sect. 7.3.2.

7.4 Analysis for the D1Q5R Model

In this section, we extend to stability analysis of the constrained runs scheme to the D1Q5R model described in Sect. 3.8.3. A rigorous generalization of the results in Chapter 6 and Sect. 7.3 requires a five point finite difference stencil and becomes extensive. Below, we present a shorter alternative.

7.4.1 Stability

The distributions $f_{\pm 2}$ for the fast particles evolve as (3.47), i.e.

$$f_{\pm 2}(x \pm 2\Delta x, t + \Delta t) = (1 - \omega - \alpha\Delta t) f_{\pm 2}(x, t) + \omega\nu_{\pm 2}\rho(x, t) \ . \quad (7.9)$$

The last term in (7.9) cancels because $\nu_{\pm 2} = 0$ (3.51). This leads to the extinction of the fast particles[1]. Because the propagation of distributions is a conservative operation [194], this iteration (both the LBM simulation and the CR scheme wrapped around it) is linearly stable if

$$|1 - \omega - \alpha\Delta t| < 1 \ . \quad (7.10)$$

The distributions $f_{\pm 1}$ evolve as

$$\begin{aligned} f_{\pm 1}(x \pm \Delta x, t + \Delta t) = (1 - \omega) f_{\pm 1}(x, t) + \omega\nu_{\pm 1}\rho(x, t) \\ + \alpha\Delta t\big(f_{+2}(x, t) + f_{-2}(x, t)\big) \ , \end{aligned} \quad (7.11)$$

where the number of slow particles is increased proportional to the number of both fast particles because of the ionization reaction. In each iteration of the CR algorithm 6.1, we "freeze" the value of the BGK equilibrium $f_i^{eq} = \nu_i\rho$ by resetting the density to its original value. Because the convergence rate for the $f_{\pm 2}$ components is given by (7.10), equation (7.11) converges at a rate $|1 - \omega - \alpha\Delta t|$ if this value dominates over $|1 - \omega|$. Indeed, under this condition, we have

$$\frac{e_{\pm 1}^{(k+1)}}{e_{\pm 1}^{(k)}} \approx \frac{2\alpha\Delta t(1 - \omega - \alpha\Delta t) e_{\pm 2}^{(k-1)}}{2\alpha\Delta t e_{\pm 2}^{(k-1)}} \approx (1 - \omega - \alpha\Delta t) \ ,$$

with $e_i^{(k)} = f_i^{(k)} - f_i(\rho^{(0)})$ the error at the k^{th} CR iteration. Alternatively, if $|1 - \omega|$ dominates over (7.10), (7.11) converges at a rate $|1 - \omega|$.

[1] When the influence of the electrical field is left out of the equation, see Sect. 3.8.1.

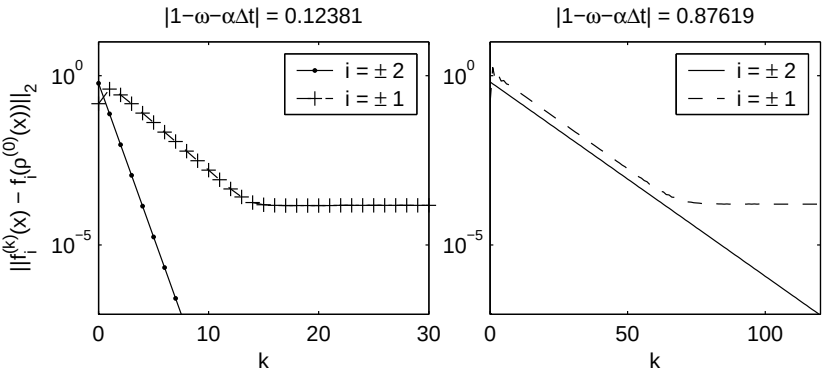


Figure 7.3: Error of the distributions $f_i^{(k)}$ in the constrained runs scheme w.r.t. the "unknown" slaved distributions $f_i(\rho^{(0)})$. The LBM is the D1Q5R model (3.47) with the f_i-dependent reaction term (3.50). Left: $|1-\omega-\alpha\Delta t| < |1-\omega| = 0.524$. Right: $|1-\omega-\alpha\Delta t| > |1-\omega| = 0.524$. Note the larger number of iterations when the reaction rate α is stronger.

So far, we have no formal proof for the convergence of the CR scheme for the full ionization model (3.45)–(3.46) when an electrical field is present, but in this case CR initialization is successful also; as was shown numerically in [175, 222]. Also, we have no analytical expression for the fixed point of the CR scheme in this setting, but we believe that the results on the accuracy from Chapter 6 generalize (as they do for the D1Q3R model from Sect. 7.3) and that the obtained initial state is a first order approximation of the respective Chapman-Enskog relations.

7.4.2 Numerical Verification

To test the convergence of the CR scheme, we first generate a slaved initial state as in Sect. 7.3.4. Because the velocity space is now five-dimensional, we have to define two extra moments on top of ρ, ϕ and ξ. Likely candidates are the third and fourth order velocity moment (compare (3.24) and [222]). For the test below however, we use the distributions directly. We implement periodic boundary conditions (6.14) and choose the parameters as $D = 8$, $\Delta x = 0.1$, $\Delta t = 0.001$ such that $\omega = 0.476$ (3.8) (and $|1-\omega| = 0.524$). We keep ω fixed and choose reaction rates $\alpha = 400$ and $\alpha = 1400$ to distinguish between the cases when $|1-\omega-400\Delta t| = 0.124 < |1-\omega|$ and $|1-\omega-1400\Delta t| = 0.876 > |1-\omega|$.

The convergence behavior of the CR scheme for the D1Q5R model is illustrated in Fig. 7.3. We chose $f_i^{(0)} = (1/5)\rho^{(0)}$ in Algorithm 6.1 to ob-

tain an evolution in $f_{\pm 2}$. A few observations can be made. First, as $f_{\pm 2}$ eventually vanishes (see (7.9)), we have a continued convergence to machine precision. Second, the convergence for $f_{\pm 1}^{(k)}$ stagnates as expected when the CR scheme reaches the approximate manifold. Third, since the reactions (3.50) are symmetrical, the behavior for the positive speeds is identical to that of the negative ones. Fourth, we note that resetting the density in the D1Q5R model amounts to the operation (compare (6.3))

$$f_0^{(k+1)} = \rho^{(0)} - \sum_{j \neq 0} f_j^{(k+1)} \, .$$

Consequently, the evolution of $f_0^{(k)}$ is determined by the (dominant) evolution of the other distributions. Finally, the convergence rate can be computed from the slopes in Fig. 7.3. From Fig. 7.3 (left), we have $\eta \approx 0.124$ for the $f_{\pm 2}$ components and $\eta \approx 0.524$ for the $f_{\pm 1}$ distributions, while for the right panel, we have $\eta \approx 0.876$ for all distributions.

7.5 Higher Order Constrained Runs Schemes

7.5.1 Constrained Runs Revisited

In Sect. 6.2, we implemented the basic CR algorithm proposed in [68] for diffusive LBM. For later use, we shorten our notation of the iteration in Algorithm 6.1 to a repetition of the following two operations:

$$\boldsymbol{\varrho}^{(k+1)} = M\big(\mathrm{LBM}_{\delta t}(M^{-1}\,\boldsymbol{\varrho}^{(k)})\big) \tag{7.12}$$

$$\rho^{(k+1)} = \rho^{(0)} \tag{7.13}$$

until the convergence heuristic aborts the iteration. In words, we first use the microscopic/mesoscopic simulator for time δt, with in- and output defined in moment space. We fix (here, we reset) the macroscopic variables to their initial values. Recall that the fixed point $\{\rho^{(0)}, \tilde{\phi}, \tilde{\xi}\}$ of the CR iteration is defined by relations (6.29) and (6.32) and corresponds up to first order to the Chapman-Enskog slaving relations (3.29). The remaining approximation error is governed by the factor $(\tilde{\rho} - \rho^{(0)})$ and spatial derivatives thereof. This error can be interpreted as a crude approximation of the macroscopic time derivative, cf. (6.34)

$$(\tilde{\rho} - \rho^{(0)}) \sim \delta t \frac{\partial \rho^{(0)}}{\partial t} \, .$$

The smaller δt is chosen, the closer the resulting fixed point is to the slow manifold. In general, it depends both on the allowed values for δt (determined by the microscopic simulator) and the level of accuracy desired by

the user, which is the proper choice. For the LBM, it is best to use $\delta t = \Delta t$ for reasons of accuracy (cf. Fig. 6.6).

Relation (6.34) suggests using higher order discretizations of the time derivative (instead of the simple resetting operation) to obtain more accurate approximations of the slaving relations for the higher order moments, i.e. more terms in the Chapman-Enskog expansion. This can be done by interpolating the higher order moments, obtained with consecutive short simulations, backward in time, while keeping the lower order moments fixed. In [64], the authors worked this out in the context of model reduction for stiff systems of singularly perturbed ODEs.

In Sect. 7.5.2 and 7.5.3, we implement such schemes based on linear backward extrapolation using respectively forward and central finite difference discretizations of the time derivative. We apply the iteration scheme to the LBM for the FHN system from Sect. 3.7. We show that, although the slow manifold is attracting, the higher order functional iteration is not always stable due to the backward extrapolation of the higher order moments.

In Sect. 7.5.4, we monitor the LBM simulation started from the initial condition generated with the basic CR scheme given in Algorithm 6.1. From the observations thus made, we propose the so-called CR scheme with manifold reconstruction in Sect. 7.5.5, which consists of a regular CR scheme with an additional postprocessing step in which the slow manifold is locally reconstructed by interpolation.

7.5.2 Constrained Runs with Linear Extrapolation

Algorithm 7.1 Constrained runs scheme with linear extrapolation for diffusive LBM

Require: $\rho^{(0)} = \rho(x,0)$ and a user-defined tolerance $\theta \ll 1$

$f_i^{(0)} = w_i\,\rho^{(0)}$; $\sum_i w_i = 1$, e.g. $w_i = \nu_i = 1/3$ — Choose $f_i^{(0)}$

$\boldsymbol{\varrho}^{(0)} = M\mathbf{f}^{(0)}$ — Equivalent moments

repeat

$\boldsymbol{\varrho}_1 = M\big(\mathrm{LBM}_{\Delta t}(M^{-1}\,\boldsymbol{\varrho}^{(k)})\big)$ — LBM simulation over time Δt

$\boldsymbol{\varrho}_2 = M\big(\mathrm{LBM}_{\Delta t}(M^{-1}\,\boldsymbol{\varrho}_1)\big)$ — LBM simulation over time Δt

$\phi^{(k+1)} = 2\phi_1 - \phi_2$ — Extrapolation of h.o. moments

$\xi^{(k+1)} = 2\xi_1 - \xi_2$

$\rho^{(k+1)} = \rho^{(0)}$ — Reset macroscopic variables

until convergence heuristic $< \theta$

In [64], Gear *et al.* present increasingly higher order variants of the 'zeroth order' CR scheme in Algorithm 6.1 that extrapolate the state backwards in time. When wrapped around a diffusive LBM, their scheme for first

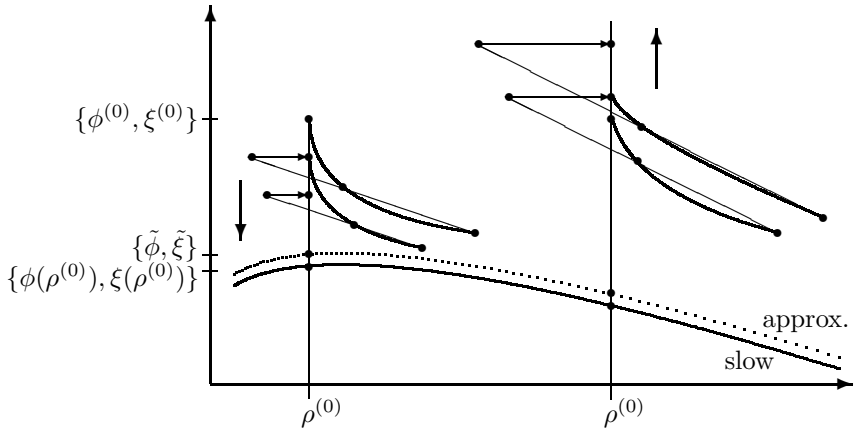


Figure 7.4: Sketch of the evolution of the constrained runs initialization scheme with linear extrapolation (Algorithm 7.1). The higher order moments ϕ and ξ are plotted with respect to the macroscopic variable ρ. We perform a backward linear extrapolation using the ϕ and ξ values obtained from two LBM simulations and reset ρ to the given $\rho^{(0)}$ afterwards. The left iteration is stable, the right one unstable.

order extrapolation is given in Algorithm 7.1. The steps of the algorithm are explained below. First, a LBM simulation is performed over time $2\Delta t$ and the moments $\boldsymbol{\varrho}_1$ and $\boldsymbol{\varrho}_2$ after respectively Δt and $2\Delta t$ are computed. Second, we use a first order forward finite difference scheme to approximate the time derivatives $\partial\phi_1/\partial t$ and $\partial\xi_1/\partial t$, and perform a backward extrapolation as follows

$$\phi^{(k+1)} = \phi_1 - \Delta t \frac{\partial \phi_1}{\partial t} = \phi_1 - \Delta t \frac{\phi_2 - \phi_1}{\Delta t} \ ,$$

and similarly for $\xi^{(k+1)}$, to obtain the next $\phi^{(k+1)}$ and $\xi^{(k+1)}$ values. Finally, the density is reset to its original value. The evolution of this iteration is sketched in Fig. 7.4. The left panel illustrates a possible scenario for a stable CR iteration, while the right panel depicts an unstable one. In both cases, the fixed point $\{\tilde{\phi}, \tilde{\xi}\}$ is uniquely defined as the approximation to the slaved state $\{\phi(\rho^{(0)}), \xi(\rho^{(0)})\}$. The former lies on an approximate manifold while the latter lies on the slow manifold described by ρ. The conditions for a stable or unstable iteration constitute an interesting topic for further research. In general, the stability depends on the physics and evolution of the LBM and consequently on the nature of the attraction ('healing') towards the manifold and the curvature of the manifold. These factors relate back to the $(1-\omega)$ parameter by which the regular CR Algorithm 6.1

converges. Note that this divergence does not only occur for our LBMs, but also for singularly perturbed ODEs [235].

The divergent behavior is shown numerically in Fig. 7.5 where we implemented Algorithm 7.1 for the FHN LBM. As always, the error is computed by comparing to the "unknown" slaved $\phi(\rho^{(0)})$ and $\xi(\rho^{(0)})$ values. Also, we used a bad initial guess for $\phi^{(0)} = -0.74\rho^{(0)}$ and $\xi^{(0)} = 0.38\rho^{(0)}$, i.e. $w_{-1} = 0.75$, $w_0 = 0.24$ and $w_1 = 0.01$, to better show linear convergence. We abuse the index k notation by plotting the actual simulation time (in units of $2\Delta t$) on the bottom axis.

The eigenvalue spectrum of the CR time stepper is plotted in Fig. 7.6 (left). The outer group of eigenvalues (the "circle with tail") corresponds to the activator species, the inner group to the inhibitor species. Note that one group is flipped over with respect to the other because $1-\omega^{ac}$ and $1-\omega^{in}$ in (6.37) have opposite signs. Since almost all eigenvalues for the activator lie outside the unit circle, it is clear that the iteration for our model problem is unstable. Note that Fig. 5.2 (a)–(b) already suggested that interpolation through the ϕ en ξ values during the healing phase can cause problems.

We conclude with the remark that the iteration for the inhibitor on its own would be stable, but due to the coupling through the reaction term with the activator species, the iteration eventually becomes unstable also (the slope is the same in Fig. 7.5). These results suggest that a restricted range of ω values around one can be found for which the CR scheme with linear extrapolation is stable. For the LBM for purely diffusive systems with $\Delta x = 0.1$, we obtain an allowed range of $\omega \in (0.690, 1.292)$.

7.5.3 Variant with Central Difference Discretization

Algorithm 7.2 Constrained runs scheme with linear extrapolation and central difference discretization for diffusive LBM

Require: $\rho^{(0)} = \rho(x,0)$ and a user-defined tolerance $\theta \ll 1$

$f_i^{(0)} = w_i\,\rho^{(0)}$; $\sum_i w_i = 1$, e.g. $w_i = \nu_i = 1/3$ — Choose $f_i^{(0)}$

$\boldsymbol{\varrho}^{(0)} = M\mathbf{f}^{(0)}$ — Equivalent moments

repeat

$\boldsymbol{\varrho}_1 = M\big(\mathrm{LBM}_{\Delta t}(M^{-1}\,\boldsymbol{\varrho}^{(k)})\big)$ — LBM simulation over time Δt

$\boldsymbol{\varrho}_2 = M\big(\mathrm{LBM}_{\Delta t}(M^{-1}\,\boldsymbol{\varrho}_1)\big)$ — LBM simulation over time Δt

$\phi^{(k+1)} = \frac{1}{2}\phi^{(k)} + \phi_1 - \frac{1}{2}\phi_2$ — Extrapolation of h.o. moments

$\xi^{(k+1)} = \frac{1}{2}\xi^{(k)} + \xi_1 - \frac{1}{2}\xi_2$

$\rho^{(k+1)} = \rho^{(0)}$ — Reset macroscopic variables

until convergence heuristic $< \theta$

In Algorithm 7.2, we present a variant of the CR scheme with linear

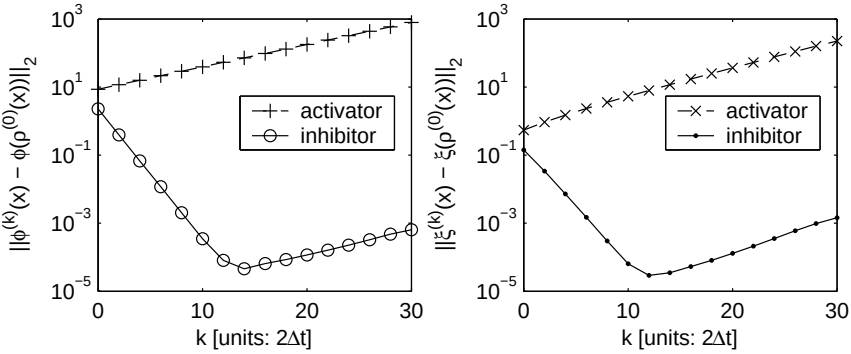


Figure 7.5: Error of $\phi^{(k)}$ and $\xi^{(k)}$ in Algorithm 7.1 for the FHN LBM.

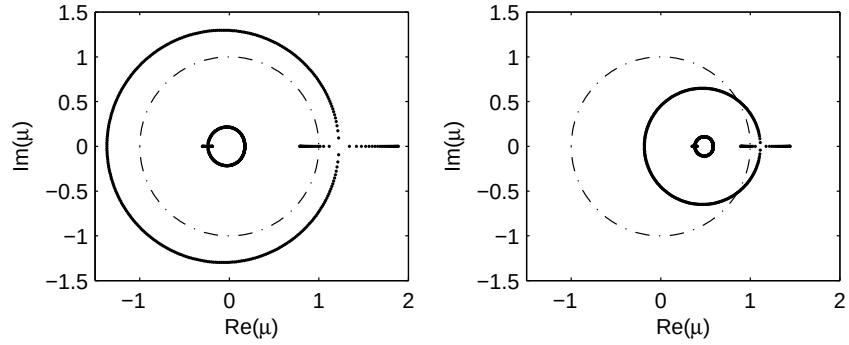


Figure 7.6: Eigenvalues of the CR iteration in Algorithm 7.1 (left) and Algorithm 7.2 (right) for the FHN LBM. The unit circle is shown in dash-dotted line.

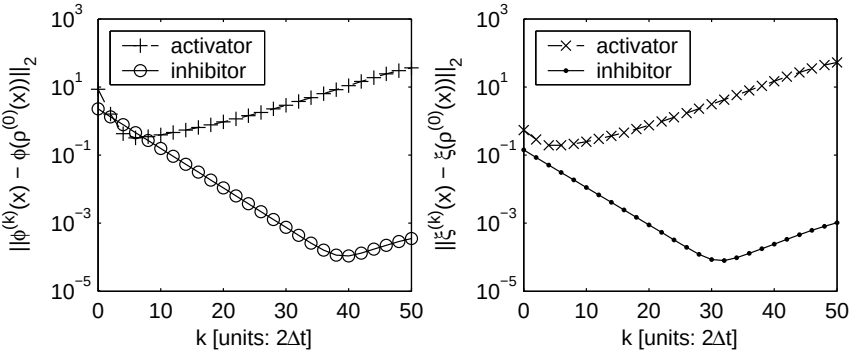


Figure 7.7: Error of $\phi^{(k)}$ and $\xi^{(k)}$ in Algorithm 7.2 for the FHN LBM.

extrapolation using a central finite difference scheme for the discretization of the time derivatives $\partial\phi_1/\partial t$ and $\partial\xi_1/\partial t$. The values $\phi^{(k+1)}$ and $\xi^{(k+1)}$ are computed as

$$\phi^{(k+1)} = \phi_1 - \Delta t \frac{\partial \phi_1}{\partial t} = \phi_1 - \Delta t \frac{\phi_2 - \phi^{(k)}}{2\Delta t} \ ,$$

and similarly for $\xi^{(k+1)}$. In each iteration, the density is constrained to the initial $\rho^{(0)}$ value. Numerically, we implemented this algorithm for the FHN LBM. Figure 7.6 (right) shows that this variant scales the eigenvalue spectrum of Fig. 7.6 (left) with 1/2. Unfortunately, it also shifts to spectrum by 1/2 along the real axis. Again, the iteration is unstable for large $|1-\omega|$ values, as the results for the activator species show in Fig. 7.7. For purely diffusive LBM with $\Delta x = 0.1$, we computed the allowed range of $\omega \in (0.399, 1.292)$. The lower bound on ω is less restrictive and the upper bound is the same, cf. what was expected by comparing the spectra in Fig. 7.6. However, the number of CR iterations is substantially larger. We conclude that the gain in using Algorithm 7.2 instead of Algorithm 7.1 is minimal.

7.5.4 Time Simulation after Constrained Runs Initialization

In this section, we study the behavior of a LBM simulation *after* initialization with the regular CR scheme from Algorithm 6.1. Note that we already studied the resulting time integration in the context of coarse-grained bifurcation analysis in Sect. 7.2. However, we explicitly focus on the time integration itself here.

The setup is as follows. Starting from the initial state (the fixed point) $\tilde{f}_i = M^{-1}[\rho^{(0)}\,\tilde{\phi}\,\tilde{\xi}]'$ iterated upon by the CR Algorithm 6.1, we evolve the FHN LBM for e.g. $30\Delta t$, and compute the moments $\boldsymbol{\varrho}$ at each time step. These values are compared to those obtained with a similar FHN LBM simulation started from the "unknown" slaved state $\{\rho^{(0)}, \phi(\rho^{(0)}), \xi(\rho^{(0)})\}$ (the result of a third a-priori LBM simulation from which we obtained the density $\rho^{(0)}$ to start up the CR iteration). The two-norm of the difference between these moments as a function of time is plotted in Fig. 7.8 for both the FHN activator and inhibitor species.

We observe an attraction of the state from the approximate manifold converged upon by the CR scheme to the slow manifold described by the density. Since the CR higher order moments $\tilde{\phi}$ and $\tilde{\xi}$ correspond only up to first order with the Chapman-Enskog relations (or equivalently since the time derivative in the CR fixed point is not correctly approximated as (6.34) shows), the higher order moments of the state will get slaved further to the density on the manifold. Again, the time this takes is approximately the healing time.

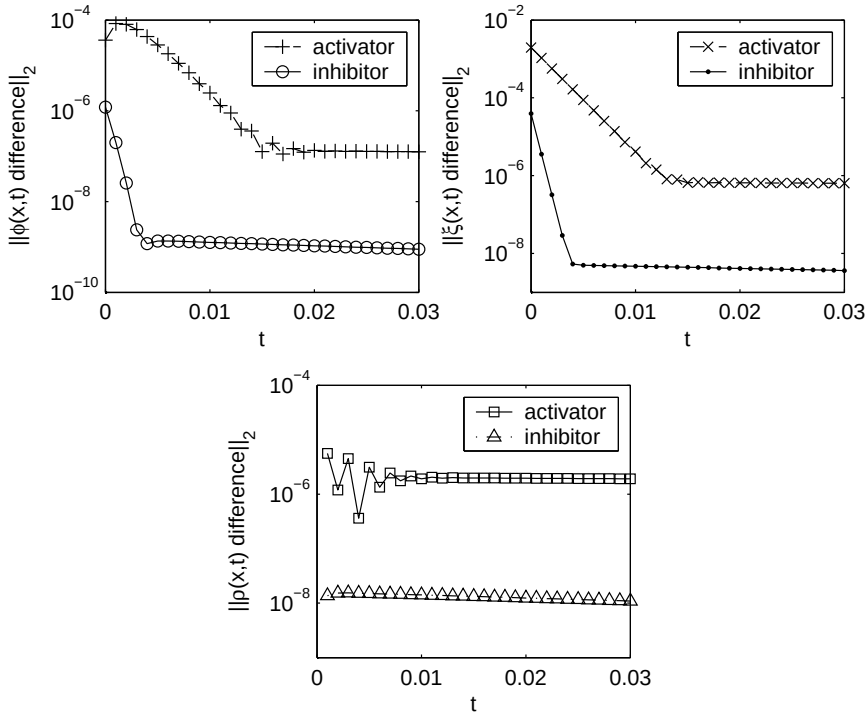


Figure 7.8: Error of the higher order moments $\phi(x,t)$ and $\xi(x,t)$ (top) and the density $\rho(x,t)$ (bottom) during time simulation with the FHN LBM started from the fixed point obtained with Algorithm 6.1. We compare to the LBM trajectory initialized from the "unknown" slaved state $\{\rho^{(0)}, \phi(\rho^{(0)}), \xi(\rho^{(0)})\}$. The starting point in this figure is the end point of Fig. 6.4.

Note that the same phenomenon from Chapter 5 occurs but on a much smaller scale. A slow mode of the solution becomes excited. This changes the macroscopic density and leads to another entry point on the manifold and thus a different transient simulation trajectory. This kick is observed in Fig. 7.8 (bottom) for the activator.

Figure 7.8 (bottom) shows that the density on the manifold for the activator and inhibitor species is respectively 1e-6 and 1e-8 accurate, which is also the accuracy obtained by $\phi(x,t)$ and $\xi(x,t)$ once their respective slaving relations are attained in Fig. 7.8 (top). Afterwards, the evolution follows the slow changes in density on the manifold. Note that this on-manifold state is a few orders more accurate than the CR fixed point we started from (compare Figs. 6.4 and 7.8).

One can check numerically that the slopes of the error curves in the top panel of Fig. 7.8 approximate the value $|1-\omega|$. This can be explained as follows. After CR initialization, the first LBM simulation starts from the given $\rho^{(0)}$ value and fairly — but not entirely — good initial values $\tilde{\phi}$ and $\tilde{\xi}$ for the higher order moments. We compare this to a second LBM evolution started from the "unknown", fully slaved, state $\{\rho^{(0)}, \phi(\rho^{(0)}), \xi(\rho^{(0)})\}$. The initial $\rho^{(0)}$ value is the same but the higher order moments are different, i.e. the initial density gradients are different. Now, if the initial $\rho(x,0) = \rho^{(0)}$ in the LBE (3.9), i.e.

$$f_i(x + c_i\Delta x, t + \Delta t) = (1-\omega) f_i(x,t) + \frac{\omega}{3}\rho(x,t) + \frac{\Delta t}{3} F(\rho(x,t)) \,,$$

is the same, $f_{\pm 1}(x,t)$ or equivalently $\phi(x,t)$ and $\xi(x,t)$ indeed change at a rate $(1-\omega)$ (compare the magnitudes of the density values w.r.t. the higher order moments in Fig. 7.8). This explains the observations made in [175]. Compare these results to the time evolution in Fig. 5.2 (a)–(b) for the less accurate reconstruction schemes with weights (4.1). There, the convergence rate is also $|1-\omega|$.

7.5.5 Constrained Runs with Manifold Reconstruction

In this section, we present a novel type of initialization scheme that combines the regular CR scheme with an additional postprocessing step. The idea is the following [216]. First, we perform regular CR iterations as in Algorithm 6.1 (one could also use a stable extrapolation-based higher order CR scheme). This requires K iterations of length Δt. The resulting fixed point $\phi^{(K)} \approx \tilde{\phi}$ and $\xi^{(K)} \approx \tilde{\xi}$ is an accurate approximation of the slaving relations up to first order terms. Second, we perform a LBM simulation for another K iterations of length Δt starting from the CR fixed point. In Sect. 7.5.4, we argued that these next K iterations bring us down to the slow manifold and thus diminish the error further. Afterwards, evolution

is dictated by the slow evolution on the manifold. Third, we exploit this property and integrate further with the LBM along the manifold for mj time steps. Fourth, from these extra states, we select $m+1$ equidistant points (we skip s points such that $j = s+1$) and interpolate them with a polynomial of degree m to reconstruct the slow manifold locally. We chose a fifth degree interpolating polynomial ($m = 5$). It depends on the problem-specific curvature of the manifold how high the degree of the polynomial should be. Fifth, we extrapolate backward (along the manifold) with this interpolating polynomial over time $-K\Delta t$. This extrapolation results in the state $\{\hat{\rho}, \hat{\phi}, \hat{\xi}\}$. To conclude, we reset the density to the given value $\rho^{(0)}$. The resulting end state $\{\rho^{(0)}, \hat{\phi}, \hat{\xi}\}$ is the initial condition for the LBM simulation "at time zero". Note that the postprocessing step can be repeated a few times r to get even more accurate results (see the comments below). The above steps are summarized in Algorithm 7.3.

Algorithm 7.3 Constrained runs scheme with additional manifold reconstruction for diffusive LBM

Require: $\rho^{(0)} = \rho(x,0)$ and a user-defined tolerance $\theta \ll 1$

$f_i^{(0)} = w_i\,\rho^{(0)}$; $\sum_i w_i = 1$, e.g. $w_i = \nu_i = 1/3$ — Choose $f_i^{(0)}$

$\boldsymbol{\varrho}^{(0)} = M\mathbf{f}^{(0)}$ — Equivalent moments

repeat

  $\boldsymbol{\varrho}^{(k+1)} = M\big(\mathrm{LBM}_{\Delta t}(M^{-1}\,\boldsymbol{\varrho}^{(k)})\big)$ — LBM simulation over time Δt

  $\rho^{(k+1)} = \rho^{(0)}$ — Reset macroscopic variables

until convergence heuristic $< \theta$

$K = k+1$ — Obtain the number of constrained iterations

$\phi^{(0)} = \phi^{(K)}$, $\xi^{(0)} = \xi^{(K)}$ — (Approximation of) CR fixed point $\tilde{\phi}, \tilde{\xi}$

$m = 5$ — Choose polynomial degree m

$s = 4$, $j = s+1$ — Choose number of skipped states s

repeat

  $k = 0$

  repeat

    $\boldsymbol{\varrho}^{(k+1)} = M\big(\mathrm{LBM}_{\Delta t}(M^{-1}\,\boldsymbol{\varrho}^{(k)})\big)$ — LBM simulation over $(K+mj)\Delta t$

  until $k+1 = K+mj$

  $\zeta = -K$

  $b_0 = (120j^5 - 274\zeta j^4 + 225\zeta^2 j^3 - 85\zeta^3 j^2 + 15\zeta^4 j - \zeta^5)/(120j^5)$

  $b_1 = \ldots, \ldots, b_m = \ldots$ — Compute polynomial coefficients

  $\hat{\boldsymbol{\varrho}} = b_0\boldsymbol{\varrho}^{(2K)} + b_1\boldsymbol{\varrho}^{(2K+j)} + \ldots + b_m\boldsymbol{\varrho}^{(2K+mj)}$ — Extrapolate

  $\rho = \rho^{(0)}$ — Reset density

  $\phi^{(0)} = \hat{\phi}$, $\xi^{(0)} = \hat{\xi}$ — Repeat the postprocessing

until current $||\hat{\rho} - \rho^{(0)}||$ > previous $||\hat{\rho} - \rho^{(0)}||$

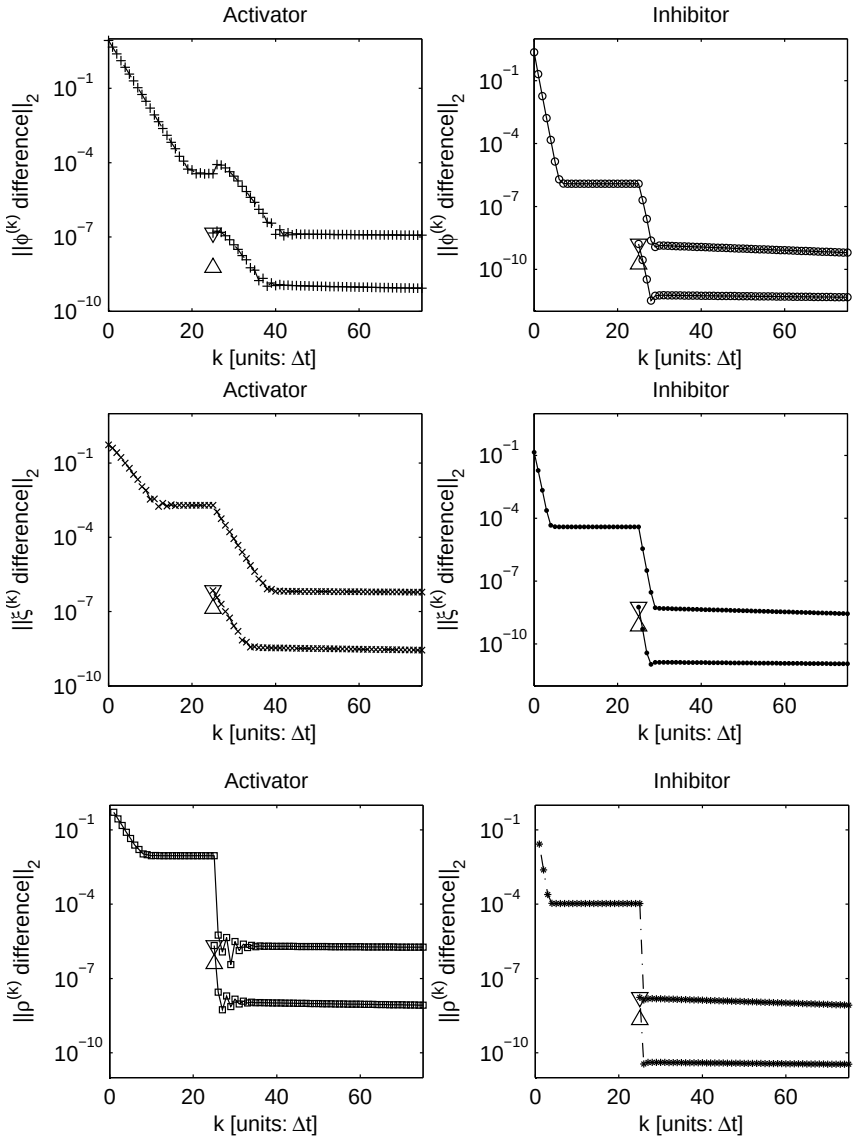


Figure 7.9: Evolution of $\phi^{(k)}$ (top), $\xi^{(k)}$ (middle) and internal density $\rho^{(k)}$ (bottom) in the constrained runs scheme with manifold reconstruction (Algorithm 7.3) for the FHN LBM. The resetting of the density is not shown. The postprocessing step is performed twice. The symbols $\triangledown$ and $\triangle$ denote the results of the first, respectively second extrapolation. Note that the extrapolation (i.e. the manifold reconstruction) is becoming unstable, still the net result is more accurate.

The convergence behavior of the iterated moments $\boldsymbol{\varrho}^{(k)}$ in Algorithm 7.3 for the FHN LBM is shown in Fig. 7.9. During the regular CR phase, the $\phi^{(k)}$ and $\xi^{(k)}$ values are compared to the "unknown" $\phi(\rho^{(0)})$ and $\xi(\rho^{(0)})$ values while the (internal) $\rho^{(k)}$-value simulated upon is compared to the known initial $\rho^{(0)}$. During the subsequent LBM simulation, these values are compared to the values obtained from another time integration from the "unknown" state $\{\rho^{(0)}, \phi(\rho^{(0)}), \xi(\rho^{(0)})\}$ with the same integration parameters. Since we used a time step of Δt in all LBM simulations, we plot the multiple k of Δt on the bottom axis. Again, to better show linear convergence, we started the algorithm with a bad choice for the higher order moments $\phi^{(0)} = -0.74\rho^{(0)}$ and $\xi^{(0)} = 0.38\rho^{(0)}$.

When repeating the postprocessing step, care must be taken since the backward extrapolation is possibly unstable (see Fig. 7.9) and repeated application can cause overall instability. A measure for the accuracy is given by the difference between the backwards projected density $\hat{\rho}$ and the initial density $\rho^{(0)}$. This difference can be used to decide how many times the postprocessing step should be repeated (in our case, the results in Fig. 7.9 suggest that $r = 2$ is sufficient). Also, $\hat{\rho}$ gives an indication of the expected accuracy of $\hat{\phi}$ and $\hat{\xi}$. Since these values are obtained from interpolating slaved on-manifold values, they are approximately slaved also.

Algorithm 7.3 requires $K + r(K + m(s + 1))$ iterations of length Δt, a number that can be large. It depends both on the application and the microscopic model if this is a severe computational burden or not. The scheme could be useful when accurate microscopic simulations in transient regimes are required. In the context of equation-free computing with repeated coarse integrations of length ΔT, the overhead might be too large if ΔT is small.

7.6 Conclusions

In this chapter, we discussed some applications and extensions of the CR scheme from Chapter 6.

First, we implemented the basic CR scheme from Sect. 6.2 as the lifting or reconstruction step in the coarse equation-free time stepper for the LBM and used the latter to perform a time stepper based numerical bifurcation analysis. We showed that the resulting bifurcation diagrams for both steady state and periodic solutions are very accurate when the coarse time step is small (on the order of the healing time).

Second, we extended our stability and convergence analysis for the basic CR scheme from Chapter 6 to the LBMs with distribution dependent reaction terms from Sect. 3.8.2 and Sect. 3.8.3. We concluded that the CR iteration is stable when the underlying LBM is stable. For the D1Q3R mod-

els, we proved that the CR fixed point is again a first order approximation of the corresponding Chapman-Enskog slaving relations.

Third, we implemented a few higher order CR schemes with improved accuracy for our LBM test case. These schemes interpolate the higher order moments while constraining the macroscopic variables. We implemented the first order CR scheme proposed in [64] for our LBM and showed that this scheme can be unstable depending on the LBM parameters. Using an alternative discretization, we implemented a scheme that is stable for a slightly larger range of parameter values. We also proposed a novel scheme with an added postprocessing step that effectively reconstructs the manifold. The latter scheme is much more accurate than the basic CR scheme.

We conclude with the following two remarks. In all our CR experiments, we compared the CR fixed point to the slaved state obtained from a preliminary LBM simulation. As a side effect, this simulation smooths out the fast components in ρ itself. For random $\rho^{(0)}$ values, the gain in accuracy might not be as large as the results for the higher order CR schemes suggest. Note that exactly the same phenomenon occurs when initializing PDEs. Extracting the lower order Fourier modes of $\rho^{(0)}$ might remedy this problem.

In this and the previous chapter, we observed that the CR schemes converge and diverge linearly. In case the CR iteration is unstable, its fixed point is still expected to be well defined as the solution of $(I - A)\boldsymbol{\varphi} = B_{disc}$, where the matrices A and B_{disc} are the blocks of the respective CR Jacobian matrices (e.g. for the regular CR scheme in Algorithm 6.1, this follows from (6.11)). As mentioned in [64], one can compute this fixed point using existing matrix-free algorithms like the Recursive Projection Method [184], the Newton-Picard method [135] or Newton-Krylov type methods like the Generalized Minimal Residual (GMRES) method [171].

Chapter 8

Hybrid Spatial Coupling

8.1 Introduction

As discussed in Chapter 2, a dynamical system can be described by different models, each at another abstraction level. Sometimes, the level of detail required to model the system changes from region to region and different models have to be used on different parts of the domain. Of particular interest are systems where the higher-level description breaks down on a localized part of the domain because there the particle interactions have become so complex that variables absent in the coarse higher-level model become important. Examples are the occurrence of cracks and defects in solids and the viscous fingering phenomena observed in ionized gases [51].

Many hybrid methods that spatially couple a particle-based to a continuum model, have already been well developed. One widely used methodology is Adaptive Mesh and Algorithm Refinement (AMAR) [63], which uses the Adaptive Mesh Refinement (AMR) [15] framework with a particle method (direct simulation Monte Carlo in [63]) at the finest grid and a continuum method (a Navier-Stokes solver) at the coarser grids. Other examples include the quasicontinuum method [183], which combines a global finite element method at the macroscopic level with atomistic computations near defects and dislocations; the hybrid coupling of a random walker and a stochastic PDE [7, 8]; the coupling of a Monte Carlo and finite volume method for capturing shocks [44]; the various coupling strategies for continuum models and molecular dynamics (MD) [49, 84, 126, 127, 153, 154, 225]; the coupling of Boltzmann and Navier-Stokes equations by flux matching [123]; modeling of polymer-solvent dynamics by coupling a LBM for the fluid and MD for the polymer chain [1, 2, 25, 62]; a hybrid LBM/MD model for the flow around a carbon nanotube [46] and the simulation of snow de-

position by a combined LBM and cellular automata model [35]. At the interface between the regions (sometimes called the 'handshaking region'), there will be a mismatch in the kind (and number) of variables used by the different models. There, the variables have to mapped to one another.

In this chapter, we analyze hybrid models obtained by spatially coupling a LBM and the finite difference discretization (FD) of a PDE describing a reaction-diffusion system in different regions of the spatial domain. We are particularly interested in the spatial discretization error of the hybrid model. In [3, 4, 122], Albuquerque *et al.* reported a second order discretization error in space (just like both the discretized PDE and LBM on the full domain). We will study this claim further and derive closed expressions for the error at steady state for some basic problems.

For analysis purposes, we consider only reaction-diffusion problems on a one-dimensional domain. For this setup, the LBM has three times as much variables (the particle distribution functions) as the PDE, which evolves only the particle density. At the interface, densities are obtained as the zeroth order velocity moments (3.3) of the distribution functions. The inverse mapping from the PDE to the LBM domain, i.e. the mapping of less macroscopic fields (here density) to more distribution functions, is not univocal. Here, we will use the property that the LBM variables contain information on the spatial derivatives of the macroscopic variables, because they are linked to the particle velocities. Note that this coupling problem is very similar to the initialization problem studied in Chapters 5, 6 and 7.

We discuss two methods to solve the mapping problem at the interface. The first, analytical method was introduced by Albuquerque *et al.* [3, 4]. They used the Chapman-Enskog expansion to write the missing distribution functions at the hybrid interface as a first order functional of the density variable. We will use the same concept but a different implementation. The second method is a point-wise iterative scheme that approximates the Chapman-Enskog relations numerically. Examples are the CR scheme developed by Gear and Kevrekidis in the context of equation-free computing and the scheme developed by Mei *et al.* [144, 22] in the context of LBM initialization (see Sect. 6.6). Here, we use the former. Recall that the CR scheme performs a series of short microscopic (here LBM) simulations and resets the lowest order velocity moment (density) to its initial value while leaving the higher order moments unchanged. We showed in Chapter 6 that the application of the scheme to the LBM from Sect. 3.2, produces a numerical approximation of the analytical Chapman-Enskog relations that is correct up to first order. The numerical interfacing method is useful when the application of the analytical method is not feasible. However, it is computationally demanding because of the constrained iterations that are needed to compute the value of the unknown distribution functions at the interface. Note that both coupling schemes must be applied in an interme-

diate region where the Chapman-Enskog relations are valid. This will affect the size of the LBM subdomain and may confine the overall efficiency in realistic applications.

The work described in this chapter is a step in the development of efficient methods for hybrid LBM/PDE coupling. In the discussion, we have made some simplifying assumptions. First, we use the same time step and grid spacing for both the LBM and discretized PDE. Using different space-time grids on the sub-domains is an interesting topic of further research. For the time dependent problem, we refer to grid refinement techniques like Adaptive Mesh Refinement [15] for the PDE and the different approaches in [56, 57, 105, 164] for the LBM and to certain implicit [24, 125, 176, 202] or outer explicit [219] time discretization schemes. For the time independent problem, ideas from multigrid [203] for the PDE and [142, 201] for the LBM or iterative methods, like the preconditioned Generalized Method of Residuals [16, 17] or the biconjugate gradient algorithm [224] could be used. Second, we limit ourself to one-dimensional diffusive problems for analysis purposes. Albuquerque, Latt and coworkers already used the Chapman-Enskog based coupling method for two-dimensional diffusion [4] and Poiseuille flow [122]. Finally, we work with LBM and PDE models that are equivalent in the macroscopic limit. Since the macroscopic solution profile is sufficiently smooth on the whole domain, we could have used either the PDE or LBM on the full domain. The coupling of a PDE and a LBM describing distinct dynamical behavior is the subject of further research.

This chapter is organized as follows. In Sect. 8.2, we sketch the hybrid setup and in Sect. 8.3, we present the different coupling schemes. We derive expressions for the steady state discretization error in Sect. 8.4. These theoretical results are verified numerically in Sect. 8.5. Finally, in Sect. 8.6, we summarize the main conclusions.

8.2 Setup

The PDE for one-dimensional reaction-diffusion systems is given by (2.4). This continuous equation is discretized with finite differences (FD) (explicit forward difference in time and central difference in space) to obtain

$$\begin{aligned}\rho(x,t+\Delta t) = \rho(x,t) + \frac{\Delta t\, D}{\Delta x^2}\big(\rho(x+\Delta x,t) - 2\rho(x,t) + \rho(x-\Delta x,t)\big) \\ + \Delta t\, F(\rho(x,t))\ ,\end{aligned} \tag{8.1}$$

with Δx and Δt the corresponding space and time step. It is well known that the discretization error for (8.1) is of first order in time and second order in space (to leading order proportional to $\Delta x^2 \partial^4\rho/\partial x^4$). Note that this

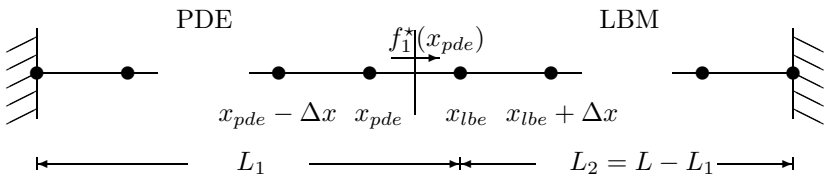


Figure 8.1: Spatial coupling of the PDE (left) and LBM (right) on a one-dimensional domain. The interface lies in between two lattice sites.

discretization typically entails a stability condition of the form $\Delta t \leq C\Delta x^2$, e.g. for pure diffusion, the constant C equals $1/(2D)$.

The corresponding LBM is described in Sect. 3.2 and its state is fully described by the slaving relations (3.26)–(3.28) derived from the Chapman-Enskog expansion. As discussed in Chapter 6, these relations can be approximated numerically by the CR scheme. Its fixed point in moment space $\{(\rho^{(0)}), \tilde{\phi}, \tilde{\xi}\}$ can also be written in terms of distribution functions as $\{\tilde{f}_{-1}, \tilde{f}_0, \tilde{f}_1\}$ using (3.25) and is given by (6.33). It is shown in [102] that the LBM discretization error is second order accurate in space.

In our spatial coupling setup shown in Fig. 8.1, the one-dimensional domain with length L is split into two non-overlapping sublattices. An alternative using one overlapping lattice site is presented in [3, 4] and will be briefly discussed in Sect. 8.5. The PDE is applied to the left sublattice and the LBM to the right sublattice. The coordinate of the first LBM lattice point is defined as $x_{lbe} = L_1$, such that the interface lies in between x_{pde} and x_{lbe} at $L_1 - \Delta x/2$. For analysis purposes, we use the same lattice spacing Δx and time step Δt for the PDE and LBM, i.e. the simplest coupled space-time lattice.

Since the PDE and LBM use a different set of variables, namely ρ versus $\mathbf{f} = [f_{-1}\, f_0\, f_1]'$, information should be exchanged carefully at the interface during time simulation. To evolve the PDE in x_{pde}, the value $\rho(x_{lbe}, t) = \rho(x_{pde} + \Delta x, t)$ is needed in (8.1). This value is computed from the LBM variables $f_i(x_{lbe}, t)$ using (3.3). The inverse problem is more difficult. We need to map a single density value onto three corresponding distributions, i.e. $\rho(x_{pde}, t) \mapsto f_i(x_{pde}, t)$ for $i \in \{-1, 0, 1\}$. Since (3.3) should hold, this leaves two degrees of freedom. In fact, we need only the value of $f_1(x_{pde}, t)$ that propagates into the LBM subdomain (see Fig. 8.1) to evolve the LBE (3.9) in x_{lbe} from t to $t + \Delta t$. We will use the analytical slaving relations (3.27)–(3.28) or the numerical approximation (6.33) by the CR scheme to derive the distributions at the interface. In the next section we discuss both strategies.

8.3 Implementation

8.3.1 Using Chapman-Enskog Slaving Relations

The key observation is that the PDE (8.1) simulates "directly" from t to $t + \Delta t$, while the LBE (3.9) executes in two phases: first, collisions and reactions to go from t to $t^\star$ and secondly, propagation of the post-collision distributions $f_i^\star$ to get from $t^\star$ to $t + \Delta t$. Thus we actually need the post-collision value $f_1^\star(x_{pde}, t^\star)$ rather than the value $f_1(x_{pde}, t)$.

We first reconstruct $f_1(x_{pde}, t)$ from the PDE density using the Chapman-Enskog relations up to first order (3.27) as in [3, 4]

$$\begin{aligned} f_1(x_{pde}, t) &= f_1^{[0]}(x_{pde}, t) + f_1^{[1]}(x_{pde}, t) \\ &= \frac{1}{3}\rho(x_{pde}, t) - \frac{\Delta x}{3\,\omega}\,\frac{\rho(x_{lbe}, t) - \rho(x_{pde} - \Delta x, t)}{2\Delta x}\ , \end{aligned} \tag{8.2}$$

where the continuous derivative $\partial\rho(x_{pde}, t)/\partial x$ is discretized with central differences (cf. Sect. 3.4). The value $\rho(x_{lbe}, t)$ is obtained from the LBM domain using (3.3).

Afterwards, the corresponding post-collision value $f_1^\star(x_{pde}, t^\star)$ is computed from (8.2) using the LBE:

$$f_1^\star(x_{pde}, t^\star) = (1-\omega) f_1(x_{pde}, t) + \frac{\omega}{3}\rho(x_{pde}, t) + \frac{\Delta t}{3} F(\rho(x_{pde}, t))\ . \tag{8.3}$$

Finally, it is this value that is propagated to x_{lbe}, i.e.

$$f_1(x_{lbe}, t + \Delta t) = f_1^\star(x_{pde}, t^\star)\ . \tag{8.4}$$

From now on, we will refer to (8.2)–(8.4) as the CE-1 coupling scheme. Note that the outgoing post-collision value $f_{-1}^\star(x_{lbe}, t^\star)$ that enters the PDE domain is never used.

Below, we define variants of the above coupling scheme using additional or fewer terms in the Chapman-Enskog expansion. By adding the term $f_1^{[2]}(x_{pde}, t)$ (3.28) (after appropriate discretization with central finite differences), i.e.

$$f_1^{[2]}(x_{pde}, t) = -\frac{(\omega - 2)}{18\omega^2}\big(\rho(x_{lbe}, t) - 2\rho(x_{pde}, t) + \rho(x_{pde} - \Delta x, t)\big)\ , \tag{8.5}$$

to (8.2), we have a second order local coupling scheme (denoted by CE-2). For reasons of comparison only, we also construct a locally zeroth order coupling scheme (CE-0) by replacing (8.2) with

$$f_1(x_{pde}, t) = f_1^{[0]}(x_{pde}, t) = \frac{1}{3}\rho(x_{pde}, t)\ . \tag{8.6}$$

In both cases, we proceed afterwards with (8.3) and (8.4) as above.

For the above reconstruction schemes, the local error at the interface is defined as the dominant term left out in the Chapman-Enskog expansion. For example, the CE-1 scheme produces a second order interface error related to $f_1^{[2]}(x_{pde}, t)$ (3.28) in each time step. In Sect. 8.4, we study the propagation of this error throughout the spatial domain.

8.3.2 Using Constrained Runs

As proven in Chapter 6, the CR scheme approximates the Chapman-Enskog slaving relations for the distribution functions up to first order. As an alternative to the procedure from Sect. 8.3.1, we can thus replace (8.2) with Algorithm 6.1 and apply (8.3) and (8.4) to the result.

Since information in the (explicit) LBE (3.9) propagates over only one lattice site in each iteration, Algorithm 6.1 requires initial density values on a sublattice with at least $2K + 1$ lattice sites, symmetrically distributed around x_{pde}, where K is the number of iterations needed for convergence of the CR algorithm. Arbitrary boundary conditions can be used on this sublattice because the boundary information will not have reached x_{pde} within K iterations.

Alternatively, one can drop the outer lattice sites (and distribution functions) during propagation in each iteration to obtain a *funneled* scheme. Here we keep only the information streaming towards x_{pde}. Again it is important that there are at least $2K+1$ initial sites, symmetrically positioned around x_{pde}. Note that this funneled scheme decreases the amount of work with a factor two. On the other hand, this implementation requires changes to the propagation step of the LBE in Algorithm 6.1, which may not be desirable.

The number of constrained runs K can be obtained a-priori by a preliminary simulation on (part of) the domain with Algorithm 6.1 to observe its convergence (see Chapter 6 and specifically Fig. 6.5). The amount of work needed by the CR scheme is $\mathcal{O}(K^2)$ lattice site updates. This can be an expensive overhead since the scheme has to be used in between each time step Δt. Of course, for situations where the analytical slaving relations (8.2) are unknown or difficult to obtain analytically, it is the only alternative.

8.4 Error Analysis at Steady State

In this section, we derive closed expressions for the global spatial discretization error $E(x)$ of the hybrid steady state solution $\rho(x)$ defined by

$$\rho(x) = \rho^c(x) + E(x) \,, \tag{8.7}$$

with $\rho^c(x)$ the exact steady state solution of the continuous PDE (2.4). In Sect. 8.4.1 and Sect. 8.4.2 we study CE-0 respectively CE-1 coupling. As the coupling with CR is also first order correct at the interface, the expressions in Sect. 8.4.2 will hold approximately. We use an appropriate example for each section. For CE-0 coupling, we consider pure diffusion. For CE-1 coupling, we use a reaction-diffusion system with constant reaction term. Both systems are provided with Dirichlet boundary conditions. Since the exact steady state solution of these model problems has zero second (respectively third) and higher order spatial derivatives, we expect that the global error is only related to the first (respectively second) derivative. The local error made in (8.6) respectively (8.2) concerns the same order of spatial derivatives. We discuss the practical use and generalization of these error expressions in Sect. 8.4.3. Finally, in Sect. 8.4.4, we study how the CE-1 results can be extended to a non-linear system.

8.4.1 CE-0 Coupling and Pure Diffusion

Consider the purely diffusive system defined by (2.4) with $F(\rho(x,t)) = 0$ and Dirichlet boundary conditions. The evolution of density over one time step in the point x_{lbe} closest to the interface in the LBM domain (see Fig. 8.1) is obtained by summing (3.9) or (3.30) over all distributions

$$\begin{aligned}\rho(x_{lbe}, t+\Delta t) = (1-\omega)\big(f_1(x_{pde},t) + f_0(x_{lbe},t) + f_{-1}(x_{lbe}+\Delta x,t)\big) \\ + \frac{\omega}{3}\big(\rho(x_{pde},t) + \rho(x_{lbe},t) + \rho(x_{lbe}+\Delta x,t)\big)\ .\end{aligned} \tag{8.8}$$

Here, $f_1(x_{pde},t)$ has the value (8.6).

The steady state solution $\rho^c(x)$ of (2.4) is a straight line connecting the boundary values. Second and higher order spatial derivatives of the solution (both exact and hybrid) are zero. As a consequence, the distributions on the LBM domain can be written as functionals up to first order in ρ (3.26)–(3.27). Substitution in (8.8) leads to

$$\begin{aligned}\rho(x_{lbe}, t+\Delta t) = \frac{1}{3}\big(\rho(x_{pde},t) + \rho(x_{lbe},t) + \rho(x_{lbe}+\Delta x,t)\big) \\ + (1-\omega)\frac{\Delta x}{3\omega}\frac{\partial\rho(x_{lbe}+\Delta x,t)}{\partial x}\ .\end{aligned} \tag{8.9}$$

At steady state, we have $\partial\rho(x,t)/\partial t = 0$ and $\rho(x_{lbe}, t+\Delta t) = \rho(x_{lbe},t) = \rho(x_{lbe})$. Equation (8.9) reduces to

$$0 = \rho(x_{pde}) - 2\rho(x_{lbe}) + \rho(x_{lbe}+\Delta x) + (1-\omega)\frac{\Delta x}{\omega}\frac{\mathrm{d}\rho(x_{lbe}+\Delta x)}{\mathrm{d}x}\ . \tag{8.10}$$

For this model problem, (8.1) holds exactly for (discretized) $\rho^c(x)$ because the FD spatial discretization error is zero (see Sect. 8.2). We subtract

(8.1) at steady state with $F(\rho^c(x)) = 0$ from (8.10) to obtain

$$0 = E(x_{pde}) - 2E(x_{lbe}) + E(x_{lbe} + \Delta x) + (1-\omega)\frac{\Delta x}{\omega}\frac{\mathrm{d}\rho(x_{lbe} + \Delta x)}{\mathrm{d}x} \ . \quad (8.11)$$

To obtain derivatives of the exact instead of the hybrid solution, we substitute (8.7) into (8.11) and get

$$\begin{aligned} 0 = {} & 2\omega E(x_{pde}) - (1+3\omega)E(x_{lbe}) + 2\omega E(x_{lbe} + \Delta x) \\ & + (1-\omega)E(x_{lbe} + 2\Delta x) + (1-\omega)2\Delta x \frac{\mathrm{d}\rho^c(x_{lbe} + \Delta x)}{\mathrm{d}x} \ , \end{aligned} \quad (8.12)$$

where we discretized $\mathrm{d}E(x_{lbe} + \Delta x)/\mathrm{d}x$ with central differences around lattice site $x_{lbe} + \Delta x$.

Away from the interface, inside the LBM domain, i.e. away from the instantaneous local error source at x_{pde} induced by (8.6), the incoming $f_1(x - \Delta x)$ is described by (3.26)–(3.27). Using the same reasoning that brought us from (8.8) to (8.10), we obtain the following equation for $\rho(x)$

$$\begin{aligned} 0 = {} & \rho(x - \Delta x) - 2\rho(x) + \rho(x + \Delta x) \\ & + (1-\omega)\frac{\Delta x}{\omega}\left(\frac{\mathrm{d}\rho(x + \Delta x)}{\mathrm{d}x} - \frac{\mathrm{d}\rho(x - \Delta x)}{\mathrm{d}x}\right) \ . \end{aligned} \quad (8.13)$$

Since the exact $\rho^c(x)$ is analytic on the whole domain and since $E(x)$ is analytic away from x_{lbe}, we use central differences for their derivatives on the LBM domain as follows

$$\frac{\mathrm{d}\{\rho^c, E\}(x + \Delta x)}{\mathrm{d}x} - \frac{\mathrm{d}\{\rho^c, E\}(x - \Delta x)}{\mathrm{d}x} = 2\Delta x \frac{\mathrm{d}^2\{\rho^c, E\}(x)}{\mathrm{d}x^2} \ . \quad (8.14)$$

Subtracting (8.1) at steady state from (8.13) and substituting (8.7) and (8.14), we obtain

$$0 = E(x - \Delta x) - 2E(x) + E(x + \Delta x) + (1-\omega)\frac{2\Delta x^2}{\omega}\frac{\mathrm{d}^2 E(x)}{\mathrm{d}x^2} \ , \quad (8.15)$$

where the term proportional to $\mathrm{d}^2\rho^c(x)/\mathrm{d}x^2 = 0$ cancels because (2.4) holds for ρ^c. From (8.15) it follows that the global error on the LBM domain is a solution of

$$0 = E(x - \Delta x) - 2E(x) + E(x + \Delta x) \ , \quad (8.16)$$

which means the discrete error points lie on a straight line. Using (8.1) and (8.7), it can be checked easily that the same holds on the PDE domain. Call s_1 and s_2 the slopes of the lines on the PDE respectively LBM domain. We then have

$$E(x_{pde}) = E(x_{lbe}) - s_1\Delta x \ , \quad E(x_{lbe} + \Delta x) = E(x_{lbe}) + s_2\Delta x \ . \quad (8.17)$$

Since (8.1) is used up to x_{pde}, the top of this tent-like function lies at x_{lbe}. Furthermore, with Dirichlet boundary conditions, we have $E(0) = 0$ and $E(L) = 0$. The slopes s_1 and s_2 are then related by $s_1 L_1 = -s_2 L_2$ with $L_1 = x_{lbe}$ and $L_2 = L - L_1$. By substituting (8.17) into (8.12), an expression for s_1 can be found.

Putting all of this together, we can conclude that the maximal error is attained at $L_1 = x_{lbe}$ and has the value $E_0 = E(x_{lbe}) = s_1 L_1$, i.e.

$$E_0 = \frac{L_1 L_2}{L_1 + L_2 \omega}(1-\omega)\frac{\mathrm{d}\rho^c(x_{lbe}+\Delta x)}{\mathrm{d}x} \,. \tag{8.18}$$

8.4.2 CE-1 Coupling and Constant Reaction Term

Here, we consider a reaction-diffusion system (2.4) with constant reaction term and Dirichlet boundary conditions. The density in x_{lbe} evolves in each time step as

$$\begin{aligned}\rho(x_{lbe},t+\Delta t) = {}& (1-\omega)\big(f_1(x_{pde},t) + f_0(x_{lbe},t) + f_{-1}(x_{lbe}+\Delta x,t)\big) \\ & + \frac{\omega}{3}\big(\rho(x_{pde},t) + \rho(x_{lbe},t) + \rho(x_{lbe}+\Delta x,t)\big) + \Delta t F(\rho(x_{lbe},t)) \\ & + \frac{\Delta t}{3}\big(F(\rho(x_{pde},t)) - 2F(\rho(x_{lbe},t)) + F(\rho(x_{lbe}+\Delta x,t))\big) \,,\end{aligned} \tag{8.19}$$

where $f_1(x_{pde},t)$ is computed with (8.2). The last line in (8.19) equates to zero because $F(\rho)$ is constant and can be dropped.

The exact steady state solution $\rho^c(x)$ now has a parabolic shape. Third and higher order spatial derivatives of the solution are zero. The distributions on the LBM domain can thus be written as functionals up to second order in ρ (3.26)–(3.28). It can be checked that substitution of (8.2) for $f_1(x_{pde})$ and (3.26)–(3.28) for $f_0(x_{lbe})$ and $f_{-1}(x_{lbe}+\Delta x)$ in (8.19) at steady state results in

$$\begin{aligned}0 = {}& \frac{1}{3}\big(\rho(x_{pde}) - 2\rho(x_{lbe}) + \rho(x_{lbe}+\Delta x)\big) \\ & + (1-\omega)\frac{\Delta x}{3\omega}\left(\frac{\mathrm{d}\rho(x_{lbe}+\Delta x)}{\mathrm{d}x} - \frac{\mathrm{d}\rho(x_{pde})}{\mathrm{d}x}\right) + \Delta t F(\rho(x_{lbe})) \\ & + (1-\omega)\frac{\Delta x^2}{18\omega^2}(\omega-2)\left(2\frac{\mathrm{d}_+^2\rho(x_{lbe})}{\mathrm{d}x^2} - \frac{\mathrm{d}^2\rho(x_{lbe}+\Delta x)}{\mathrm{d}x^2}\right) \,.\end{aligned} \tag{8.20}$$

Note that $\mathrm{d}_+^2\rho(x_{lbe})/\mathrm{d}x^2$ is defined on the LBM domain only (the hybrid $\rho(x)$ is non-differentiable at x_{lbe} and right hand differences should be used when discretizing).

As in Sect. 8.4.1, the FD spatial discretization error of (8.1) is zero because all higher-than-second derivatives are zero. Consequently, (8.1) holds exactly for $\rho^c(x)$. Multiplying this expression by 1/3 and subtracting the result from (8.20), we obtain the following for the error at steady state

$$\begin{aligned} 0 = {} & \frac{1}{3}\big(E(x_{pde}) - 2E(x_{lbe}) + E(x_{lbe}+\Delta x)\big) + \Delta t F(\rho(x_{lbe})) \\ & - \frac{\Delta x^2}{3D} F(\rho^c(x_{lbe})) + (1-\omega)\frac{\Delta x}{3\omega}\left(\frac{\mathrm{d}\rho(x_{lbe}+\Delta x)}{\mathrm{d}x} - \frac{\mathrm{d}\rho(x_{pde})}{\mathrm{d}x}\right) \\ & + (1-\omega)\frac{\Delta x^2}{18\omega^2}(\omega-2)\left(2\frac{\mathrm{d}_+^2\rho(x_{lbe})}{\mathrm{d}x^2} - \frac{\mathrm{d}^2\rho(x_{lbe}+\Delta x)}{\mathrm{d}x^2}\right) . \end{aligned} \tag{8.21}$$

We now substitute (8.7) into (8.21). Since $\rho^c(x)$ is analytic on the whole domain, we can use (8.14) around x_{lbe} for its derivatives. As the reaction terms are independent of ρ for our model problem, they both cancel with (8.14) in (8.21) because (2.4) holds for ρ^c. By contrast, we cannot use (8.14) around x_{lbe} for the derivatives of $E(x)$ because we expect $E(x)$ to be non-differentiable at x_{lbe}. Instead, we discretize $\mathrm{d}E(x_{lbe}+\Delta x)/\mathrm{d}x$ and $\mathrm{d}E(x_{pde})/\mathrm{d}x$ separately with central differences around $x_{lbe}+\Delta x$ and x_{pde}. We then obtain a relation in terms of derivatives of the exact solution

$$\begin{aligned} 0 = {} & (1-\omega)E(x_{pde}-\Delta x) + 2\omega E(x_{pde}) - 2(1+\omega)E(x_{lbe}) \\ & + 2\omega E(x_{lbe}+\Delta x) + (1-\omega)E(x_{lbe}+2\Delta x) \\ & + (1-\omega)\frac{\Delta x^2}{3\omega}(\omega-2)\left(2\frac{\mathrm{d}^2\rho^c(x_{lbe})}{\mathrm{d}x^2} - \frac{\mathrm{d}^2\rho^c(x_{lbe}+\Delta x)}{\mathrm{d}x^2}\right) \\ & + (1-\omega)\frac{\Delta x^2}{3\omega}(\omega-2)\left(2\frac{\mathrm{d}_+^2E(x_{lbe})}{\mathrm{d}x^2} - \frac{\mathrm{d}^2E(x_{lbe}+\Delta x)}{\mathrm{d}x^2}\right) . \end{aligned} \tag{8.22}$$

Away from the interface, there is no instantaneous local error contribution (8.2) and the incoming $f_1(x-\Delta x)$ can be written as (3.26)–(3.28). Inside the LBM domain, we have an equation for $\rho(x)$ very similar to (8.20), except that it has a contribution

$$-(1-\omega)\frac{\Delta x^2}{18\omega^2}(\omega-2)\left(\frac{\mathrm{d}^2\rho(x-\Delta x)}{\mathrm{d}x^2} - 2\frac{\mathrm{d}^2\rho(x)}{\mathrm{d}x^2} + \frac{\mathrm{d}^2\rho(x+\Delta x)}{\mathrm{d}x^2}\right) , \tag{8.23}$$

instead of just the last two terms in (8.20). In (8.23), the terms between brackets can be replaced by the shorthand $\Delta x^2 \mathrm{d}^4\rho(x)/\mathrm{d}x^4$. When substituting (8.7) into (8.23), we get a term proportional to $\mathrm{d}^4\rho^c(x)/\mathrm{d}x^4 = 0$ and one proportional to $\mathrm{d}^4E(x)/\mathrm{d}x^4$. The latter is explicitly presumed to be negligible here. Skipping a few steps elaborated on previously, we find that, except for x_{lbe}, the global error $E(x)$ on both the LBM and PDE domain is a solution of (8.16). Again, we obtain a tent-shaped error function with

top at x_{lbe} and the relation $s_1 L_1 = -s_2 L_2$ between the slopes s_1 and s_2. By substituting (8.17) into (8.22), an expression for s_1 can be found. Because $E(x)$ is piecewise linear, its second derivatives are zero and the last term in (8.22) cancels. The maximal error is attained at $L_1 = x_{lbe}$ and has the value $E_1 = E(x_{lbe}) = s_1 L_1$

$$E_1 = \frac{L_1 L_2}{L}(1-\omega)\frac{\Delta x}{6\omega}(\omega-2)\left(2\frac{\mathrm{d}^2\rho^c(x_{lbe})}{\mathrm{d}x^2} - \frac{\mathrm{d}^2\rho^c(x_{lbe}+\Delta x)}{\mathrm{d}x^2}\right) . \quad (8.24)$$

8.4.3 Discussion

When ω is kept constant, the global steady state error (8.18) of the CE-0 scheme remains constant as Δx decreases; i.e. it is of zeroth order in Δx. This is opposed to the instantaneous local error made in each time step that is of first order (cf. Sect. 8.3.1). Similarly, the global error (8.24) of the CE-1 scheme is of first order in Δx for constant ω, while the local error is of second order. In this chapter, we will not derive a closed expression for the error of the CE-2 coupling scheme, but we verify numerically in Fig. 8.6 (left) that using the CE-2 coupling scheme (with a third order local error) also leads to an accuracy loss of one order, i.e. we obtain a second order global error. We also show in Sect. 8.5 that the results with the CE-1 scheme are sufficiently accurate for practical computations.

By substituting (8.17) into (8.11) instead of (8.12) we can obtain an alternate expression for E_0 in terms of the derivative of the hybrid solution

$$E_0 = \frac{L_1 L_2}{L}(1-\omega)\frac{1}{\omega}\frac{\mathrm{d}\rho(x_{lbe}+\Delta x)}{\mathrm{d}x} . \quad (8.25)$$

For CE-1 coupling, the derivatives in (8.24) can be replaced by those of the hybrid density also because $E(x)$ is piecewise linear (compare (8.21) and (8.22)). Such expressions are more practical than (8.18) and (8.24) to compute the a-posteriori error of the hybrid system. As $\rho^c(x) = \rho(x) - E(x)$, the $E(x)$ values could even be used to correct the hybrid solution.

In the above accuracy analysis, we studied the propagation of a highly localized error in space and its influence on the global error on the full domain. We focused on LB/FD hybrid models, but the problem is more general. Loosely stated, we solve the following continuous point source equation for the global steady state error $E(x)$

$$\frac{\mathrm{d}^2 E(x)}{\mathrm{d}x^2} + \tilde{F}(E(x)) = A\Delta x^p \delta(x - x_{lbe}) , \quad (8.26)$$

where $\tilde{F}(E(x))$ is a problem-specific force term; the power p is determined by the coupling scheme and the Dirac delta function $\delta(x - x_{lbe})$ represents the

localized error source at the interface x_{lbe}. The amplitude A is also problem-specific and contains derivatives of the solution around x_{lbe}. Equation (8.26) can be retrieved from the combination of (8.11) and (8.16) for CE-0 coupling and (8.22)–(8.16) for CE-1 coupling.

8.4.4 CE-1 Coupling and Non-Linear Reaction Term

In this section, we study how the results from Sect. 8.4.2 extend to reaction-diffusion systems with a reaction term that is non-linear in ρ. The Fisher equation (2.4) with reaction term $F(\rho) = \alpha\rho(1-\rho)$, $\alpha \in \mathbb{R}$ and Dirichlet boundary conditions serves as our model problem.

Again, we focus on the interface first. The evolution of $\rho(x_{lbe}, t)$ in one time step is still described by (8.19) with $f_1(x_{pde}, t)$ given by (8.2). However, the last line in (8.19) cannot be dropped.

Because of the non-linearity, higher order spatial derivatives of the solution will be non-zero. This leads to two main approximations. First, substitution of the Chapman-Enskog slaving relations (3.26)–(3.28) up to second order in (8.19) at steady state still leads to (8.20) (including the last line of (8.19)) but (8.20) is now only an approximation. Second, (8.1) will no longer hold exactly for $\rho^c(x)$ because of the now non-zero FD discretization error. Therefore, we redefine $E(x)$ as

$$\rho(x) = \rho^{FD}(x) + E(x) \,, \tag{8.27}$$

with $\rho^{FD}(x)$ the FD solution of (8.1). We then subtract (8.1) from (8.20) to obtain equation (8.21) for $E(x)$ defined by (8.27).

We proceed further from (8.21) by substituting (8.27). For the Fisher equation, the dominant force terms in (8.21) result in a contribution

$$\left(\Delta t - \frac{\Delta x^2}{3D}\right) F(\rho^{FD}(x_{lbe})) + \Delta t\alpha\big(1-2\rho^{FD}(x_{lbe})\big)E(x_{lbe}) - \Delta t\alpha E^2(x_{lbe}) \,. \tag{8.28}$$

As in Sect. 8.4.2, the first term in (8.28) cancels with (8.14). For practical computations, (8.27) can be substituted in the remainder of (8.28) to obtain an expression that is independent of $\rho^{FD}(x_{lbe})$. The approximate equation for $E(x_{lbe})$ is then given by

$$\begin{aligned} 0 = {} & (1-\omega)E(x_{pde}-\Delta x) + 2\omega E(x_{pde}) - 2(1+\omega)E(x_{lbe}) \\ & + 2\omega E(x_{lbe}+\Delta x) + (1-\omega)E(x_{lbe}+2\Delta x) \\ & + 6\omega\Delta t\alpha\big(1-2\rho(x_{lbe})\big)E(x_{lbe}) + 6\omega\Delta t\alpha E^2(x_{lbe}) \\ & + 2\omega\Delta t\big(F(\rho(x_{pde})) - 2F(\rho(x_{lbe})) + F(\rho(x_{lbe}+\Delta x))\big) \\ & + (1-\omega)\frac{\Delta x^2}{3\omega}(\omega-2)\left(2\frac{\mathrm{d}_+^2\rho(x_{lbe})}{\mathrm{d}x^2} - \frac{\mathrm{d}^2\rho(x_{lbe}+\Delta x)}{\mathrm{d}x^2}\right), \end{aligned} \tag{8.29}$$

where we kept the last line in terms of hybrid derivatives for computational purpose (we want to compute the a-posteriori error).

Away from the interface inside the LBM domain, $E(x)$ is an approximate solution of (8.29) without the last line. Alternatively, we can use (8.14) for the first derivatives of $E(x)$ and find that $E(x)$ is the solution of

$$0 = (2-\omega)\big(E(x-\Delta x) - 2E(x) + E(x+\Delta x)\big) + 3\omega\Delta t\alpha\big(1-2\rho(x)\big)E(x) + 3\omega\Delta t\alpha E^2(x) + \omega\Delta t\big(F(\rho(x-\Delta x)) - 2F(\rho(x)) + F(\rho(x+\Delta x))\big)\ . \tag{8.30}$$

On the PDE domain, the hybrid $\rho(x)$ and $\rho^{FD}(x)$ are approximate solutions of (8.1) at steady state (up to the FD discretization error). Subtracting these expressions from each other (and using relation (3.21) between D and ω), we obtain an equation similar to (8.30)

$$0 = \frac{2-\omega}{3\omega}\big(E(x-\Delta x) - 2E(x) + E(x+\Delta x)\big) + \Delta t\alpha\big(1-2\rho(x)\big)E(x) + \Delta t\alpha E^2(x)\ . \tag{8.31}$$

The system, consisting of (8.31) on the PDE subdomain, (8.29) at x_{lbe} and (8.30) on the remainder of the LBM domain, can be solved for $E(x)$ with boundary conditions $E(0) = E(L) = 0$. As a further approximation, the non-linear term $\Delta t\alpha E^2(x)$ can be dropped. Otherwise, Newton's method can be used. In our tests for Example 8.3, the latter had a negligible impact on the result.

8.5 Numerical Results

In this section, we construct the hybrid LB/FD models from Sect. 8.3 for several reaction-diffusion examples with appropriate Dirichlet boundary conditions. For the LBM, the boundary condition is implemented as (6.20). We also compute the spatial discretization error to illustrate the theoretical results from Sect. 8.4.

Example 8.1 (Pure diffusion). *Consider the purely diffusive problem* (2.4) *with* $F(\rho(x,t)) = 0$ *on the one-dimensional domain* $[0, L]$ *with Dirichlet boundary conditions* $\rho(0,t) = 0$, $\rho(L,t) = 1$ *and initial condition* $\rho(x,0) = 0$. *The exact time-dependent solution can be computed as*

$$\rho^c(x,t) = \sum_{n=1}^{\infty}(-1)^n\frac{2}{n\pi}\exp\left(-\frac{Dn^2\pi^2\,t}{L^2}\right)\sin\left(\frac{n\pi\,x}{L}\right) + \frac{x}{L}\ , \tag{8.32}$$

with steady state $\rho^c(x) = x/L$. *The same example was used in [3, 4].*

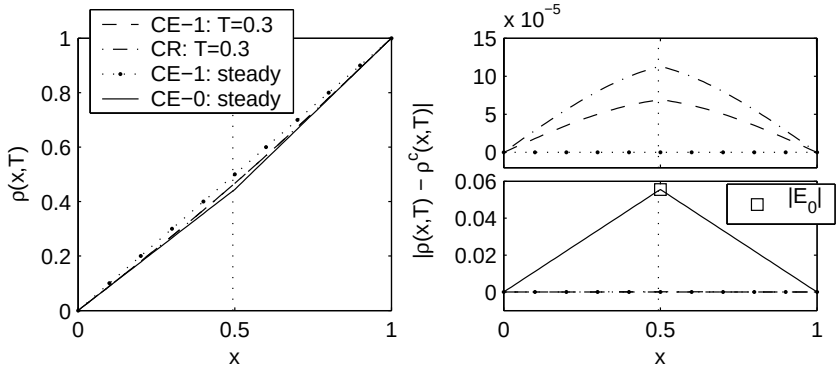


Figure 8.2: Hybrid density (left) and corresponding error (right) with respect to the exact solution at time $t = T = 0.3$ and at steady state for Example 8.1. Results for CE-0, CE-1 and CR coupling are shown. The square marks the theoretical $|E_0|$ value (8.18). Notice the scale difference in the right figures. The dotted line denotes the interface.

In Fig. 8.2, we plot the hybrid density $\rho(x, T)$ (left) and the corresponding error $|\rho(x, T) - \rho^c(x, T)|$ in absolute value (right) for Example 8.1. Results are shown for $t = T = 0.3$ and for $t = T = 10$, where the latter approximates the steady state. Parameters are $D = 1$, $L = 1$, $L_1 = 0.5$ and $K = 10$. The number of lattice points $N = 81$ ($\Delta x = 1/80$) while $\Delta t = 3.125\text{e-}5$ such that $\omega = 1.25$ (3.21). As the steady state in a purely diffusive problem only has a non-zero first derivative, the errors of CE-1 and CR coupling die out as time increases (the latter because (6.33) is proven first order accurate). The fact that CR coupling is a little less accurate than CE-1 coupling can be attributed to the crude approximation of the time derivative in the local error made in (6.33) compared to (3.28).

Observe that coupling with the CE-0 scheme (8.6) results in a tent-shaped error at steady state as predicted in Sect. 8.4.1. This steady state behavior can also be observed in [3, 4]. Its maximal value is attained at $x_{lbe} = L_1$ and can be computed as $\max|\rho(x) - \rho^c(x)| = 0.0555$, which corresponds up to 13 digits to the theoretical value $|E_0|$ from (8.18) and (8.25). It can be checked that this error remains constant as Δx is decreased for constant ω.

Next, we compute the discretization error of the CE-1 coupling scheme for Example 8.1. For an increasing number of discretization points $N = 21$, 41, 81, 161, 321, i.e. for decreasing values of Δx, we compute the hybrid solution at time $T = 0.3$ (away from the steady state) and compare to the exact solution (8.32).

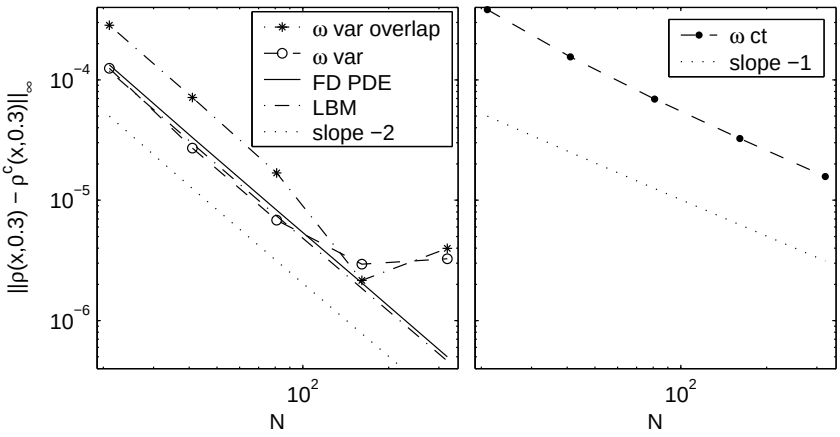


Figure 8.3: Log-log plot of the discretization error at time $T = 0.3$ as a function of N for the hybrid model from Example 8.1 with CE-1 coupling. The hybrid coupling scheme for our setting (constant ω) is only first order accurate in space (right). Results for variable ω, both for the implementation with one overlapping site from Albuquerque *et al.* [3, 4] (labeled ω var overlap) and our implementation from Sect. 8.3 (labeled ω var), are shown to the left, together with the second order behavior of the FD PDE and LBM on the full domain. Dotted lines with slopes -1 and -2 are added for convenience.

Because Δx and Δt are interdependent through ω (3.21), we alter Δt when decreasing Δx along a refinement path of constant ω. We kept $\Delta t/\Delta x^2 = 1/5$ such that $\omega = 1.25$. This way, the hybrid solution relaxes in the same way for each refinement. This is different from the approach taken in [4]. There, the authors fix a very small value of Δt by adjusting the value of ω. In our opinion, this is done to keep only the error contribution in terms of Δx dominant. Note that for small Δt, ω approximates 2, which is not a very interesting simulation regime.

Figure 8.3 (right) shows the maximum (infinity) norm of the discretization error at $T = 0.3$ using CE-1 coupling for our setting (constant ω). Although we have a second order error locally in (8.2), we observe only first order behavior globally as predicted by (8.24). To the left, the error obtained with varying ω (and $\Delta t =$ 1e-7) is shown, both for our implementation and for the implementation from [3, 4] (using one overlapping site and also first order slaving relations (3.27)). The discretization error appears to be second order for the first few refinements, as reported in [3, 4], but for smaller Δx — the case of interest when looking at discretization errors — this is clearly no longer the case. In Fig. 8.6 we will come back to this.

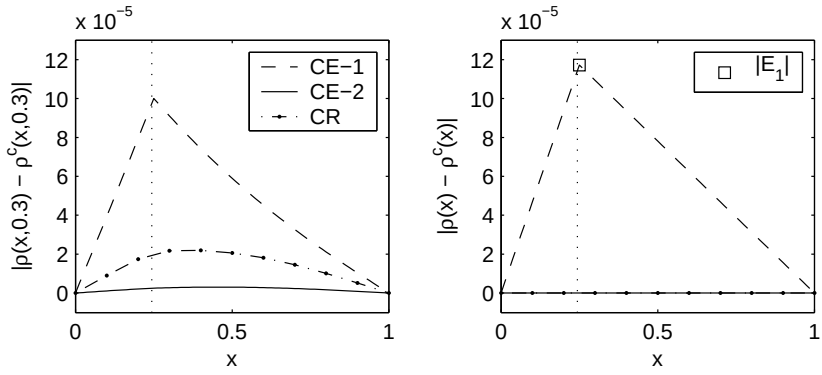


Figure 8.4: Error of the hybrid density w.r.t. the exact solution (8.33) at time $t = T = 0.3$ (left) and at steady state (right) for Example 8.2. The square marks the theoretical $|E_1|$ value (8.24). The dotted line denotes the interface.

For completeness, we also show the (second order) error of both the LBM (with constant ω) and PDE simulated independently on the full domain. As a guide to the eye, dotted lines with slope -2 (left) and -1 (right) are drawn. We observe in the left figure that the use of an overlapping site hardly changes the results. Note that the result with an overlapping site and constant ω is also first order accurate (not shown).

As the steady state for pure diffusion only has a non-zero first derivative, we now turn our attention to an example with a non-zero second derivative to study the steady state error of the CE-1 coupling scheme.

Example 8.2 (Constant reaction term). *Consider a reaction-diffusion system* (2.4) *with constant reaction term* $F(\rho(x,t)) = 2D$. *We impose Dirichlet boundary conditions* $\rho(0,t) = \rho(L,t) = 0$ *and initial condition* $\rho(x,0) = 0$. *The exact solution can be derived as*

$$\rho^c(x,t) = \sum_{n=0}^{\infty} \frac{-8L^2}{(2n+1)^3\pi^3} \exp\left(-\frac{D(2n+1)^2\pi^2\, t}{L^2}\right) \sin\left(\frac{(2n+1)\pi\, x}{L}\right) + x(L-x)\,. \tag{8.33}$$

The steady state solution is $\rho^c(x) = x(L-x)$ *such that* $\mathrm{d}^2\rho^c(x)/\mathrm{d}x^2 = -2$.

Figure 8.4 shows the error of the hybrid solution from Example 8.2 at time $t = T = 0.3$ (left) and at steady state ($T = 10$) (right). Parameters are $D = 1$, $L = 1$, $L_1 = 0.25$, $K = 13$, $\Delta x = 1/80$ and $\Delta t = 3.125\text{e-}5$. In addition to the local coupling with CE-1 and CR, we also implemented

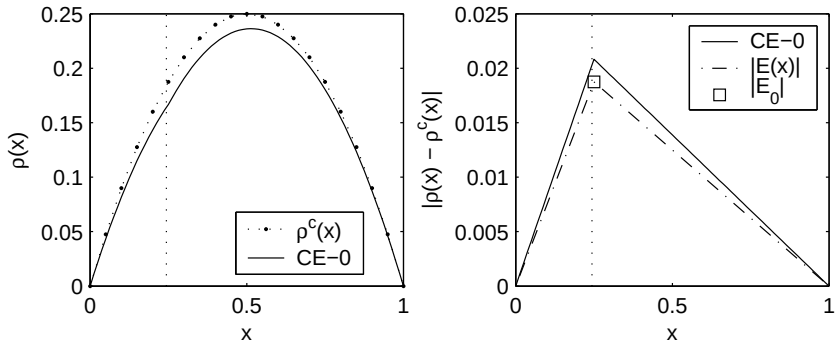


Figure 8.5: Left: Hybrid density $\rho(x)$ at steady state for the CE-0 coupling scheme applied to Example 8.2 compared to the exact solution $\rho^c(x) = x(L-x)$. Right: the corresponding error compared to the theoretical $|E(x)|$ from Sect. 8.4.1.

the second order CE-2 coupling scheme (8.5). A few observations can be made. First, the steady state error for CE-1 coupling behaves as predicted in Sect. 8.4.2, with $|E_1| = 1.172\text{e-}4$. Second, CR coupling is more accurate than CE-1 coupling for this example (compare to Fig. 8.2, where we observed the opposite). This can be explained by comparing (6.33) to (3.26)–(3.28). We see that the CR scheme correctly computes the force term in the second order contribution $f_1^{[2]}(x_{pde}, t)$, which CE-1 coupling obviously does not do. Finally, because the steady state solution for this model problem has non-zero spatial derivatives up to second order only and $\partial\rho/\partial t = 0$ in (3.28) and $\tilde{\rho} - \rho^{(0)} = 0$ in (6.33), the error for both the CE-2 as well as the CR coupling scheme approaches zero as time increases.

As a further illustration of the theoretical results from Sect. 8.4.1 and 8.4.2, we apply the CE-0 hybrid to the system of Example 8.2. The left panel of Fig. 8.5 shows the resulting hybrid steady state density compared to $\rho^c(x) = x(L-x)$. The right panel shows the corresponding error compared to the theoretical $E(x)$ value from Sect. 8.4.1. The deviation w.r.t. $E(x)$ is due to the fact that in Sect. 8.4.1 we neglected the $\mathrm{d}^2\rho(x)/\mathrm{d}x^2$ contributions in the Chapman-Enskog expansion (3.26)–(3.28), which are clearly non-zero in the case of Example 8.2.

In Fig. 8.6, we plot the infinity norm of the discretization error using CE-1 coupling as a function of the number of discretization points N. Again, we choose Δt such that $\omega = 1.25$ for all Δx. Shown left is the steady state discretization error (at $T = 10$) for our setting compared to the expression for the maximum defined by (8.24). The maxima correspond up to at least 13 digits. The global error behavior is again first order in space. Figure 8.6

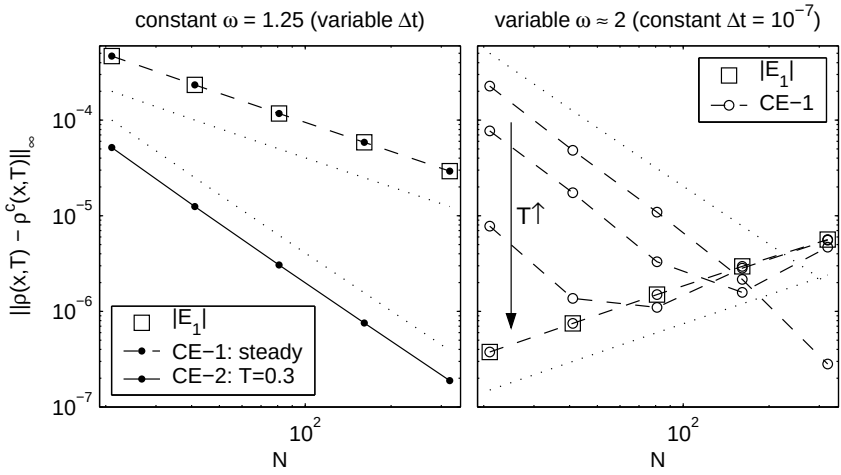


Figure 8.6: Log-log plot of the discretization error of the hybrid model with CE-1 coupling for Example 8.2 w.r.t. N. Left: the steady state error computed with our CE-1 hybrid model as well as the error at $T = 0.3$ for CE-2 coupling. Right: The error for the CE-1 hybrid model with variable ω (and no overlap) at respective times $T = 0.04, 0.3, 0.6$ and 10 (the latter at steady state). It is clear that the initially apparent second order is an artefact. In both figures, expression (8.24) for the maximal CE-1 error is also plotted. Dotted lines with slopes -1, -2 (left) and -2, $+1$ (right) are added as a guide to the eye.

also shows numerically that the global discretization error for CE-2 coupling is of second order when ω is kept constant, which confirms our statement in Sect. 8.4.3. It follows that the global error of the CR scheme *at steady state* is second order also (cf. Sect. 6.4).

The right panel of Fig. 8.6 shows the discretization error of the CE-1 hybrid model with variable ω and constant but small Δt = 1e-7 (for our implementation without overlap). As the simulation time is increased from $T = 0.04$ over $T = 0.3$ and 0.6 to $T = 10$ (the steady state), we see that the apparent second order behavior reported in [3, 4] breaks down and is merely an artefact of the choice for a constant Δt. At steady state the error is proportional to $N = 1/\Delta x$. In this case also, the theoretical E_1 value (8.24) is in excellent accordance with the numerical steady state error.

Example 8.3 (Non-linear system). *Consider the Fisher equation defined by* (2.4) *with* $F(\rho(x,t)) = 50\rho(x,t)(1-\rho(x,t))$. *We apply Dirichlet boundary conditions* $\rho(0,t) = \rho(L,t) = 0$ *and use* $\rho(x,0) = x(L-x)$ *as initial condition. The exact steady state solution is approximated by the PDE*

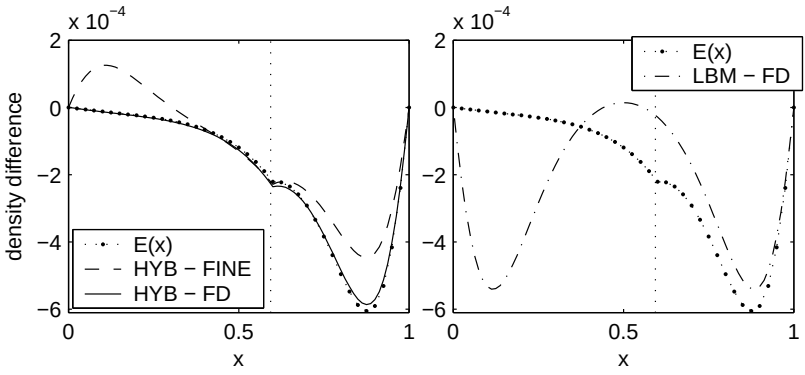


Figure 8.7: Steady state error $E(x)$ of the CE-1 hybrid model for the Fisher Example 8.3 computed as described in Sect. 8.4.4. Also shown to the left: the difference $\rho(x) - \rho^c(x)$, with $\rho^c(x)$ approximated by the FD PDE solution on a very fine lattice (labeled HYB - FINE) and the difference of the hybrid w.r.t. the FD density for $\Delta x = 1/80$ (labeled HYB - FD). To the right, $E(x)$ is compared to the modeling error, i.e. the density difference between the LBM and FD PDE on the full domain for $\Delta x = 1/80$ (labeled LBM - FD). The dotted line denotes the interface.

(or the LBM) solution on the full domain for fine $\Delta x = 1/2560$.

We choose $L_1 = 0.6$ and use the same values as in the previous two examples for the other system parameters. In Fig. 8.7, we plot the steady state error $E(x)$ of the CE-1 hybrid model for Example 8.3, computed numerically from the equations described in Sect. 8.4.4. To the left, we compare $E(x)$ to the density difference of a) the hybrid and "exact" solution and b) the hybrid and PDE solution on the full domain for $\Delta x = 1/80$. To the right, we compare $E(x)$ to a measure for the modeling error, being the difference between the solution of a LBM and PDE simulation on the full domain for $\Delta x = 1/80$.

While the hybrid error is again non-differentiable at $x_{lbe} = L_1$, its maximum is now clearly attained elsewhere due to the non-linearity of the system. Because we had to redefine $E(x)$ to (8.27) in Sect. 8.4.4, the $E(x)$ curve is a better approximation of the error w.r.t. the FD solution for $\Delta x = 1/80$ than w.r.t. the exact solution. If we compare $E(x)$ to the modeling error between LBM and PDE (Fig. 8.7 right), we see that the accuracy of CE-1 coupling is sufficient for practical computations.

Finally, we plot $||\rho(x) - \rho^c(x)||_\infty$ for the CE-1 hybrid model at $T = 10$ (the steady state) in Fig. 8.8. On the bottom axis, we increased the spatial resolution to $N = 1281$. We compare these values to the measure for the

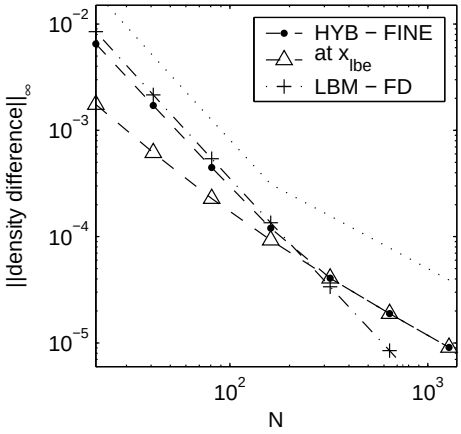


Figure 8.8: Log-log plot of the steady state error of the hybrid model with CE-1 coupling for Example 8.3 w.r.t. N. The labels denote the same as in Fig. 8.7. In addition, the values $|\rho(x_{lbe}) - \rho^c(x_{lbe})|$ are plotted. The dotted lines with slopes -2 and -1 guide the eye.

modeling error defined before and to $|\rho(x_{lbe}) - \rho^c(x_{lbe})|$. Clearly, the second order modeling error is the dominant contribution to the error for values of Δx up to $1/160$. The maxima of the hybrid and modeling error agree reasonably well and are attained at the same positions (see Fig. 8.7). For values of $\Delta x = 1/320$ and smaller (i.e. $N > 161$), the first order contribution (due to the spatial coupling) in the global error becomes predominant and its maximum is attained at the interface x_{lbe} as Fig. 8.8 indicates.

More numerical results for the FHN reaction-diffusion system and the D1Q3R growth-diffusion system from Sect. 3.8.2 can be found in [215].

8.6 Conclusions

In this chapter, we studied the hybrid models obtained by spatially coupling a LBM and a finite difference discretization (FD) of a PDE, each defined on separate regions of the spatial domain. We focused on the analysis of the spatial discretization error of the hybrid models. We limited ourselves to reaction-diffusion systems on a one-dimensional domain.

At the interface between the two models, we have to map the PDE density to more LBM distribution functions. This mapping problem can be solved analytically with relations derived from the Chapman-Enskog expansion, which express the distribution functions as a functional of the density

and its derivatives — an idea first introduced in [3, 4] — or numerically with the iterative constrained runs scheme [68, 64], which approximates these relations numerically up to first order (and up to second order at steady state, cf. Sect. 6.4). The second method is useful when the Chapman-Enskog based relations are unavailable or difficult to obtain analytically, but is computationally much more expensive. At the interface, we used the Chapman-Enskog relations up to zeroth (labeled CE-0), first (CE-1) and second (CE-2) order. The local error at the interface is the dominant term left out in this expansion.

Most importantly, we have shown that the global spatial discretization error of the hybrid model loses one order of accuracy with respect to the local error made at the interface. We derived closed expressions for the global steady state discretization error of the hybrid model for the CE-0 and CE-1 coupling scheme. Furthermore, we have shown how these results can be extended when the reaction term is non-linear by deriving approximate equations from which the steady state error can be computed. The results were verified numerically for several model problems. Our results suggest that the accuracy of the CE-1 scheme is sufficient for most practical computations by factoring in the modeling error between the LBM and PDE. On the other hand, only the use of the CE-2 scheme assures a global second order error behavior.

For analysis purposes, we used the same space and time step Δx and Δt on both sublattices. The focus was on the details of the coupling and how information is exchanged. The use of different Δx and Δt values in both regions optimized to local stability properties would be a further development, see [15, 24, 56, 57, 105, 125, 164, 176, 202, 219] and [16, 17, 142, 201, 203, 224] for guidelines. Also, we used LBM and PDE models that are equivalent in the macroscopic limit. However, we expect that the results can be carried over to LB/FD hybrid models where the submodels describe distinct dynamical behavior. It is important that the interface is situated in an intermediate region where the evolution is described well by both the LBM and PDE such that the relations from the Chapman-Enskog expansion are valid there. Although the error expressions derived in this chapter are clearly problem- and model-specific, we foresee that the global accuracy loss of one order due to a local coupling error will occur in other types of hybrid models also.

Chapter 9

Conclusions

We summarize the main conclusions of the dissertation in Sect. 9.1. Section 9.2 highlights our contributions and provides acknowledgements to those who have helped obtaining the results. Finally, we give some guidelines for further research in Sect. 9.3.

9.1 Main Conclusions

In this thesis, we have addressed several issues in multiscale and equation-free computing with a focus on multiscale interfacing and analysis. The equation-free framework developed by Kevrekidis *et al.* [108] enables an efficient macroscopic time evolution using only a microscopic simulator. An important premise, present in many dynamical systems, is that the properties of interest of the microscopic model can be described by a reduced, but possibly unknown, macroscopic model, either after some time or locally in space. Here, we assume that a separation of time scales exists between the macroscopic variables of interest and the higher order modes derived from the microscopic quantities. Lattice Boltzmann models (LBMs) are so-called mesoscopic models that exhibit such a time scale separation. To analyze the equation-free framework, we used LBMs as a substitute for the microscopic simulator.

First, we focussed on the bifurcation analysis of LBMs. We have shown that methods developed for time stepper based numerical bifurcation analysis of PDEs can be used for the bifurcation analysis of both steady states and periodic solutions of LBMs as well. The time stepper can either be the (deterministic) LBM itself or the coarse equation-free time stepper wrapped around the LBM.

Second, we focussed on the multiscale interfacing problem. Given a few

macroscopic quantities, meaningful values for more microscopic variables have to be derived. This one-to-many mapping problem occurs both when initializing the microscopic model, here the LBM, from the macroscopic observables (in the context of equation-free computing the initialization is called the lifting or reconstruction step) and when spatially coupling the LBM to a macroscopic model, here a PDE.

We have shown that the lifting or reconstruction can have a significant impact on the accuracy and the minimal allowable time step of the coarse time stepper, which contradicted some earlier claims. Although the separation of time scales ensures that the evolution of the state is quickly attracted to a lower dimensional manifold described by the macroscopic variables, the resulting state on the manifold and subsequent transient time trajectory can be quite different from the intended one (i.e. the trajectory described by the PDE started from the same macroscopic initial condition). Therefore, the lifting is the most crucial phase in an equation-free integration. These observations also hold for the initialization of a LBM simulation outside the equation-free framework.

To enable an accurate lifting, Gear *et al.* developed the constrained runs initialization scheme in the context of stiff singularly perturbed ODE systems [68, 64]. The basic constrained runs scheme performs a series of short microscopic simulations and resets the lowest moments of the microscopic variables to the macroscopic initial condition after each run while leaving the higher order moments unchanged. We analyzed the behavior of this scheme for LBMs. We proved that the scheme is unconditionally stable and convergent. The convergence rate is $|1-\omega|$, with ω the BGK relaxation parameter. Most importantly, we have proven that the state converged upon is a first order accurate approximation of the slaved state defined by the Chapman-Enskog relations, i.e. the microscopic state corresponding to the macroscopic initial condition. The approximation error can be expressed analytically as a functional of the error made by resetting the macroscopic variables. We have also implemented higher order constrained runs schemes for the LBM considered that use interpolation techniques to improve accuracy. We have shown that these schemes can become unstable depending on the LBM parameters.

When a LBM is spatially coupled to a discretized PDE, one has the same mapping problem at the interface as with initialization. To compute the LBM variables from the PDE variables at the interface in each time step, we used either the Chapman-Enskog based slaving relations or the constrained runs scheme. The latter scheme is more expensive, but useful when the Chapman-Enskog relations are unavailable or difficult to obtain analytically. Our analysis of the global spatial discretization error of the hybrid model has shown that this error is one order less accurate than the local error made at the interface. However, by factoring in the modeling

error between the LBM and PDE, we have shown that the accuracy of the Chapman-Enskog based coupling using first order relations (with first order global error and second order local error) is sufficient for most practical computations.

9.2 Contributions and Acknowledgements

In Chapter 3, we presented a model problem that is very well suited to study various aspects of the equation-free framework. The model problem is made up of the lattice Boltzmann BGK model for one-dimensional reaction-diffusion systems and has the following advantages. First, the system's state can be unambiguously defined in both "microscopic" and moment space. The relations between both descriptions can be derived from the Chapman-Enskog expansion. The system's evolution is given by either the LBE or by the equations in moment space derived in Sect. 3.5. Second, there exists a separation of time scales between the lower order moments (the macroscopic variables) and the higher order moments. Third, these models are deterministic, which enables a rigorous analysis. To study the effects of a stochastic microscopic model on the equation-free framework, other test cases must be developed.

Chapter 4 presented our results on time stepper based bifurcation analysis for LBMs. We extended the coarse-grained bifurcation analysis for LBMs by Theodoropoulos *et al.* [199] in several ways. First, we computed steady state as well as periodic solutions using the Newton-Picard method [135] instead of the Recursive Projection Method [184]. Second, we compared our results for the PDE and coarse equation-free LBM to the results obtained with the LBM itself. Finally, in Chapter 5, we showed that the lifting can have a significant impact on the accuracy of the coarse equation-free time stepper, which contradicts earlier claims made in [69, 108, 199]. If the lifting is not carefully executed, the minimal coarse time step ΔT must be large. This was joint work with K. Lust (University of Groningen) and I.G. Kevrekidis (Princeton University). These results led to the publications [210, 211, 212].

Because of these lifting issues, Gear and Kevrekidis developed the constrained runs initialization scheme [68, 64] in the context of singularly perturbed ODEs. In Chapter 6, we presented a stability and convergence analysis of the constrained runs scheme in the context of reaction-diffusion LBMs. We showed that the scheme is unconditionally stable and that it converges to a first order accurate approximation of the Chapman-Enskog slaving relations. This chapter was the result of joint work and discussions with W. Vanroose (University of Antwerp) and D. Roose (K.U.Leuven). The proofs in Appendix C are joint work with M. Van Barel (K.U.Leuven). Our re-

search was submitted for publication as [214].

In Chapter 7, we extended the analysis of Chapter 6 to (a simplified version of) the LBMs developed in [222]. Techniques to compute the traveling wave solutions of these LBMs are discussed in [175]. In this chapter, we also implemented some of the higher order constrained runs schemes from [64] for our LBM and showed that the resulting iteration can be unstable. We also presented a novel initialization scheme that reconstructs part of the slow manifold. The research described in this chapter benefitted much from discussions with W. Vanroose and C. Vandekerckhove (K.U.Leuven).

Chapter 8 presented our analysis of the spatial discretization error of the hybrid model obtained by spatially coupling a LBM and the finite difference discretization of a PDE. We showed that the global discretization error of the hybrid model is one order less accurate than the local error made at the interface. This research was published as [215, 213] and was the result of joint work and discussions with C. Vandekerckhove, W. Vanroose and D. Roose.

During his PhD research, the author has also enjoyed collaborations with W. Vanroose [222] and C. Vandekerckhove [219, 220] on work not reported in this manuscript.

9.3 Directions for Future Research

9.3.1 Efficient Lattice Boltzmann Simulations

In this text, we have stressed that an accurate initialization of the LBM is important both in terms of efficiency and accuracy. It allows for the computation of the correct transients and eliminates the unreasonably large simulation times needed to damp any resulting initialization errors (cf. Fig. 5.2). The approach in [189], the constrained runs (CR) schemes [68, 64] (see Chapters 6 and 7) and the scheme in [144] perform accurate initializations.

The efficiency can be increased further by accelerating the LBM simulations in time. Because the time step Δt is coupled to the spatial lattice size Δx through the BGK parameter ω (3.21) and because the value of ω is optimally chosen close to one, the value of Δt must be rather small. Existing acceleration methods for LBMs can be subdivided into two categories: a time dependent and a time independent approach.

In the time dependent approach, i) the LBM time stepper can be combined with different local grid refinement approaches [164, 56, 57, 105]; ii) the body force can be artificially modified during time simulation to accelerate the convergence to steady state [103, 104]; iii) the reactive and diffusive part can be solved for separately by a time splitting technique [5]; iv) certain implicit methods can be used for the more general time depen-

dent discrete Boltzmann equation [24, 125, 176, 202]. As shown in [219], a number of short LBM simulations can also be combined with an outer extrapolation method (in casu the projective integration or multistep state extrapolation method). These methods work on top of the LBM, which potentially enables a combination with most of the acceleration techniques mentioned above.

In the time independent approach, one computes a steady state by equating the time derivative of the distributions $\partial f_i(x,t)/\partial t$ in the Boltzmann equation to zero (but retaining the propagation) and accelerate by i) modifying the BGK equilibrium [82]; ii) using a multigrid approach for the discretized Boltzmann equation [201] or the LBM [142]; iii) solving the time-independent LBM with iterative methods, like the preconditioned Generalized Minimal Residual (GMRES) method [16, 17] or the biconjugate gradient algorithm [224].

9.3.2 Hybrid Spatial Coupling

In Chapter 8, we discussed two methods to couple a LBM to a discretized PDE. One uses the analytical Chapman-Enskog slaving relations as proposed by Albuquerque *et al.* [3, 4], the other, numerical method uses the CR scheme at the interface. We used the same space and time step for both models, because the focus was on the analysis of the spatial discretization error. In realistic applications, these values differ to increase the computational efficiency. Various existing space-time grid coupling techniques (see Sect. 9.3.1) can be adapted for the hybrid LBM/PDE model. Using implicit schemes for the PDE time integration would require Schwarz iterations [170].

In Sect. 3.8, we briefly introduced LBMs with distribution dependent reaction terms used to model the ionization reaction of moving electrons in a molecular gas under the influence of a strong electrical field [222]. This model needs to be extended to more dimensions. In multiple dimensions, the front of moving electrons can locally exhibit very complex behavior, depending on the parameters of the system. This phenomenon is called "fingering". In this region, the PDE model for the ionization front developed in [14] is not valid anymore. The LBM from [222] can be used there, because it allows the incorporation of more complicated physics through the distribution dependent reaction terms. Coupling the two models in space will allow for efficient computations.

9.3.3 Equation-Free Computing

For the coarse-grained bifurcation analysis from Chapter 4, we used the most basic variant of the coarse equation-free time stepper, i.e. we performed

a sequence of consecutive lift-run-restrict cycles of length ΔT within the time interval $[0, T]$. We focussed on the coarse-grained bifurcation analysis and the effects of the lifting and allowed values of ΔT. As mentioned on several occasions already, the efficiency of the coarse time stepper can be increased in time by combining it with techniques like projective integration [65, 66, 124], the multistep state extrapolation method [218, 217] or the acceleration methods described in [47, 50]. The spatial efficiency can be increased by applying gap-tooth or patch dynamics schemes [108, 172, 173, 174]. Studying the behavior of the bifurcation analysis methods when the resulting time stepper is used to integrate the system is an interesting area of further research.

In many realistic applications, the evolution of the microscopic model leads to advection at the macroscopic level. For such systems, an initialization with the CR scheme from Chapter 6 is not accurate enough[1]. Extending our analysis for reaction-diffusion problems to advection-type problems will certainly give guidelines on how to remedy this problem. Computationally, a shift-back of the solution might be necessary, either external to the LBM [166, 175] or internal by modifying the equilibrium [82].

The results in Sect. 7.5 on higher order CR schemes leave much room for further research. First, the convergence/divergence issues need to be investigated more closely. Note that this divergence not only occurs for LBM, but also for stiff ODE systems [235]. The close similarities between equation-free computing and the work of Gorban and Karlin [74, 75, 76, 77] could shed light on this issue. Here, one iterates from a sequence of quasi-equilibrium manifolds to the inertial manifold describing the slow dynamics by monitoring the system's entropy. The CR scheme evolves in a similar way. Starting from a local equilibrium, we iterate towards an approximate manifold that is fully described by (6.29) and (6.32). Starting from the CR fixed point, the LBM simulation brings us down to the invariant slow manifold described by the macroscopic variables. Second, even if the CR iteration is unstable, the fixed point can be computed with matrix-free fixed point methods, e.g. Newton-Krylov based methods like GMRES. Third, the analysis in Chapter 6 and 7 for a LBM should be compared to the analysis in [64] for stiff ODE systems. Here, $(1 - \omega)$ seems closely related to the perturbation parameter. The methodology of the convergence proof in Sect. 6.4 can be extended for the higher order CR schemes from Sect. 7.5 to show that the fixed point of the latter corresponds up to higher order terms to the Chapman-Enskog relations. Finally, we showed in Sect. 6.6 that our analysis of the CR scheme for one-dimensional diffusive LBM with the BGK collision model also holds for the alternative initialization scheme of Mei *et al.* [144]. Most importantly, we showed that the distribution functions (and

[1]The values $\tilde{\rho}$ and $\rho^{(0)}$ will be too far apart in (6.29) and (6.32).

corresponding higher order moments thereof) are only first order accurate, which goes beyond the analysis in [22]. A further comparison for more realistic lattice Boltzmann models (other force terms, two-dimensional D2Q9 model, MRT instead of BGK collisions) would certainly have its merit.

In this dissertation, we focussed on the analysis of the coarse equation-free time stepper using a deterministic model as the "microscopic" model. This enabled a rigorous analysis and brought insight into the behavior of the coarse equation-free time stepper itself (most notably, in the lifting phase). From this point of view, our research can be seen as a fundamental step in the analysis of the equation-free framework. Although historically, the principles of equation-free computing were first illustrated using the FHN LBM example in [69, 108, 199], the equation-free framework has most potential for truly microscopic (and possibly stochastic) models. In the latter context, it has already been applied in a wide range of applications. Examples are individual-based models to describe the dynamics of epidemic diseases [38], bacterial chemotaxis [53, 177], the self-organization of impurities in the presence of system defects [83], micelle formation [111], coupled oscillators [148], reactions on catalytic surfaces [185], the dynamics of liquid crystalline polymers [187], the kinetics of peptide fragments in water [99] and the dynamics of water molecules moving through carbon nanotubes [191]. With so much applications, there is an urgent need for numerical analysis when the microscopic model is stochastic (for model problems, we refer to [72]). We strongly believe that the analysis and issues discussed in this text can aid future analysis of the equation-free framework when truly microscopic models are used.

Appendix A

Third Order Terms

In Sect. 3.3, we derived the third order contribution $f_i^{[3]}$ to the distributions using a classical Chapman-Enskog expansion for the reaction-diffusion LBMs from Sect. 3.2. When computing the momentum $\phi = f_1 - f_{-1}$ from the expansion (3.26) of f_i, we obtain, up to third order,

$$\phi = -\frac{2\Delta x}{3\omega}\frac{\partial \rho}{\partial x} + \frac{\Delta x \Delta t}{3\omega^2}\frac{(-\omega^2 + 4\omega - 2)}{(\omega - 2)}\frac{\partial F(\rho)}{\partial x} + \frac{\Delta x \Delta t}{3\omega^2}\frac{(-\omega^2 + 2\omega - 2)}{(\omega - 2)}\frac{\partial^2 \rho}{\partial x \partial t}. \tag{A.1}$$

Analytically, the time derivative in the last term can be substituted with the help of the PDE (3.20), resulting in the following expression

$$\phi = -\frac{2\Delta x}{3\omega}\frac{\partial \rho}{\partial x} + \frac{\Delta x \Delta t}{3\omega^2}\frac{(-2\omega^2 + 6\omega - 4)}{(\omega - 2)}\frac{\partial F(\rho)}{\partial x} + \frac{\Delta x^3}{9\omega^3}(\omega^2 - 2\omega + 2)\frac{\partial^3 \rho}{\partial x^3}\ . \tag{A.2}$$

It can be checked that this is equivalent to

$$\phi = -\frac{2\Delta x}{3\omega}\left(\frac{\partial \rho}{\partial x} + \frac{\Delta x^2}{6}\frac{\partial^3 \rho}{\partial x^3}\right) + (\ldots)\frac{\partial F(\rho)}{\partial x} + \frac{\Delta x^3}{9\omega^3}(2\omega^2 - 2\omega + 2)\frac{\partial^3 \rho}{\partial x^3}\ , \tag{A.3}$$

where the coefficient of $\partial F(\rho)/\partial x$ remains unchanged. In the first factor between large brackets, one can recognize the second order central finite difference discretization of $\partial \rho/\partial x$ around x_j up to fourth order. Indeed for an arbitrary function $\partial g(x)/\partial x$, we have

$$\frac{g(x_{j+1}) - g(x_{j-1})}{2\Delta x} = \frac{\partial g(x_j)}{\partial x} + \frac{\Delta x^2}{6}\frac{\partial^3 g(x_j)}{\partial x^3} + \mathcal{O}(\Delta x^4)\ . \tag{A.4}$$

When we substitute (A.4) into the first term in (A.3), we obtain

$$\phi = -\frac{2\Delta x}{3\omega}\,\frac{\rho(x_{j+1})-\rho(x_{j-1})}{2\Delta x}+(\ldots)\frac{\partial F(\rho)}{\partial x}+\frac{\Delta x^3}{9\omega^3}(2\omega^2-2\omega+2)\frac{\partial^3\rho}{\partial x^3}\ . \quad \text{(A.5)}$$

Expression (A.5) is correct up to fifth order $\mathcal{O}(\Delta x^5)$.

From a LBM point of view, the continuous derivatives arising from the second order LBM are really a shorthand description of the discrete LBE evolution (the propagation of particles from left and right neighboring lattice sites into the current lattice site x). In Appendix B, we demonstrate how the continuous spatial derivatives $\partial/\partial x$ arise naturally due to propagation as a shorthand for second order central finite difference schemes (see also [100, 101]). By substitution of the shorthand notation

$$\frac{\rho(x_{j+1})-\rho(x_{j-1})}{2\Delta x} = \frac{\partial\rho(x_j)}{\partial x}\ , \quad \text{(A.6)}$$

in (A.5), we can write

$$\phi = -\frac{2\Delta x}{3\omega}\frac{\partial\rho}{\partial x}+\frac{\Delta x\Delta t}{3\omega^2}\frac{(-2\omega^2+6\omega-4)}{(\omega-2)}\frac{\partial F(\rho)}{\partial x}+\frac{\Delta x^3}{9\omega^3}(2\omega^2-2\omega+2)\frac{\partial^3\rho}{\partial x^3}\ . \quad \text{(A.7)}$$

Using the PDE (3.20) again, this is equivalent to

$$\phi = -\frac{2\Delta x}{3\omega}\frac{\partial\rho}{\partial x}+\frac{\Delta x\Delta t}{3\omega^2}\frac{(4\omega-2)}{(\omega-2)}\frac{\partial F(\rho)}{\partial x}+\frac{\Delta x\Delta t}{3\omega^2}\frac{(-2\omega^2+2\omega-2)}{(\omega-2)}\frac{\partial^2\rho}{\partial x\partial t}. \quad \text{(A.8)}$$

The latter expression is the slaving relation for ϕ given in (3.29). Up to fifth order, the analytical expressions (A.7)–(A.8) are completely equivalent to expressions (A.1)–(A.2) as long as the first spatial derivative in (A.7)–(A.8) is implemented as (A.6). Relations (A.1)–(A.2) need to be implemented using an, at least fourth order accurate, finite difference scheme for $\partial\rho/\partial x$.

We conclude by noting that relations (A.7)–(A.8) have an interesting interpretation. Because these relations mimic the nature of the LBE propagation, they are exact in steady state computations. Using the central difference interpretation/implementation for the spatial derivatives, (A.8) reduces to the following at steady state

$$\phi(x_j) = -\frac{1}{3\omega}\big(\rho(x_{j+1})-\rho(x_{j-1})\big)+\frac{\Delta t}{6\omega^2}\frac{(4\omega-2)}{(\omega-2)}\big(F(x_{j+1})-F(x_{j-1})\big). \quad \text{(A.9)}$$

Comparing (A.9) to (B.4), we see that we have obtained a fully discrete version of the slaving relations commensurate with the LBE. Moreover, no discretization errors are made. Upon implementation of (A.9), the — in a sense — "truly discrete" relations are indeed accurate to machine precision, while the "numerical" relations (A.1)–(A.2) at steady state are not.

Appendix B

Evolution Equations in Moment Space: Part 2

B.1 Discrete Evolution Equations for the Moments

In Sect. 3.5, we derived the continuous evolution equations for ρ, ϕ and ξ using a second order Taylor series expansion of (3.30). In Sect. 6.3, we discretized these equations using standard central differences in order to obtain the elements in the corresponding Jacobian matrix. Here, we describe a discrete alternative derived directly from the LBE. The key element is writing the moments after propagation $\boldsymbol{\varrho}(x_j, t + \Delta t)$ as a function of the moments before collisions $\boldsymbol{\varrho}(x_{j-i}, t)$. Away from the boundaries in lattice sites x_j, $j = 2, \ldots, N-1$, the momentum after one LBM time step Δt can be written as

$$\phi(x_j, t + \Delta t) = f_1(x_j, t + \Delta t) - f_{-1}(x_j, t + \Delta t) \tag{B.1}$$

$$= f_1^\star(x_{j-1}, t^\star) - f_{-1}^\star(x_{j+1}, t^\star) \tag{B.2}$$

$$= (1-\omega)\big(f_1(x_{j-1}, t) - f_{-1}(x_{j+1}, t)\big) + \frac{\omega}{3}\big(\rho(x_{j-1}, t) - \rho(x_{j+1}, t)\big) + \frac{\Delta t}{3}\big(F(\rho(x_{j-1}, t)) - F(\rho(x_{j+1}, t))\big) \tag{B.3}$$

$$= \frac{(1-\omega)}{2}\big(\phi(x_{j-1}, t) + \phi(x_{j+1}, t)\big) + (1-\omega)\big(\xi(x_{j-1}, t) - \xi(x_{j+1}, t)\big) + \frac{\omega}{3}\big(\rho(x_{j-1}, t) - \rho(x_{j+1}, t)\big) + \frac{\Delta t}{3}\big(F(\rho(x_{j-1}, t)) - F(\rho(x_{j+1}, t))\big)\,. \tag{B.4}$$

Equation (B.1) is just the definition of momentum after propagation. Propagation of distributions to the neighboring sites according to their velocity direction leads to (B.2). As in Sect. 3.2, $f_i^\star$ denotes the value of the post-collision (or pre-propagation) distribution with velocity c_i. By imposing BGK collisions and reactions as in (3.9), (B.3) is obtained. Rewriting (B.3) as a function of the pre-collision moments using $\mathbf{f} = M^{-1}\boldsymbol{\varrho}$ (3.25), we get (B.4).

The same type of derivation can be done for the energy after one time step, leading to

$$\xi(x_j, t+\Delta t) = \frac{1}{2}\big(f_1(x_j, t+\Delta t) + f_{-1}(x_j, t+\Delta t)\big) \tag{B.5}$$

$$= \frac{1}{2}\big(f_1^\star(x_{j-1}, t^\star) + f_{-1}^\star(x_{j+1}, t^\star)\big) \tag{B.6}$$

$$= \frac{(1-\omega)}{2}\big(f_1(x_{j-1}, t) + f_{-1}(x_{j+1}, t)\big) + \frac{\omega}{6}\big(\rho(x_{j-1}, t) + \rho(x_{j+1}, t)\big) + \frac{\Delta t}{6}\big(F(\rho(x_{j-1}, t)) + F(\rho(x_{j+1}, t))\big) \tag{B.7}$$

$$= \frac{(1-\omega)}{4}\big(\phi(x_{j-1}, t) - \phi(x_{j+1}, t)\big) + \frac{(1-\omega)}{2}\big(\xi(x_{j-1}, t) + \xi(x_{j+1}, t)\big) + \frac{\omega}{6}\big(\rho(x_{j-1}, t) + \rho(x_{j+1}, t)\big) + \frac{\Delta t}{6}\big(F(\rho(x_{j-1}, t)) + F(\rho(x_{j+1}, t))\big)\,. \tag{B.8}$$

Using relations (6.13), it can be seen that (B.4) and (B.8) precisely make up the Jacobian matrix (6.12). Writing (B.4) and (B.8) respectively as

$$\begin{aligned}\phi(x_j, t+\Delta t) &= (1-\omega)\phi(x_j, t) - \frac{2(1-\omega)}{2}\big(\xi(x_{j+1}, t) - \xi(x_{j-1}, t)\big) \\ &+ \frac{(1-\omega)}{2}\big(\phi(x_{j+1}, t) - 2\phi(x_j, t) + \phi(x_{j-1}, t)\big) \\ &- \frac{2\omega}{6}\big(\rho(x_{j+1}, t) - \rho(x_{j-1}, t)\big) - \frac{2\Delta t}{6}\big(F(\rho(x_{j+1}, t)) - F(\rho(x_{j-1}, t))\big),\end{aligned} \tag{B.9}$$

$$\begin{aligned}\xi(x_j, t+\Delta t) &= -\frac{(1-\omega)}{4}\big(\phi(x_{j+1}, t) - \phi(x_{j-1}, t)\big) \\ &+ (1-\omega)\left(\xi(x_j, t) + \frac{1}{2}\big(\xi(x_{j+1}, t) - 2\xi(x_j, t) + \xi(x_{j-1}, t)\big)\right) \\ &+ \frac{\omega}{3}\rho(x_j, t) + \frac{\omega}{6}\big(\rho(x_{j+1}, t) - 2\rho(x_j, t) + \rho(x_{j-1}, t)\big) + \frac{\Delta t}{3}F(\rho(x_j, t)) \\ &+ \frac{\Delta t}{6}\big(F(\rho(x_{j+1}, t)) - 2F(\rho(x_j, t)) + F(\rho(x_{j-1}, t))\big)\,,\end{aligned} \tag{B.10}$$

we obtain the discretization by central differences of (3.33) and (3.34). The discrete version of the evolution equation for ρ (3.32) can be obtained in the same way. For the sake of completeness, we obtain

$$\begin{aligned}
\rho(x_j,t+\Delta t) &= f_{-1}(x_j,t+\Delta t) + f_0(x_j,t+\Delta t) + f_1(x_j,t+\Delta t) && \text{(B.11)}\\
&= f^\star_{-1}(x_{j+1},t^\star) + f^\star_0(x_j,t^\star) + f^\star_1(x_{j-1},t^\star) && \text{(B.12)}\\
&= (1-\omega)\big(f_{-1}(x_{j+1},t) + f_0(x_j,t) + f_1(x_{j-1},t)\big)\\
&\quad + \frac{\omega}{3}\big(\rho(x_{j-1},t) + \rho(x_j,t) + \rho(x_{j+1},t)\big)\\
&\quad + \frac{\Delta t}{3}\big(F(\rho(x_{j-1},t)) + F(\rho(x_j,t)) + F(\rho(x_{j+1},t))\big) && \text{(B.13)}\\
&= \rho(x_j,t) - \frac{(1-\omega)}{2}\big(\phi(x_{j+1},t) - \phi(x_{j-1},t)\big)\\
&\quad + (1-\omega)\big(\xi(x_{j+1},t) - 2\xi(x_j,t) + \xi(x_{j-1},t)\big)\\
&\quad + \frac{\omega}{3}\big(\rho(x_{j-1},t) - 2\rho(x_j,t) + \rho(x_{j+1},t)\big) + \Delta t F(\rho(x_j,t))\\
&\quad + \frac{\Delta t}{3}\big(F(\rho(x_{j-1},t)) - 2F(\rho(x_j,t)) + F(\rho(x_{j+1},t))\big)\,. && \text{(B.14)}
\end{aligned}$$

The accuracy of the diffusive D1Q3 LBM (second order in space and first order in time) can also be derived from the discrete nature of the LBE. In this section, we showed that the propagation in space and the explicit time stepping of the discrete LBE naturally leads to the use of central spatial finite differences and forward temporal finite differences to represent the corresponding continuous derivatives in discrete form (see also [100, 101]). The resulting finite difference errors are indeed $\mathcal{O}(\Delta x^2)$ and $\mathcal{O}(\Delta t)$ respectively.

For the special case $\omega = 1$, it was shown that the LBMs for diffusion [206, 227, 228], convection-diffusion [205, 207, 209] and fluid flow [100] are nothing but particular finite difference or finite volume discretizations of the corresponding PDE. E.g. Wolf-Gladrow shows in [227, 228] that the LBM for diffusion is equivalent to the FD discretization of the corresponding PDE with explicit differences in time and central differences in space when $\omega = 1$. The same is observed here. For $\omega = 1$, (B.14) reduces to the explicit in time and central in space FD discretization (8.1) of (2.4) (up to second order). Equations (B.9) and (B.10) reduce to the slaving relations (3.29) up to first order. This is exactly the order that needs to be substituted to obtain the reduced PDE, see Sect. B.2. Because the type of FD discretization follows from the LBM propagation and the choice of lattice stencil (here D1Q3), the direct reduction to the PDE for $\omega = 1$ also holds for the continuous formulation of the density equation (3.32) in Sect. 3.5.

This reduction for $\omega = 1$ also occurs in the CR scheme from Chapter 6. Because the CR convergence factor equals $|1-\omega|$, no iterations will be

performed. In fact, the CR scheme simplifies to the initial guess used for the moments, which is typically the BGK equilibrium as in Algorithm 6.1. We conclude with the remark that the choice $\omega = 1$ is not interesting in the context of equation-free computing because of the explicit assumption that the reduced macroscale equation is unavailable.

B.2 Reduced PDE on the Manifold

In this section, we show how the reduced equation (the PDE) on the slow manifold can be derived from the general evolution equation for $\rho(x,t)$ (3.32). Recall from Chapter 2 that, after a short period of time, the microscopic/mesoscopic evolution can be described in a lower dimensional state space (the slow manifold) due to a separation of time scales between the macroscopic variables $\rho(x,t)$ and the higher order moments $\phi(x,t)$ and $\xi(x,t)$. Once the corresponding slaved state is obtained, the evolution on this manifold is described by a reduced macroscopic equation in terms of the macroscopic slow variable only.

In our context, the slaving relations (3.29) for $\phi(x,t)$ and $\xi(x,t)$ or alternatively (3.27)–(3.28) for $f_i(x,t)$, are attained after the initial healing time. When we substitute (3.29) up to first order (compare Sect. 3.3) in (3.32), we obtain

$$\rho(x,t+\Delta t) = \rho(x,t) + (1-\omega)\frac{2\Delta x^2}{3\omega}\frac{\partial^2\rho(x,t)}{\partial x^2} + (1-\omega)\frac{\Delta x^2}{3}\frac{\partial^2\rho(x,t)}{\partial x^2} + \frac{\omega\Delta x^2}{3}\frac{\partial^2\rho(x,t)}{\partial x^2} + \Delta t F(\rho(x,t)) + \frac{\Delta t\Delta x^2}{3}\frac{\partial^2 F(\rho(x,t))}{\partial x^2}\,.$$

Gathering the terms in $\partial^2\rho(x,t)/\partial x^2$ and using (3.21), we have

$$\rho(x,t+\Delta t) = \rho(x,t) + D\Delta t\frac{\partial^2\rho}{\partial x^2} + \Delta t F(\rho(x,t)) + \frac{\Delta t\Delta x^2}{3}\frac{\partial^2 F(\rho(x,t))}{\partial x^2}\,.$$

After switching to continuous form, we obtain the reduced PDE (2.4). The last term can be seen as a the difference between the LBM and PDE *model*, i.e. as a kind of modeling error on the evolution of $\rho(x,t)$. This term is a fourth order contribution (cf. Sect. 3.3 and 3.4) and can be dropped when deriving the second order PDE. When exactly this difference is important, the term stays, as in (8.30) compared to (8.31).

Appendix C

Proofs of the Matrix Lemmas

In this appendix, we prove the lemmas from Sect. 6.3.1. These lemmas were used to show that the CR scheme is stable for the LBM with different types of boundary conditions.

C.1 Proof of Lemma 6.1

The $2N \times 2N$ matrix A (6.4) can be written as

$$A = b\,\hat{A}\,, \tag{C.1}$$

such that the corresponding eigenvalues are related as

$$\mu = b\,\hat{\mu}\,. \tag{C.2}$$

We will now prove that the eigenvalues $\hat{\mu}$ of $\hat{A}$ lie on the unit circle with angular distance $2\pi/N$.

Both matrices A (6.4) and $\hat{A}$ (C.1) are so-called *compound-circulant* matrices. From [198, 221, 223], it follows that the eigenvalues $\hat{\mu}$ of $\hat{A}$ can be found as the union of eigenvalues λ of the 2×2 matrices

$$H_m = \begin{bmatrix} 1/2 & -1 \\ -1/4 & 1/2 \end{bmatrix} r_m + \begin{bmatrix} 1/2 & 1 \\ 1/4 & 1/2 \end{bmatrix} r_m^{N-1}\,, \tag{C.3}$$

where r_m is any N^{th} root of unity:

$$r_m = \exp(i\,m\frac{2\pi}{N}) = \cos(m\frac{2\pi}{N}) + i\sin(m\frac{2\pi}{N})\,; \quad m = 0, 1, \ldots, N-1\,. \tag{C.4}$$

Table C.1: Multiplication table for the 2×2 matrices α, β, γ and δ (C.8).

$\cdot$	α	β	γ	δ
α	0	α	0	γ
β	0	β	0	δ
γ	α	0	γ	0
δ	β	0	δ	0

The eigenvalues λ of H_m are the roots of the characteristic equation $\det(H_m - \lambda I) = 0$ (with I the 2×2 unit matrix), i.e.

$$\lambda^2 - (r_m + r_m^{N-1})\lambda + 1 = 0 \, .$$

Using definition (C.4) and the fact that the complex conjugate $\overline{r_m} = r_m^{N-1} = r_{N-m}$, it is readily found that

$$\lambda_{1,m} = r_m \quad \text{and} \quad \lambda_{2,m} = \overline{r_m} = r_{N-m} \, . \tag{C.5}$$

Since these eigenvalues are defined for any r_m, it follows that $\hat{\mu}_m = r_m$; $m = 0, 1, \ldots, N-1$, each with multiplicity 2. Multiplying these eigenvalues by b to obtain μ_m (C.2) proves the theorem.

C.2 Proof of Lemma 6.2

For the matrix A in (6.6), we will prove that the eigenvalues $\hat{\mu}$ of the corresponding matrix $\hat{A}$ (C.1) are the $2N^{th}$ roots of unity $\hat{\mu}_m = \exp(i\, m\, \pi/N)$; $m = 0, 1, \ldots, 2N-1$. Since (C.2) holds, this will prove the theorem. In practice, we have to prove that the characteristic equation of $\hat{A}$ equals

$$p(\lambda) = \lambda^{2N} - 1 = 0 \, . \tag{C.6}$$

By definition, the roots of $p(\lambda) = 0$ are the eigenvalues $\hat{\mu}$ of $\hat{A}$. First, we prove that

$$p(\hat{A}) = \hat{A}^{2N} - I = 0 \tag{C.7}$$

holds (where I is now the $2N \times 2N$ unit matrix).

Define the 2×2 submatrices α, β, γ and δ as

$$\alpha = \begin{bmatrix} -1/2 & 1 \\ -1/4 & 1/2 \end{bmatrix} , \qquad \beta = \begin{bmatrix} 1/2 & -1 \\ -1/4 & 1/2 \end{bmatrix} ,$$
$$\gamma = \begin{bmatrix} 1/2 & 1 \\ 1/4 & 1/2 \end{bmatrix} , \qquad \delta = \begin{bmatrix} -1/2 & -1 \\ 1/4 & 1/2 \end{bmatrix} . \tag{C.8}$$

One can compute the multiplication table C.1 for the matrices (C.8). For the example $2N = 10$, the powers of the compound matrix $\hat{A}$ (see (C.9) and compare $(1/b)A$ (6.6)) are

$$\hat{A} = \begin{bmatrix} \alpha & \beta & & & \\ \gamma & & \beta & & \\ & \gamma & & \beta & \\ & & \gamma & & \beta \\ & & & \gamma & \delta \end{bmatrix}, \qquad \hat{A}^9 = \begin{bmatrix} \delta & \gamma & & & \\ \beta & & \gamma & & \\ & \beta & & \gamma & \\ & & \beta & & \gamma \\ & & & \beta & \alpha \end{bmatrix}, \tag{C.9}$$

$$\hat{A}^2 = \begin{bmatrix} & \alpha & \beta & & \\ \alpha & & & \beta & \\ \gamma & & & & \beta \\ & \gamma & & & \delta \\ & & \gamma & \delta & \end{bmatrix}, \qquad \hat{A}^8 = \begin{bmatrix} & \delta & \gamma & & \\ \delta & & & \gamma & \\ \beta & & & & \gamma \\ & \beta & & & \alpha \\ & & \beta & \alpha & \end{bmatrix}, \tag{C.10}$$

$$\hat{A}^3 = \begin{bmatrix} & & \alpha & \beta & \\ & \alpha & & & \beta \\ \alpha & & & & \delta \\ \gamma & & & \delta & \\ & \gamma & \delta & & \end{bmatrix}, \qquad \hat{A}^7 = \begin{bmatrix} & & \delta & \gamma & \\ & \delta & & & \gamma \\ \delta & & & & \alpha \\ \beta & & & \alpha & \\ & \beta & \alpha & & \end{bmatrix}, \tag{C.11}$$

$$\hat{A}^4 = \begin{bmatrix} & & & \alpha & \beta \\ & & \alpha & & \delta \\ & \alpha & & \delta & \\ \alpha & & \delta & & \\ \gamma & \delta & & & \end{bmatrix}, \qquad \hat{A}^6 = \begin{bmatrix} & & & \delta & \gamma \\ & & \delta & & \alpha \\ & \delta & & \alpha & \\ \delta & & \alpha & & \\ \beta & \alpha & & & \end{bmatrix}, \tag{C.12}$$

$$\hat{A}^5 = \begin{bmatrix} & & & & \alpha+\delta \\ & & & \alpha+\delta & \\ & & \alpha+\delta & & \\ & \alpha+\delta & & & \\ \alpha+\delta & & & & \end{bmatrix}. \tag{C.13}$$

It can be checked that $\hat{A}^{2N} = \hat{A}^{10} = I$, which proves (C.7).

Secondly, we prove that there is no polynomial $q(\lambda)$ with degree less than $2N$ such that $q(\hat{A}) = 0$. Define $q(\lambda)$ as

$$d_{2N-1}\lambda^{2N-1} + d_{2N-2}\lambda^{2N-2} + \ldots + d_2\lambda^2 + d_1\lambda + d_0 \,, \tag{C.14}$$

with arbitrary coefficients d_n ; $n = 0, 1, \ldots, 2N-1$. From the structure of

the powers of $\hat{A}$ (C.9)–(C.13), it follows that $q(\hat{A}) = 0$ holds if and only if

$$\begin{aligned} d_n\alpha + d_{2N-n}\delta = 0\ , \quad d_n\gamma + d_{2N-n}\beta = 0\ , \\ d_n\delta + d_{2N-n}\alpha = 0\ , \quad d_n\beta + d_{2N-n}\gamma = 0\ . \end{aligned} \tag{C.15}$$

Equations (C.15) hold only when $d_n = 0$; $\forall\, n = 1, \ldots, 2N-1$. Thus there is no polynomial like (C.14) that makes $q(\hat{A}) = 0$. We conclude that $p(\lambda)$ (C.6) is the sole monic polynomial of degree $2N$ that is annihilated by $\hat{A}$. As a consequence of the Cayley-Hamilton theorem, we can then state that (C.6) is indeed the characteristic equation of $\hat{A}$.

C.3 Numerical Verification of Conjecture 6.3

We will verify Conjecture 6.3 numerically, without giving a formal proof for the derivation of the characteristic equation. We have to show that the eigenvalues $\hat{\mu}$ of $\hat{A}$ (C.1) for A (6.7) are the $2N-2$ roots of unity, complemented with two extra eigenvalues $\hat{\mu}_0 = 1$, or equivalently, that these $\hat{\mu}$ values are the roots of the following equation

$$p(\lambda) = (\lambda - 1)^2(\lambda^{2N-2} - 1) = 0\ . \tag{C.16}$$

If (C.16) is the characteristic equation of $\hat{A}$, the Cayley-Hamilton theorem states that $\hat{A}$ satisfies the same equation, i.e.

$$p(\hat{A}) = (\hat{A} - I)^2(\hat{A}^{2N-2} - I) = 0\ . \tag{C.17}$$

Note that eigenvalue $\hat{\mu}_0 = 1$ can be found directly in both the second and last row of matrix $\hat{A} = A/b$ (6.7). When dropping both the second and last rows and columns, the resulting $(2N-2) \times (2N-2)$ matrix should satisfy $(\lambda^{2N-2} - 1) = 0$. This (and (C.17)) can be verified numerically for arbitrary N using MATLAB© or MAPLE©. The numerically computed eigenvalues $\hat{\mu}$ satisfy (C.16). Using (C.2), the eigenvalues μ of A are found.

Bibliography

[1] P. Ahlrichs and B. Dünweg. Lattice Boltzmann simulation of polymer-solvent systems. *International Journal of Modern Physics C*, 9(8):1429–1438, 1998.

[2] P. Ahlrichs and B. Dünweg. Simulation of a single polymer chain in solution by combining lattice Boltzmann and molecular dynamics. *Journal of Chemical Physics*, 111(17):8225–8239, 1999.

[3] P. Albuquerque, D. Alemani, B. Chopard, and P. Leone. Coupling a lattice Boltzmann and a finite difference scheme. In M. Bubak, G. D. van Albada, P. M. Sloot, and J. Dongarra, editors, *International Conference on Computational Science – ICCS 2004*, volume 3039 of *Lecture Notes in Computer Science*, pages 540–547. Springer-Verlag, 2004.

[4] P. Albuquerque, D. Alemani, B. Chopard, and P. Leone. A hybrid lattice Boltzmann finite difference scheme for the diffusion equation. *International Journal for Multiscale Computational Engineering*, 4(2):209–219, 2006.

[5] D. Alemani, B. Chopard, J. Galceran, and J. Buffle. LBGK method coupled to time splitting technique for solving reaction-diffusion processes in complex systems. *Physical Chemistry Chemical Physics*, 7:3331–3341, 2005.

[6] F. J. Alexander, S. Chen, and J. D. Sterling. Lattice Boltzmann thermodynamics. *Physical Review E*, 47:2249–2252, 1993.

[7] F. J. Alexander, A. L. Garcia, and D. M. Tartakovsky. Algorithm refinement for stochastic partial differential equations: I. Linear diffusion. *Journal of Computational Physics*, 182:47–66, 2002.

[8] F. J. Alexander, A. L. Garcia, and D. M. Tartakovsky. Algorithm refinement for stochastic partial differential equations: II. Correlated systems. *Journal of Computational Physics*, 207:769–787, 2005.

[9] H. C. Andersen. RATTLE: A "velocity" version of the SHAKE algorithm for molecular dynamics calculations. *Journal of Computational Physics*, 52:24–34, 1983.

[10] U. Ascher, R. Mattheij, and R. Russell. *Numerical solution of boundary value problems for ordinary differential equations*. Prentice-Hall, Englewood Cliffs, 1988.

[11] D. Barkley, I. G. Kevrekidis, and A. M. Stuart. The moment map: Nonlinear dynamics of density evolution via a few moments. *SIAM Journal on Applied Dynamical Systems*, 5(3):403–434, 2006.

[12] E. Belov, S. Lomov, I. Verpoest, T. Peeters, D. Roose, R. Parnas, K. Hoes, and H. Sol. Modelling of permeability of textile reinforcements: Lattice Boltzmann method. *Composites Science and Technology*, 64:1069–1080, 2004.

[13] R. Benzi and S. Succi. Two-dimensional turbulence with the lattice Boltzmann equation. *Journal of Physics A: Mathematical and General*, 23:L1–L5, 1990.

[14] R. Benzi, S. Succi, and M. Vergassola. The lattice Boltzmann equation: Theory and applications. *Physics Reports*, 222(3):145–197, 1992.

[15] M. J. Berger and J. Oliger. Adaptive mesh refinement for hyperbolic partial differential equations. *Journal of Computational Physics*, 53(3):484–512, 1984.

[16] M. Bernaschi, S. Succi, and H. Chen. Accelerated lattice Boltzmann schemes for steady-state flow simulations. *Journal of Scientific Computing*, 16(2):135–144, 2001.

[17] M. Bernaschi, S. Succi, H. Chen, and R. Zhang. Computing steady state flows with an accelerated lattice Boltzmann technique. *International Journal of Modern Physics C*, 13(5):675–687, 2002.

[18] P. L. Bhatnagar, E. P. Gross, and M. Krook. A model for collision processes in gases. I. Small amplitude processes in charged and neutral one-component systems. *Physical Review*, 94(3):511–525, May 1954.

[19] G. A. Bird. *Molecular Gas Dynamics & the direct simulation of gas flows*. Oxford University Press, 2nd edition, 1994.

[20] R. Blaak and P. M. A. Sloot. Lattice dependence of reaction-diffusion in lattice Boltzmann modeling. *Computer Physics Communications*, 129:256–266, 2000.

[21] P. N. Brown, A. C. Hindmarsh, and L. R. Petzold. Consistent initial condition calculation for differential-algebraic systems. *SIAM Journal on Scientific Computing*, 19(5):1495–1512, 1998.

[22] A. Caiazzo. Analysis of lattice Boltzmann initialization routines. *Journal of Statistical Physics*, 121(1-2):37–48, October 2005. Special Issue on Mesoscopic Methods in Engineering and Science. Guest Editors: M. Krafczyk, A. J. C. Ladd, and L.-S. Luo.

[23] A. Cancelliere, C. Chang, E. Foti, D. H. Rothman, and S. Succi. The permeability of a random medium: Comparison of simulation with theory. *Physics of Fluids A*, 2(12):2085–2088, 1990.

[24] N. Cao, S. Chen, S. Jin, and D. Martínez. Physical symmetry and lattice symmetry in the lattice Boltzmann method. *Physical Review E*, 55(1):R21–R24, 1997.

[25] A. Chatterji and J. Horbach. Combining molecular dynamics with lattice Boltzmann: A hybrid method for the simulation of (charged) colloidal systems. *Journal of Chemical Physics*, 122:184903–1–12, 2005.

[26] H. Chen, S. Chen, and W. H. Matthaeus. Recovery of the Navier-Stokes equations using a lattice-gas Boltzmann method. *Physical Review A*, 45(8):R5339–R5342, 1992.

[27] H. Chen, S. Kandasamy, S. Orszag, R. Shock, S. Succi, and V. Yakhot. Extended Boltzmann kinetic equation for turbulent flows. *Science Magazine*, 301(5633):633–636, August 2003.

[28] H. Chen, S. Succi, and S. Orszag. Analysis of subgrid scale turbulence using the Boltzmann Bhatnagar-Gross-Krook kinetic equation. *Physical Review E*, 59(3):R2527–R2530, 1999.

[29] S. Chen, H. Chen, D. Martinez, and W. Matthaeus. Lattice Boltzmann model for simulation of magnetohydrodynamics. *Physical Review Letters*, 67(27):3776–3779, 1991.

[30] S. Chen, S. P. Dawson, G. D. Doolen, D. R. Janecky, and A. Lawniczak. Lattice methods and their applications to reacting systems. *Computers and Chemical Engineering*, 19(6/7):617–646, 1995.

[31] S. Chen and G. D. Doolen. Lattice Boltzmann method for fluid flows. *Annual Review of Fluid Mechanics*, 30:329–364, 1998.

[32] Y. Chen, H. Ohashi, and M. Akiyama. Thermal lattice Bhatnagar-Gross-Krook model without nonlinear deviations in macrodynamic equations. *Physical Review E*, 50(4):2776–2783, October 1994.

[33] B. Chopard and M. Droz. *Cellular Automata Modeling of Physical Systems*. Cambridge University Press, 1998.

[34] B. Chopard, A. Dupuis, A. Masselot, and P. Luthi. Cellular automata and lattice Boltzmann techniques: An approach to model and simulate complex systems. *Advances in Complex Systems*, 5(2/3):103–246, 2002.

[35] B. Chopard and A. Masselot. Cellular automata and lattice Boltzmann methods: A new approach to computational fluid dynamics and particle transport. *Future Generation Computer Systems*, 16(2/3):249–257, 1999.

[36] A. Chorin, A. P. Kast, and R. Kupferman. Optimal prediction of underresolved dynamics. *Proceedings of the National Academy of Sciences*, 95(8):4094–4098, 1998.

[37] A. J. Chorin, O. H. Hald, and R. Kupferman. Optimal prediction and the Mori-Zwanzig representation of irreversible processes. *Proceedings of the National Academy of Sciences*, 97(7):2968–2973, 2000.

[38] J. Cisternas, C. W. Gear, S. Levin, and I. G. Kevrekidis. Equation-free modeling of evolving diseases: Coarse-grained computations with individual-based models. *Proceedings of the Royal Society A: Mathematical, Physical and Engineering Sciences*, 460(2050):2761–2779, 2004.

[39] P. Constantin, C. Foias, B. Nicolaenko, and R. Temam. *Integral Manifolds and Inertial Manifolds for Dissipative Partial Differential Equations*, volume 70 of *Applied Mathematical Sciences*. Springer-Verlag, 1989.

[40] D. Dab, J.-P. Boon, and Y.-X. Li. Lattice-gas automata for coupled reaction-diffusion equations. *Physical Review Letters*, 66(19):2535–2538, 1991.

[41] S. P. Dawson, S. Chen, and G. D. Doolen. Lattice Boltzmann computations for reaction-diffusion equations. *Journal of Chemical Physics*, 98(2):1514–1523, 1993.

[42] A. Dhooge, W. Govaerts, and Y. A. Kuznetsov. MATCONT: A MATLAB package for numerical bifurcation analysis of ODEs. *ACM Transactions on Mathematical Software*, 29(2):141–164, 2003.

[43] D. d'Humières. Generalized lattice-Boltzmann equations. In B. D. Shizgal and D. P. Weaver, editors, *Rarefied Gas Dynamics: Theory*

and Simulations, volume 159 of *Progress in Astronautics and Aeronautics*. American Institute of Aeronautics and Astronautics (AIAA), 1992.

[44] G. Dimarco and L. Pareschi. Hybrid multiscale methods I. Hyberbolic relaxation problems. *Communications in Mathematical Sciences*, 4(1):155–177, 2006.

[45] E. Doedel, R. Paffenroth, A. Champneys, T. Fairgrieve, Y. Kuznetsov, B. Oldeman, B. Sandstede, and X. Wang. AUTO2000: Continuation and bifurcation software for ordinary differential equations (with HomCont). Technical report, Concordia University, 2002.

[46] A. Dupuis, E. M. Kotsalis, and P. Koumoutsakos. Coupling lattice Boltzmann and molecular dynamics models for dense fluids. Technical Report cond-mat/0610774, arXiv e-Print archive, October 2006.

[47] W. E. Analysis of the heterogeneous multiscale method for ordinary differential equations. *Communications in Mathematical Sciences*, 1(3):423–436, 2003.

[48] W. E and B. Engquist. The heterogeneous multiscale methods. *Communications in Mathematical Sciences*, 1(1):87–133, 2003.

[49] W. E, B. Engquist, X. Li, W. Ren, and E. Vanden-Eijnden. Heterogeneous multiscale methods: A review. *Communications in Computational Physics*, 2(3):367–450, 2007.

[50] W. E, D. Liu, and E. Vanden-Eijnden. Analysis of multiscale methods for stochastic differential equations. *Communications on Pure and Applied Mathematics*, 58:1544–1585, 2005.

[51] U. Ebert, W. van Saarloos, and C. Caroli. Propagation and structure of planar streamer fronts. *Physical Review E*, 55(2):1530–1549, 1997.

[52] C. Elphick, A. Hagberg, and E. Meron. Dynamic front transitions and spiral-vortex nucleation. *Physical Review E*, 51(4):3052–3058, 1995.

[53] R. Erban, I. G. Kevrekidis, and H. G. Othmer. An equation-free computational approach for extracting population-level behavior from individual-based models for biological dispersal. *Physica D: Nonlinear Phenomena*, 215(1):1–24, 2006.

[54] P. Espanol. *Statistical Mechanics of Coarse-Graining*, volume 640 of *Lecture Notes in Physics*, pages 69–115. Springer-Verlag, 2004.

[55] P. Espanol and P. Warren. Statistical mechanics of dissipative particle dynamics. *Europhysics Letters*, 30(4):191–196, 1995.

[56] O. Filippova and D. Hänel. Grid refinement for lattice-BGK models. *Journal of Computational Physics*, 147:219–228, 1998.

[57] O. Filippova and D. Hänel. Acceleration of lattice-BGK schemes with grid refinement. *Journal of Computational Physics*, 165:407–427, 2000.

[58] R. FitzHugh. Impulses and physiological states in theoretical models of nerve membranes. *Biophysical Journal*, 1:445–466, 1961.

[59] D. Frenkel and B. Smit. *Understanding Molecular Simulation: From Algorithms to Applications*. Academic Press, 2002.

[60] U. Frisch, D. d'Humières, B. Hasslacher, P. Lallemand, Y. Pomeau, and J.-P. Rivet. Lattice gas hydrodynamics in two and three dimensions. *Complex Systems*, 1:649–707, 1987.

[61] U. Frisch, B. Hasslacher, and Y. Pomeau. Lattice-gas automata for the Navier-Stokes equation. *Physical Review Letters*, 56(14):1505–1508, 1986.

[62] M. G. Fyta, S. Melchionna, E. Kaxiras, and S. Succi. Multiscale coupling of molecular dynamics and hydrodynamics: Application to DNA translocation through a nanopore. *Multiscale Modeling & Simulation*, 5(4):1156–1173, 2006.

[63] A. L. Garcia, J. B. Bell, W. Y. Crutchfield, and B. J. Alder. Adaptive mesh and algorithm refinement using direct simulation Monte Carlo. *Journal of Computational Physics*, 154:134–155, 1999.

[64] C. W. Gear, T. J. Kaper, I. G. Kevrekidis, and A. Zagaris. Projecting to a slow manifold: Singularly perturbed systems and legacy codes. *SIAM Journal on Applied Dynamical Systems*, 4(3):711–732, 2005.

[65] C. W. Gear and I. G. Kevrekidis. Projective methods for stiff differential equations: Problems with gaps in their eigenvalue spectrum. *SIAM Journal on Scientific Computing*, 24(4):1091–1106, 2003.

[66] C. W. Gear and I. G. Kevrekidis. Telescopic methods for parabolic differential equations. *Journal of Computational Physics*, 187(1):95–109, 2003.

[67] C. W. Gear and I. G. Kevrekidis. Computing in the past with forward integration. *Physics Letters A*, 321(5-6):335–343, 2004.

[68] C. W. Gear and I. G. Kevrekidis. Constraint-defined manifolds: A legacy code approach to low-dimensional computation. *Journal of Scientific Computing*, 25(1):17–28, October 2005. Can also be obtained as Technical Report physics/0312094, arXiv e-Print archive.

[69] C. W. Gear, I. G. Kevrekidis, and C. Theodoropoulos. 'Coarse' integration/bifurcation analysis via microscopic simulators: Micro-Galerkin methods. *Computers and Chemical Engineering*, 26(7/8):941–963, 2002.

[70] D. T. Gillespie. A general method for numerically simulating the stochastic time evolution of coupled chemical reactions. *Journal of Computational Physics*, 2:403–434, 1976.

[71] I. Ginzbourg and P. M. Adler. Boundary flow condition analysis for the three-dimensional lattice Boltzmann model. *Journal of Physics II France*, 4:191–214, 1994.

[72] D. Givon, R. Kupferman, and A. Stuart. Extracting macroscopic dynamics: Model problems and algorithms. *Nonlinearity*, 17:R55–R127, 2004.

[73] R. E. Goldstein, D. J. Muraki, and D. M. Petrich. Interface proliferation and the growth of labyrinths in a reaction-diffusion system. *Physical Review E*, 53(4):3933–3957, 1996.

[74] A. N. Gorban. Basic types of coarse-graining. In A. N. Gorban, N. Kazantzis, I. G. Kevrekidis, H. C. Ottinger, and C. Theodoropoulos, editors, *Model Reduction and Coarse-Graining Approaches for Multiscale Phenomena*, Complexity, pages 107–160. Springer, Berlin–Heidelberg–New York, 2006.

[75] A. N. Gorban and I. V. Karlin. *Invariant Manifolds for Physical and Chemical Kinetics*. Lecture Notes in Physics. Springer, 2005.

[76] A. N. Gorban and I. V. Karlin. Quasi-equilibrium closure hierarchies for the Boltzmann equation. *Physica A*, 360:325–364, 2006.

[77] A. N. Gorban, I. V. Karlin, P. Ilg, and H. C. Öttinger. Corrections and enhancements of quasi-equilibrium states. *Journal of Non-Newtonian Fluid Dynamics*, 96:203–219, 2001.

[78] H. Grabert. *Projection Operator Techniques in Nonequilibrium Statistical Mechanics*, volume 95 of *Springer Tracts in Modern Physics*. Springer-Verlag, 1982.

[79] D. Grunau, S. Chen, and K. Eggert. A lattice Boltzmann model for multi-phase fluid flows. *Physics of Fluids A*, 5(10):2557–2562, 1993.

[80] A. K. Gunstensen and D. H. Rothman. Lattice Boltzmann model of immiscible fluids. *Physical Review A*, 43(8):4320–4327, 1991.

[81] A. K. Gunstensen and D. H. Rothman. Microscopic modeling of immiscible fluids in three dimensions by a lattice Boltzmann method. *Europhysics Letters*, 18(2):157–161, 1992.

[82] Z. Guo, T. S. Zhao, and Y. Shi. Preconditioned lattice-Boltzmann method for steady flows. *Physical Review E*, 70:066706–1–8, 2004.

[83] M. Haataja, D. J. Srolovitz, and I. G. Kevrekidis. Apparent hysteresis in a driven system with self-organized drag. *Physical Review Letters*, 92(16):160603–1–4, 2004.

[84] N. G. Hadjiconstantinou. Hybrid atomistic-continuum formulations and the moving contact-line problem. *Journal of Computational Physics*, 154:245–265, 1999.

[85] A. Hagberg and E. Meron. From labyrinthine patterns to spiral turbulence. *Physical Review Letters*, 72(15):2494–2497, 1994.

[86] X. He, S. Chen, and G. Doolen. A novel thermal model for the lattice Boltzmann method in incompressible limit. *Journal of Computational Physics*, 146:282–300, 1998.

[87] X. He and L.-S. Luo. A priori derivation of the lattice Boltzmann equation. *Physical Review E*, 55(6):R6333–R6336, 1997.

[88] X. He and L.-S. Luo. Theory of the lattice Boltzmann method: From the Boltzmann equation to the lattice Boltzmann equation. *Physical Review E*, 56(6):6811–6817, 1997.

[89] X. He, X. Shan, and G. D. Doolen. Discrete Boltzmann equation model for nonideal gases. *Physical Review E*, 57(1), 1998.

[90] X. He, Q. Zou, L.-S. Luo, and M. Dembo. Analytic solutions of simple flows and analysis of nonslip boundary conditions for the lattice Boltzmann BGK model. *Journal of Statistical Physics*, 87(1/2):115–136, 1997.

[91] F. J. Higuera and J. Jiménez. Boltzmann approach to lattice gas simulations. *Europhysics Letters*, 9(7):663–668, 1989.

[92] F. J. Higuera, S. Succi, and R. Benzi. Lattice gas dynamics with enhanced collisions. *Europhysics Letters*, 9(4):345–349, 1989.

[93] A. C. Hindmarsch. ODEPACK, A systematized collection of ODE solvers. In R. Stepleman, M. Carver, R. Peskin, W. Ames, and R. Vichnevetsky, editors, *Scientific Computing*, volume 1 of *IMACS Transactions on Scientific Computing*, pages 55–64. North-Holland, Amsterdam, 1983.

[94] A. L. Hodgkin and A. F. Huxley. A quantitative description of membrane current and its application to conduction and excitation in nerve. *Journal of Physiology*, 117(4):500–544, 1952.

[95] D. J. Holdych, D. R. Noble, J. G. Georgiadis, and R. O. Buckius. Truncation error analysis of lattice Boltzmann models. *Journal of Computational Physics*, 193:595–619, 2004.

[96] P. J. Hoogerbrugge and J. M. V. A. Koelman. Simulating microscopic hydrodynamic phenomena with dissipative particle dynamics. *Europhysics Letters*, 19(3):155–160, 1992.

[97] W. Huisinga, C. Schütte, and A. M. Stuart. Extracting macroscopic stochastic dynamics: Model problems. *Communications on Pure and Applied Mathematics*, 55:0001–0036, 2002.

[98] M. A. Hulsen, A. P. G. van Heel, and B. H. A. A. van den Brule. Simulation of viscoelastic flows using Brownian configuration fields. *Journal of Non-Newtonian Fluid Mechanics*, 70:79–101, 1997.

[99] G. Hummer and I. G. Kevrekidis. Coarse molecular dynamics of a peptide fragment: Free energy, kinetics, and long-time dynamics computations. *Journal of Chemical Physics*, 118:10762–10774, 2003.

[100] M. Junk. A finite difference interpretation of the lattice Boltzmann method. *Numerical Methods for Partial Differential Equations*, 17(4):383–402, 2001.

[101] M. Junk and A. Klar. Discretizations for the incompressible Navier-Stokes equations based on the lattice Boltzmann method. *SIAM Journal on Scientific Computing*, 22(1):1–19, 2000.

[102] M. Junk, A. Klar, and L.-S. Luo. Asymptotic analysis of the lattice Boltzmann equation. *Journal of Computational Physics*, 210(2):676–704, 2005.

[103] D. Kandhai, A. Koponen, A. Hoekstra, M. Kataja, J. Timonen, and P. Sloot. Implementation aspects of 3D lattice-BGK: Boundaries, accuracy, and a new fast relaxation method. *Journal of Computational Physics*, 150:482–501, 1999.

[104] D. Kandhai, A. Koponen, A. Hoekstra, and P. Sloot. Iterative momentum relaxation for fast lattice-Boltzmann simulations. *Future Generation Computer Systems*, 18:89–96, 2001.

[105] D. Kandhai, W. Soll, S. Chen, A. Hoekstra, and P. Sloot. Finite-difference lattice-BGK methods on nested grids. *Computer Physics Communications*, 129:100–109, 2000.

[106] H. Keller. *Numerical methods for two-point boundary value problems.* Blaisdell, New-York, 1968.

[107] H. B. Keller. Numerical solution of bifurcation and nonlinear eigenvalue problems. In P. H. Rabinowitz, editor, *Applications of Bifurcation Theory*, pages 359–384. Academic Press, New York, 1977.

[108] I. G. Kevrekidis, C. W. Gear, J. M. Hyman, P. G. Kevrekidis, O. Runborg, and C. Theodoropoulos. Equation-free, coarse-grained multiscale computation: Enabling microscopic simulators to perform system-level analysis. *Communications in Mathematical Sciences*, 1(4):715–762, 2003.

[109] A. Klar. Relaxation scheme for a lattice-Boltzmann-type discrete velocity model and numerical Navier-Stokes limit. *Journal of Computational Physics*, 148(2):416–432, 1999.

[110] J. M. V. A. Koelman. A simple lattice Boltzmann scheme for Navier-Stokes fluid flow. *Europhysics Letters*, 15(6):603–607, 1991.

[111] D. I. Kopelevich, A. Z. Panagiotopoulos, and I. G. Kevrekidis. Coarse-grained kinetic computations for rare events: Application to micelle formation. *Journal of Chemical Physics*, 122:044908, 2005.

[112] A. Koponen, D. Kandhai, E. Hellén, M. Alava, A. Hoekstra, M. Kataja, K. Niskanen, P. Sloot, and J. Timonen. Permeability of three-dimensional random fiber webs. *Physical Review Letters*, 80(4):716–719, 1998.

[113] A. J. C. Ladd. Numerical simulations of particulate suspensions via a discretized Boltzmann equation. Part I. Theoretical foundation. *Journal of Fluid Mechanics*, 271:285–309, 1994.

[114] A. J. C. Ladd. Numerical simulations of particulate suspensions via a discretized Boltzmann equation. Part II. Numerical results. *Journal of Fluid Mechanics*, 271:311–339, 1994.

[115] A. J. C. Ladd and R. Verberg. Lattice-Boltzmann simulations of particle-fluid suspensions. *Journal of Statistical Physics*, 104(5/6):1191–1251, 2001.

[116] P. Lallemand and L.-S. Luo. Theory of the lattice Boltzmann method: Dispersion, dissipation, isotropy, Galilean invariance and stability. *Physical Review E*, 61(6):6546–6562, 2000.

[117] P. Lallemand and L.-S. Luo. Hybrid finite-difference thermal lattice Boltzmann equation. *International Journal of Modern Physics B*, 17(1-2):41–47, 2003.

[118] P. Lallemand and L.-S. Luo. Theory of the lattice Boltzmann method: Acoustic and thermal properties in two and three dimensions. *Physical Review E*, 68(036706), 2003.

[119] S. H. Lam. Using CSP to understand complex chemical kinetics. *Combustion Science and Technology*, 5-6:375–404, 1993.

[120] S. H. Lam and D. A. Goussis. The CSP method for simplifying kinetics. *International Journal of Chemical Kinetics*, 26:461–486, 1994.

[121] M. Laso and H. C. Öttinger. Calculation of viscoelastic flow using molecular models: the CONNFFESSIT approach. *Journal of Non-Newtonian Fluid Mechanics*, 47:1–20, 1993.

[122] J. Latt, B. Chopard, and P. Albuquerque. Spatial coupling of a lattice Boltzmann fluid model with a finite difference Navier-Stokes solver. Technical Report physics/0511243, arXiv e-Print archive, November 2005.

[123] P. Le Tallec and F. Mallinger. Coupling Boltzmann and Navier-Stokes equations by half fluxes. *Journal of Computational Physics*, 136:51–67, 1997.

[124] S. L. Lee and C. W. Gear. Second-order accurate projective integrators for multiscale problems. *Journal of Computational and Applied Mathematics*, 201(1):258–274, 2007.

[125] T. Lee and C.-L. Lin. An Eulerian description of the streaming process in the lattice Boltzmann equation. *Journal of Computational Physics*, 185:445–471, 2003.

[126] J. Li, D. Liao, and S. Yip. Coupling continuum to molecular-dynamics simulation: Reflecting particle method and the field estimator. *Physical Review E*, 57(6):7259–7267, 1998.

[127] J. Li, D. Liao, and S. Yip. Nearly exact solution for coupled continuum/MD fluid simulation. *Journal of Computer-Aided Materials Design*, 6(2-3):95–102, 1999.

[128] Q. Li, C.-G. Zheng, N.-C. Wang, and B.-C. Shi. LBGK simulations of Turing patters in CIMA model. *Journal of Scientific Computing*, 16(2):121–134, 2001.

[129] E. Luna-Ortiz and C. Theodoropoulos. An input/output model reduction-based optimization scheme for large-scale systems. *SIAM Multiscale Modeling and Simulation*, 4(2):691–708, 2005.

[130] L.-S. Luo. Unified theory of lattice Boltzmann models for nonideal gases. *Physical Review Letters*, 81(8):1618–1621, 1998.

[131] L.-S. Luo. Theory of the lattice Boltzmann method: Lattice Boltzmann models for nonideal gases. *Physical Review E*, 62(4):4982–4996, 2000.

[132] K. Lust. PDEcont. URL: www.math.rug.nl/˜kurt/r_PDEcont.html.

[133] K. Lust. *Numerical Bifurcation Analysis of Periodic Solutions of Partial Differential Equations*. PhD thesis, Katholieke Universiteit Leuven, 1997.

[134] K. Lust and D. Roose. Computation and bifurcation analysis of periodic solutions of large-scale systems. In E. Doedel and L. Tuckerman, editors, *Numerical methods for bifurcation problems and large-scale dynamical systems*, volume 119 of *The IMA volumes in mathematics and its applications*, pages 265–302. Springer-Verlag, New York, 2000.

[135] K. Lust, D. Roose, A. Spence, and A. Champneys. An adaptive Newton-Picard algorithm with subspace iteration for computing periodic solutions. *SIAM Journal on Scientific Computing*, 19(4):1188–1209, 1998.

[136] U. Maas and S. B. Pope. Simplifying chemical kinetics: Intrinsic low-dimensional manifolds in composition space. *Combustion and Flame*, 88:239–264, 1992.

[137] A. J. Majda, I. Timofeyev, and E. Vanden-Eijnden. A mathematical framework for stochastic climate models. *Communications on Pure and Applied Mathematics*, 54:0891–0974, 2001.

[138] A. G. Makeev, D. Maroudas, and I. G. Kevrekidis. "Coarse" stability and bifurcation analysis using stochastic simulators: Kinetic Monte Carlo examples. *Journal of Chemical Physics*, 116(23):10083–10091, 2002.

[139] A. G. Makeev, D. Maroudas, A. Z. Panagiotopoulos, and I. G. Kevrekidis. Coarse bifurcation analysis of kinetic Monte Carlo simulations: A lattice-gas model with lateral interactions. *Journal of Chemical Physics*, 117(18):8229–8240, 2002.

[140] A. Malevanets and R. Kapral. Microscopic model for FitzHugh-Nagumo dynamics. *Physical Review E*, 55(5):5657–5670, 1997.

[141] A. Malevanets and R. Kapral. Reactive lattice gas model for FitzHugh-Nagumo dynamics. *Nonlinear Science Today*, 1997.

[142] D. J. Mavriplis. Multigrid solution of the steady-state lattice Boltzmann equation. *Computers & Fluids*, 35(8-9):793–804, 2006.

[143] G. R. McNamara and G. Zanetti. Use of the Boltzmann equation to simulate lattice-gas automata. *Physical Review Letters*, 61(20):2332–2335, November 1988.

[144] R. Mei, L.-S. Luo, P. Lallemand, and D. d'Humières. Consistent initial conditions for lattice Boltzmann simulations. *Computers & Fluids*, 35(8/9):855–862, 2006.

[145] A. Mezrhab, M. Bouzidi, and P. Lallemand. Hybrid lattice-Boltzmann finite-difference simulation of convective flows. *Computers & Fluids*, 33:623–641, 2004.

[146] J. Möller, O. Runborg, P. G. Kevrekidis, K. Lust, and I. G. Kevrekidis. Effective equations for discrete systems: A time stepper based approach. *International Journal of Bifurcation and Chaos*, 15(3):975–996, 2005.

[147] J. J. Monaghan. Smoothed particle hydrodynamics. *Reports on Progress in Physics*, 68:1703–1759, 2005.

[148] S. J. Moon, R. Ghanem, and I. G. Kevrekidis. Coarse graining the dynamics of coupled oscillators. *Physical Review Letters*, 96:144101–1–4, April 2006.

[149] H. Mori. Statistical-mechanical theory of transport in fluids. *Physical Review*, 112(6):1829–1842, 1958.

[150] J. D. Murray. *Mathematical Biology*. Springer-Verlag, 1990.

[151] J. Nagumo, S. Arimoto, and S. Yoshizawa. An active pulse transmission line simulating nerve axon. *Proceedings of the IRE*, 50:2061–2070, 1962.

[152] W. Ngamsaad, W. Triampo, P. Kanthang, I.-M. Tang, N. Nuttawut, and C. Modjung. A lattice Boltzmann method for modeling the dynamic pole-to-pole oscillations of Min proteins for determining the position of the midcell division plane. *Journal of Korean Physical Society*, 46(4):1025–1030, 2005.

[153] X. Nie, S. Chen, and M. O. Robbins. Hybrid continuum-atomistic simulation of singular corner flow. *Physics of Fluids*, 16(10):55–64, 2004.

[154] X. B. Nie, S. Y. Chen, W. N. E, and M. O. Robbins. A continuum and molecular dynamics hybrid method for micro- and nano-fluid flow. *Journal of Fluid Mechanics*, 500:55–64, 2004.

[155] T. Ohta, A. Ito, and A. Tetsuka. Self-organization in an excitable reaction-diffusion system: Synchronization of oscillatory domains in one dimension. *Physical Review A*, 42(6):3225–2332, 1990.

[156] E. S. Oran, C. K. Oh, and B. Z. Cybyk. Direct simulation Monte Carlo: Recent advances and applications. *Annual Reviews of Fluid Mechanics*, 30:403–441, 1998.

[157] E. Orlandini, M. R. Swift, and J. Yeomans. A lattice Boltzmann model of binary-fluid mixtures. *Europhysics Letters*, 32(6):463–468, 1995.

[158] D. M. Petrich and R. E. Goldstein. Nonlocal contour dynamics model for chemical front motion. *Physical Review Letters*, 72(7):1120–1123, 1994.

[159] K. H. Prendergast and K. Xu. Numerical hydrodynamics from gas-kinetic theory. *Journal of Computational Physics*, 109:53–66, 1993.

[160] Y.-H. Qian. *Gaz sur Réseaux et Théorie Cinétique sur Réseaux Appliquée à l'Equation de Navier-Stokes*. PhD thesis, l'Université Pierre et Marie Curie, Paris, 1990.

[161] Y. H. Qian, D. d'Humières, and P. Lallemand. Lattice BGK models for Navier-Stokes equation. *Europhysics Letters*, 17(6):479–484, 1992.

[162] Y. H. Qian and S. A. Orszag. Scalings in diffusion-driven reaction $A + B \rightarrow C$: Numerical simulations by lattice BGK models. *Journal of Statistical Physics*, 81(1/2):237–253, 1995.

[163] D. Raabe. Overview of the lattice Boltzmann method for nano- and microscale fluid dynamics in materials science and engineering. *Modelling and Simulation in Materials Science and Engineering*, 12:R13–R46, 2004.

[164] M. Rheinländer. A consistent grid coupling method for lattice-Boltzmann schemes. *Journal of Statistical Physics*, 121(1-2):49–74, 2005. Special Issue on Mesoscopic Methods in Engineering and Science. Guest Editors: M. Krafczyk, A. J. C. Ladd, and L.-S. Luo.

[165] R. Rico-Martínez, C. W. Gear, and I. G. Kevrekidis. Coarse projective kMC integration: Forward/reverse initial and boundary value problems. *Journal of Computational Physics*, 196(2):474–489, 2004.

[166] C. W. Rowley and J. E. Marsden. Reconstruction equations and the Karhunen-Loève expansion for systems with symmetry. *Physica D: Nonlinear Phenomena*, 142:1–19, 2000.

[167] O. Runborg, C. Theodoropoulos, and I. G. Kevrekidis. Effective bifurcation analysis: A time-stepper-based approach. *Nonlinearity*, 15(2):491–511, 2002.

[168] J.-P. Ryckaert, G. Ciccotti, and H. J. C. Berendsen. Numerical integration of the cartesian equations of motion of a system with constraints: Molecular dynamics of n-alkanes. *Journal of Computational Physics*, 23:327–341, 1977.

[169] Y. Saad. *Numerical Methods for Large Eigenvalue Problems*. Algorithms and architectures for advanced scientific computing. Manchester University Press, Manchester, 1992.

[170] Y. Saad. *Iterative Methods for Sparse Linear Systems*. Society for Industrial and Applied Mathematics, second edition, 2003.

[171] Y. Saad and M. H. Schultz. GMRES: A generalized minimal residual algorithm for solving nonsymmetric linear systems. *SIAM Journal on Scientific and Statistical Computing*, 7(3):856–869, 1986.

[172] G. Samaey. *Patch Dynamics: Macroscopic Simulation of Multiscale Systems*. PhD thesis, Katholieke Universiteit Leuven, 2006.

[173] G. Samaey, D. Roose, and I. G. Kevrekidis. The gap-tooth scheme for homogenization problems. *Multiscale Modeling & Simulation*, 4(1):278–306, 2005.

[174] G. Samaey, D. Roose, and I. G. Kevrekidis. Patch dynamics with buffers for homogenization problems. *Journal of Computational Physics*, 213(1):264–287, 2006.

[175] G. Samaey, D. Roose, W. Vanroose, and I. G. Kevrekidis. Coarse-grained computation of traveling waves of lattice Boltzmann models with Newton-Krylov methods. Technical Report TW 456, Katholieke

Universiteit Leuven, Department of Computer Science, April 2006. submitted to Journal of Computational Physics.

[176] T. Seta and R. Takahashi. Numerical stability analysis of FDLBM. *Journal of Statistical Physics*, 107(1/2):557–572, 2002.

[177] S. Setayeshgar, C. W. Gear, H. G. Othmer, and I. G. Kevrekidis. Application of coarse integration to bacterial chemotaxis. *Multiscale Modeling & Simulation*, 4(1):307–327, 2005.

[178] R. Seydel. *Practical Bifurcation and Stability Analysis: From Equilibrium to Chaos*. Springer-Verlag, 1994.

[179] X. Shan and H. Chen. Lattice Boltzmann model for simulating flows with multiple phases and components. *Physical Review E*, 47(3):1815–1819, 1993.

[180] X. Shan and H. Chen. Simulation of non-ideal gases and liquid-gas phase transitions by the lattice Boltzmann equation. *Physical Review E*, 49(4):2941–2948, 1994.

[181] X. Shan and G. Doolen. Multicomponent lattice-Boltzmann model with interparticle interaction. *Journal of Statistical Physics*, 81(1/2):379–393, 1995.

[182] X. Shan and X. He. Discretization of the velocity space in the solution of the Boltzmann equation. *Physical Review Letters*, 80(1):65–68, 1998.

[183] V. B. Shenoy, R. Miller, E. B. Tadmor, D. Rodney, R. Phillips, and M. Ortiz. An adaptive finite element approach to atomic-scale mechanics – the quasicontinuum method. *Journal of Mechanics and Physics of Solids*, 47:611–642, 1999.

[184] G. M. Shroff and H. B. Keller. Stabilization of unstable procedures: The recursive projection method. *SIAM Journal on Numerical Analysis*, 30(4):1099–1120, 1993.

[185] S. Y. Shvartsman, E. Shütz, R. Imbihl, and I. G. Kevrekidis. Dynamics on microcomposite catalytic surfaces: The effect of active boundaries. *Physical Review Letters*, 83(14):2857–2860, 1999.

[186] C. I. Siettos, A. Armaou, A. G. Makeev, and I. G. Kevrekidis. Microscopic/stochastic timesteppers and "coarse" control: A kMC example. *American Institute of Chemical Engineers Journal*, 49(7):1922–1926, 2004.

[187] C. I. Siettos, M. D. Graham, and I. G. Kevrekidis. Coarse brownian dynamics for nematic liquid crystals: Bifurcation diagrams via stochastic simulation. *Journal of Chemical Physics*, 118(22):10149–10156, 2003.

[188] C. I. Siettos, D. Maroudas, and I. G. Kevrekidis. Coarse bifurcation diagrams via microscopis simulators: A state-feedback control-based approach. In *Proceedings of the 11th Mediterranean Conference on Control and Automation*, pages T7–097, 2003. also arXiv e-Print archive: nlin.AO/0302005.

[189] P. A. Skordos. Initial and boundary conditions for the lattice Boltzmann method. *Physical Review E*, 48(6):4823–4842, 1993.

[190] B. P. Sommeijer. Increasing the real stability boundary of explicit methods. *Computers & Mathematics with Applications*, 19(6):37–49, 1990.

[191] S. Sriraman, I. G. Kevrekidis, and G. Hummer. Coarse nonlinear dynamics and metastability of filling-emptying transitions: Water in carbon nanotubes. *Physical Review Letters*, 95:130603–1–4, 2005.

[192] J. D. Sterling and S. Chen. Stability analysis of lattice Boltzmann models. *Journal of Computational Physics*, 123(1):196–206, 1996.

[193] S. H. Strogatz. *Nonlinear Dynamics and Chaos with Applications in Physics, Biology, Chemistry and Engineering*. Addison-Wesley, 1994.

[194] S. Succi. *The Lattice Boltzmann Equation for Fluid Dynamics and Beyond*. Numerical Mathematics and Scientific Computation. Oxford University Press, 2001.

[195] S. Succi, E. Foti, and F. Higuera. Three-dimensional flows in complex geometries with the lattice Boltzmann method. *Europhysics Letters*, 10(5):433–438, 1989.

[196] M. R. Swift, E. Orlandini, W. Osborn, and J. Yeomans. Lattice Boltzmann simulations of liquid-gas and binary fluid systems. *Physical Review E*, 54(5):5041–5052, 1996.

[197] M. R. Swift, W. R. Osborn, and J. M. Yeomans. Lattice Boltzmann simulation of non-ideal fluids. *Physical Review Letters*, 75(5):830–833, 1995.

[198] G. J. Tee. Eigenvectors of compound-circulant and alternating circulant matrices. Technical Report 479, University of Auckland, Department of Mathematics, March 2002.

[199] C. Theodoropoulos, Y. H. Qian, and I. G. Kevrekidis. "Coarse" stability and bifurcation analysis using time-steppers: A reaction-diffusion example. *Proceedings of the National Academy of Sciences*, 97(18):9840–9843, 2000.

[200] C. Theodoropoulos, K. Sankaranarayanan, S. Sundaresan, and I. G. Kevrekidis. Coarse bifurcation studies of bubble flow lattice Boltzmann simulations. *Chemical Engineering Science*, 59(12):2357–2362, 2004.

[201] J. Tölke, M. Krafczyk, and E. Rank. A multigrid-solver for the discrete Boltzmann equation. *Journal of Statistical Physics*, 107(1/2):573–591, 2002.

[202] J. Tölke, M. Krafczyk, M. Schulz, and E. Rank. Implicit discretization and non-uniform mesh refinement approaches for FD discretizations of LBGK models. *International Journal of Modern Physics C*, 9:1143–1155, 1998.

[203] U. Trottenberg, C. Oosterlee, and A. Schüller. *Multigrid*. Academic Press, London, 2001.

[204] L. S. Tuckerman and D. Barkley. Bifurcation analysis for timesteppers. In E. Doedel and L. Tuckerman, editors, *Numerical methods for bifurcation problems and large-scale dynamical systems*, volume 119 of *The IMA volumes in mathematics and its applications*, pages 453–466. Springer-Verlag, New York, 2000.

[205] R. G. M. van der Sman. *Lattice Boltzmann Schemes for Convection-Diffusion Phenomena: Applications to Packages of Agricultural Products*. PhD thesis, Landbouwuniversiteit Wageningen, May 1999.

[206] R. G. M. van der Sman. Diffusion on unstructured triangular grids using lattice Boltzmann. *Future Generation Computer Systems*, 20(6):965–971, 2004.

[207] R. G. M. van der Sman. Finite Boltzmann schemes. *Computers & Fluids*, 35(8-9):849–859, 2006.

[208] R. G. M. van der Sman and M. H. Ernst. Diffusion lattice Boltzmann scheme on a orthorhombic lattice. *Journal of Statistical Physics*, 94(1/2):203–217, 1999.

[209] R. G. M. van der Sman and M. H. Ernst. Convection-diffusion lattice Boltzmann scheme for irregular lattices. *Journal of Computational Physics*, 160(2):766–782, 2000.

[210] P. Van Leemput and K. Lust. Numerical bifurcation analysis of lattice Boltzmann models: A reaction-diffusion example. In M. Bubak, G. D. van Albada, P. M. Sloot, and J. Dongarra, editors, *Computational Science – ICCS 2004*, volume 3039 of *Lecture Notes in Computer Science*, pages 572–579. Springer-Verlag, 2004.

[211] P. Van Leemput, K. Lust, and I. G. Kevrekidis. Coarse-grained numerical bifurcation analysis of lattice Boltzmann models. *Physica D: Nonlinear Phenomena*, 210(1–2):58–76, 2005.

[212] P. Van Leemput, G. Samaey, K. Lust, D. Roose, and I. G. Kevrekidis. Coarse-grained simulation and bifurcation analysis using microscopic time-steppers. In A. Di Bucchianico, R. Mattheij, and M. Peletier, editors, *Progress in Industrial Mathematics at ECMI 2004*, volume 8 of *Mathematics in Industry*, pages 626–630. The European Consortium for Mathematics in Industry, Springer, 2006.

[213] P. Van Leemput, C. Vandekerckhove, W. Vanroose, and D. Roose. Accuracy of hybrid lattice Boltzmann/finite difference schemes for reaction-diffusion systems. Technical Report TW 476, Katholieke Universiteit Leuven, Department of Computer Science, November 2006. Accepted in Multiscale Modeling & Simulation.

[214] P. Van Leemput, W. Vanroose, and D. Roose. Initialization of a lattice Boltzmann model with constrained runs. Technical Report TW 444, Katholieke Universiteit Leuven, Department of Computer Science, December 2005.

[215] P. Van Leemput, W. Vanroose, and D. Roose. Numerical and analytical spatial coupling of a lattice Boltzmann model and a partial differential equation. In A. N. Gorban, N. Kazantzis, I. G. Kevrekidis, H. C. Ottinger, and C. Theodoropoulos, editors, *Model Reduction and Coarse-Graining Approaches for Multiscale Phenomena*, pages 423–441. Springer, 2006.

[216] C. Vandekerckhove. private communication, 2006.

[217] C. Vandekerckhove and D. Roose. Accuracy analysis of time integration schemes for stiff multiscale problems. Technical Report TW 457, Katholieke Universiteit Leuven, Department of Computer Science, 2006. To appear in Journal of Computational and Applied Mathematics.

[218] C. Vandekerckhove, D. Roose, and K. Lust. Numerical stability analysis of an acceleration scheme for step size constrained time integrators.

Journal of Computational and Applied Mathematics, 200(2):761–777, 2007.

[219] C. Vandekerckhove, P. Van Leemput, and D. Roose. Acceleration of lattice Boltzmann models through state extrapolation: A reaction-diffusion example. Technical Report TW 466, Katholieke Universiteit Leuven, Department of Computer Science, August 2006. Submitted to Applied Numerical Mathematics.

[220] C. Vandekerckhove, P. Van Leemput, and D. Roose. Accuracy and stability of the coarse time-stepper for a lattice boltzmann model. submitted to Journal of Algorithms & Computational Technology, February 2007.

[221] S. Vandewalle. *Parallel Multigrid Waveform Relaxation for Parabolic Problems*. B. G. Teubner Stuttgart, 1993.

[222] W. Vanroose, G. Samaey, and P. Van Leemput. Coarse-grained analysis of a lattice boltzmann model for planar streamer fronts. Technical Report TW 479, Katholieke Universiteit Leuven, Department of Computer Science, December 2006.

[223] R. S. Varga. Eigenvalues of circulant matrices. *Pacific Journal of Mathematics*, 4(1):151–160, 1954.

[224] R. Verberg and A. J. C. Ladd. Simulation of low-Reynolds-number flow via a time-independent lattice-Boltzmann method. *Physical Review E*, 60(3):3366–3373, 1999.

[225] H. S. Wijesinghe and N. G. Hadjiconstantinou. A discussion of hybrid atomistic-continuum methods for multiscale hydrodynamics. *International Journal for Multiscale Computational Engineering*, 2(2):189–202, 2004.

[226] A. T. Winfree. Stable particle-like solutions to the nonlinear wave equations of three-dimensional excitable media. *SIAM Review*, 32(1):1–53, 1990.

[227] D. Wolf-Gladrow. A lattice Boltzmann equation for diffusion. *Journal of Statistical Physics*, 79(5/6):1023–1032, 1995.

[228] D. A. Wolf-Gladrow. *Lattice-Gas Cellular Automata and Lattice Boltzmann Models – An Introduction*. Springer, 2000.

[229] K. Xu and K. H. Prendergast. Numerical Navier-Stokes solutions from gas kinetic theory. *Journal of Computational Physics*, 114:9–17, 1994.

[230] G. Yan and L. Yuan. Lattice Bhatnagar-Gross-Krook model for the Lorenz attractor. *Physica D*, 154(1-2):43–50, 2001.

[231] G. Yan and L. Yuan. A lattice Boltzmann method for the chemical clock in the Belousov-Zhabotinskii reaction. *Chinese Physics Letters*, 18(7):918–920, 2001.

[232] H. Yu, S. S. Girimaji, and L.-S. Luo. DNS and LES of decaying isotropic turbulence with and without frame rotation using lattice Boltzmann method. *Journal of Computational Physics*, 209(2):599–616, 2005.

[233] H. Yu, S. S. Girimaji, and L.-S. Luo. Lattice Boltzmann simulations of decaying homogeneous isotropic turbulence. *Physical Review E*, 71(1):016708–1–5, 2005.

[234] H. Yu, L.-S. Luo, and S. S. Girimaji. LES of turbulent square jet flow using an MRT lattice Boltzmann model. *Computers & Fluids*, 35(8/9):957–965, 2006.

[235] A. Zagaris. private communication, 2006.

[236] A. Zagaris, H. G. Kaper, and T. J. Kaper. Fast and slow dynamics for the computational singular perturbation method. *Multiscale Modelling and Simulation*, 2(4):613–638, 2004.

[237] A. Zagaris, H. G. Kaper, and T. J. Kaper. Two perspectives on reduction of ordinary differential equations. *Mathematische Nachrichten*, 278(12-13):1629–1642, 2005.

[238] R. Zwanzig. Memory effects in irreversible thermodynamics. *Physical Review*, 124(4):983–992, 1961.

Scientific Résumé

Publications

- P. Van Leemput, C. Vandekerckhove, W. Vanroose, and D. Roose. Accuracy of hybrid lattice Boltzmann/finite difference schemes for reaction-diffusion systems, accepted in *Multiscale Modeling and Simulation*, April 2007.
- C. Vandekerckhove, P. Van Leemput, and D. Roose. Accuracy and stability of the coarse time-stepper for a lattice Boltzmann model, submitted to *Journal of Algorithms & Computational Technology*, February 2007.
- W. Vanroose, G. Samaey, and P. Van Leemput. Coarse-grained analysis of a lattice Boltzmann model for planar streamer fronts, submitted. Also Technical Report TW 479, Dept. of Computer Science, K.U.Leuven, December 2006.
- C. Vandekerckhove, P. Van Leemput, and D. Roose. Acceleration of lattice Boltzmann models through state extrapolation: A reaction-diffusion example, submitted to *Applied Numerical Mathematics*. Also Technical Report TW 466, Dept. of Computer Science, K.U.Leuven, August 2006.
- P. Van Leemput, W. Vanroose, and D. Roose. Numerical and analytical spatial coupling of a lattice Boltzmann model and a partial differential equation, *Model Reduction and Coarse-Graining Approaches for Multiscale Phenomena* (A.N. Gorban, N. Kazantzis, I.G. Kevrekidis, H.C. Ottinger, C. Theodoropoulos eds.), pp. 423–441. Springer, 2006.
- P. Van Leemput, G. Samaey, K. Lust, D. Roose, and I.G. Kevrekidis. Coarse-grained simulation and bifurcation analysis using microscopic time-steppers, *Progress in Industrial Mathematics at ECMI 2004* (A. Di Bucchianico, R.M.M. Mattheij, M.A. Peletier eds.), *Mathematics in Industry Series*, vol. 8, pp. 626–630, Springer, 2006.

- P. Van Leemput, W. Vanroose, and D. Roose. Initialization of a lattice Boltzmann model with constrained runs, submitted. Also Technical Report TW 444, Dept. of Computer Science, K.U.Leuven, December 2005.

- P. Van Leemput, K. Lust, and I.G. Kevrekidis. Coarse-grained numerical bifurcation analysis of lattice Boltzmann models, *Physica D – Nonlinear Phenomena* 210 (1-2), pp. 58–76, 2005.

- P. Van Leemput, and K. Lust. Numerical bifurcation analysis of lattice Boltzmann models: A reaction-diffusion example, *Computational Science – ICCS 2004* (M. Bubak, G.D. van Albada, P.M.A. Sloot and J. Dongarra, eds.), vol 3039, Lecture Notes in Computer Science, pp. 572–579, 2004.

Contributions at International Conferences

- Equation-free lifting: A lattice Boltzmann case study. *Mathematics of Model Reduction*, University of Leicester, UK, August 28-30, 2007.

- Accuracy of hybrid spatially coupled LBM/FD schemes, *Fourth International Conference for Mesoscopic Methods in Engineering and Science (ICMMES)*, Munich, Germany, July 16-20, 2007.

- Multiscale coupling of macroscopic and mesoscopic models, *SIAM Conference on Applications of Dynamical Systems*, Snowbird, Utah, USA, May 28-June 1, 2007.

- Equation-free lifting with constrained runs: A lattice Boltzmann case study, *Workshop on Topics in Nonlinear Dynamics and Complexity*, Puebla, Mexico, February 19-23, 2007 *(presented by D. Roose)*.

- Numerical analysis of the constrained runs initialization scheme for a lattice Boltzmann model, *Third International Conference for Mesoscopic Methods in Engineering and Science (ICMMES)*, Hampton, Virginia, USA, July 24-28, 2006.

- Multiscale interfacing for lattice Boltzmann models using constrained runs, *Seventh World Congress on Computational Mechanics (WCCM)*, Los Angeles, California, USA, July 16-22, 2006.

- Multiscale lattice Boltzmann interfacing, *Twelfth International Congress on Computational and Applied Mathematics (ICCAM)*, Leuven, Belgium, July 10-14, 2006.

- Multiscale computing: Macroscopic dynamics from microscopic models, *Eight European Multigrid Conference (EMG)*, Scheveningen, the Netherlands, September 27-30, 2005 *(presented by D. Roose)*.
- Micro/macro interfacing for lattice Boltzmann models, *Model Reduction and Coarse-Graining for Multiscale Phenomena*, Leicester, UK, August 24-26, 2005.
- Constructing the coarse-grained time stepper for a lattice Boltzmann model, *SIAM Conference on Computational Science & Engineering*, Orlando, Florida, USA, February 12-15, 2005.
- The coarse-grained time stepper for a lattice Boltzmann model, *First International Conference for Mesoscopic Methods in Engineering and Science (ICMMES)*, Braunschweig, Germany, July 26-30, 2004.
- Coarse-grained simulation and bifurcation analysis using microscopic time-steppers, *Thirteenth European Conference on Mathematics for Industry (ECMI)*, Eindhoven, the Netherlands, June 21-25, 2004 *(presented by D. Roose)*.
- Numerical bifurcation analysis of lattice Boltzmann models: A reaction-diffusion example, *International Conference on Computational Science (ICCS)*, Krakow, Poland, June 6-9, 2004.
- Numerical bifurcation analysis of lattice Boltzmann models, *Workshop on Continuation and Analysis of Bifurcations 2004*, Sevilla, Spain, May 19-21, 2004 *(presented by K. Lust)*.
- Numerical bifurcation analysis of lattice Boltzmann models: With or without equations?, *SIAM Conference on Applications of Dynamical Systems*, Snowbird, Utah, USA, May 27-31, 2003 *(presented by K. Lust)*.

Minisymposium Organization

- Dimension Reduction Methodologies for Spatially Extended Systems, *SIAM Conference on Applications of Dynamical Systems*, Snowbird, Utah, USA, May 29, 2007 *(together with dr. A. Zagaris)*.

Further Conferences and Workshops Attended

- *Woudschoten Conference of the Dutch-Flemish Numerical Analysis Communities*, Zeist, the Netherlands, October 11-13, 2006, October 12-14, 2005, October 6-8, 2004, October 1-3, 2003.

- *Workshop on Applied Dynamical Systems: Advanced Numerical Methods for Mathematical Modeling*, Ghent University, June 22-23, 2006.
- *CCP5 and Marie Curie Actions: Methods in Molecular Simulation Summer School*, University of Cardiff, Wales, UK, July 11-19, 2005.
- *Qualitative Numerical Analysis of High-dimensional Nonlinear Systems*, University of Bristol, Bristol, UK, March 21-24, 2005.
- *Course on Particle-Based Modeling of Transport Phenomena*, Wageningen University, Ede, the Netherlands, October 12-15, 2004.
- *Multiscale Methods in Science and Engineering*, Uppsala University, Uppsala, Sweden, January 26-28, 2004.
- *Equadiff 2003: International Conference on Differential Equations*, Hasselt, Belgium, July 22-26, 2003.
- *Workshop on Mathematical and Numerical Methods for Modelling in the Life Sciences*, Ghent University, Belgium, November 28-29, 2002.

Teaching Assistant

- Numerical Simulation of Differential Equations. Second year Master of Applied Sciences and Engineering: Mathematical Engineering (2002 – 2007).
- Higher Mathematics III. Second year Bachelor of Applied Sciences and Engineering: Architecture (2002 – 2007).
- Numerical Mathematics. Second year Bachelor of Applied Sciences and Engineering (2006 – 2007).
- Mathematical Analysis I. First year Bachelor of Applied Sciences and Engineering (2005 – 2006).

Supervision of Master Thesis

- Pieter Ghysels. Development of a parallel lattice Boltzmann simulator. Promotors: D. Roose and W. Vanroose (2005 – 2006).

Meerschalige en Vergelijkingsvrije Simulaties met Rooster Boltzmann Modellen

Pieter Van Leemput
Departement Computerwetenschappen, K.U.Leuven
Celestijnenlaan 200A, B-3001 Leuven, België

Samenvatting

Vele fysische en scheikundige processen kunnen op verschillende abstractieniveaus beschreven worden omwille van een scheiding van tijd- en ruimteschalen in hun dynamica. We beschouwen twee meerschalige modelleringstechnieken die deze scheiding uitbuiten. Het vergelijkingsvrije raamwerk, ontwikkeld door Kevrekidis en collega's, laat een tijdsevolutie toe voor een onbekend macroscopisch model door enkel microscopische of mesoscopische simulaties te gebruiken. Ruimtelijk hybride modellen koppelen een microscopisch of mesoscopisch deeltjes-gebaseerd model aan een macroscopisch model in de ruimte. Op microscopisch/mesoscopisch niveau beschouwen we rooster Boltzmann modellen voor eendimensionale reactie-diffusie systemen.

Eerst tonen we aan hoe tijdstapper-gebaseerde methodes voor numerieke bifurcatieanalyse, ontwikkeld voor partiële differentiaalvergelijkingen, kunnen gebruikt worden voor rooster Boltzmann modellen. We gebruiken zowel het rooster Boltzmann model zelf als de tijdstapper, als de vergelijkingsvrije tijdstapper gebaseerd op het rooster Boltzmann model.

Vervolgens spitsen we ons toe op het probleem van de meerschalige koppeling. Tijdens initialisatie en ruimtelijke koppeling moet men de gegeven macroscopische grootheden afbeelden op een grotere verzameling van onbekende microscopische of mesoscopische variabelen. Dit leidt tot een aantal vrijheidsgraden die correct moeten ingevuld worden. We bestuderen de invloed van het initialisatieproces op de minimale tijdstap van de vergelijkingsvrije tijdstapper en de nauwkeurigheid van de resultaten. Verder analyseren we het gedrag van het *constrained runs* (simulatie-met-beperkingen) initialisatiealgoritme voor de beschouwde rooster Boltzmann modellen. We bewijzen dat dit algoritme onvoorwaardelijk stabiel is en dat het algoritme convergeert tot op een eerste orde benadering van de Chapman-Enskog relaties. We implementeren ook initialisatiealgoritmes die interpolatietechnieken gebruiken om een grotere nauwkeurigheid te bekomen.

Tenslotte analyseren we de ruimtelijke discretizatiefout van het hybride model dat ontstaat door een rooster Boltzmann model ruimtelijk te koppelen met een eindige differentie discretisatie van een partiële differentiaalvergelijking. We tonen aan dat de globale fout één orde minder nauwkeurig is dan de lokale fout die gemaakt wordt in de koppelingszone. Voor de koppeling kunnen zowel de Chapman-Enskog relaties als het *constrained runs* algoritme gebruikt worden.

Nederlandstalige Samenvatting

Inhoudsopgave

1 Modellering op Verschillende Niveaus **182**

2 Meerschalige en Vergelijkingsvrije Simulaties **183**

3 Rooster Boltzmann Modellen **184**
3.1 Rooster Boltzmann Modellen voor Reactie-Diffusie 184
3.2 Beschrijving van de Toestand 185

4 Tijdstapper-Gebaseerde Bifurcatieanalyse **186**

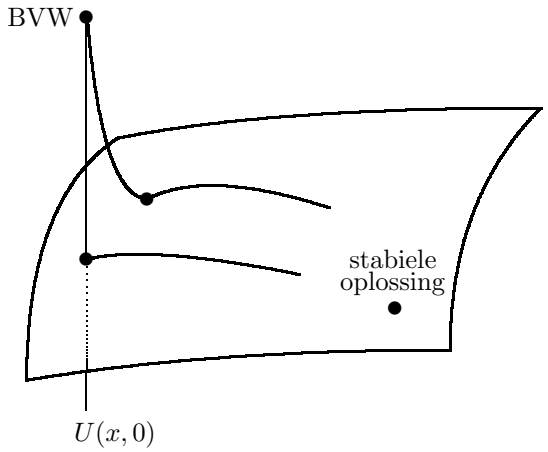
5 Initialisatie **188**

6 Analyse van het Constrained Runs Algoritme **190**
6.1 Algoritme 191
6.2 Stabiliteit en Convergentie 191

7 Constrained Runs: Toepassingen en Uitbreidingen **192**

8 Hybride Ruimtelijke Koppeling **194**
8.1 Opzet en Implementatie 194
8.2 Foutenanalyse bij Statisch Evenwicht 195
8.3 Numerieke Resultaten 195

9 Besluiten **196**
9.1 Belangrijkste Bijdragen en Besluiten 196
9.2 Richtlijnen voor Verder Onderzoek 197



Figuur 1: Schets van een trage aantrekkende meervoudigheid in de faseruimte. We nemen aan dat er een stabiele statische oplossing bestaat.

1 Modellering op Verschillende Niveaus

Wanneer men de dynamica van een fysisch of scheikundig systeem wil beschrijven, kan men vaak kiezen uit een heel scala van modellen. Op macroscopisch niveau zijn er de gewone of partiële differentiaalvergelijkingen (PDE) die het systeem beschrijven aan de hand van enkele macroscopisch observeerbare en traag variërende grootheden $U(x,t)$, functie van ruimte x en tijd t. De macroscopische grootheden zijn typisch gedefinieerd als de laagste orde momenten van de microscopische variabelen $u(x,t)$ van een onderliggend meer microscopisch model. Een voorbeeld is de dichtheid $\rho(x,t)$.

Dikwijls heeft men echter een beschrijving van het dynamische systeem op een lager, meer microscopisch niveau als een verzameling van ruimtelijk verspreide deeltjes (atomen of moleculen) met welbepaalde interactie- en gedragsregels. Vaak organiseren deze deeltjes zich zo dat er macroscopisch waarneembare fenomenen ontstaan zoals patronen en golven. Veelgebruikte modellen op microscopisch niveau zijn moleculaire dynamica en kinetische Monte Carlo modellen. Daartussenin definieert men zogenaamde mesoscopische modellen, zoals rooster Boltzmann modellen (LBM), die de evolutie van verdelingsfuncties van deeltjes beschrijven. De keuze voor een bepaald model hangt af van de complexiteit van de microscopische interacties en de graad van detail die nodig is voor een correcte simulatie of die gewenst is door de gebruiker.

Microscopische deeltjessimulaties hebben het nadeel dat ze een enorme rekenkracht vergen waardoor ze vaak beperkt zijn tot korte simulaties over kleine ruimtelijke domeinen. In vele gevallen is er echter een scheiding van

tijd- en ruimteschalen in de effectieve dynamica van het meerschalige dynamische systeem waardoor een volledige microscopische beschrijving na een bepaalde tijd of in bepaalde delen van de ruimte nodeloos complex is. Tijdens de simulatie gebeurt typisch het volgende (zie Fig. 1). Startend van een microscopische beginvoorwaarde (BVW), overeenkomstig de macroscopische beginvoorwaarde $U(x,0)$, worden de microscopische variabelen $u(x,t)$ na een korte overgangsfase functionaal van de macroscopische variabelen $U(x,t)$, d.i. $u = s(U)$ waarbij de functionalen (de *slaving* relaties) $s(U)$ probleemafhankelijk zijn. Daarna kan de gehele evolutie beschreven worden door een macroscopische gereduceerde (PDE) vergelijking voor U op de zogenaamde trage meervoudigheid (*manifold*), d.i. het gedeelte van de faseruimte waartoe alle overgangstrajecten worden aangetrokken. Door de gepaste hogere orde momenten V van u te definiëren, kan men de volledige faseruimte ook beschrijven in functie van U en V.

2 Meerschalige en Vergelijkingsvrije Simulaties

Het efficiënt gebruik van het microscopische model in beperkte tijds- en/of ruimteintervallen kan leiden tot een grote reductie van de rekenkundige complexiteit waardoor simulaties over grotere tijdsintervallen en ruimtelijke domeinen mogelijk worden. We concentreren ons in deze tekst op twee meerschalige methodes die hierop gebaseerd zijn, zijnde vergelijkingsvrije en hybride modellering.

Vaak is het expliciet opstellen van een macroscopisch model in functie van enkele $U(x,t)$ erg moeilijk, hoewel conceptueel wel mogelijk. De vergelijkingsvrije tijdstapper (of tijdsimulator) ontwikkeld door Kevrekidis en collega's [108] laat toe om op efficiënte wijze een macroscopische tijdsevolutie uit te voeren voor het onbekende macroscopische model, daarbij enkel gebruik makend van microscopische simulaties. De tijdstapper is een opeenvolging van de volgende stappen: 1) reconstructie (*lifting*), d.i. initialisatie van de microscopische variabelen $u(x,0)$ of de hogere orde momenten $V(x,0)$ op basis van enkele macroscopische beginvoorwaarden $U(x,0)$; 2) simulatie met het microscopisch model over een bepaald tijdsinterval ΔT; en 3) restrictie, d.i. berekening van $U(x,\Delta T)$ op basis van de bekomen $u(x,\Delta T)$. Deze tijdsintegrator kan dan gecombineerd worden met versnellingstechnieken om de simulatie efficiënter te maken. Mits enkele aanpassingen kunnen bestaande macroscopische numerieke methodes die oorspronkelijk ontwikkeld werden voor PDE, hierop toegepast worden. Door het onderliggende microscopische (en mogelijk stochastische) model te vervangen door een deterministisch mesoscopisch rooster Boltzmann model, zijn we in staat om een grondige analyse uit te voeren van het vergelijkingsvrije model zelf. Merk op dat we daarom de termen microscopisch en mesoscopisch door elkaar gebruiken. Dit houdt in dat de meeste vergelijkingsvrije technieken ook

rechtstreeks kunnen toegepast worden op LBM simulaties. We benadrukken dat men bij vergelijkingsvrije modellering enkel beschikt over het microscopische model voor $u(x,t)$. De gereduceerde vergelijking voor $U(x,t)$ en de functionaalrelaties $u = s(U)$ zijn onbekend.

Hybride modellen ontstaan door het ruimtelijke domein in stukken op te delen en op elk stuk een gepast microscopisch of macroscopisch model te gebruiken. Daar waar de interacties microscopisch erg complex zijn, moet een microscopisch model gebruikt worden, terwijl in een ander deel van de ruimte een macroscopisch model voldoende is. Zo wordt het gebruik van de rekenintensieve microscopische simulaties beperkt tot de gebieden van de ruimte waar ze strikt noodzakelijk zijn, wat een aanzienlijke tijdswinst oplevert. De heterogene modellen moeten op een wiskundig correcte wijze aan elkaar gekoppeld worden.

Bij zowel vergelijkingsvrije als hybride modellering moet er informatie uitgewisseld worden tussen de macroscopische en de microscopische beschrijving. Bij hybride modellen moeten er voor de ruimtelijke koppeling van de modellen randvoorwaarden voorzien worden. Typisch worden de macroscopische variabelen $U(x,t)$ eenduidig berekend door uitmiddeling van de microscopische $u(x,t)$. Het omgekeerde probleem, zijnde de vertaling van $U(x,t)$ naar een groter aantal $u(x,t)$ is helemaal niet eenduidig. Bij de initialisatiefase in het vergelijkingsvrije raamwerk stelt zich hetzelfde probleem (zie hoger).

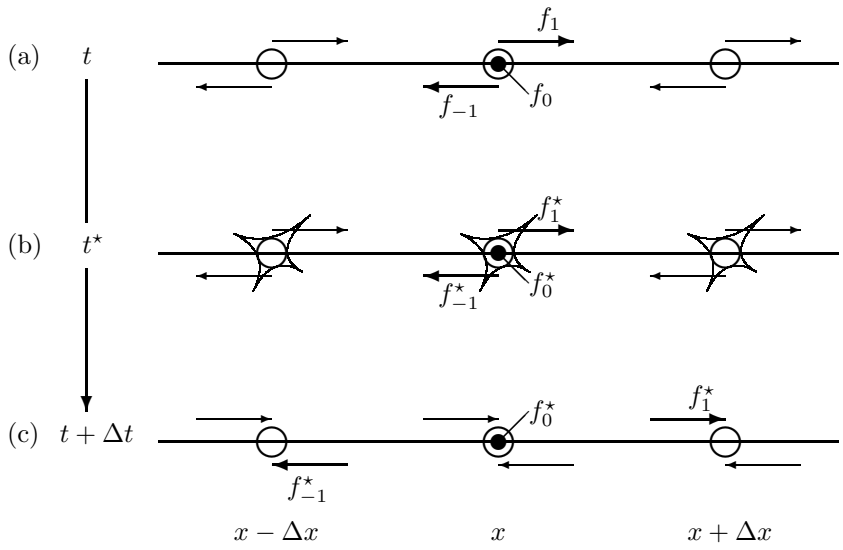
3 Rooster Boltzmann Modellen

In deze sectie beschrijven we de rooster Boltzmann modellen (LBM) die in de tekst als modelproblemen gebruikt worden. We focussen ons op LBM voor reactie-diffusie systemen op een eendimensionaal domein. We tonen aan hoe deze modellen passen binnen het vergelijkingsvrije raamwerk.

3.1 Rooster Boltzmann Modellen voor Reactie-Diffusie

Rooster Boltzmann modellen [34] beschrijven de evolutie van verdelingsfuncties $f_i(x,t)$ voor deeltjes met snelheid v_i die bewegen op een ruimtelijk rooster. We beschouwen slechts drie snelheden $v_i = c_i \Delta x/\Delta t$ met $c_i = i \in \{-1, 0, 1\}$ op het eendimensionale domein. De variabele Δx is de ruimtelijke roosterafstand, Δt de tijdstap en c_i de dimensieloze roostersnelheid. Dit komt overeen met deeltjes die naar links ($c_{-1} = -1$), rechts ($c_1 = 1$) en niet ($c_0 = 0$) bewegen. De vergelijking die de evolutie van de verdelingsfuncties beschrijft, is gedefinieerd als

$$f_i(x + c_i\Delta x, t + \Delta t) = (1-\omega) f_i(x,t) + \omega f_i^{eq}(x,t) + \frac{\Delta t}{3} F(\rho(x,t)) \ , \quad (1)$$



Figuur 2: LBM evolutie voor een tijdstap Δt rond het roosterpunt x. (a) De verdelingsfuncties $f_i(x,t)$ ondergaan lokale botsingen en reacties (b). De bekomen waarden $f_i^\star(x,t^\star)$ propageren daarna naar naburige roosterpunten (c).

met $i \in \{-1,0,1\}$. Het lokale evenwicht $f_i^{eq}(x,t)$ voor de diffusieve botsingen wordt berekend als $f_i^{eq}(x,t) = (1/3)\rho(x,t)$. De LBM evolutie is stabiel als de parameter $\omega \in (0,2)$. De deeltjesdichtheid $\rho(x,t)$ is de macroscopische grootheid en is gedefinieerd als het nulde orde snelheidsmoment van de verdelingsfuncties

$$\rho(x,t) = \sum_{i=-1}^{1} f_i(x,t) \; . \tag{2}$$

De LBM evolutie verloopt in twee stappen. In de lokale botsingsstap wordt eerst het rechterlid van (1) geëvalueerd. Dit leidt tot de waarden $f_i^\star(x,t^\star)$ na botsing. Daarna propageren de deeltjes naar een naburig roosterpunt volgens hun roostersnelheid, d.i. $f_i(x+c_i\Delta x, t+\Delta t) = f_i^\star(x,t^\star)$. Dit gedrag wordt geïllustreerd in Fig. 2.

3.2 Beschrijving van de Toestand

Analoog aan de definitie van de dichtheid (2) definiëren we de volgende geschaalde hogere orde snelheidsmomenten: het eerste moment, de 'impuls'

$\phi(x,t) = \sum_i c_i f_i(x,t)$ en het tweede, de (kinetische) 'energie' $\xi(x,t) = (1/2)\sum_i c_i^2 f_i(x,t)$. De toestandsvector van het LBM kan nu door zowel de drie verdelingsfuncties $\mathbf{f} = [f_{-1}\ f_0\ f_1]'$ als de drie momenten $\boldsymbol{\varrho} = [\rho\ \phi\ \xi]'$ beschreven worden. Men kan makkelijk van de ene voorstelling naar de andere overgaan via

$$\boldsymbol{\varrho} = \begin{bmatrix} \rho \\ \phi \\ \xi \end{bmatrix} = \begin{bmatrix} 1 & 1 & 1 \\ -1 & 0 & 1 \\ \frac{1}{2} & 0 & \frac{1}{2} \end{bmatrix} \begin{bmatrix} f_{-1} \\ f_0 \\ f_1 \end{bmatrix} = M\,\mathbf{f} \tag{3}$$

en omgekeerd $\mathbf{f} = M^{-1}\boldsymbol{\varrho}$. De analogie met de notatie in Sect. 1–2 is als volgt: $U = \rho$, $V = [\phi\ \xi]'$ en $u = f_i$.

Wanneer de dichtheid voldoende zacht verlopend is, kan de LBM vergelijking (1) gereduceerd worden tot de equivalente PDE

$$\frac{\partial \rho(x,t)}{\partial t} = D\frac{\partial^2 \rho(x,t)}{\partial x^2} + F(\rho(x,t))\ , \tag{4}$$

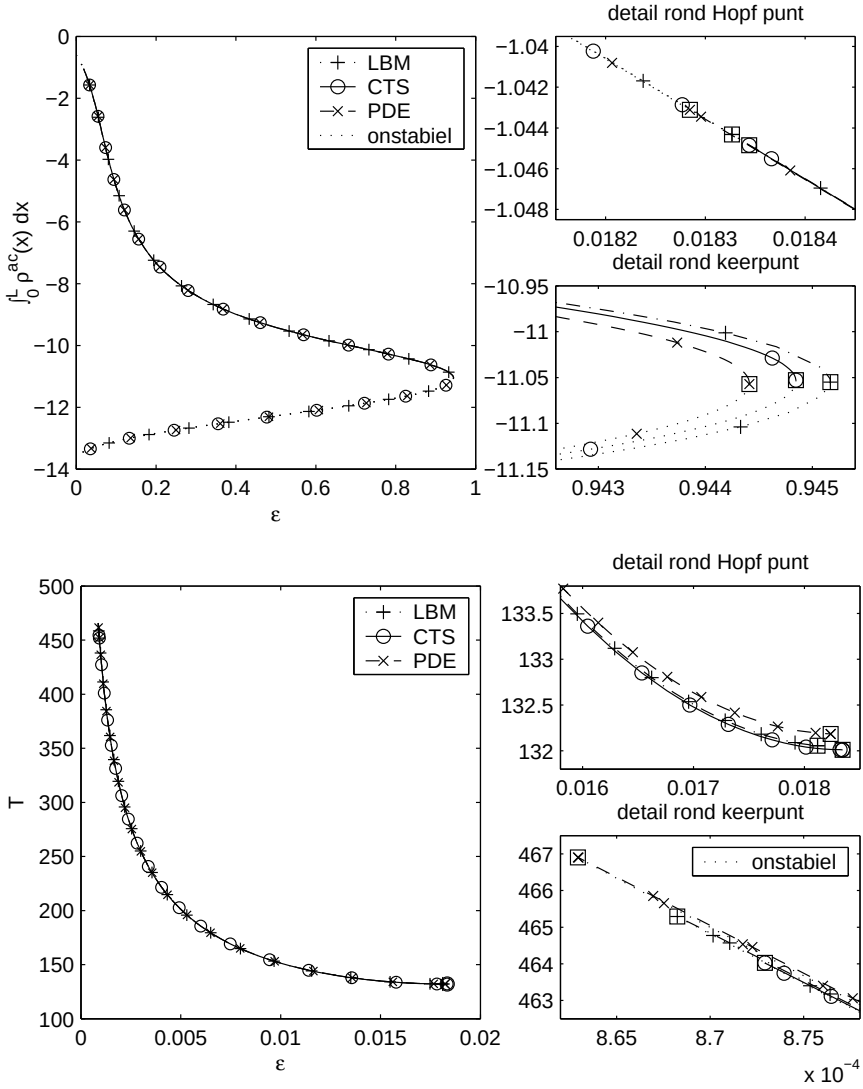
met D de diffusiecoëfficient en F de macroscopische reactieterm die afhangt van de verschillende deeltjesdichtheden. De reductie gebeurt met behulp van een meerschalige Chapman-Enskog expansie. Hierbij worden de hogere orde momenten (of de verdelingsfuncties) uitgedrukt als functionalen van de macroscopische variabelen op de trage meervoudigheid waarop ook de PDE beschrijving geldt. Deze functionaalrelaties (de zogenaamde *slaving* relaties) kunnen afgeleid worden als

$$\begin{aligned} \phi &= -\frac{2\Delta x}{3\,\omega}\frac{\partial \rho}{\partial x} + \frac{\Delta x \Delta t}{3\omega^2}\frac{(4\omega-2)}{(\omega-2)}\frac{\partial F(\rho)}{\partial x} + \frac{\Delta x \Delta t}{3\omega^2}\frac{(-2\omega^2+2\omega-2)}{(\omega-2)}\frac{\partial^2 \rho}{\partial x \partial t}\ , \\ \xi &= \frac{1}{3}\rho - \frac{\Delta t}{6\,\omega}\left(F(\rho) - \frac{\partial \rho}{\partial t}\right) + \mathcal{O}(\Delta x^4)\ . \end{aligned} \tag{5}$$

Tenslotte kan de volledige evolutie van het LBM ook beschreven worden via vergelijkingen voor de momenten (door (1) en (3) te combineren).

4 Tijdstapper-Gebaseerde Bifurcatieanalyse

Tijdsintegratie is een voor de hand liggende methode om de invloed van variërende parameters in een dynamisch systeem te bestuderen. Deze aanpak is echter tijdrovend als er veel mogelijke parameterwaarden zijn. Bifurcatieanalyse biedt een meer systematische aanpak om het asymptotische gedrag van parameterafhankelijke systemen te bestuderen. Men berekent takken van oplossingen (bijvoorbeeld statische of periodieke oplossingen) en zoekt naar kritische parameterwaarden (de bifurcatiepunten) die een verandering



Figuur 3: Bifurcatiediagram van statische (boven) en periodieke (onder) oplossingen voor het FitzHugh-Nagumo LBM, het vergelijkingsvrije LBM (aangeduid met CTS) en de PDE. De macroscopische tijdstap bedraagt $\Delta T = 5 = 5000\Delta t$. De stippellijnen duiden onstabiele oplossingen aan. De bifurcatiepunten worden aangeduid met een vierkant symbool.

in de stabiliteit van de oplossing en/of een overgang tussen de verschillende soorten oplossingen aanduiden.

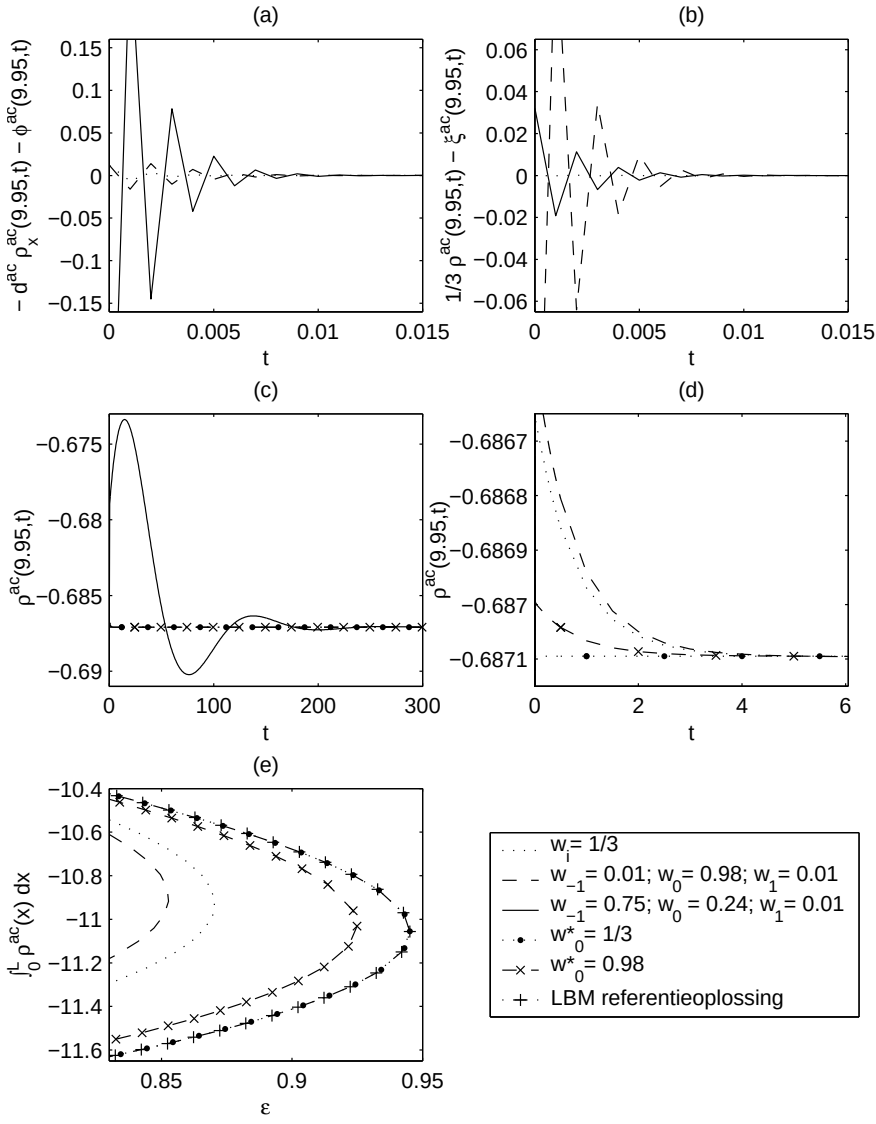
De stabiliteit van een oplossing wordt bepaald door de eigenwaarden van de Jacobiaanmatrix van het gelineariseerde model. Voor hoog-dimensionale systemen is het opstellen van deze matrix echter erg rekenintensief. Recent werden er zogenaamde matrix-vrije methodes ontwikkeld voor de bifurcatieanalyse van PDE die de directe berekening van de Jacobiaanmatrix vermijden. Wij gebruiken de tijdstapper-gebaseerde Newton-Picard methode [135]. We tonen aan dat zulke tijdstapper-gebaseerde methodes ook kunnen gebruikt worden voor de bifurcatieanalyse van LBM. Als tijdstapper gebruiken we het LBM zelf of de vergelijkingsvrije tijdstapper voor het LBM. Deze laatste is gedefinieerd als volgt. Na de reconstructie- of initialisatiefase (zie Sect. 5–7) evolueren we het LBM (1) over een macroscopische tijdstap ΔT. Daarna berekenen we $\rho(x, t + \Delta T)$ via (2) in de restrictiefase. Als $\Delta T < T$ wordt deze procedure herhaald binnen het tijdsinterval $[0, T]$.

Figuur 3 toont de takken van statische en periodieke oplossingen voor het FitzHugh-Nagumo reactie-diffusie systeem als functie van de bifurcatieparameter ε van het systeem. We gebruiken de integraal van de dichtheid over het domein en de periode T als maat voor de oplossing. De gebruikte modellen zijn het LBM, de vergelijkingsvrije LBM tijdstapper (aangeduid met CTS) en de PDE. Als bifurcatiepunten vinden we een keerpunt voor $\varepsilon \approx 0945$ en een Hopf punt voor $\varepsilon \approx 0.0183$. De berekende oplossingen, de bifurcatiepunten en de dominante eigenwaarden die de stabiliteit bepalen, komen erg goed overeen.

5 Initialisatie

De initialisatie van een microscopische simulatie op basis van gegeven macroscopische beginvoorwaarden introduceert een aantal vrijheidsgraden omdat er typisch meer microscopische variabelen dan macroscopische initiële gegevens zijn. Dit probleem stelt zich zowel bij pure microscopische simulaties als in de reconstructiestap bij vergelijkingsvrije modellering. Met behulp van het LBM in Sect. 3 demonstreren we dat de scheiding van tijdschalen en het bijhorende snel functionaal worden van de hogere orde momenten ϕ en ξ t.o.v. het laagste orde moment ρ, niet noodzakelijk de garantie biedt dat de effecten van een onnauwkeurige initialisatie snel verdwijnen. Integendeel, we tonen aan dat een slordige initialisatie een significante invloed kan hebben op zowel de nauwkeurigheid van de vergelijkingsvrije tijdstapper als op de minimale grootte van de macroscopische tijdstap ΔT.

Wanneer de relaties (5) bekend zijn, kunnen deze gebruikt worden om het model te initialiseren. In de context van vergelijkingsvrije simulatie (en voor bepaalde LBM simulaties) zijn deze relaties echter niet gekend. Men initialiseert het microscopische model dan traditioneel met een lokaal



Figuur 4: Evolutie van (a) $-d^{ac}\rho_x^{ac}(x,t) - \phi^{ac}(x,t)$, (b) $(1/3)\rho^{ac}(x,t) - \xi^{ac}(x,t)$ en (c) de dichtheid $\rho^{ac}(x,t)$ in roosterpunt $x = 9.95$. (d) is een detailopname van (c). (e) Statisch bifurcatiediagram voor de vergelijkingsvrije LBM tijdstapper met $\Delta T = 0.02$. Het statische bifurcatiediagram voor het volledige LBM van Fig. 3 wordt ook getoond ter vergelijking. Voor de betekenis van $w_i^\star$ verwijzen we naar Sect. 5.3 in de Engelstalige tekst.

evenwicht gebaseerd op de gegeven macroscopische grootheden. Voor het LBM is dit bijvoorbeeld het diffusieve evenwicht f_i^{eq} in (1). Zulk een initialisatie biedt geen enkele garantie op een correcte berekening van het trage overgangsgedrag van het systeem.

In [199] werd het volgende reconstructieschema voorgesteld om de LBM variabelen te initialiseren op basis van de gegeven dichtheid $\rho(x,0)$

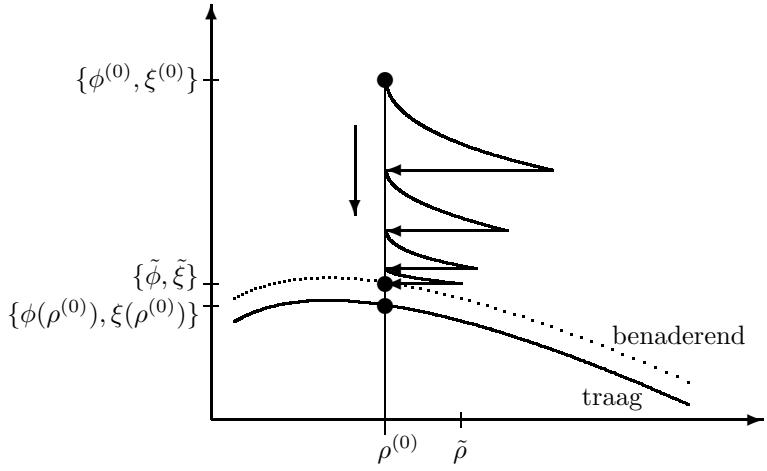
$$f_i(x,0) = w_i\,\rho(x,0) \quad \text{met} \quad \sum_{i=-1}^{1} w_i = 1\ . \tag{6}$$

Dit laat twee vrijheidsgraden over voor de keuze van de gewichten w_i en bepaalt aldus de keuze van de initiële hogere orde momenten ϕ en ξ. De keuze $w_i = 1/3$ (cfr. f_i^{eq} in (1)) komt overeen met $\phi(x,0) = 0$ en $\xi(x,0) = (1/3)\rho(x,0)$, hetgeen een zeer grove benadering van (5) is.

Figuur 4 toont de momenten ϕ, ξ en ρ voor simulaties met het FitzHugh-Nagumo LBM op verschillende tijdschalen. De initialisatie gebeurt via (6). De startwaarde is de $\rho(x)$-waarde van de stabiele statische oplossing bij $\varepsilon = 0.05$. Figuur 4 (a) en (b) toont het verschil van ϕ en ξ t.o.v. de eerste, respectievelijk nulde orde term in de theoretische functionaalrelaties (5). Na 10 à 20 LBM tijdstappen $\Delta t = 0.001$ zijn ϕ en ξ functionaal van ρ geworden. Door de slechte initialisatie van de hogere orde momenten is er echter een significant verschil tussen het transiënte traject op de trage meervoudigheid beschreven door $\rho(x,t)$ en het verwachte — hier constante — traject, zoals Fig. 4 (c) en (d) toont. Pas na langere tijd (bijvoorbeeld $\Delta T = 5 = 5000\Delta t$ in Fig. 4 (d)) verdwijnen deze effecten. Het bifurcatiediagram in Fig. 4 (e) voor het vergelijkingsvrije LBM met $\Delta T = 20\Delta t$ is dan ook zeer onnauwkeurig. Dit toont dat het erg belangrijk is om de functionaalrelaties zo goed mogelijk te benaderen tijdens de initialisatie (dus niet via (6)). We merken nog op dat deze relaties ook tot uiting komen in de eigenvectoren horende bij de dominante eigenwaarden van het gelineariseerde LBM.

6 Analyse van het Constrained Runs Algoritme

In de vorige sectie hebben we aangetoond dat een nauwkeurige initialisatie erg belangrijk is voor zowel vergelijkingsvrije modellering als voor pure LBM simulaties. Naar aanleiding van deze bevindingen ontwikkelden Gear en Kevrekidis het zogenaamde *constrained runs* (CR, simulatie-met-beperkingen) initialisatiealgoritme [68, 64]. Wij analyseren de stabiliteit en convergentie van dit algoritme voor het LBM (1). De theoretische resultaten worden numeriek geverifieerd. Tenslotte tonen we aan dat onze analyse ook geldig is voor het initialisatieschema van Mei en collega's [144, 22] toegepast op het LBM (1). Hieronder schetsen we kort het algoritme en de belangrijkste stellingen.



Figuur 5: Schets van de evolutie van het *constrained runs* algoritme.

6.1 Algoritme

Het CR algoritme is een iteratieschema dat de volledige microscopische toestand van een tijdsimulator berekend overeenkomstig de gegeven macroscopische variabelen. Voor het LBM van Sect. 3 berekent het schema dus ϕ en ξ voor een gegeven $\rho^{(0)} = \rho(x, 0)$. Figuur 5 schetst de evolutie van het algoritme. Startend van een willekeurige $\phi^{(0)}$ en $\xi^{(0)}$ worden er korte LBM simulaties uitgevoerd waarna de dichtheid telkens wordt teruggezet naar de waarde $\rho^{(0)}$. De uiteindelijke oplossing, het zogenaamde *vast punt*, duiden we aan als $\{\tilde{\phi}, \tilde{\xi}\}$. Dit vast punt is slechts een benadering van de toestand $\{\phi(\rho^{(0)}), \xi(\rho^{(0)})\}$ op de trage meervoudigheid. Deze laatste wordt volledig bepaald door $\rho^{(0)}$ via de relaties (5). De waarde $\tilde{\rho}$ is de dichtheid overeenkomstig $\{\tilde{\phi}, \tilde{\xi}\}$ (vlak voor de laatste terugzet-operatie naar $\rho^{(0)}$).

6.2 Stabiliteit en Convergentie

Stelling 1 (Stabiliteit). *Het* constrained runs *algoritme voor het rooster Boltzmann model* (1) *met periodieke, homogene Neumann of Dirichlet randvoorwaarden, is onvoorwaardelijk stabiel. De asymptotische convergentiefactor is* $\eta = |1 - \omega|$.

Bewijs. De eigenwaarden μ_m van de linearizatie (de Jacobiaanmatrix) van het CR algoritme bepalen de stabiliteit van het algoritme. Als alle eigenwaarden binnen de eenheidscirkel liggen, is de iteratie stabiel. We bewijzen dat de Jacobiaanmatrices (voor de verschillende randvoorwaarden) een spe-

cifieke ijle structuur hebben die leidt tot eigenwaarden μ_m, gelegen op een cirkel rond de oorsprong met straal $r = |1 - \omega|$. Per definitie is dit meteen ook de asymptotische convergentiefactor η. De CR iteratie is onvoorwaardelijk stabiel omdat $\omega \in (0, 2)$ (zie Sect. 3) en dus steeds $|\mu_m| = r < 1$. □

Stelling 2 (Convergentie). *Het* constrained runs *algoritme voor het LBM beschreven in stelling 1 convergeert naar een eerste orde nauwkeurige benadering* $\{\tilde{\phi}, \tilde{\xi}\}$ *van de toestand* (5) *op de trage meervoudigheid. De benaderingsfout wordt bepaald door het verschil* $\tilde{\rho} - \rho^{(0)}$ *en zijn afgeleiden.*

Bewijs. Omwille van de stabiliteit is er ook convergentie naar een vast punt. We bewijzen dat dit vast punt $\{\tilde{\phi}, \tilde{\xi}\}$ gegeven wordt door

$$\tilde{\phi} = -\frac{2\Delta x}{3\,\omega}\frac{\partial \rho^{(0)}}{\partial x} + \frac{\Delta x \Delta t}{3\omega^2}\frac{(4\omega - 2)}{(\omega - 2)}\frac{\partial F(\rho^{(0)})}{\partial x} + \frac{\Delta x}{\omega^2}\frac{(-2\omega + 2)}{(\omega - 2)}\frac{\partial(\tilde{\rho} - \rho^{(0)})}{\partial x}\,.$$
$$\tilde{\xi} = \frac{1}{3}\rho^{(0)} - \frac{\Delta t}{6\,\omega}F(\rho^{(0)}) + \frac{1}{2\omega}(\tilde{\rho} - \rho^{(0)})\,. \tag{7}$$

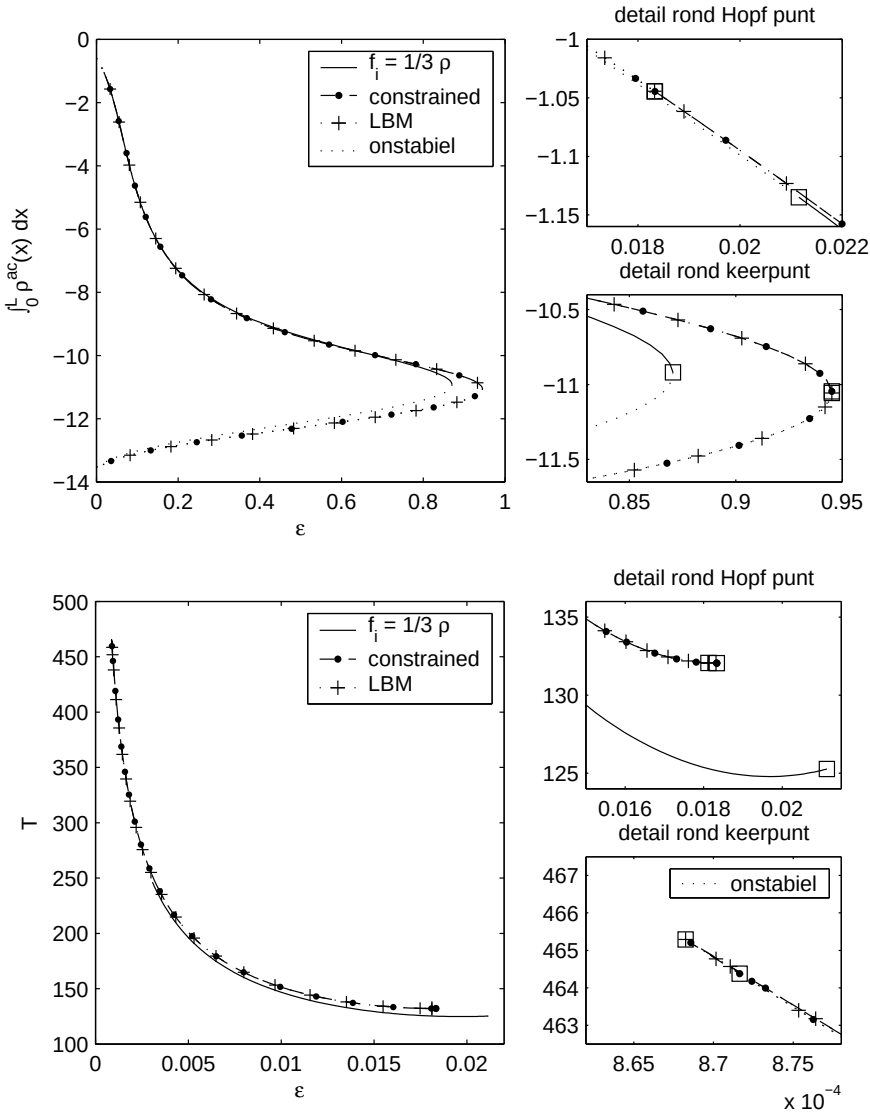
Bij vergelijking van deze relaties met de Chapman-Enskog relaties (5), zien we dat de eerste twee termen overeenkomen. □

7 Constrained Runs: Toepassingen en Uitbreidingen

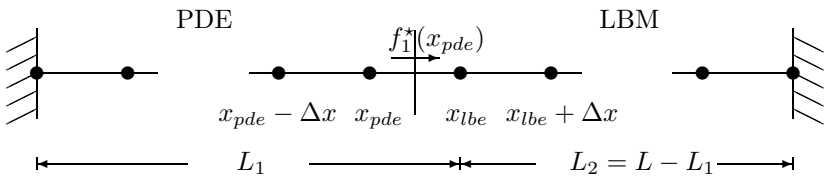
We gebruiken het *constrained runs* initialisatiealgoritme uit de vorige sectie als de reconstructieprocedure in de vergelijkingsvrije tijdstapper voor het FitzHugh-Nagumo LBM. Deze tijdstapper gebruiken we in een tijdstappergebaseerde bifurcatieanalyse zoals in Sect. 4. We vergelijken de resultaten met diegene berekend met de vergelijkingsvrije tijdstapper die het reconstructieschema (6) met $w_i = 1/3$ gebruikt. De tijdstap is $\Delta T = 0.02 = 20\Delta t$, dit is de tijd nodig om de functionaalrelaties te doen gelden uit simulatie (zie Fig. 4 (a)–(b)). Ter referentie tonen we de bifurcatiediagrammen berekend met het volledige LBM uit Fig. 3. Figuur 6 toont duidelijk dat de resultaten voor het CR algoritme zeer goed overeenkomen met de referentieoplossing.

Verder breiden we de stabiliteits- en convergentieanalyse van het CR algoritme uit voor bepaalde types LBM met een reactieterm die rechtstreeks afhangt van de mesoscopische f_i in plaats van de macroscopische ρ. De analyse verloopt analoog aan die in Sect. 5. We besluiten dat het CR algoritme stabiel is als het onderliggende LBM stabiel is.

Tenslotte implementeren we ook enkele meer complexe CR algoritmes die gebruik maken van interpolatietechnieken om een hogere orde nauwkeurigheid te bekomen (zie ook [64]). Door de relaties (7) voor het CR vast punt $\{\rho^{(0)}, \tilde{\phi}, \tilde{\xi}\}$ te vergelijken met de Chapman-Enskog relaties (5), zien we dat de benaderingsfout bepaald wordt door de factor $(\tilde{\rho} - \rho^{(0)})$ en zijn



Figuur 6: Bifurcatiediagram van statische (boven) en periodieke (onder) oplossingen voor het FitzHugh-Nagumo systeem. De vergelijkingsvrije tijdstappers gebruiken het reconstructieschema $f_i(x,0) = (1/3)\,\rho(x,0)$ (6) of het constrained runs algoritme. De tijdstap bedraagt $\Delta T = 0.02 = 20\Delta t$. We tonen ook de takken voor het volledige LBM ter referentie. De stippellijnen duiden onstabiele oplossingen aan. De bifurcatiepunten worden aangeduid met een vierkant symbool.



Figuur 7: Ruimtelijke koppeling van de PDE en het LBM.

ruimtelijke afgeleiden. Deze factor kan geïnterpreteerd worden als een grove benadering van de macroscopische tijdsafgeleide $\Delta t \partial \rho^{(0)}/\partial t$. In plaats van de dichtheid simpelweg terug te zetten, kan deze afgeleide benaderd worden door hogere orde discretisaties. We tonen numeriek aan dat de bekomen CR algoritmes slechts stabiel zijn voor een beperkt ω-interval. Tenslotte stellen we nog een variant voor die na de CR iteratie en een korte simulatie lokaal de trage meervoudigheid benadert om zo de nauwkeurigheid op te drijven.

8 Hybride Ruimtelijke Koppeling

De complexiteit van een dynamisch systeem varieert vaak in de ruimte. Bij de modellering kan het dan ook voordelig zijn om een meer microscopisch model te gebruiken op plaatsen waar de interacties tussen de deeltjes complex zijn, terwijl elders een macroscopisch model dat enkel het gedrag van de traag variërende macroscopische grootheden beschrijft, voldoende is. Door deze modellen ruimtelijk te koppelen bekomt men zogenaamde hybride modellen. Omdat deze modellen dikwijls zeer verschillende variabelen gebruiken, is een goede koppelingsstrategie erg belangrijk.

8.1 Opzet en Implementatie

We koppelen het LBM (1) met de PDE (4) zoals in Fig. 8.1. In de koppelingsregio kan de PDE dichtheid ρ makkelijk uit de LBM verdelingsfuncties $\mathbf{f} = [f_{-1}\, f_0\, f_1]'$ berekend worden via (2). De omgekeerde afbeelding is echter niet eenduidig (zie ook Sect. 5–7). Hiervoor gebruiken we de analytische Chapman-Enskog relaties (5) of het numerieke *constrained runs* algoritme uit Sect. 6. We gaan na hoe lokale informatie zich verspreidt doorheen het domein en tonen aan dat de globale ruimtelijke discretisatiefout een orde minder nauwkeurig is dan de lokale fout die gemaakt wordt in de koppelingszone.

We definiëren de lokale fout in de koppelingszone als de dominante term die overblijft als we de Chapman-Enskog relaties (5) afbreken tot op een bepaalde orde voor praktisch gebruik. Door (5) af te breken tot op eerste

orde termen en door gepaste discretisatie van de ruimtelijke afgeleide (en via $\mathbf{f} = M^{-1}\boldsymbol{\varrho}$ (3)) bekomen we het CE-1 schema

$$f_1(x_{pde}, t) = \frac{1}{3}\rho(x_{pde}, t) - \frac{\Delta x}{3\,\omega}\,\frac{\rho(x_{lbe}, t) - \rho(x_{pde} - \Delta x, t)}{2\Delta x}\ . \tag{8}$$

We gebruiken dit om de onbekende $f_1(x_{pde}, t)$ te berekenen die het LBM domein binnenkomt (cfr. Fig. 7). De lokale discretisatiefout van (8) is van grootteorde $\mathcal{O}(\Delta x^2)$. Omdat het CR algoritme uitdrukking (8) exact benadert (zie Sect. 6), verwachten we analoog gedrag voor het CR schema.

8.2 Foutenanalyse bij Statisch Evenwicht

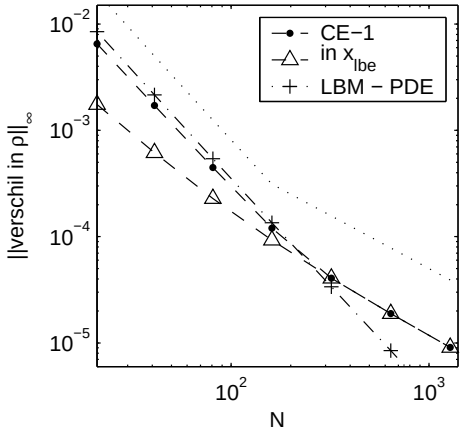
Om kwantificeerbare uitspraken te kunnen doen, leiden we analytische uitdrukkingen af voor de globale ruimtelijke discretisatiefout $E(x) = \rho(x) - \rho^c(x)$ van het hybride model in statisch evenwicht. Met $\rho^c(x)$ duiden we de exacte evenwichtsoplossing van de PDE (2.4) aan. Voor een gepast modelprobleem bewijzen we dat de maximale fout $E_1 = E(x_{lbe})$ van het CE-1 koppelingsschema bereikt wordt in $L_1 = x_{lbe}$ (zie Fig. 7) met waarde

$$E_1 = \frac{L_1 L_2}{L}(1-\omega)\frac{\Delta x}{6\omega}(\omega - 2)\left(2\frac{\mathrm{d}^2\rho^c(x_{lbe})}{\mathrm{d}x^2} - \frac{\mathrm{d}^2\rho^c(x_{lbe} + \Delta x)}{\mathrm{d}x^2}\right)\ . \tag{9}$$

Deze uitdrukking voorspelt dat de globale discretisatiefout zich gedraagt als $\mathcal{O}(\Delta x)$ voor constante ω, wat een verlies aan orde inhoudt.

8.3 Numerieke Resultaten

De theoretische uitdrukkingen werden uitvoerig numeriek getest. We bespreken hier slechts één van de numerieke resultaten, namelijk dat voor de zogenaamde Fisher vergelijking met niet-lineaire reactieterm. Figuur 8 toont de globale fout voor CE-1 koppeling bij statisch evenwicht in functie van het aantal roosterpunten N. Ook tonen we de waarde van deze fout in het punt x_{lbe} en de modelleerfout, zijnde het verschil tussen de oplossingen berekend met het LBM en de PDE apart op het volledige domein. Wanneer het aantal roosterpunten N groot is (dus voor kleine roosterafstand Δx), is de globale fout duidelijk van eerste orde en wordt het maximum bereikt in x_{lbe}, net zoals (9) ook voorspelt. Door de niet-lineaire koppeling wordt de maximale fout voor gematigde Δx-waarden echter niet meer bereikt in x_{lbe}. Integendeel, de (tweede orde) modelleringsfout tussen de gekoppelde modellen blijkt dominant te zijn. Dit suggereert dat de nauwkeurigheid van het CE-1 koppelingsschema voldoende is voor praktische berekeningen. Merk wel op dat enkel het gebruik van de volgende term in het Chapman-Enskog gebaseerde koppelingsschema (en dus een lokale derde orde fout) een globale tweede orde nauwkeurigheid waarborgt.



Figuur 8: De globale fout voor CE-1 koppeling (8) en de modelleerfout bij statisch evenwicht in functie van het aantal roosterpunten N. De stippellijnen met helling -2 en -1 zijn hulplijnen voor de lezer.

9 Besluiten

9.1 Belangrijkste Bijdragen en Besluiten

In dit proefschrift hebben we een aantal aspecten van meerschalige en vergelijkingsvrije modellering nader onderzocht. De nadruk lag hierbij op de analyse en meerschalige koppeling van de modellen. Het vergelijkingsvrije raamwerk ontwikkeld door Kevrekidis en collega's laat een macroscopische integratie toe van een onbekend macroscopisch model door zo efficiënt mogelijk gebruik te maken van microscopische simulaties. We implementeerden een klasse van mesoscopische rooster Boltzmann modellen (LBM) als de "microscopische" simulator om het vergelijkingsvrije raamwerk zelf grondig te kunnen analyseren.

Eerst toonden we aan dat tijdstapper-gebaseerde numerieke methodes ontwikkeld voor de bifurcatieanalyse van partiële differentiaalvergelijkingen ook gebruikt kunnen worden voor de bifurcatieanalyse van LBM. De tijdstapper kan zowel het volledige LBM zijn, alsook de vergelijkingsvrije tijdstapper voor het LBM.

Vervolgens richtten we de aandacht op het probleem van de meerschalige koppeling. Gegeven enkele macroscopische variabelen moet men consistente waarden genereren voor de microscopische of mesoscopische variabelen. Dit probleem doet zich voor bij de initialisatie van het LBM, de reconstructiestap in het vergelijkingsvrije raamwerk en de hybride meerschalige koppeling.

We toonden aan dat de reconstructie (ook wel *lifting* of initialisatie genoemd) een grote impact kan hebben op de nauwkeurigheid van de vergelijkingsvrije tijdstapper en de grootte van de macroscopische tijdstap. Dezelfde conclusie geldt voor de initialisatie van het LBM zelf. Om een nauwkeurige vergelijkingsvrije initialisatie mogelijk te maken, ontwikkelden Gear en Kevrekidis het *constrained runs* (simulatie-met-beperkingen) algoritme. Wij analyseerden dit algoritme voor het beschouwde LBM. We bewezen dat het algoritme onvoorwaardelijk stabiel is en convergeert met factor $|1 - \omega|$. De geconvergeerde oplossing komt tot op eerste orde termen overeen met de analytische Chapman-Enskog relaties, zijnde de microscopische toestand overeenkomstig de macroscopische beginvoorwaarden. Verder implementeerden we nog andere *constrained runs* schema's die gebruik maken van interpolatietechnieken om een grotere nauwkeurigheid te bekomen.

Bij de hybride koppeling van een LBM en een partiële differentiaalvergelijking kan men in de koppelingszone zowel de Chapman-Enskog relaties als het *constrained runs* algoritme gebruiken om de LBM variabelen te genereren uit de PDE variabelen. Een analyse van de globale ruimtelijke discretisatiefout van het hybride model toonde aan dat deze fout een orde minder nauwkeurig dan de lokale fout die gemaakt wordt in de koppelingsregio.

9.2 Richtlijnen voor Verder Onderzoek

De toepassing van bestaande numerieke technieken op LBM simulaties om de efficiëntie te verhogen is een recente trend in de LBM onderzoeksgemeenschap met nog voldoende ruimte voor nieuwe inbreng. Gevestigde technieken, zoals *multigrid*, of recentere technieken, zoals de vergelijkingsvrije tijdsversnellingsmethodes, kunnen hier zeker hun nut bewijzen.

Verder onderzoek naar hybride LBM/PDE modellen kan gebeuren door Δx en Δt verschillend te kiezen in de modellen en zo de efficiëntie te verhogen. Hiervoor kan gekeken worden naar bestaande roosterkoppelingstechnieken in beide onderzoeksdomeinen. In realistische toepassingen zijn het LBM en PDE model op de verschillende deeldomeinen niet equivalent in de macroscopische limiet, wat bijkomende gevolgen kan hebben voor de hybride methode.

Wat betreft de vergelijkingsvrije modellering is het interessant om een bifurcatieanalyse uit te voeren voor een meer efficiënte vergelijkingsvrije tijdstapper die gebruik maakt van één van de technieken beschreven in [47, 65, 108, 172, 218]. Verder kan de analyse van het *constrained runs* algoritme nog significant uitgebreid worden. We vermelden i) een analyse voor advectieproblemen; ii) een vergelijking met het onderzoek van Gorban en Karlin [74, 75, 76, 77]; iii) een vergelijking met de analyse voor stijve differentiaalvergelijkingen in [64]; iv) het gebruik van Newton-Krylov gebaseerde acceleratietechnieken; v) vergelijking met de initialisatieschema's in

[144, 189] voor meer realistische LBM.

In deze tekst spitsten we ons toe op de analyse van het vergelijkingsvrije raamwerk door een deterministisch mesoscopisch rooster Boltzmann model te gebruiken als substituut voor een echt microscopisch model. Vanuit dit oogpunt kan ons onderzoek dus beschouwd worden als een fundamentele stap in de analyse van vergelijkingsvrije modellering. Vergelijkingsvrije simulaties werden reeds gebruikt in heel wat toepassingen gemodelleerd door een echt microscopisch deeltjes-gebaseerd (en vaak stochastisch) model. De noodzakelijke numerieke analyse blijft echter voorlopig uit, niet in het minst omdat ze erg complex is. We hebben er alle vertrouwen in dat het onderzoek in dit proefschrift nuttig zal zijn bij de verdere analyse van het vergelijkingsvrije raamwerk wanneer meer microscopische modellen gebruikt worden.